MECHANICAL ENGINEERING AND SOLID MECHANICS SERIES

MATHEMATICAL AND MECHANICAL ENGINEERING SET

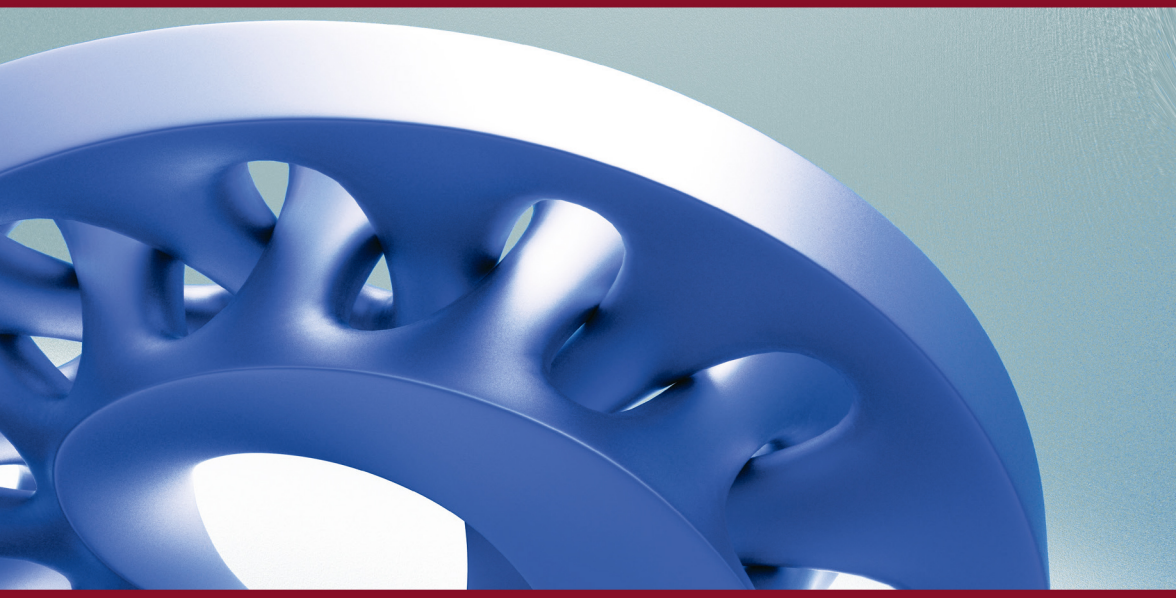

Volume 14

Thermal Convexity Analysis of a Solar Water Heating System

Moulay Abdelghani-Idrissi
Lamiae Vernières-Hassimi
Soufiane Abdelghani-Idrissi

ISTE

WILEY

Thermal Convexity Analysis of a Solar Water Heating System

Mathematical and Mechanical Engineering Set

coordinated by
Abdelkhalak El Hami

Volume 14

Thermal Convexity Analysis of a Solar Water Heating System

Moulay Abdelghani-Idrissi
Lamiae Vernières-Hassimi
Soufiane Abdelghani-Idrissi

ISTE

WILEY

First published 2025 in Great Britain and the United States by ISTE Ltd and John Wiley & Sons, Inc.

ISTE Ltd
27-37 St George's Road
London SW19 4EU
UK

www.iste.co.uk

John Wiley & Sons, Inc.
111 River Street
Hoboken, NJ 07030
USA

www.wiley.com

Library of Congress Control Number: 2025944981

British Library Cataloguing-in-Publication Data
A CIP record for this book is available from the British Library
ISBN 978-1-83669-083-2

The manufacturer's authorized representative according to the EU General Product Safety Regulation is Wiley-VCH GmbH, Boschstr. 12, 69469 Weinheim, Germany, e-mail: Product_Safety@wiley.com.

Contents

Preface vii

Chapter 1. Global Energy Context 1

1.1. Global energy consumption 1
1.2. Solar energy development 5

Chapter 2. Thermal Solar Systems 11

2.1. High-temperature solar thermal 14
2.1.1. Parabolic concentrators 15
2.1.2. Tower plants 31
2.1.3. Cylindrical-parabolic collectors 36
2.2. Low-temperature solar thermal 69
2.2.1. Solar pool heating 73
2.2.2. Solar space heating 75
2.2.3. Domestic hot water 77
2.3. Solar panels 82
2.3.1. Types of solar panels 82
2.3.2. Solar collector efficiency 86

Chapter 3. Thermal Convexity Principle 117

3.1. Single-phase fluid mixing 117
3.2. Fluid heat exchange through an isotherm surface 120
3.3. Heat exchange along a pipe crossing an isotherm compartment 121
3.4. Solar receiver 123
3.5. Heat exchange along a tubular heat exchanger 124

Chapter 4. Solar Water Heating Analysis 139

4.1. Thermal modeling of solar water heating 139
4.1.1. Collector model 139
4.1.2. Heat exchanger 143
4.1.3. Storage tank 146
4.1.4. Solar water heating global model 148
4.2. Solar position and radiation 149
4.2.1. Sun position 150
4.2.2. Solar radiation 155
4.3. Simulation and discussion 158
4.3.1. Daily response to variation in solar radiation 159
4.3.2. Effect of the calorific fluid flow rate 161
4.4. Experimental results with a fixed solar collector 170
4.4.1. Without consumption of domestic hot water 170
4.4.2. With consumption of domestic hot water 177
4.5. Experimental results with the solar tracker 181

Conclusion 193

Appendix. Principles of Heat Transfer 201

References 241

Index 247

Preface

The urgent global need for sustainable energy has placed *solar energy* at the forefront of technological innovation. Among the different renewable solutions, *solar thermal systems* represent a highly efficient and environmentally friendly approach to producing heat for domestic, industrial, and energy applications. However, the optimization of their design and operation remains a scientific and engineering challenge.

This book introduces and develops the concept of *thermal convexity*, a novel theoretical framework that provides deeper understanding into *heat transfer processes* in solar water heating systems. By combining *fundamental principles of conduction, convection, and radiation* with advanced modeling techniques, thermal convexity offers a new perspective for analyzing system efficiency and guiding design improvements.

This book is structured to progress from the *global energy context* to the fundamentals of solar thermal technologies, before applying thermal convexity to the *simulation and experimental validation of solar water heating systems*. The inclusion of both *theoretical developments and experimental results* ensures a balance between scientific approach and practical relevance.

This book is intended for *researchers, engineers, and graduate students* working in the fields of *renewable energy, thermal sciences, and process engineering*. It aims to contribute not only to academic knowledge but also to the practical advancement of sustainable technologies, where innovation is urgently needed.

We hope readers will find in these pages both the *scientific foundations* and the *inspiration* to pursue new directions in solar thermal research and applications.

September 2025

1

Global Energy Context

1.1. Global energy consumption

In the context of sustainable development, the world faces a dual global challenge corresponding to the imminent depletion of fossil energy resources and the escalating issues of climate change. The urgency of these challenges is compounded by the relentless growth in global energy consumption. As depicted in Figure 1.1, which illustrates the annual evolution of global primary energy consumption by type, there is a clear trend of increasing demand across various energy sources.

This figure reveals the shifting dynamics in energy consumption patterns, reflecting the rising energy needs of a growing global population and expanding economies. The detailed analysis extends beyond mere consumption trends, delving into the implications of these patterns for future energy policies and strategies. It examines the sustainability of current energy practices, considering the environmental impact of continued reliance on fossil fuels. The exploration of the potential of renewable energy sources is necessary to meet the increasing energy demand while mitigating adverse environmental effects.

Moreover, the economic and technological challenges associated with the transition to sustainable energy systems have to be considered. These aspects evaluate the role of innovative technologies and policy interventions in promoting energy efficiency and reducing carbon footprints. By providing a comprehensive overview of the global energy landscape, the critical importance of integrating sustainability into energy planning and decision-making processes is highlighted.

To address the pressing challenges of energy sustainability and climate change, robust incentives are being implemented to accelerate the development of renewable energy sources.

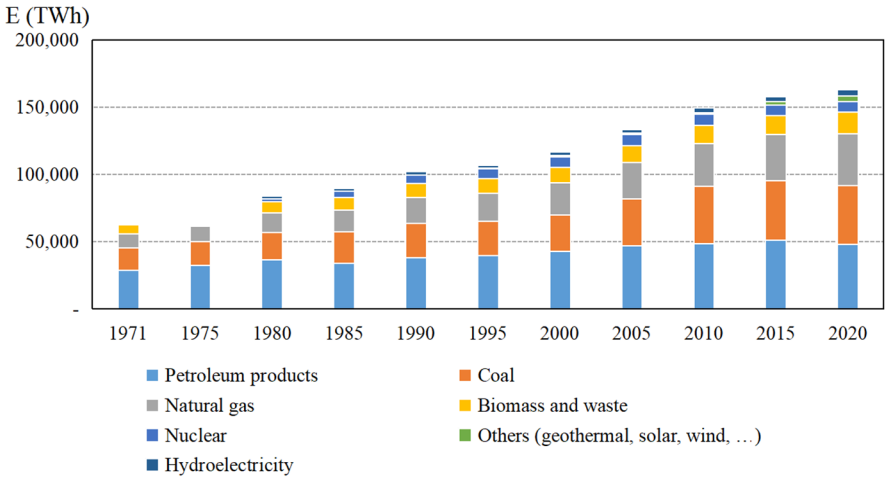

Figure 1.1. *Evolution of the global primary energy consumption[1]. For a color version of this figure, see www.iste.co.uk/abdelghani-idrissi/solarwaterheating.zip*

These measures aim to significantly reduce greenhouse gas emissions and provide alternatives for rapidly depleting fossil energy resources. The urgency of these efforts is underscored by the continuous rise in global energy consumption and the adverse environmental impacts associated with fossil fuels. The introduction and expansion of renewable energy technologies are crucial components of this strategy. The progress in the generation of modern renewable energy from 1971 to 2022 is illustrated in Figure 1.2 (Ritchie et al. 2020). This figure (OurWorldInData.org) highlights the substantial growth in renewable energy capacity, reflecting the global commitment to transitioning toward more sustainable energy systems. The analysis of renewable energy development encompasses various technologies, including solar, wind, hydroelectric and bioenergy. Each of these technologies has seen significant advancements in efficiency, cost reduction and deployment scale. Solar energy, for example, has benefited from technological innovations in photovoltaic (PV) cells and energy storage systems, making it more accessible and cost-effective. Wind energy has similarly experienced technological improvements, leading to larger, more efficient turbines and expanded offshore wind farms. In addition to technological advancements, the role of policy and regulatory frameworks is critically examined.

Government incentives, such as tax credits, subsidies and feed-in tariffs, have played a pivotal role in fostering the growth of renewable energy. International

1 Based on data from IEA (International Energy Agency).

agreements and national policies aimed at reducing carbon emissions have further spurred investment and research in renewable technologies.

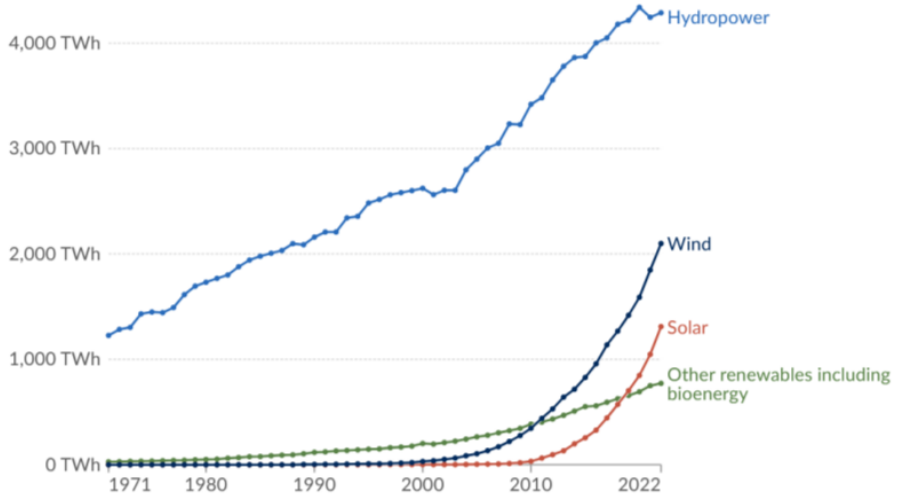

Figure 1.2. *Modern renewable energy generation by source*

Furthermore, the socioeconomic benefits of transitioning to renewable energy are explored. These include job creation in the renewable energy sector, energy security through reduced dependence on imported fossil fuels and the potential for rural development through decentralized energy systems.

The curves in Figure 1.2 demonstrate a marked acceleration in the adoption of wind and solar energy starting in the 2000s and 2010s, respectively. Despite this progress, the global share of renewable energy remained around 15% in 2019, a modest proportion compared with the consumption of primary fossil energy sources. This disparity highlights a significant challenge in meeting the sustainable development goals (SDGs), which include ambitious targets for 2050, particularly the attainment of net zero emissions (NZEs). The current contribution of renewable energies is insufficient to meet the projected energy demand and the emissions reduction trajectory outlined in forecast scenarios. Consequently, there is a pressing need for the development and deployment of new energy resources coupled with efficient and reliable technologies. These advancements are essential to bridge the gap between current capabilities and future energy needs. An in-depth analysis of the progress in renewable energy reveals that, while substantial advancements have been made, particularly in solar and wind technologies, the pace of transition must significantly increase. Solar energy has benefitted from advancements in PV

technology, improving efficiency and reducing costs, whereas wind energy has seen enhancements in turbine design and offshore wind farm development.

Moreover, policy frameworks and regulatory incentives have been instrumental in driving renewable energy growth. Government initiatives, such as tax incentives, subsidies and renewable energy mandates, have encouraged investment and innovation in the sector. However, to achieve the 2050 targets, these policies must be expanded and strengthened.

The potential socioeconomic benefits of an accelerated transition to renewable energy are substantial. Increased investment in renewable technologies can drive job creation, enhance energy security by reducing dependence on imported fossil fuels, and promote sustainable economic growth. Additionally, decentralized renewable energy systems can contribute to rural development and increase access to electricity in underserved regions.

To realize these benefits and meet the NZE targets, a multifaceted approach is necessary. This includes advancing research and development in emerging technologies, such as advanced energy storage, smart grids and next-generation biofuels. Furthermore, international cooperation and knowledge sharing can expedite technological advancements and implementation strategies across different regions. Notably, while significant strides have been made in the adoption of renewable energy, the current levels are insufficient to meet the ambitious global targets set for 2050. This state of affairs underscores the need for accelerated development and deployment of renewable energy technologies. Achieving a sustainable and resilient energy future will require robust policy support, technological innovation and collaborative efforts on a global scale.

The primary forms of energy utilized across various sectors include electrical, thermal and mechanical energy. Electrical energy is generated from a diverse array of sources, including nuclear, thermal, hydroelectric, wind and solar power plants. This form of energy is extensively used to power household appliances, lighting systems, electric heating systems, electronic devices and industrial machinery.

The thermal energy associated with heating and cooling plays a crucial role in several applications. It is used for heating buildings, generating steam in thermal and nuclear power plants, powering thermal engines in internal combustion vehicles and facilitating various industrial processes. This energy form is fundamental for maintaining comfortable indoor environments and enabling the functionality of numerous industrial operations.

Mechanical energy, which is linked to motion and force, is essential in a multitude of contexts. It is harnessed in internal combustion and electric motors to

propel vehicles, drive industrial machinery and operate lifting and transportation devices. Mechanical energy is a cornerstone of modern industry, contributing to the operation of equipment and infrastructure that support daily life and economic activity.

The energy needs of humanity are highly variable and influenced by factors such as geographic region, level of economic development, consumption habits and lifestyle. In economically developed regions, the demand for electrical and thermal energy is significantly greater because of the widespread use of electronic devices, extensive heating and cooling systems, and industrial activities. On the other hand, in less developed regions, the energy demand may be lower but still crucial for basic needs such as cooking, heating and transportation.

Understanding the diverse applications and demands for these primary forms of energy underlines the complexity of meeting global energy needs. As societies continue to evolve, the efficient and sustainable management of electrical, thermal and mechanical energy becomes increasingly vital. This requires not only technological advancements and infrastructure development but also comprehensive policies and international cooperation to ensure a balanced and equitable distribution of energy resources.

1.2. Solar energy development

The transition to renewable energy sources is paramount in addressing the dual challenges of resource depletion and climate change. By leveraging advancements in technology and fostering innovation, it is possible to increase the efficiency and sustainability of energy production and consumption. This holistic approach is essential for achieving long-term energy security and environmental sustainability, ensuring that the energy needs of future generations are met without compromising the planet's ecological balance.

The development of solar energy offers a vital alternative to curbing the overexploitation of fossil fuels, which are major contributors to extensive greenhouse gas emissions and, consequently, climate change. Solar energy, as a renewable and environmentally friendly resource, has compelling advantages that make it a crucial component of sustainable energy strategies worldwide.

One of the primary benefits of solar energy is its widespread availability. Unlike fossil fuels, which are concentrated in specific regions and require extensive extraction and transportation efforts, solar energy can be harnessed directly from Sun radiation available across diverse geographical areas. This widespread availability

reduces the geopolitical risks associated with the energy supply and enhances energy security for many nations.

However, the abundance of solar energy is subject to significant fluctuations based on local meteorological conditions. As depicted in Figure 1.3, which shows the annual solar radiation distribution across the world, certain regions receive higher levels of solar radiation than others. Areas near the equator, for example, generally experience more consistent and intense solar radiation, making them prime locations for solar energy projects. Conversely, regions with frequent cloud cover or higher latitudes may experience less consistent solar availability, which can impact the efficiency and output of solar energy systems.

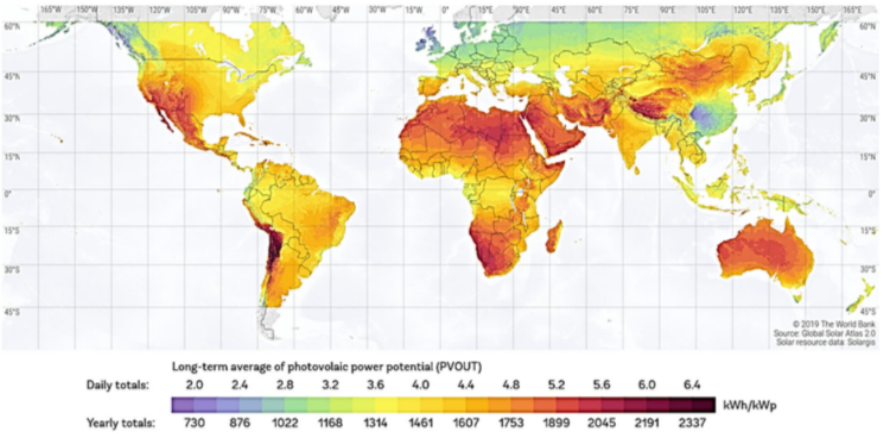

Figure 1.3. *World map of global solar radiation (available at: https://solargis.com/maps-and-gis-data/overview). For a color version of this figure, see www.iste.co.uk/abdelghani-idrissi/solarwaterheating.zip*

Despite these variations, advancements in solar technology have made it increasingly feasible to harness solar energy efficiently, even under less optimal conditions. Innovations such as PV cells with higher conversion efficiencies, concentrated solar power systems and improved energy storage solutions have significantly enhanced the viability of solar energy. These technologies allow for better capture, conversion and storage of solar energy, ensuring a more reliable and continuous energy supply.

Moreover, solar energy systems are modular and scalable, making them suitable for a wide range of applications, from small residential installations to large-scale solar farms. This flexibility allows for tailored solutions that can meet specific energy needs and local conditions. In rural and remote areas, for example,

decentralized solar energy systems can provide a critical source of electricity, reducing reliance on centralized power grids and fostering local development.

The environmental benefits of solar energy are substantial. Unlike fossil fuel-based energy production, which releases significant amounts of carbon dioxide and other pollutants, solar energy systems generate electricity without emitting greenhouse gases. This reduction in emissions is crucial for mitigating climate change and improving air quality. Additionally, solar energy systems have a smaller ecological footprint compared to other energy sources, as they do not require extensive water use or large-scale land disturbances, once installed.

The economic implications of solar energy development are also noteworthy. The growing solar industry has become a significant source of job creation, spanning manufacturing, installation, maintenance, and research and development. Investment in solar energy infrastructure can stimulate economic growth, create new markets and reduce energy costs over the long term. Furthermore, as the cost of solar technology continues to decrease, solar energy is becoming increasingly competitive with traditional fossil fuels, making it an attractive option for both developed and developing economies.

Solar energy, derived from the radiation emitted by the Sun, is a plentiful resource. The amount of solar radiation that reaches the Earth's surface is substantial enough to meet global energy demands. Given the vast surface area of the Earth, the distribution of solar radiation is extensive, allowing significant energy capture and utilization across various regions. This widespread availability is a critical advantage of solar energy, ensuring that it can be harnessed in diverse geographical locations to fulfill energy needs.

Note that solar energy can be effectively integrated with other energy sources to create a more robust and efficient energy system. This blending, or hybridization, can address the intermittent nature of solar power, which varies with weather conditions and time of day. By combining solar energy with wind, hydro or even conventional fossil fuels, energy systems can achieve greater reliability and stability. For example, solar energy can provide power during the day, whereas other sources can supplement it during nighttime or cloudy periods. This optimized mix can enhance energy security and reduce dependency on any single energy source.

One of the notable advantages of solar energy is its decentralized distribution. Solar panels and installations can be deployed at the point of consumption, such as on rooftops of residential, commercial, and industrial buildings. This decentralized approach eliminates the need for the extensive transportation infrastructure that is typically required for fossil fuels, which have to be mined, processed and transported over long distances. Consequently, solar energy reduces logistical

challenges and associated costs, making it a more efficient and accessible energy solution.

Promoting the growth of solar energy is essential for diversifying the global energy mix. A diversified energy portfolio enhances resilience against market fluctuations, geopolitical tensions and supply chain disruptions. Solar energy, being a renewable and inexhaustible resource, provides a stable and predictable addition to the energy mix. By investing in solar energy infrastructure, countries can reduce their reliance on imported fuels and mitigate the risks associated with energy supply shortages. This diversification also supports environmental sustainability by reducing greenhouse gas emissions and combating climate change.

Solar energy reaches the Earth in approximately eight light-minutes, highlighting the immediacy and directness of solar radiation. Annually, the Earth receives an immense amount of solar energy, estimated to be 10,000 times greater than the total energy consumption by humans. This vast potential underscores the feasibility of using solar energy as a primary energy source. Harnessing even a fraction of this energy could significantly exceed current global energy demands, emphasizing the need for advanced solar technologies and efficient energy capture systems.

The Sun, with an estimated lifespan of 5–10 billion years, represents a virtually boundless energy resource from a human perspective. This longevity ensures that solar energy will remain a viable and sustainable resource for the foreseeable future. Unlike finite fossil fuels, solar energy does not deplete over time, providing a continuous source of energy. This characteristic makes solar power a cornerstone of long-term energy strategies aimed at achieving sustainability and energy independence.

Solar energy is a versatile resource that can be harnessed and converted into both electrical and thermal energy. These two forms of energy conversion play crucial roles in modern energy systems, each with distinct methods and applications. The primary method of converting solar energy into electrical energy is through the PV effect.

This process begins when Sun radiation, which is composed of photons, strikes the surface of a PV material, typically semiconductor silicon. The photon energy is absorbed by the material, which excites electrons, enabling them to break free from their atomic structure. This liberation creates an electron–hole pair: the free electron is now mobile, and the positively charged hole is left behind. An intrinsic electric field within the PV material drives these free electrons and holes in opposite directions. Metal contacts, strategically placed on the top and bottom of the material, capture free electrons, generating an electric current. This current is then available to power electrical devices or can be stored in batteries for future use.

Solar energy can also be converted into thermal energy, which involves increasing the thermal agitation of atoms and molecules in a material when solar photons are absorbed. This process increases the kinetic energy of the particles, manifesting as heat. The generated heat can be efficiently transferred to a fluid, such as water or air, via a heat exchanger. This fluid then transports the thermal energy to an insulated storage tank, where it can be utilized for various applications, including domestic heating, industrial processes or electricity generation through steam turbines.

The conversion of solar energy into electrical and thermal forms offers a wide range of applications, enhancing energy efficiency and sustainability. PV systems are commonly used in residential, commercial and utility-scale installations, providing clean and renewable electricity. These systems can be integrated into buildings, installed on open land or used in remote areas to provide off-grid power solutions.

Thermal energy systems, on the other hand, are employed in solar water heaters, space heating and industrial heat processes. Concentrated solar power plants use mirrors or lenses to focus sunlight onto a small area, generating high temperatures that produce steam for electricity generation. This method leverages the thermal properties of solar energy to create a reliable and scalable energy source.

As technology advances, the efficiency of both PV and thermal conversion processes continues to improve. Innovations in materials science, such as the development of perovskite solar cells, promise higher efficiency and lower costs for PV systems. Similarly, advancements in thermal storage technologies, including molten salt and phase-change materials, enhance the capability to store and utilize solar thermal energy effectively.

2

Thermal Solar Systems

As previously discussed, the conversion of solar energy into thermal energy is achieved primarily through the use of advanced solar collectors. These collectors play a critical role in harnessing solar radiation, capturing the sun's energy and transferring it as heat to the materials from which they are constructed. The effectiveness of this thermal transfer depends significantly on the materials' capacity to absorb a wide range of solar wavelengths, with a particular emphasis on infrared radiation, which carries a substantial portion of solar energy.

Materials that possess strong absorption characteristics across the full solar spectrum, encompassing ultraviolet, visible and infrared wavelengths, tend to undergo more pronounced heating. This ability to absorb and convert solar energy directly into heat is central to the efficiency of solar thermal systems. Collectors crafted from materials with high spectral absorption rates not only maximize energy capture but also enhance overall thermal performance, making them indispensable in applications that range from solar water heating to large-scale solar power plants.

Thus, the careful selection of materials, with consideration for their spectral absorption properties, plays a pivotal role in optimizing the functionality of solar collectors, ensuring that they efficiently convert solar radiation into usable thermal energy.

Several fundamental characteristics define an effective thermal absorber, each contributing to its ability to efficiently capture and transfer heat. Among these factors is the thermal conductivity, which governs the rate at which heat can move through the material. A high thermal conductivity ensures that once solar energy is absorbed, it can be rapidly and evenly distributed across the material, enhancing the overall performance of the system. This property is especially essential in

applications where the efficient transfer of heat to adjacent systems or storage units is important for maximizing energy use.

Another key factor is the color of the material, which plays a significant role in its capacity to absorb solar radiation. Darker-colored materials, particularly those with black or near-black surfaces, are well known for their higher absorption rates than lighter-colored materials. This advantage arises from the fact that darker hues absorb a wider spectrum of solar radiation, including visible and infrared wavelengths, allowing them to capture more energy from sunlight. Lighter shades, in contrast, tend to reflect more solar radiation, reducing their effectiveness as thermal absorbers.

Moreover, the surface texture of the absorber can also influence its performance. Materials with rough or matte surfaces are generally more efficient at trapping and retaining solar radiation, as they reduce reflection and increase the surface area available for energy absorption. These combined factors, such as thermal conductivity, color and surface texture, work synergistically to increase the efficiency of a thermal absorber, making them key considerations in the design and selection of materials for solar energy systems.

The solar thermal system harnesses this absorbed heat by transferring it to a fluid medium, typically water, although air is occasionally used as well. Solar collectors are meticulously designed to optimize the absorption and transfer of solar energy, thereby ensuring maximum efficiency in the heat recovery process.

Solar thermal systems encompass a diverse range of technologies, each tailored to operate across different temperature ranges. Figure 2.1 shows the different types of solar collectors according to their temperature range. This inherent variability in solar thermal systems allows them to be finely tuned for a wide range of specific applications and thermal requirements, underscoring the remarkable versatility and adaptability of solar energy utilization.

High-temperature solar thermal systems are meticulously designed to meet the demands of applications that require elevated thermal outputs, often exceeding several hundred degrees Celsius. These systems are particularly well suited for energy-intensive industrial processes, such as steam generation, chemical production, metal smelting and other operations that rely on significant thermal energy input to sustain production efficiency. Concentrated solar power (CSP) plants, for example, use high-temperature collectors, such as parabolic troughs or solar towers, to achieve the necessary heat for driving turbines or other large-scale industrial mechanisms.

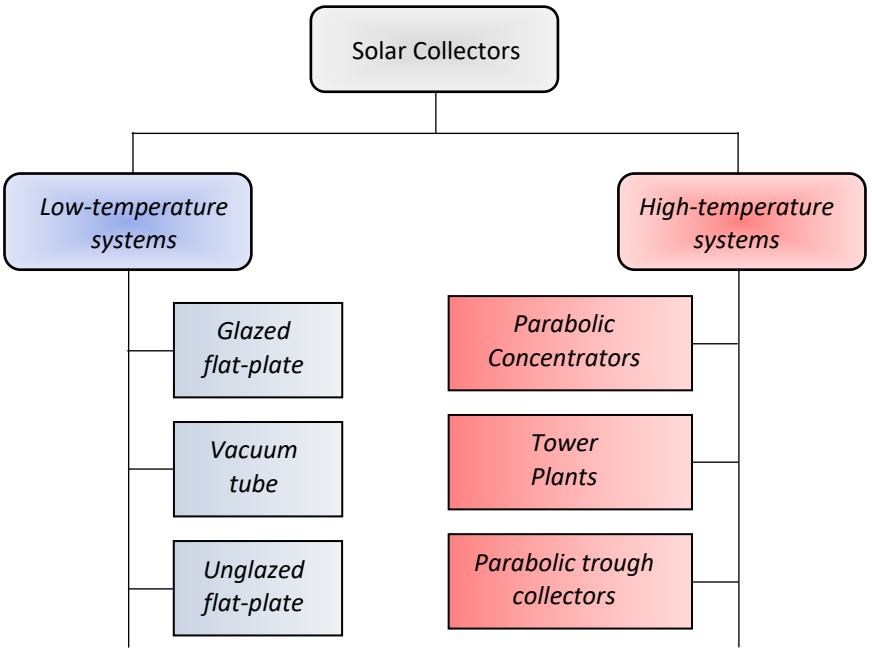

Figure 2.1. *Different type of solar collectors according to the temperature range application*

On the other hand, low-temperature solar thermal systems are specifically tailored for applications that demand comparatively lower levels of heat, typically below 100°C. These systems are widely used in residential and commercial settings, where the primary requirements include tasks such as water heating, space heating and pool heating. For example, solar water heaters efficiently harness solar energy to provide hot water for domestic use, reducing reliance on conventional energy sources and lowering utility costs. In colder climates, low-temperature solar systems can also be integrated into underfloor heating systems, maintaining comfortable indoor environments while minimizing energy consumption.

The ability to customize solar thermal solutions according to precise temperature requirements enhances the broad applicability of solar energy across different sectors. Whether addressing the high-energy needs of industrial operations or the everyday thermal demands of households, solar thermal technology offers scalable solutions that can be adapted to diverse operational environments. This flexibility not only maximizes energy efficiency but also positions solar energy as a viable and sustainable alternative to traditional energy sources, catering to both large-scale industrial applications and small-scale residential needs.

2.1. High-temperature solar thermal

CSP stands out as one of the most economically viable methods for attaining the elevated temperatures required for steam generation in practical applications, typically ranging from 400°C to 1,000°C. This innovative technique employs advanced optical devices, such as mirrors or lenses, to focus solar radiation onto a concentrated area that is strategically positioned between the solar source and the absorber.

By concentrating solar energy, CSP minimizes the effective surface area of the absorber, thereby significantly reducing radiative energy losses. This concentrated approach not only enhances the overall efficiency of the system but also allows for the generation of high-temperature steam, which is essential for powering turbines in electricity generation or driving various industrial processes.

Furthermore, the design of CSP systems can vary, encompassing various configurations such as parabolic troughs, solar towers and dish systems, each tailored to optimize the collection and conversion of solar energy based on specific operational needs. For example, parabolic trough systems utilize curved mirrors to focus sunlight onto a receiver pipe containing heat-transfer fluid, whereas solar towers use a field of mirrors to direct sunlight to a central receiver atop a tall tower.

The ability of CSP systems to store thermal energy for later use further amplifies their appeal, enabling continuous power generation, even when sunlight is not available.

By integrating thermal energy storage solutions, such as molten salt, CSP plants can provide a reliable energy supply, thereby supporting grid stability and enhancing the overall utility of solar energy in both residential and industrial contexts. As such, CSP not only represents a cutting-edge approach to solar energy utilization but also plays an important role in the transition toward sustainable energy solutions.

However, these technologies predominantly rely on the direct normal irradiance component of solar resources. Consequently, regions characterized by consistently clear skies and abundant direct sunlight are especially well suited for the deployment and optimization of CSP systems.

Once the solar energy is concentrated and absorbed, it generates, for example, heat that produces steam. This steam then powers a turbine for rotation, which drives a generator to convert mechanical energy into electrical energy. This process, known as heliothermodynamics, demonstrates a highly efficient method of converting solar energy into usable electrical power.

There are three primary technologies utilized in CSP plants to effectively harness solar energy and convert it into usable thermal energy:

– Parabolic concentrators: these innovative systems employ parabolic mirrors to concentrate sunlight onto a receiver strategically positioned at the focal point of the mirror. The design allows the mirrors to track the Sun movement throughout the day, ensuring optimal sunlight capture. When the sunlight is focused, it generates high temperatures within the receiver, where a heat-transfer fluid circulates to absorb and transport the thermal energy for steam generation.

– Solar power towers: in this configuration, an array of flat, movable mirrors known as heliostats work in unison to direct sunlight toward a central receiver mounted atop a tall tower. The heliostats adjust their angles to follow the Sun trajectory, maximizing solar radiation capture throughout the day. This concentrated solar energy is then used to heat a fluid within the receiver, producing steam that can drive turbines for electricity generation. Solar power towers are particularly effective in achieving high temperatures, making them ideal for large-scale energy production.

– Parabolic dish systems: these systems feature a parabolic dish-shaped mirror that focuses sunlight onto a receiver situated at its focal point. The design is compact and highly efficient, as the dish can track the Sun to optimize solar capture. The concentrated sunlight heats a working fluid within the receiver, which can then be converted into mechanical energy or used to generate electricity. Parabolic dish systems are versatile, allowing for both small-scale applications and integration into larger energy systems.

Together, these three technologies exemplify the diversity and adaptability of CSP systems. Each method offers unique advantages, enabling CSP plants to cater to varying energy demands while significantly contributing to the transition toward sustainable energy solutions.

2.1.1. *Parabolic concentrators*

As previously mentioned, parabolic concentrators are designed to focus sunlight onto a single point known as the focal point of a parabola. By utilizing curved mirrors or reflective surfaces, they concentrate incoming Sun rays onto a receiver located at the focal point. The intense heat generated at this focal point can then be used to produce steam for electricity generation.

A parabolic dish system features an intricately designed array of mirrors, each meticulously shaped as a parabolic dish, reminiscent of the contours of a circular paraboloid, similar to that of a satellite dish. This typical design is purposefully

engineered to convert incoming plane waves, which travel parallel to the axis of the dish, into converging spherical waves that are focused toward a fixed focal point.

One of the defining characteristics of parabolic dish systems is their ability to maintain a stationary focus. Unlike other systems, where the focal point can shift in response to various factors, the design of the parabolic dish ensures that the focal point remains constant. To achieve this precision, the reflectors are finely adjusted to ensure that they are perfectly aligned with the incoming waves, thereby maximizing the system's efficiency and performance.

The process of attaining this precise focus is not without its challenges. It requires an extraordinary level of accuracy during manufacturing, as even slight misalignments can lead to significant losses in performance. This meticulous attention to detail is crucial, as the efficiency of the system hinges on the ability to direct and concentrate waves effectively. These manufacturing challenges underscore the complexity of creating a parabolic dish system that operates at optimal performance levels, highlighting the intersection of advanced engineering and precision craftsmanship (Luna et al. 2018).

Moreover, the stationary nature of the focal point allows for a range of applications in various fields, from telecommunications to astronomy, where consistent and reliable wave convergence is essential. This versatility, combined with the technical challenges involved, highlights the significance of parabolic dish systems in modern technology.

The system operates by using mirrors and lenses to concentrate sunlight onto a fixed focal point, where a receiver is strategically positioned. The concentrated solar energy heats the transfer fluid within the receiver to the desired temperature and pressure. This heated fluid then drives an engine attached to the receiver, thereby generating electricity. The entire process is based on the ability to maintain a consistent and highly focused beam of solar energy onto the receiver.

Parabolic dish collectors present numerous advantages over centralized power supply systems, making them an attractive option for harnessing solar energy. One of the most significant benefits is their higher optical efficiency. The parabolic shape of the mirrors is meticulously designed to concentrate a high percentage of incoming solar radiation onto the receiver, maximizing energy capture. This design allows for effective focusing of sunlight, which translates into enhanced thermal energy conversion and improved overall system performance.

Furthermore, parabolic dish systems exhibit minimal start-up losses, a significant advantage in energy generation. These systems are capable of rapidly reaching operational temperatures, enabling them to begin generating power with minimal

delay. This quick responsiveness is particularly beneficial during fluctuating sunlight conditions, allowing for more consistent energy production throughout the day.

Another noteworthy advantage of parabolic dish collectors is their remarkable modularity. Each dish operates independently, providing a level of flexibility that centralized systems cannot match. This modular approach allows for incremental increases in capacity, enabling users to expand their energy generation capabilities in line with their specific needs and resources. As a result, parabolic dish systems can be deployed in a variety of settings, from small-scale residential applications to larger commercial projects.

This inherent flexibility not only enhances operational efficiency but also contributes to the cost-effectiveness of parabolic dish systems compared with traditional centralized power generation. By reducing the need for extensive infrastructure and allowing for tailored scaling, these systems can adapt to varying energy demands and budgetary constraints. Collectively, these advantages position parabolic dish collectors as a compelling alternative to conventional energy generation methods, promoting sustainable energy practices and fostering the transition toward renewable energy solutions.

The economic and operational benefits of parabolic dish systems stem from their ability to maximize the concentration of solar energy, resulting in higher temperatures and more efficient power generation. This makes them particularly suitable for decentralized applications where flexibility and scalability are necessary.

Figure 2.2 illustrates a dish concentrator that effectively focuses radiation onto a receiver, showcasing both the involved design and the operational functionality of this advanced technology. The figure shows the parabolic shape of the dish, which is engineered to optimize the collection of solar radiation by directing sunlight toward a specific focal point. This focal point is where the receiver is positioned, allowing it to efficiently absorb the concentrated energy.

The figure highlights the various components of the dish concentrator, including the arrangement of the mirror, which is carefully angled to ensure maximum reflectivity and minimal loss of energy. Additionally, it highlights the alignment of the receiver within the focal zone, where it converts the focused radiation into usable thermal or electrical energy.

To determine the appropriate size of a symmetric parabolic concentrator, the dimensions of the parabola are closely related by the fundamental equation of a parabola. This equation defines the geometric relationship between the focus, vertex

and directrix of the parabola, establishing a precise framework for the design of the concentrator.

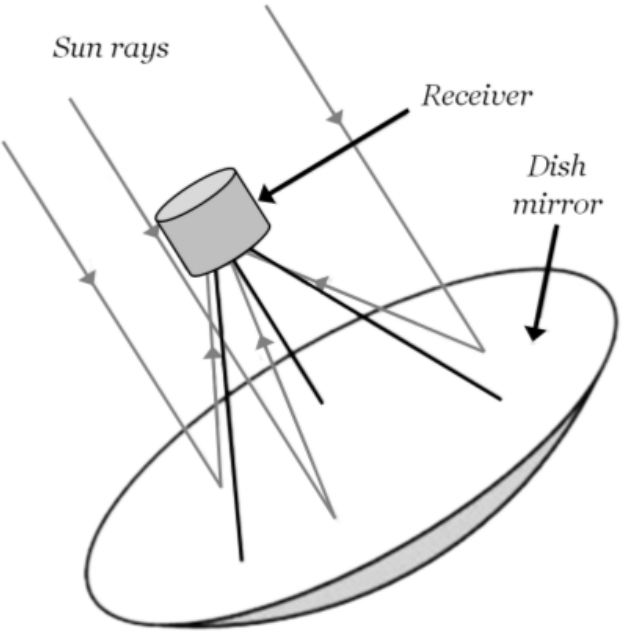

Figure 2.2. *Parabolic dish concentrator scheme*

In a symmetrical parabolic plate, the focal point represents where incoming parallel rays of light converge after reflection from the parabolic surface. The parabola equation can be expressed in the standard form:

$$H = \frac{1}{4F} R^2 \qquad [2.1]$$

where F represents the focal length, H is the depth of the dish and R is the radius of the dish edge from the center. H is measured along the axis of symmetry from the vertex to the plane of the rim, as illustrated in Figure 2.3.

This relationship is crucial to dish sizing because it determines how the curvature and depth of the parabolic surface influence the effectiveness of focusing light on the receiver.

As the dimensions of the parabola increase, the relationship described by the parabola equation allows the angle of the mirrors to be adjusted, ensuring optimal

alignment with the Sun rays throughout the day. By applying this equation, designers can calculate the necessary parameters, such as the dish diameter, depth and area needed to maximize concentrator performance while maintaining structural integrity.

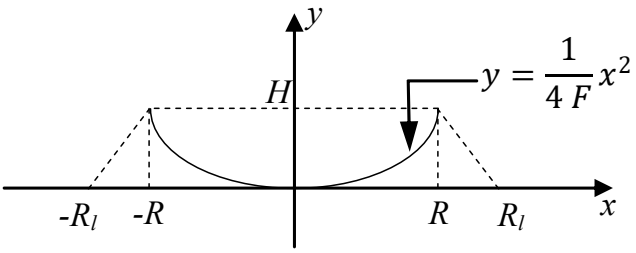

Figure 2.3. *Geometrical parameters of the parabola*

Thus, the parabola equation forms a fundamental element in the design process, guiding the sizing and shaping of symmetrical parabolic concentrators to achieve maximum optical efficiency and power production in solar applications.

The linear diameter of the dish, defined as the arc along its surface, corresponds to the diameter of a flat, circular sheet of material, typically metal, which is appropriately sized to be cut and shaped into the dish.

This linear diameter, denoted as $D_l = 2R_l$, can be determined by assessing the arc of the parabola between two opposite edges.

The arc can be derived from the sum of infinitesimal arcs of length *dl*:

$$dl = \sqrt{1 + \left(\frac{dy}{dx}\right)^2}\, dx \qquad [2.2]$$

The linear diameter is given as:

$$D_l = 2\int_0^{+R} \left(\sqrt{1 + \frac{x^2}{4F^2}}\right) dx \qquad [2.3]$$

The integration of relations [2.3] leads to the exact following solution:

$$D_l = R\sqrt{1 + \frac{4H^2}{R^2}} + \frac{R^2}{2\,H}\, Ln\left(\sqrt{1 + \frac{4H^2}{R^2}} + \frac{2\,H}{R}\right) \qquad [2.4]$$

Expression [2.4] provides the means to size the parabola. By selecting the rim diameter *2R* and the height of the parabola *H*, the linear diameter can be calculated.

The use of the diagram depicted in Figure 2.4 can also be pertinent in determining the linear diameter according to the ratio of height to diameter.

This calculation is essential for determining the amount of material required for manufacturing the dish. With the known dimensions of the rim and height, the appropriate size of the flat, circular sheet of material, usually metal, can be determined, ensuring that it is the correct size to be cut and bent into the desired parabolic shape.

Once the parabola is manufactured, the receiver must be positioned at the focal distance, which is determined by the specific geometric properties of the parabola. This focal distance is calculated based on the dimensions of the parabola, including its rim diameter and height. The correct placement of the receiver at this focal point is crucial to ensure that all of the reflected Sun radiations converge accurately, maximizing the efficiency and performance of the parabolic dish.

The focal distance formula is as follows:

$$F = \frac{R^2}{4\,H} \qquad [2.5]$$

where *R* and *H* are defined above.

Proper alignment at this focal distance ensures the optimal functionality of the parabolic system.

There are several types of concentrators that continue to attract significant interest in the fields of solar energy and optical systems. These concentrators can be classified based on a range of criteria, allowing for a more nuanced understanding of their design and application. One key distinction lies in their optical characteristics, which differentiate between imaging and non-imaging systems.

Imaging concentrators are designed to focus light such that a clear image of the light source is formed at the focal point. These systems can be further divided into two main categories: linear concentrators, which focus light along a line, and point-focus concentrators, which focus light on a single point.

Each type of imaging concentrator has its own set of advantages and applications, depending on the specific energy or optical requirements.

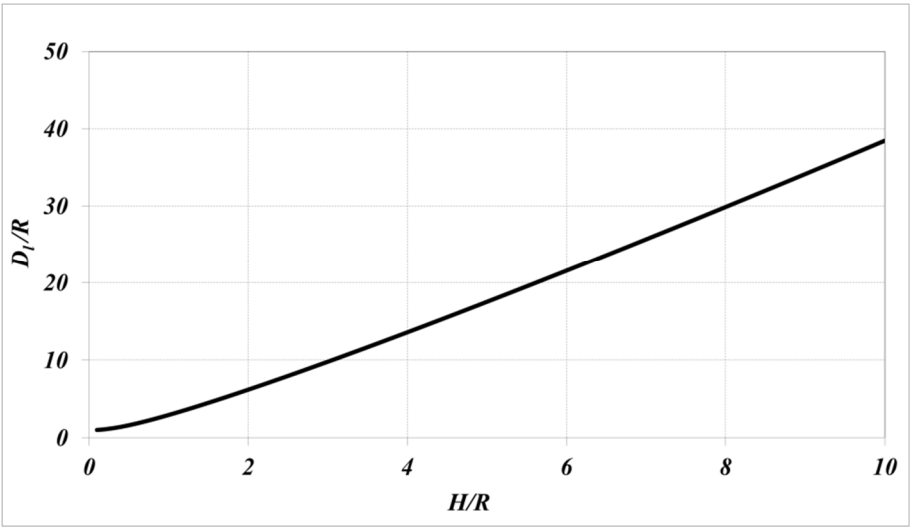

Figure 2.4. *Linear diameter as a function of the height of the parabolic concentrator*

On the other hand, non-imaging concentrators are not designed to create an image of the light source. Instead, they maximize the amount of energy directed toward a receiver without focusing on the creation of a distinct image. These concentrators are often more efficient in terms of energy capture, making them suitable for applications where energy collection is the primary goal.

Parabolic concentrators, a specific type of point–focus concentrator, are distinguished by their concentration ratio, denoted as C. This concentration ratio is a relevant parameter that defines the ability of a system to concentrate solar radiation or light onto a receiver. The most common definition of the concentration ratio is based on the concept of surface area. Specifically, it is expressed as the ratio of the aperture area, through which light enters the system, to the receiver area, where the concentrated light is directed.

This ratio, fundamental in determining the efficiency and performance of parabolic concentrators, as it directly impacts the intensity of the focused energy, is given as:

$$C = \frac{A_a}{A_{ab}} \qquad [2.6]$$

where A_a and A_{ab} are the concentrator aperture and the absorber areas, respectively.

The concentration ratio plays a crucial role in determining the operational temperatures of solar collectors based on its range of values:

– Low concentrations (where $1 < C < 10$) allow for temperatures of approximately 150°C.

– Medium concentrations (where $10 < C < 100$) can reach temperatures of approximately 300°C.

– High concentrations (where $C > 100$) result in temperatures exceeding 500°C.

As shown in Figure 2.5, the graphical representation of temperature ranges for different solar collector types aligns with data from the literature (Kalogirou 2013). The geometric characteristics of these collectors are further distinguished by the system dimensionality, either two-dimensional or three-dimensional. Their pointing modes classify them as either fixed, periodically oriented, mobile around a single axis or mobile around two axes.

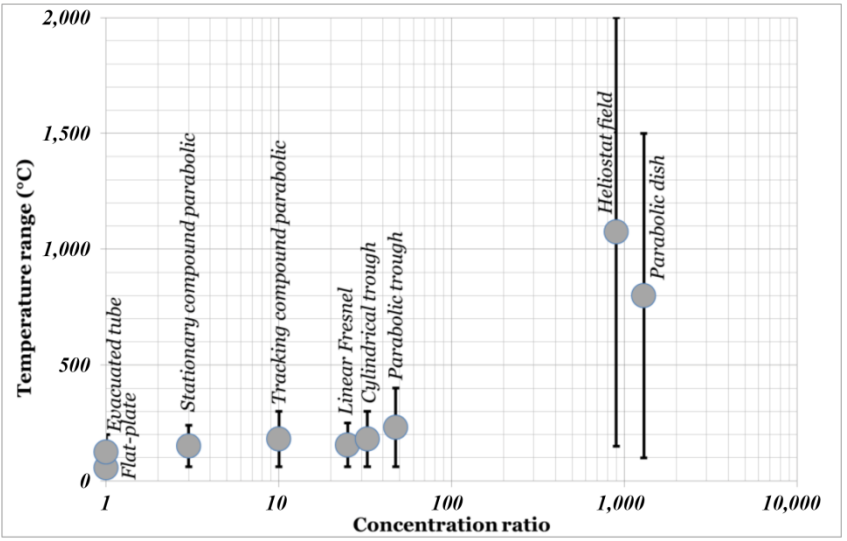

Figure 2.5. *Temperature range use according to the solar collector types*

The development of compound parabolic concentrator solar collectors began in the early 1960s, initially as tools for radiation detection. However, by 1975, Winston and Hinterberger identified their potential for solar energy collection, setting the stage for a technological shift that would lead to the widespread adoption of compound parabolic concentrator in solar water heating systems (Winston and

Hinterberger 1975). Early research on compound parabolic concentrator solar collectors focused on flat solar receivers, but advancements soon enabled the development of tubular designs. This innovation allowed fluids to be used as heat transfer media, significantly improving the efficiency and versatility of these systems.

In 1976, a significant advancement in the field of solar energy came with the analytical calculation of the average reflection of solar radiation into compound parabolic concentrator collectors. This breakthrough, achieved by Rübel (1976), significantly improved the optical analysis of compound parabolic concentrators, laying the groundwork for more accurate and efficient designs. This research opened the door to optimizing the concentration and reflection of sunlight, ensuring that more solar energy could be captured and utilized effectively.

Building on this, Hsieh (1981) developed a comprehensive mathematical model that focused on the thermal analysis of compound parabolic concentrator collectors equipped with absorber tubes. This model allowed for a deeper understanding of the heat transfer mechanisms involved, greatly enhancing the overall efficiency and performance of compound parabolic concentrator systems. These key developments were instrumental in advancing compound parabolic concentrator technology, making it a highly reliable and efficient solution for solar water heating and other solar energy applications (Kalogirou 2013). Over time, these innovations have helped compound parabolic concentrator solar collectors become a decisive component in sustainable energy solutions.

The introduction of compound parabolic concentrators represented a major breakthrough in solar concentrator technology, as they introduced the concept of non-imaging concentrators. Unlike traditional imaging concentrators, which focus light to a single point or image, compound parabolic concentrators are designed to efficiently redirect a large portion of incoming solar radiation toward the absorber, even if the radiation does not directly strike the focal area (Jadhav et al. 2013). These concentrators are often dome shaped, resembling parabolic structures, which optimize the reflection and concentration of sunlight.

Figure 2.6 illustrates the fundamental shape and configuration of a compound parabolic concentrator, showing how the design consists of two parabolic mirror segments, each with its own focal point. This innovative design enables compound parabolic concentrators to capture both direct solar radiation and diffuse sunlight, which significantly enhances their versatility in solar energy applications. As they are not limited to direct sunlight alone, compound parabolic concentrators can operate efficiently in a wider range of weather conditions, making them highly adaptable for various climates.

One of the advantages of compound parabolic concentrators is their ability to achieve high operating temperatures, which makes them ideal for applications that require significant heat output. Furthermore, they can be easily integrated into existing solar collectors, often serving as secondary concentrators that increase the performance of solar water heating systems. This integration potential makes them particularly valuable for improving the efficiency of both residential and industrial solar energy installations (Pranesh et al. 2019).

By combining high-temperature generation with adaptability and ease of integration, compound parabolic concentrators continue to play a significant role in advancing solar energy technologies.

In the design of solar dish collectors, geometrical characteristics play a crucial role in maximizing performance and efficiency. The key to enhancing the efficiency of these collectors lies in achieving symmetry and an ideal concentration ratio. These two factors are fundamental, as they significantly influence the geometry of the reflector. The design must incorporate curves that optimize the collection and concentration of solar energy, which directly affects the amount of energy directed toward the absorber.

Symmetry is essential for ensuring that the reflected solar energy is uniformly distributed across the absorber surface. A balanced and symmetrical design prevents hotspots and reduces energy loss, enabling the system to capture and utilize solar radiation more efficiently.

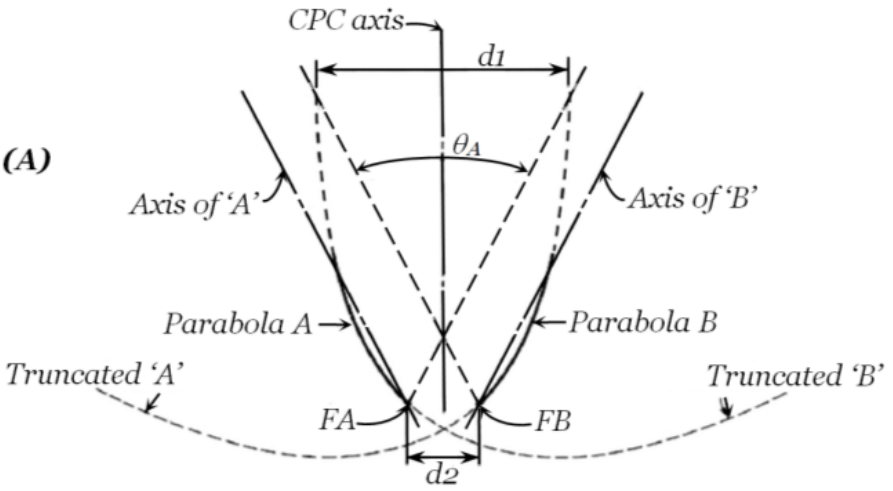

Figure 2.6. *Geometrical components of a compound parabolic concentrator*

Moreover, the concentration ratio, defined previously as the ratio of the aperture area through which sunlight enters the absorber area, the surface where the energy is focused, is a critical parameter. An optimal concentration ratio ensures that the maximum amount of sunlight is focused onto the absorber, enhancing the overall thermal efficiency of the collector.

To meet these design goals, solar dish reflectors are constructed using two distinct types of curves, as explored in various studies (Winston and Hinterberger 1975; Rübel 1976). The first curve, known as the involute or cusped section, is depicted as curve AB in Figure 2.7. This curve is designed to direct incoming solar rays tangentially onto the absorber, minimizing optical losses by ensuring that most of the captured radiation is redirected with minimal deflection. The involute curve precise geometry is key to maintaining system symmetry and optimal concentration capabilities, ensuring that the reflected energy reaches the absorber efficiently.

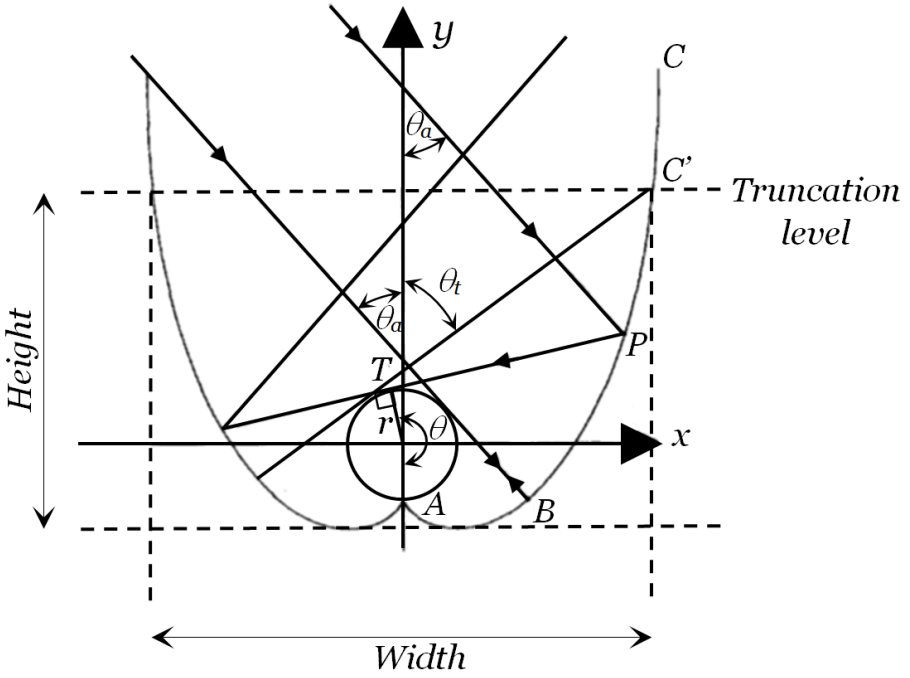

Figure 2.7. *Coordinate system and elements used in the description of the CPC reflector*

The second curve, referred to as the upper reflector section, is illustrated as curve BC in Figure 2.7. Unlike the involute section, the upper reflector offers a degree of

flexibility in its design. This section can be truncated, shortened or adjusted, depending on specific design needs. The truncation of the upper reflector is indicated by BC. This adaptability is especially important in applications where the physical dimensions of the collector might be limited by the available space, installation requirements or aesthetic considerations.

Truncation allows designers to modify the size and shape of the solar collector without compromising its core functionality. For example, in situations where space is constrained, the upper reflector section can be adjusted to fit within the physical limits of the installation site. However, this flexibility comes with a challenge: designers must carefully balance the extent of truncation to avoid negatively affecting the overall efficiency of the collector. Excessive truncation may reduce the concentration ratio, leading to a loss in the ability of the system to focus solar energy effectively. Therefore, when making adjustments to the upper reflector, ensuring that the design continues to meet the optimal requirements for energy capture and concentration is crucial.

In practice, the process of truncation involves determining the optimal point at which the upper reflector section can be shortened without significantly affecting the concentration of solar energy on the absorber. This involves specific calculations to ensure that the reflector maintains its ability to direct the maximum amount of solar radiation onto the absorber despite the reduced surface area.

To accurately calculate and design parabolic solar collectors, a Cartesian plane is typically used to represent the geometric configuration. The collector geometry primarily consists of two key components, a curve and a parabola, both of which are defined in relation to the dimensions of the absorber tube. The shape of the parabolic solar collector is constrained using equations that account for the rotation of the absorber tube about its center point, which is counterclockwise from the positive x-axis. This method, as proposed by Baum and Gordon (1984), provides a mathematical framework for determining the collector geometry, including the precise shape of its curves and parabolic sections within the coordinate plane.

A meaningful aspect of this design process involves understanding the angles that define the geometric and optical characteristics of the reflector, as illustrated in Figure 2.7. These angles are fundamental to the design and performance of solar collectors, as they directly influence the efficiency with which solar energy is concentrated in the absorber.

One of the most important angles in this context is θ_a, known as the half-angle of acceptance. This angle represents the span between the extreme accepted ray and the optic axis of the collector. It defines the range of incoming solar rays that the collector can capture and focus onto the absorber. A wider half-angle of acceptance

allows the collector to accommodate a broader range of incident angles, which in turn enhances the ability of the system to harness solar energy throughout the day, even as the position of the Sun changes. Thus, θ_a plays a key role in determining the overall effectiveness of the solar collector.

Another essential angle to consider is θ_t, which represents the angle between the optical (y) axis and the edge ray after truncation. Truncation refers to the deliberate shortening of the reflector upper section to meet practical design constraints, such as spatial limitations or manufacturing considerations, without substantially compromising optical performance. If the reflector remains untruncated, then θ_t is equal to θ_a, as the geometry remains intact. However, when truncation is applied, θ_t must be recalculated to ensure that the modified reflector continues to efficiently direct solar rays toward the absorber. As discussed before, truncation allows flexibility in the design but requires careful analysis to avoid significant losses in efficiency.

Within the geometric structure of the reflector, the involute section, marked as curve AB in the diagram, is crucial for directing solar rays effectively onto the absorber. This section of the reflector is characterized by its unique curvature, which is mathematically designed to ensure that incoming solar rays are directed tangentially onto the absorber, thus minimizing optical losses and maximizing energy capture. The involute curve spans from point A to point B and is an essential component of the reflector geometry.

To accurately model this involute section, it is important to determine the coordinates of any point P along the curve, which is situated between points A and B. The position of point P is defined within a specific angular range, represented by the interval $[0\ , \left(\frac{\pi}{2} + \theta_a\right)]$. Here, θ represents the angle associated with the involute curve, whereas θ_a (the half-angle of acceptance) defines the range of incident solar rays that the reflector can efficiently capture. The coordinates of point P, denoted as (x,y), are derived from the geometric properties of the involute curve.

By calculating these coordinates within the specified angular range, the exact shape of the involute section can be determined. This precise mapping is vital for practical implementation in solar collector design, ensuring that the reflector is optimized to direct as much solar energy as possible toward the absorber, thereby maximizing the collector efficiency. Understanding and applying these geometric principles allows for the creation of highly effective solar collectors that are capable of operating under diverse conditions while maintaining high performance.

$$\begin{cases} x = \ r\big(sin(\theta) - \theta\ cos(\theta)\big) \\ y = -r\big(cos(\theta) + \theta\ sin(\theta)\big) \end{cases} \qquad [2.7]$$

The upper reflector section extends from point B to point C and plays a meaningful role in further concentrating solar rays onto the absorber after they have passed through the initial involute section. This part of the reflector ensures that any solar rays not captured by the involute section are efficiently redirected toward the absorber, optimizing the ability of the system to focus as much solar energy as possible. By considering these additional rays, the upper reflector enhances the overall concentration and efficiency of the solar collector.

To accurately model the upper reflector section, it is necessary to determine the coordinates (x,y) of a representative point P along this segment. Point P lies within a specific angular range, denoted by the interval $[\left(\frac{\pi}{2}+\theta_a\right), \left(\frac{3\pi}{2}-\theta_a\right)]$, where θ represents the angular position of the point and where θ_a is the half-angle of acceptance that defines the range of solar rays the reflector can handle.

By calculating the coordinates of point P within this angular range, the shape and curvature of the upper reflector can be precisely defined, ensuring that it functions optimally to capture and redirect solar energy onto the absorber.

This detailed geometric description is essential for ensuring that the solar collector achieves maximum efficiency in harnessing solar energy.

A function $M(\theta)$ is introduced to consider these considerations to evaluate the coordinates (x,y) as:

$$\begin{cases} x = r\left(sin(\theta) - M(\theta)\, cos(\theta)\right) \\ y = -r\left(cos(\theta) + M(\theta)\, sin(\theta)\right) \end{cases} \quad [2.8]$$

where

$$M(\theta) = \frac{\frac{\pi}{2} + \theta_a + \theta - cos(\theta - \theta_a)}{1 + sin(\theta - \theta_a)} \quad [2.9]$$

The elementary arc of the reflector is similar to the curvilinear arc presented previously for a parabolic dish concentrator via relation [2.2]:

$$dl = \sqrt{(dx)^2 + (dy)^2} \quad [2.10]$$

The linear length of a truncated compound parabolic concentrator is given as:

$$D_l = 2\int_{AB} dl + 2\int_{BC'} dl \quad [2.11]$$

By reporting dx and dy from equations [2.7] and [2.8], the following expression is obtained:

$$D_l = 2\,r \int_0^{\frac{\pi}{2}+\theta_a} \theta\, d\theta + 2\,r \int_{\frac{\pi}{2}+\theta_a}^{\frac{3\pi}{2}-\theta_t} \left(M(\theta)^2 + \sqrt{1 - \left(\frac{dM}{d\theta}\right)^2} \right) d\theta \quad [2.12]$$

By explicitly expressing $M(\theta)$ and its derivative $\frac{dM}{d\theta}$ as derived from equations [2.9], the following relationship is obtained.

This formulation establishes a direct connection between the functional dependence of *Dl* and its integration with respect to θ.

$$D_l = r\left(\theta_a + \frac{\pi}{2}\right)^2 + 2\sqrt{2}\,r \int_{\frac{\pi}{2}+\theta_a}^{\frac{3\pi}{2}-\theta_t} \left(\left(\frac{\frac{\pi}{2} + \theta_a + \theta}{\left(1 + sin(\theta - \theta_a)\right)^{3/2}} \right) - \left(\frac{cos(\theta - \theta_a)}{\left(1 + sin(\theta - \theta_a)\right)^{3/2}} \right) \right) d\theta \quad [2.13]$$

$$D_l = r\left(\theta_a + \frac{\pi}{2}\right)^2 - 2\,r \left(1 - \frac{1}{sin\left(\frac{1}{2}(\theta_t + \theta_a)\right)} \right) + 2\sqrt{2}\,r \int_{\frac{\pi}{2}+\theta_a}^{\frac{3\pi}{2}-\theta_t} \left(\left(\frac{\frac{\pi}{2} + \theta_a + \theta}{\left(1 + sin(\theta - \theta_a)\right)^{3/2}} \right) \right) d\theta \quad [2.14]$$

By changing the variable θ to $\varphi = \theta - \theta_a$, the reflector arc length can be written in the following form:

$$D_l = r\left(\theta_a + \frac{\pi}{2}\right)^2 - 2\ r\left(1 - \frac{1}{sin(\theta_m)}\right)$$
$$+ 2\sqrt{2}\, r \int_{\frac{\pi}{2}}^{\frac{3\pi}{2}-\theta_t-\theta_a} \left(\left(\frac{\frac{\pi}{2} + 2\,\theta_a + \varphi}{\left(1 + sin(\varphi)\right)^{3/2}}\right)\right) d\varphi \quad [2.15]$$

where θ_m is the average value of θ_a and θ_t. The third term of expression [2.15] is complex and necessitates series development.

$$D_l = r\left(\theta_a + \frac{\pi}{2}\right)^2 - 2\ r\left(1 - \frac{1}{sin(\theta_m)}\right)$$
$$+ 2\ r\ (\pi - \theta_m + \theta_a)\left(\left(\frac{\cos(\theta_m)}{sin^2(\theta_m)}\right) - Ln\left(tg\left(\frac{\theta_m}{2}\right)\right)\right) \quad [2.16]$$
$$-4\, r\left(S(\theta_m) - S\left(\frac{\pi}{2}\right)\right)$$

where $S(\theta)$ represents a series as given:

$$S(\theta) = \sum_{n=0}^{\infty} \frac{sin\big((2n+1)\theta\big)}{(2n+1)^2} \quad [2.17]$$

Note that $S\left(\frac{\pi}{2}\right)$ represents the Catalan constant, which is equal to:

$$S\left(\frac{\pi}{2}\right) = \sum_{n=0}^{\infty} \frac{(-1)^n}{(2n+1)^2} \approx 0.915\ 965\ 594$$

To assess the height of the collector with an arbitrary degree of truncation, calculation of the reduced concentration ratio C_t is needed:

$$C_t = -cos(\theta_t) + \left(\frac{2\pi + 2(\theta_m - \theta_t) + sin(2\theta_m)}{1 - cos(2\theta_m)}\right) sin(\theta_t) \quad [2.18]$$

For the collector, the corresponding analytic expression of the height is provided:

$$H = \frac{\pi\, r}{2} + \pi\, r\, C_t\, cot(\theta_t) + \frac{r}{sin(\theta_t)} \quad [2.19]$$

Through this geometrical analysis, the design of a compound parabolic concentrator can be achieved according to the specified truncation.

2.1.2. *Tower plants*

Tower-based solar power plants represent one of the most advanced and efficient methods for capturing solar energy on a large scale. These facilities employ a vast array of mirrors, known as heliostats, often numbering in the hundreds or even thousands, which are carefully positioned to follow the sun's movement across the sky. Each heliostat is equipped with precise tracking systems, ensuring that they continuously reflect and concentrate sunlight onto a central receiver located at the top of a tall solar tower. This process of concentrating solar rays significantly amplifies the amount of energy delivered to the receiver, making it an integral component of the plant's power generation system.

The central receiver, situated at the highest point of the tower, is where concentrated solar energy is collected and utilized. The receiver is designed to absorb intense solar radiation, which is then used to heat a working fluid, commonly molten salt or water. Molten salt is often the preferred choice for many modern solar tower plants because of its superior heat retention properties. It can store large amounts of thermal energy, enabling the system to generate electricity even after the Sun has set or during periods of cloudy weather. This capability for thermal energy storage is a key advantage, as it provides a steady and reliable supply of electricity, reducing the intermittency that often challenges other forms of solar power.

Once the fluid is heated, it undergoes a process that converts the stored thermal energy into mechanical energy. In the case of molten salt, heat is transferred to a secondary system where it produces steam. This steam is then directed to drive a turbine, which generates mechanical energy as it spins. The turbine is connected to a generator, where the mechanical energy is converted into electrical energy that can be supplied to the grid.

One of the standout features of tower-based solar power plants is their ability to operate at extremely high temperatures, often exceeding 500°C, which greatly improves the overall efficiency of the energy conversion process. Higher operating temperatures allow for more efficient steam generation and greater power output from the turbine. This high-temperature operation enhances the thermodynamic efficiency of the power cycle, allowing for more effective and economical electricity production.

Additionally, the design of tower-based solar power plants facilitates scalability. The modular nature of heliostats and the centralized receiver allow for the expansion of plant capacity by simply adding more mirrors and adjusting the size of the receiver and associated infrastructure. This flexibility makes tower-based solar power plants a versatile solution for both large-scale industrial applications and smaller, localized power generation needs.

Furthermore, these plants are designed to maximize land use efficiency. The heliostats are arranged in circular patterns around the tower to minimize shading and to ensure that each mirror has an optimal angle for reflecting sunlight onto the receiver. The ability to store thermal energy in molten salt further enhances the flexibility of the system, making it one of the most promising technologies for meeting large-scale energy demands with renewable sources.

Figure 2.8 shows a detailed depiction of a solar tower plant specifically designed for high-efficiency electricity production. The diagram highlights the plant's ability to achieve substantial power outputs, typically approximately 10 MW, making it a key player in the realm of large-scale renewable energy generation. This notable capacity is a demonstration of the effectiveness and scalability of tower-based solar power plants, which are engineered to harness concentrated solar energy with remarkable precision.

The design shown in the figure emphasizes the coordinated operation of hundreds or even thousands of heliostats, each individually tracking the Sun and reflecting sunlight onto the central receiver atop the tower. The efficiency of this configuration enables the plant to concentrate solar energy to extremely high levels, which is crucial for generating the kind of thermal energy required to produce significant amounts of electricity.

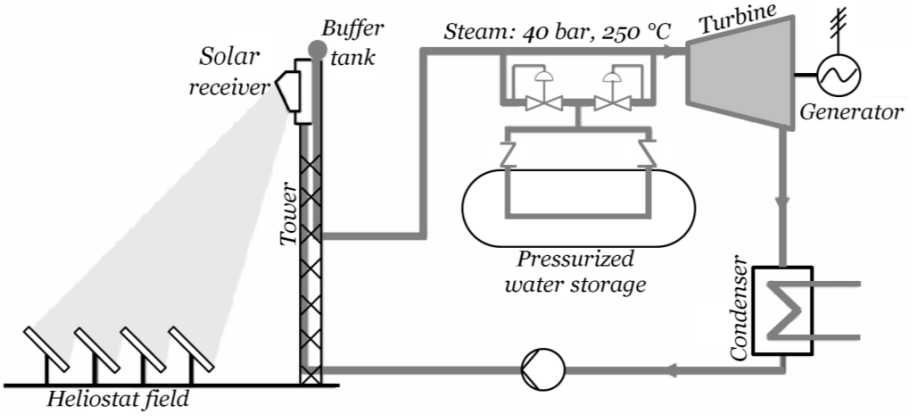

Figure 2.8. *Diagram of a solar tower power plant*

A 10 MW capacity, as illustrated, is not only representative of a medium-sized solar tower plant but also demonstrates the potential of these systems to be scaled up for even larger power outputs. The scalability of this technology allows for flexibility in its application, whether it is for powering smaller communities or

contributing to a regional grid with larger capacities of 50 MW or more. Furthermore, the inclusion of thermal energy storage, typically using molten salt, ensures that electricity production can continue even during periods of low sunlight, such as at night or on cloudy days. This storage capability enhances the reliability of solar tower plants and addresses one of the main challenges of renewable energy corresponding to intermittency.

In addition, the diagram likely illustrates the strategic layout of the heliostat field surrounding the tower, demonstrating how this arrangement optimizes land use and maximizes the capture of solar energy. The heliostats are carefully positioned to avoid shading and to ensure that the reflected sunlight is focused precisely on the receiver. By doing so, the plant is able to sustain a continuous flow of energy, translating into consistent electricity production at the 10 MW level.

The solar tower power reaches approximately 400 MW worldwide. Table 2.1 illustrates a list of some major solar tower stations with capacities of at least 50 MW.

Station	Country	Electrical capacity
Ivanpah Solar Power Facility	USA	392 MW
Crescent Dunes Solar Energy	USA	125 MW
Megalim Power Station (Negev Energy)	Israel	121 MW
Shouhang Dunhuang	China	100 MW
Khi Solar One	South Africa	50 MW
Supcon Solar Delingha	China	50 MW

Table 2.1. *List of major solar tower stations of at least 50 MW*

To further advance the development of solar receivers that are both highly efficient in energy collection and resilient to variations in solar resources, researchers have explored a wide array of geometric configurations. These innovative designs are specifically aimed at optimizing the performance of solar receivers in diverse and often challenging operational environments. The following sections outline several notable examples of these advanced geometries.

Honeycomb receiver (Olalde and Pierrot 1988)

The honeycomb receiver is designed with an intricate array of hexagonal cells, resembling a honeycomb structure. This configuration is engineered to maximize

surface area exposure to incoming solar radiation while minimizing thermal losses. The hexagonal cells create a large surface area, which enhances the absorption of sunlight, improving heat transfer and retention. This structure is particularly effective at capturing and concentrating solar energy while preventing excessive heat dissipation, making it a highly efficient design for solar energy collection.

Air–surface receiver

In the air–surface receiver, the design focuses on facilitating direct interaction between the air and the heated surface of the receiver. The configuration is optimized for enhanced convective heat transfer, where air flows directly over the surface and is heated by concentrated solar radiation. This design allows for efficient capture and transfer of solar energy, making it particularly suitable for applications where rapid heat exchange is crucial. Direct air–surface contact improves the receiver's ability to cool and heat air simultaneously, leading to faster and more efficient energy conversion.

Pressurized air volumetric receiver (Hischier et al. 2009)

The pressurized air volumetric receiver incorporates a porous material that is exposed to concentrated solar radiation. Air is pressurized and forced through this porous medium, which absorbs solar energy and heats the air as it passes through. The volumetric design allows for an even distribution of heat across the porous surface, leading to high thermal efficiency and enabling the receiver to achieve elevated temperatures. This design is ideal for applications requiring high-temperature output, such as driving thermodynamic cycles in power generation. Its ability to operate at high temperatures makes it a valuable asset in CSP plants where efficiency and power output are critical.

Fluidized bed receiver (Gueguen et al. 2023)

The fluidized bed receiver consists of a bed of solid particles that are fluidized by a stream of gas. When exposed to concentrated solar radiation, the particles are heated, and the fluidized motion ensures a uniform temperature distribution throughout the system. The continuous movement of the particles improves the heat transfer efficiency, whereas the fluidized bed allows for greater heat storage capacity. This design is particularly advantageous for applications requiring high thermal stability and capacity, as the particles can store large amounts of heat and transfer it effectively. The fluidized bed receiver is well suited for industrial processes that require stable and prolonged heat delivery, as well as for integration into systems that need consistent high-temperature output.

Each of these receiver geometries represents a strategic solution for overcoming the challenges of efficient solar energy collection while ensuring resilience to varying solar resource conditions. By exploring and refining these designs,

researchers can significantly improve the performance of solar receivers, ensuring optimal efficiency under different environmental conditions and enhancing the overall sustainability of solar power technologies.

These innovations are essential for pushing the boundaries of solar energy technology, as they provide scalable, reliable solutions for meeting the growing demand for renewable energy. From the honeycomb receiver enhanced surface area to the fluidized bed receiver robust thermal capacity, these designs offer significant improvements in capturing, storing and converting solar energy into usable power, paving the way for more efficient and sustainable solar energy systems in the future.

Solar updraft tower power plants stand out for their innovative and unique design, consisting of a tall central tower surrounded by a vast, greenhouse-like structure that is typically made of plastic or glass (Zhou and Xu 2016). This structure captures solar energy by heating the air within the greenhouse, which then rises through the tower due to natural convection, creating an upward airflow that drives turbines at the base of the tower (dos Santos Bernardes and Aurélio 2010). This design taps into the natural process of solar heating and air movement, offering a clean, low-maintenance way to generate electricity.

One of the major advantages of solar updraft towers is their efficiency and cost-effectiveness, making them particularly appealing for deployment in remote areas where other renewable energy options, such as wind or hydropower, may not be viable. Several pilot projects around the world are currently testing this technology (Saini et al. 2022). These plants are simple to construct and operate and have low maintenance costs, which increase their attractiveness. The greenhouse structure that surrounds the base of the tower is optimized to capture as much solar heat as possible, even under overcast conditions, ensuring a consistent rise of heated air into the tower. This creates a continuous airflow, allowing the turbines to generate power throughout the day, even when direct sunlight is not at its peak. The ability to generate electricity under varying weather conditions enhances the reliability and resilience of solar updraft towers, making them a dependable source of renewable energy.

The environmental impact of solar updraft tower power plants is minimal. Compared with more complex renewable technologies such as wind farms or large-scale solar arrays, simple designs require fewer resources. The tower footprint is relatively small, making it a suitable solution for areas where land is scarce or where minimal disruption to the environment is desired. The greenhouse structure does not require extensive mechanical systems or complex technologies, reducing the carbon footprint associated with its construction and operation. This makes solar updraft towers an eco-friendly solution for generating clean energy, especially in regions where preserving local ecosystems is important.

However, the simplicity of the solar updraft tower also introduces some limitations. These plants are best suited for regions with mild to moderate weather conditions. In areas prone to extreme weather, such as hurricanes, high winds or heavy storms, additional structural reinforcements would be necessary to ensure the stability of the tower, which could increase both the cost and complexity of the project. Despite this challenge, ongoing research and development efforts aim to improve design resilience and adaptability. Researchers are investigating ways to optimize updraft solar towers for use in a wider range of environments, including the possibility of using locally sourced materials to further reduce construction costs.

The greenhouse effect created within the solar updraft tower structure plays a main role in its functionality. By trapping solar heat efficiently, the greenhouse maximizes temperature differentials between the air inside the structure and the cooler air outside. This temperature difference drives the updraft, creating a continuous flow of air that turns the turbines and generates electricity. The inherent simplicity of this process ensures that the system is durable and requires minimal upkeep, making it an ideal solution for regions with limited technical infrastructure or resources.

Current efforts to enhance solar updraft tower power plants are focused on improving their efficiency, scalability and adaptability. Researchers are experimenting with various design modifications to increase heat retention and airflow dynamics, allowing the towers to function more effectively in different climates and geographies. This makes solar updraft towers not only a practical solution for isolated communities but also a potential contributor to national or regional grids in suitable environments.

Moreover, solar updraft towers offer a unique advantage over other renewable energy technologies in terms of space efficiency. Unlike wind farms, which require vast expanses of land to install multiple turbines, or solar farms, which need large areas for photovoltaic panels, solar updraft towers have a relatively small physical footprint. This makes them ideal for regions where land availability is limited or where there is a desire to minimize disruption to the landscape. Additionally, because they rely on natural airflows and solar heating, these plants do not pose significant threats to wildlife or ecosystems, making them a responsible choice for sustainable energy generation.

2.1.3. *Cylindrical-parabolic collectors*

Parabolic collectors are widely recognized for their durability and energy efficiency, making them a primary component in solar power generation (Tripathy et al. 2018; Ahmad et al. 2024). These sensors are designed to reach high

temperatures, making them suitable for both heat and electricity generation. The technology relies on a sophisticated system in which cylindrical and parabolic elements are specifically assembled to focus sunlight onto a heat transfer tube located at the focal point of the collector. This concentrated solar energy is then used to produce steam, which is used to generate electricity, much like traditional power plants that rely on parabolic concentrators.

As illustrated in Figure 1.9, the parabolic trough reflector has a distinct shape. It is linear in one dimension and curved in the other two dimensions (Bellos and Tzivanidis 2018). This design allows the system to capture and efficiently concentrate solar radiation. The incoming sunlight enters the trough parallel to its axis of symmetry, and the reflective surface is curved such that the rays are directed toward the focal line. Positioned just above the center of the trough, the receiver tube captures this concentrated energy. The tube is typically cylindrical and coated with a selective material, often blackened, to maximize the absorption of solar radiation and minimize reflective losses (Lu et al. 2013). This selective coating is essential for enhancing the overall efficiency of the system, as it ensures that a broad spectrum of sunlight is absorbed while minimizing heat loss through radiation and convection.

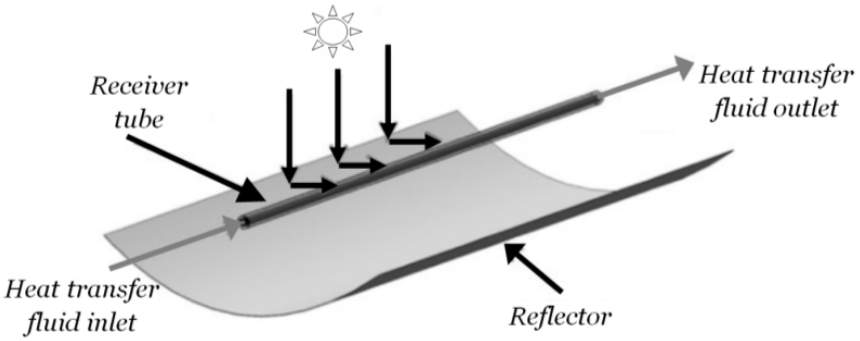

Figure 2.9. *Typical parabolic trough collector*

The operation of parabolic trough systems is highly efficient because of their ability to track the Sun along a single axis throughout the day. By continuously adjusting the orientation of the trough to follow the sun's movement, the system ensures that sunlight remains concentrated on the heat transfer tube, maximizing energy capture. The concentrated solar radiation heats a fluid, typically synthetic oil, within the tube, and this fluid can reach temperatures as high as 400°C. The high-temperature fluid is then used to transfer its thermal energy to water via a heat exchanger, producing steam. The steam drives a turbine connected to an electrical generator, ultimately converting solar energy into electricity.

One of the key advantages of parabolic trough collectors is their remarkable efficiency in converting solar energy into thermal energy. The precise curvature of the parabolic reflector ensures that the maximum amount of Sun rays is focused on the receiver tube, reducing energy losses. Additionally, the selective coating on the receiver tube is specially tailored to absorb a wide range of solar wavelengths while minimizing heat dissipation through radiation and convection, further increasing the efficiency.

An added benefit of parabolic trough systems is their compatibility with thermal energy storage technologies. These systems are capable of storing excess thermal energy collected during peak sunlight hours in storage media such as molten salts. This stored energy can be utilized to generate electricity during periods when sunlight is unavailable, such as at night or during overcast conditions. This feature significantly enhances the reliability and flexibility of parabolic trough power plants, enabling them to provide a continuous and dependable source of renewable energy.

The integration of thermal energy storage makes these systems particularly valuable in ensuring grid stability and meeting energy demands, even when solar input fluctuates. By storing energy during periods of high solar radiation and deploying it during low solar activity, parabolic trough power plants can operate more consistently and contribute to a more reliable supply of renewable energy.

The thermal analysis of the receiver tube is crucial for evaluating the efficiency of parabolic trough concentrators, as it directly influences the system's ability to convert solar energy into usable thermal energy. Figure 2.10 presents a detailed diagram of the parabolic trough solar receiver, illustrating its design and functionality. At the heart of the receiver is a stainless-steel tube that is meticulously coated with a selective metal-ceramic layer. This innovative configuration is enveloped within an evacuated, antireflective glass tube, a design choice made to minimize thermal losses and shield the absorber surface from oxidative degradation. The vacuum within this envelope operates below the Knudsen gas conduction threshold, typically around 10^{-4} mm Hg. This low-pressure environment is instrumental in significantly reducing convective heat losses in the annular space surrounding the absorber tube.

The metal–ceramic multilayer coating applied to the stainless steel tube is important for optimizing the receiver performance. This coating is specifically engineered to exhibit optimal optical properties: it boasts high absorptivity for direct solar radiation while maintaining low thermal emissivity at operational temperatures. These properties are vital for minimizing radiative heat losses, which, if unregulated, can severely diminish the overall efficiency of the solar energy system.

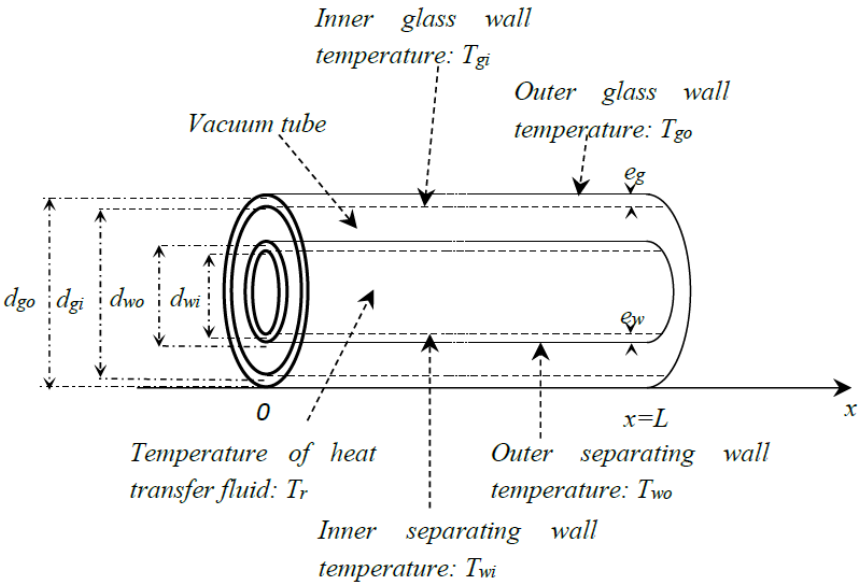

Figure 2.10. *Diagram of a parabolic through solar receiver*

Moreover, the outer glass cylinder is enhanced with an antireflective coating, which is strategically designed to reduce Fresnel reflective losses from the glass surface. By diminishing the reflection of incident solar rays, this antireflective layer maximizes solar transmittance, allowing a greater proportion of solar energy to be absorbed by the receiver. This maximized absorption is fundamental for improving the overall thermal efficiency of the system.

The heat transfer process within the receiver is multifaceted, involving the heat transfer fluid circulating through the stainless-steel tube, the annular space between the absorber and the glass envelope and the external environment of the collector. The heat transfer fluid, often synthetic oil or molten salt, is heated by the concentrated solar radiation absorbed by the receiver. As the fluid passes through the tube, it captures thermal energy, which is then transported away to generate steam or facilitate other thermal energy applications.

In addition to the physical components, various factors, including the fluid dynamics within the heat transfer medium, temperature gradients and thermal conductivity of materials, must be considered in thermal analysis. Understanding these dynamics is essential for optimizing the design and operation of parabolic trough solar receivers. For example, precise control of fluid flow rates can increase heat transfer efficiency, whereas careful selection of materials can further reduce thermal losses.

The steady-state linear energy balance, governed by both advection and convection processes, is an essential aspect of understanding the thermal interactions between the heat transfer fluid and the separating wall along its inner surface, denoted A_{wi}.

This energy balance can be described mathematically to describe the mechanisms at play in the thermal transfer process:

$$\dot{m}_r \, C_{pr} \frac{dT_r}{dx}(x) + \frac{d\phi}{dx} = 0 \qquad [2.20]$$

where the mass flow rate of the heat transfer fluid circulating through the inner tube of the receiver is denoted as $\dot{m}_r$ and its specific heat capacity is represented by C_{pr}.

The linear thermal power exchanged by convection between the heat transfer fluid and the inner wall of the receiver tube can be described via Newton's law. This principle states that the rate of heat transfer is proportional to the temperature difference between the fluid and the wall surface, along with the convective heat transfer coefficient and the surface area in contact with the fluid.

$$\dot{\phi}(x) = \frac{d\phi}{dx} = \frac{h_r \, A_{wi}}{L} \left(T_r(x) - T_{wi}(x)\right) \qquad [2.21]$$

L is the length of the collector and A_{wi} is the inner lateral area of the tube. As described in the Appendix, the convective heat transfer coefficient h_r is obtained from the Nusselt number and the thermal conductivity k_r of the heat transfer fluid:

$$h_r = \frac{Nu_r \, k_r}{d_{wi}} \qquad [2.22]$$

The linear thermal flux can also be expressed as a function of the thermal convective resistance:

$$\dot{\phi}(x) = \frac{1}{R_{th,r}} \left(T_r(x) - T_{wi}(x)\right) \qquad [2.23]$$

The Nusselt number serves as the main dimensionless number in fluid dynamics, representing the ratio of convective to conductive heat transfer across a boundary. Its value is contingent upon various factors, including flow configurations, such as laminar or turbulent flow, and specific geometric characteristics of the system, including pipe diameter and surface roughness. Additionally, it is closely tied to dimensionless numbers such as the Prandtl number, which characterizes the ratio of momentum diffusivity to thermal diffusivity, and the Reynolds number, which indicates the flow regime.

To increase the accuracy of Nusselt number predictions in pipes and ducts, the Gnielinski correlation has been developed as an advanced empirical relationship. This correlation provides a more reliable means of estimating heat transfer rates by integrating insights from existing correlations, particularly the Dittus–Boelter and Petukhov equations.

The Dittus–Boelter equation is traditionally used for turbulent flow in heated pipes and suggests that the Nusselt number can be determined on the basis of the Reynolds and Prandtl numbers. However, it does not account for the impact of friction factors, which can significantly affect heat transfer. On the other hand, the Petukhov equation provides a correction for the friction factor but may not be as straightforward in its application.

By bridging these two approaches, the Gnielinski correlation offers a more comprehensive framework for calculating the Nusselt number. It directly incorporates the friction factor, which accounts for the effects of flow resistance in the heat transfer process. This makes the Gnielinski correlation particularly useful in several applications, where precise predictions are essential for the design and optimization of heat exchangers, pipelines and other thermal systems.

$$Nu_r = \frac{\left(\frac{f}{8}\right)(Re - 1{,}000)Pr_r}{1 + 12.7\left(\frac{f}{8}\right)^{0.5}\left(Pr_r{}^{2/3} - 1\right)}\left(\frac{Pr_r}{Pr_{wi}}\right)^{0.11} \quad [2.24]$$

Pr_r and Pr_{wi} are the Prandtl numbers in the center of the tube and close to the separating wall, respectively.

The expression of the Prandtl number is:

$$Pr = \frac{\vartheta}{\alpha} \quad [2.25]$$

where ϑ and α are the kinematic viscosity and thermal diffusivity, respectively.

Re is the Reynolds number, which is given as a function of the velocity v:

$$Re = \frac{v\,D}{\vartheta} \quad [2.26]$$

The friction coefficient is given according to the Petukhov correlation for smooth tubes:

$$f = \frac{1}{(0.790\ln(Re) - 1.64)^2} \quad [2.27]$$

Under steady-state conditions, the linear thermal flux can be defined as the sum of two key components: the heat transferred by conduction through the thickness of the tube separating wall and the portion of solar radiation that penetrates the envelope and is absorbed by the receiver tube. Conductive heat transfer occurs as thermal energy moves from the hotter outer surface of the tube to the cooler inner surface, which is in contact with the heat transfer fluid. The physical characteristics of the receiver tube, such as its material properties and thermal conductivity, are designed to ensure maximum absorption of this incoming radiation. All of the radiations transmitted through the envelope are assumed to be fully absorbed by the receiver tube, effectively converting the radiant energy into thermal energy.

At the inner radius of the tube, denoted as r_{wi}, the linear thermal flux can be mathematically expressed as the conductive heat flux, which represents the flow of thermal energy per unit length across a given cross-sectional area:

$$\dot{\phi}(x) = \left.\frac{\partial \phi_w}{\partial x}\right|_{r=r_{wi}} \quad [2.28]$$

The solar radiation transmitted, after crossing the envelope, to the outer surface of the receiver tube corresponds to:

$$G_w = \eta_w C\, G_0 \quad [2.29]$$

where G_0 represents the direct and indirect solar radiation intensities close to the reflector. The concentration of solar radiation by the reflector produces a concentrated radiation value with a ratio of C. η_w corresponds to the solar radiation transmitted to and absorbed by the inner tube.

This parameter takes into account the reflection and absorption properties of the outer glass tube:

$$\eta_w = \eta_{w0}(1-R)^2\, e^{-\alpha_g e_g} \quad [2.30]$$

where the reflection and absorption coefficients of the envelope are R and α_g, respectively, and e_g is the envelope thickness. The term η_{w0} is introduced to take into account the angle of incidence of the Sun rays with regard to the inner tube.

While reaching the receiver tube, the solar radiation generates volumetric heat at its thickness. This heat is assumed to be uniform within the volume. The following expression is related to the volume-generated heat in the thickness of the tube:

$$q_{w,sol} = \eta_w C\, G_0 \frac{A_{wo}}{V_w} \quad [2.31]$$

As previously mentioned, the convective boundary condition at the inner surface of the tube ($r = r_{wi}$) is defined by the following expression:

$$\left.\frac{\partial \phi_w}{\partial x}\right|_{r=r_{wi}} = -k_w \frac{A_{wi}}{L} \left.\frac{\partial T_w}{\partial r}\right|_{r=r_{wi}} = \dot{\phi}(x) \quad [2.32]$$

By taking into account the radial configuration, the conductive heat equation integration leads to relation [2.33], which is composed of the conductive heat transfer and a term linked to the heat generated by the solar thermal volumetric energy within the receiver thickness:

$$\dot{\phi}(x) = \frac{2\,\pi\,k_w}{ln\left(\frac{d_{wo}}{d_{wi}}\right)} \left(T_{wi}(x) - T_{wo}(x)\right) + \delta_{wi}\, q_{w,sol} \quad [2.33]$$

where the parameter δ_{wi} is related to the geometrical specifications of the inner tube:

$$\delta_{wi} = S_{wi} - \frac{1}{2}\frac{(S_{wo} - S_{wi})}{ln\left(\frac{d_{wo}}{d_{wi}}\right)} \quad [2.34]$$

Here, k_w is the thermal conductivity of the separating wall. S_{wi} and S_{wo} represent the inner and outer tube sections, respectively:

$$\begin{cases} S_{wi} = \pi\, r_{wi}^2 \\ S_{wo} = \pi\, r_{wo}^2 \end{cases} \quad [2.35]$$

The linear heat flux can also be expressed as a function of the thermal resistance of the inner tube:

$$\dot{\phi}(x) = \frac{1}{R_{th,w}} \left(T_{wi}(x) - T_{wo}(x)\right) + \delta_{wi}\, q_{w,sol} \quad [2.36]$$

where

$$R_{th,w} = \frac{ln\left(\frac{d_{wo}}{d_{wi}}\right)}{2\,\pi\,k_w} \quad [2.37]$$

In a vacuum within an annular space characterized by a pressure of less than 1 mmHg, heat transfer predominantly occurs via free molecular conduction rather than conventional convection (Ratzel et al. 1979). At these extremely low pressures, the mean free path of gas molecules becomes significant compared with the dimensions

of the annular space. As a result, the gas can no longer be regarded as a continuous medium, necessitating a shift in how heat transfer is analyzed. In this regime, heat transfer is dictated by the kinetic behavior of the gas, which encompasses the movement and collisions of individual gas molecules.

In this context, the convection coefficient is determined using specialized equations designed for rarefied gas conduction. These formulas take into account crucial factors such as the molecular mean free path, the specific properties of the gas and the geometric configuration of the annular space. This approach enables a more accurate analysis of heat transfer phenomena in low-pressure environments, where traditional convection principles fall short.

Moreover, in addition to molecular conduction, radiative heat exchange is another important mechanism influencing heat transfer within a vacuum. Radiative transfer occurs due to the emission and absorption of thermal radiation by the surfaces involved. Thus, the combined effects of molecular conduction and radiative heat exchange must be considered to fully understand the thermal dynamics at play.

The linear heat flux between the outer surface of the inner tube and the annular vacuum can be expressed using the following boundary condition, which embodies the principles of energy conservation at the interface, which is defined at the radius $r = r_{wo}$:

$$\frac{\partial \phi_{v,cond}}{\partial x} + \frac{\partial \phi_{v,rad}}{\partial x} = -k_w \frac{A_{wo}}{L} \frac{\partial T_w}{\partial r}\Big|_{r=r_{wo}} \quad [2.38]$$

The molecular conduction is given by:

$$\frac{\partial \phi_{v,cond}}{\partial x} = \frac{2\,\pi\, k_{v,eff,cond}}{ln\left(\frac{d_{gi}}{d_{wo}}\right)} \left(T_{wo}(x) - T_{gi}(x)\right) \quad [2.39]$$

where $k_{v,eff,cond}$ is the effective thermal conductivity of the vacuum, which is approximated as a function of the conductivity K_v and pressure P_{atm} under atmospheric conditions and vacuum pressure P:

$$k_{v,eff,cond} = k_v \frac{P}{P_{atm}} f(Kn) \quad [2.40]$$

Kn represents the Knudsen dimensionless number, which is defined as the ratio of the mean free path of the gas molecules to a characteristic length scale. When Kn is very high ($Kn >> 1$), the gas is in the free molecular regime.

The annular space vacuum is also subjected to radiative exchange between the outer surface of the inner tube and the inner surface of the glass envelope.

This radiative heat exchange can be calculated using the Stefan–Boltzmann equation:

$$\frac{\partial \phi_{v,rad}}{\partial x} = \frac{\sigma\, \epsilon_{eff}}{L} A_{wo} \left(T_{wo}^4(x) - T_{gi}^4(x)\right) \quad [2.41]$$

The effective emissivity is given according to those of the inner tube ε_w and glass envelope ε_g:

$$\epsilon_{eff} = \left(\frac{1}{\epsilon_w} + \frac{d_{wo}}{d_{gi}}\left(\frac{1}{\epsilon_g} - 1\right)\right)^{-1} \quad [2.42]$$

where σ is the Stefan–Boltzmann constant.

For simplification, radiative exchange can be expressed as a heat flux with effective radiative conductivity, which is a function of the mean temperature:

$$\frac{\partial \phi_{v,rad}}{\partial x} = \frac{2\,\pi\, k_{v,eff,rad}}{ln\left(\frac{d_{gi}}{d_{wo}}\right)} \left(T_{wo}(x) - T_{gi}(x)\right) \quad [2.43]$$

where

$$k_{v,eff,rad} = 2\,\sigma\,\epsilon_{eff}\,T_m^3\, ln\left(\frac{d_{gi}}{d_{wo}}\right) \quad [2.44]$$

T_m represents the mean temperature in the vacuum. With these considerations, the boundary condition between the inner tube and the vacuum is expressed as:

$$-\frac{2\,\pi\, k_{v,eff}}{ln\left(\frac{d_{gi}}{d_{wo}}\right)} \left(T_{gi}(x) - T_{wo}(x)\right) = -k_w \frac{A_{wo}}{L} \frac{\partial T_w}{\partial r}\bigg|_{r=r_{wo}} \quad [2.45]$$

where

$$k_{v,eff} = k_{v,eff,cond} + k_{v,eff,rad} \quad [2.46]$$

The boundary condition [2.45] can be expressed as a function of the thermal resistance:

$$\frac{1}{R_{th,v}}\left(T_{wo}(x) - T_{gi}(x)\right) = \frac{1}{R_{th,w}}\left(T_{wi}(x) - T_{wo}(x)\right) + \delta_{wo}\, q_{w,sol} \quad [2.47]$$

where the surface parameter δ is given as:

$$\delta_{wo} = S_{wo} - \frac{1}{2}\frac{(S_{wo} - S_{wi})}{ln\left(\frac{d_{wo}}{d_{wi}}\right)} \quad [2.48]$$

The thermal resistance of vacuum is expressed as:

$$k_{th,v} = \frac{ln\left(\frac{d_{gi}}{d_{wo}}\right)}{2\,\pi\,k_{v,eff}} \quad [2.49]$$

The principle of energy conservation at the interface between the vacuum and the glass envelope must account for the internal heat generation caused by the absorption of solar radiation. As solar irradiance penetrates the glass envelope, a portion of the energy is absorbed at different radial depths, resulting in localized heat generation. This absorption process can be effectively described using the Beer–Lambert law, which models the attenuation of solar radiation as it travels through a medium. The law provides a framework to quantify how the intensity of solar radiation diminishes at a given radial depth within the thickness of the glass envelope.

The Beer–Lambert law takes into account the material properties of the glass, such as its absorption coefficient, as well as the optical path length, which represents the distance traveled by the solar rays. The law expresses how the transmitted intensity decreases exponentially as it passes through the material, shedding radiation on the energy balance within the system. By integrating the effects of this internal heat generation, a more accurate model of energy conservation can be established, which is essential for optimizing the thermal performance of the solar receiver and ensuring efficient heat transfer within the system. Hence, the fraction of solar irradiance at a radial depth r within the thickness of the glass envelope can be modeled as an exponential decay along the radius of the receiver tube:

$$G_g(r) = \eta_g\, C\, G_0\, e^{-\alpha_g(r_{go} - r)} \quad [2.50]$$

$C\,G_0$ represents the solar irradiance incident on the outer surface of the envelope, where α_g denotes the optical absorption coefficient of the envelope material. This

coefficient characterizes the ability of a material to absorb solar radiation as it passes through. Additionally, η_g signifies the fraction of solar irradiance that is successfully transmitted through the thickness of the envelope. This factor accounts for the energy that penetrates the envelope after some portion is absorbed or reflected, contributing to the total solar energy reaching the inner layers.

$$\eta_g = \eta_{g0}(1 - R) \quad [2.51]$$

The absorbed part of the envelope thickness is given as:

$$G_{g,abs}(r) = \eta_g \; C \; G_0 \left(1 - e^{-\alpha_g (r_{go} - r)}\right) \quad [2.52]$$

Similarly, for the inner tube, the term η_{g_o} is introduced to account for the angle of incidence of the solar rays on the envelope. This parameter adjusts for the variation in solar radiation as it strikes the surface at different angles, influencing the amount of energy absorbed or transmitted through the glass.

The boundary condition at the interface between the vacuum and the inner surface of the glass envelope (at $r = r_{gi}$) is expressed as follows:

$$\frac{1}{R_{th,v}} \left(T_{wo}(x) - T_{gi}(x)\right) = -k_g \frac{A_{gi}}{L} \frac{\partial T_g}{\partial r}\bigg|_{r=r_{gi}} \quad [2.53]$$

To accurately define the thermal flux across the thickness of the glass envelope, it is crucial to solve the radial heat conduction equation, incorporating the internal absorption of solar radiation. In this context, the Beer–Lambert law governs how solar radiation is absorbed within glass. According to this law, the intensity of the absorbed radiation decreases exponentially as it penetrates the material, gradually diminishing until it reaches the inner surface of the glass. Once there, the thermal energy propagates across the vacuum space toward the outer surface of the inner tube.

The exponential decay of absorbed heat introduces complexity to the mathematical solution of the heat equation, as it requires the handling of intricate integrals and special functions, such as the exponential integral function. This function helps to quantify how the absorbed radiation diminishes through the glass envelope thickness, which can be challenging to analytically manage.

To simplify the resolution of this heat transfer problem, the average amount of absorbed solar radiation is often considered instead of handling the full exponential decay. By approximating heat absorption as an average value throughout the material thickness, the heat conduction equation becomes more tractable. The

volumetric heat generation term within the glass can then be expressed in a simplified manner, where the heat generation is averaged across the glass envelope rather than considering its exact spatial distribution. This approach streamlines the calculation of the thermal flux, making it feasible to predict how heat flows from the outer surface of the envelope to the inner surface and ultimately through the vacuum space toward the receiver tube.

This method allows more efficient estimation of the thermal performance while still capturing the essential physics of heat absorption and transmission in solar receivers, ensuring that the system thermal efficiency is maintained without overly complex calculations.

In this case, the volumetric heat generated into the thickness is given as:

$$q_{g,sol} = \frac{A_{go}}{V_g}\,\overline{G}_{g,abs} \qquad [2.54]$$

where A_{go} represents the outer lateral surface area of the glass envelope and V_g denotes the volume of the glass envelope thickness. The term $\overline{G}_{g,abs}$ refers to the mean absorbed radiation intensity throughout the envelope thickness. This average intensity accounts for the amount of solar radiation absorbed by the glass as it traverses from the outer to the inner surfaces of the envelope. The value of $\overline{G}_{g,abs}$ can be derived using the formula provided in equation [2.52], which incorporates factors such as incident solar radiation, material optical properties and absorption behavior governed by the Beer–Lambert law.

This average radiation intensity is essential for calculating the overall thermal performance of the system, as it directly influences heat generation within the glass envelope.

By considering both the surface area and the volume, as well as the mean amount of absorbed radiation, it becomes possible to assess the total energy absorbed by the glass envelope and how effectively this energy is transferred to adjacent components in the system.

$$q_{g,sol} = \frac{A_{go}}{V_g}\,\frac{1}{e_g}\int_{\frac{d_{gi}}{2}}^{\frac{d_{go}}{2}} \eta_g\, C\, G_0 \left(1 - e^{-\alpha_g (r_{go} - r)}\right) dr \qquad [2.55]$$

The integration of expression [2.55] leads to:

$$q_{g,sol} = \frac{A_{go}}{V_g}\,\eta_g C\, G_0 \left(1 - \frac{1 - e^{-\alpha_g\, e_g}}{\alpha_g\, e_g}\right) \qquad [2.56]$$

The resolution of the heat equation, which incorporates an internal volumetric energy source as described in relation [2.56], yields significant insights into the thermal behavior of the system. This equation accounts for the energy generated within the material due to the absorption of solar radiation. As this energy propagates through the thickness of the glass envelope, it interacts with the surrounding environment, particularly at the boundary where the vacuum space meets the inner surface of the envelope.

The boundary condition at this interface reflects the energy conservation principles at play, ensuring that all of the thermal energy generated within the envelope is either absorbed by the inner surface or dissipated into the vacuum space. Specifically, the boundary condition delineates how the absorbed energy translates into a thermal flux, allowing characterization of the temperature distribution across the envelope and prediction of the efficiency of the energy transfer process.

The solution of the heat equation with the internal volumetric source of energy expressed by relation [2.56] leads to the boundary condition at the frontier between the vacuum space and the inner surface of the envelope:

$$\frac{T_{wo}(x) - T_{gi}(x)}{R_{th,v}} = \frac{T_{gi}(x) - T_{go}(x)}{R_{th,g}} + \delta_{gi}\, q_{g,sol} \qquad [2.57]$$

where δ_{gi} is related to the geometrical specifications and is expressed as a function of the cross-sections of the glass envelope:

$$\delta_{gi} = S_{gi} - \frac{1}{2}\frac{(S_{go} - S_{gi})}{ln\left(\frac{d_{go}}{d_{gi}}\right)} \qquad [2.58]$$

The thermal resistance of the glass envelope is given as a function of its thermal conductivity k_g:

$$R_{th,g} = \frac{ln\left(\frac{d_{go}}{d_{gi}}\right)}{2\,\pi\,k_g} \qquad [2.59]$$

The envelope of the solar receiver is subjected to heat transfer mechanisms that include convective heat transfer with the ambient environment and radiative exchanges with the sky. As the receiver itself is relatively small in size compared to the vast surroundings, which encompass not only the immediate atmosphere but also extend infinitely upward to the open sky, it is crucial to consider these interactions when establishing the relevant boundary conditions.

At the outer surface of the envelope, convective heat transfer occurs as ambient air comes into contact with the envelope, facilitating the movement of heat away from the receiver. This process is influenced by factors such as the wind speed, ambient temperature and surface characteristics of the envelope. Additionally, the envelope also participates in radiative heat exchange with the environment, primarily emitting thermal radiation into the colder atmosphere.

To accurately model these interactions, the boundary condition at the outer surface of the envelope can be described mathematically, accounting for both the convective and radiative heat transfer components. Therefore, the boundary condition at the outer surface of the envelope can be similarly expressed as follows:

$$\frac{h_a A_{go}}{L}\left(T_a - T_{go}(x)\right) = -k_g \frac{A_{go}}{L}\frac{\partial T_g}{\partial r}\bigg|_{r=r_{go}} \qquad [2.60]$$

The heat transfer coefficient is an essential parameter in modeling the thermal dynamics of a system, as it encompasses both effective convection and apparent convective heat transfer resulting from radiative heat exchange. This relationship can be mathematically expressed as:

$$h_a = h_{a,conv} + h_{a,rad} \qquad [2.61]$$

In this equation, $h_{a,conv}$ represents the convective heat transfer coefficient that quantifies the heat transfer occurring between the outer surface of the glass envelope and the surrounding environment. This coefficient is influenced by factors such as the wind speed, temperature differential and physical properties of the surrounding air, all of which contribute to the rate at which heat is lost from the envelope into the ambient surroundings.

On the other hand, the apparent convective heat transfer coefficient due to radiative heat exchange, denoted as $h_{a,rad}$, accounts for the heat transfer that occurs through radiation. This form of heat transfer becomes particularly significant in scenarios where the temperature of the glass envelope is elevated relative to the environment. Radiation heat transfer depends on the temperature difference between the glass surface and the surrounding surfaces, as well as the emissivity of the glass, which reflects its effectiveness in emitting energy such as thermal radiation.

By considering both convective and radiative components, the overall heat transfer coefficient h_a provides a full appreciation of how heat is dissipated from the glass envelope into the environment. This dual consideration is essential for accurately modeling the thermal performance of the system, especially in applications where maintaining optimal temperatures is crucial for efficiency.

The apparent convective heat transfer coefficient due to radiative heat exchange $h_{a,rad}$ can be approximated by:

$$h_{a,rad} \approx 4\,\sigma\,\epsilon_g\,T_{gm}^3 \qquad [2.62]$$

T_{mg} is the mean temperature of the glass envelope thickness and the ambient temperature.

The expression [2.60] leads to the following boundary energy conservation:

$$\frac{T_a - T_{go}(x)}{R_{th,a}} = \frac{T_{gi} - T_{go}(x)}{R_{th,g}} + \delta_{go}\,q_{g,sol} \qquad [2.63]$$

The thermal resistance $R_{th,a}$, which combines convective and radiative heat exchange between the glass envelope and the environment, is given by the following expression:

$$R_{th,a} = \frac{L}{\left(h_{a,conv} + h_{a,rad}\right) A_{go}} \qquad [2.64]$$

The surface parameter δ_{go} is given as:

$$\delta_{go} = S_{go} - \frac{1}{2}\frac{\left(S_{go} - S_{gi}\right)}{ln\left(\frac{d_{go}}{d_{gi}}\right)} \qquad [2.65]$$

The convective heat transfer coefficient $h_{a,conv}$ can vary significantly on the basis of climatic conditions, such as the wind speed and direction. In particular, the presence of wind can profoundly influence the thermal boundary layer that forms around the surface of the envelope.

As wind flows over the surface, it disrupts this boundary layer, reducing its thickness and increasing the rate of convective heat transfer. This phenomenon results in more efficient cooling or heating of the surface, depending on the surrounding temperature.

To account for these variations in heat transfer due to different environmental factors accurately, the convective heat transfer coefficient can be expressed as a combination of natural and forced convection components. Natural convection occurs due to buoyancy effects caused by temperature differences, where warmer air rises and cooler air moves to replace it. Conversely, forced convection involves the movement of air driven by external forces, such as wind, which increases the rate of heat transfer.

The combined effect of these two convection modes is often represented empirically through the following relationship:

$$h_{a,conv} = \left(h_{nat}^{m} + h_{forced}^{m}\right)^{\frac{1}{m}} \quad [2.66]$$

In this equation, h_{nat} represents the natural convection coefficient, which can be influenced by the temperature gradient between the glass envelope and the surrounding air, whereas h_{forced} denotes the forced convection coefficient, which is impacted by the wind speed and other dynamic environmental conditions.

Empirical correlations and formulas are typically used to determine these coefficients, considering factors such as fluid properties (e.g. density and viscosity), surface geometry and temperature differences. By incorporating both natural and forced convection contributions, the overall convective heat transfer coefficient provides a more accurate representation of the heat transfer processes occurring at the surface of the glass envelope under varying climatic conditions.

For practical calculations, a simple linear combination might be used with m = 1:

$$h_{a,conv} = h_{nat} + h_{forced} \quad [2.67]$$

For natural convection, a variety of empirical correlations have been developed to predict the heat transfer behavior within specific ranges of the Rayleigh number. These correlations are often based on experimental data and are valid only for certain geometries, temperature gradients and fluid properties, as indicated in Table 2.2.

Ra	$[10^{-2}$ to $10^{2}]$	$[10^{2}–10^{9}]$	$[10^{9}–10^{12}]$
Nu	$0.675 + \dfrac{0.057\ Ra^{0.5}}{\left(1 + \left(\dfrac{0.4}{Pr}\right)^{2/3}\right)^{0.25}}$	$0.53\ Ra^{0.25}$	$0.13\ Ra^{0.13}$

Table 2.2. *Correlations for natural convection around a horizontal tube*

The Rayleigh number is a dimensionless quantity that combines the effects of buoyancy forces and thermal diffusion. It is crucial in determining whether convection will occur and how strong it will be.

The Rayleigh number is mathematically defined as:

$$Ra = Gr\ Re \quad [2.68]$$

Here, *Gr* represents the Grashof number and *Pr* is the Prandtl number, which relates the fluid viscosity to its thermal diffusivity. Together, these numbers help characterize the nature of convective heat transfer.

The Grashof number *Gr*, a dimensionless parameter, measures the ratio of buoyancy forces, which drive convection, to viscous forces, which resist motion. It plays a critical role in defining the onset and strength of natural convection. The Grashof number was calculated using the following formula:

$$Gr = \frac{g\,\beta\,(T_{go} - T_{\infty})d_{go}^3}{\nu^2} \quad [2.69]$$

In this expression:

– g is the gravitational acceleration (typically 9.81 m/s^2);

– β is the coefficient of thermal expansion of the fluid, which measures how much the fluid expands or contracts with changes in temperature;

– T_{go} is the temperature of the object or surface generating heat (often referred to as the surface temperature);

– T_{∞} is the ambient or surrounding temperature of the fluid far from the surface;

– d_{go} is the characteristic length, which could represent dimensions such as the diameter of a pipe or the height of a vertical plate, depending on the specific scenario;

– ν is the kinematic viscosity of the fluid, which represents its resistance to flow.

This equation shows that the Grashof number increases with greater temperature differences ($T_{go}-T_{\infty}$) and larger characteristic lengths, promoting stronger natural convection. A high Grashof number suggests that buoyancy forces dominate, leading to vigorous convective currents, whereas a low Grashof number indicates that viscous forces inhibit convection.

A commonly used empirical correlation for calculating the Nusselt number in forced convection over a horizontal cylinder is the Churchill–Bernstein equation. This equation provides a practical means of predicting convective heat transfer by relating the Nusselt number to key dimensionless parameters such as the Reynolds number and the Prandtl number. The Churchill–Bernstein correlation is expressed as follows:

$$Nu = 0.3 + \frac{0.62\,Re^{1/2}\,Pr^{1/3}}{\left(1 + \left(\frac{0.4}{Pr}\right)^{2/3}\right)^{0.25}}\left(1 + \left(\frac{Re}{282{,}000}\right)^{5/8}\right)^{4/5} \quad [2.70]$$

The Churchill–Bernstein equation accounts for both the laminar and turbulent flow regimes over the cylinder by incorporating a range of Reynolds numbers and adjusting for different Prandtl numbers. The first term, 0.3, represents a base heat transfer level, whereas the rest of the expressions reflect how the Nusselt number scales with increasing Reynolds and Prandtl numbers. The combination of these factors makes the equation versatile for a wide variety of fluids and flow conditions.

The equation structure shows how the contribution of forced convection increases with the square root of the Reynolds number and how heat transfer is further influenced by the fluid thermal properties, as represented by the Prandtl number. The various exponents and correction terms are designed to ensure accuracy over a broad range of flow conditions, from laminar to turbulent.

By rearranging the previous boundary conditions at various interfaces between different media and incorporating the effects of advection, the differential equation for the fluid temperature can be derived. This equation provides a way to calculate the temperature of the heat transfer fluid at any point along its path. It is expressed as:

$$T_r(x) - T_a = R_{th}\,\dot{\phi}(x) + \lambda_w\, q_{w,sol} + \lambda_g\, q_{g,sol} \qquad [2.71]$$

R_{th} is the total thermal resistance:

$$R_{th} = R_{th,r} + R_{th,w} + R_{th,v} + R_{th,g} + R_{th,a} \qquad [2.72]$$

The different thermal resistances are defined previously for each element of the receiver.

The parameters λ_w and λ_g are given by the following expressions:

$$\begin{aligned} \lambda_w &= \left(R_{th,v} + R_{th,g} + R_{th,a}\right)\delta_{wo} \\ &- \left(R_{th,w} + R_{th,v} + R_{th,g} + R_{th,a}\right)\delta_{wi} \\ \lambda_g &= R_{th,a}\,\delta_{go} - \left(R_{th,g} + R_{th,a}\right)\delta_{gi} \end{aligned} \qquad [2.73]$$

The heat transfer fluid obeys the following differential equation:

$$L\frac{dT_r}{dx} + NTU\,(T_r(x) - T_a) = NTU\,\Delta T_{sol} \qquad [2.74]$$

where

$$NTU = \frac{L}{R_{th}\,\dot{m}_r\,C_{pr}} \qquad [2.75]$$

and

$$\Delta T_{sol} = \lambda_w \, q_{w,sol} + \lambda_g \, q_{g,sol} \qquad [2.76]$$

ΔT_{sol} is a representative temperature that quantifies the effect of solar radiation on the receiver.

By solving equation [2.74], the temperature of the heat transfer fluid is given as:

$$T_r(x) = T_a + \left(T_{r,in} - T_a - \Delta T_{sol}\right) e^{-NTU\frac{x}{L}} + \Delta T_{sol} \qquad [2.77]$$

The model outlined in this section provides a detailed description of the thermal behavior of the solar receiver. When conducting temperature simulations, it is essential to iteratively adjust the thermal resistances related to radiative heat transfer over several iterations to ensure that they are aligned with the average temperatures of the system. This step is crucial for accurately capturing the effects of radiative heat exchange under various conditions.

For example, Figure 2.11 illustrates the relationship between the efficiency of the solar receiver and the outlet temperature of the heat transfer fluid as a function of the fluid inlet temperature.

Additionally, this figure demonstrates how the temperature difference between the outer lateral surface of the receiver envelope and the surrounding ambient environment changes with the inlet temperature.

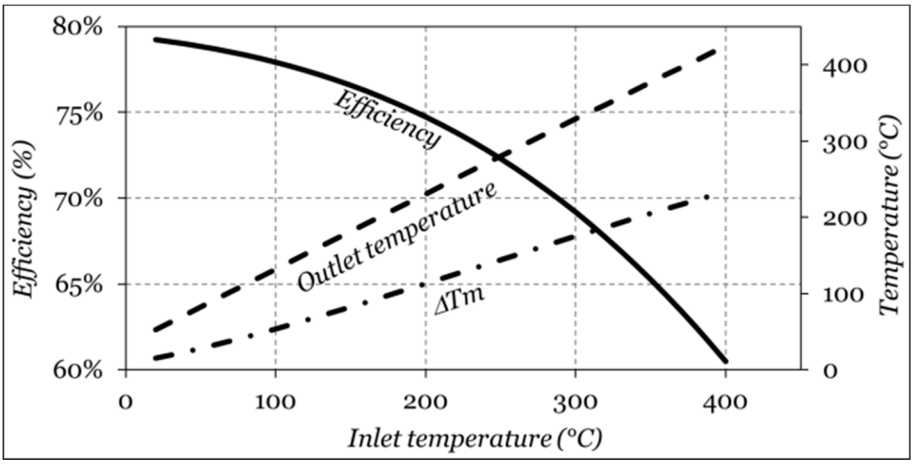

Figure 2.11. *Solar receiver efficiency as a function of the heat transfer fluid inlet temperature*

As the inlet temperature of the heat transfer fluid increases, the receiver efficiency tends to decrease. This is primarily due to the increasing heat losses that occur at elevated temperatures, especially radiative losses, which become more pronounced as the temperature increases. Radiative heat loss is a major factor in this decrease in efficiency because higher temperatures lead to greater emission of thermal radiation from the receiver surface.

Moreover, the figure also shows that as the temperature difference between the outer surface of the receiver and the ambient environment increases, thermal losses become even more significant. This additional heat loss further reduces the overall efficiency of the system. The larger the temperature gradient between the receiver surface and its surroundings, the greater the rate of heat transfer to the environment, leading to a compounding effect on efficiency reduction. These outcomes highlight the critical role that temperature management plays in optimizing the performance of solar receivers, particularly in minimizing radiative and conductive losses.

Figure 2.12 illustrates how both the efficiency and outlet temperature of the system vary as a function of the number of transfer units (NTUs). The NTU is a dimensionless parameter that quantifies the effectiveness of heat exchangers by measuring the heat transfer capability of the system relative to its thermal resistance.

As the NTU increases, a noticeable trend emerges: the efficiency of the system decreases, whereas the outlet temperature of the heat transfer fluid increases.

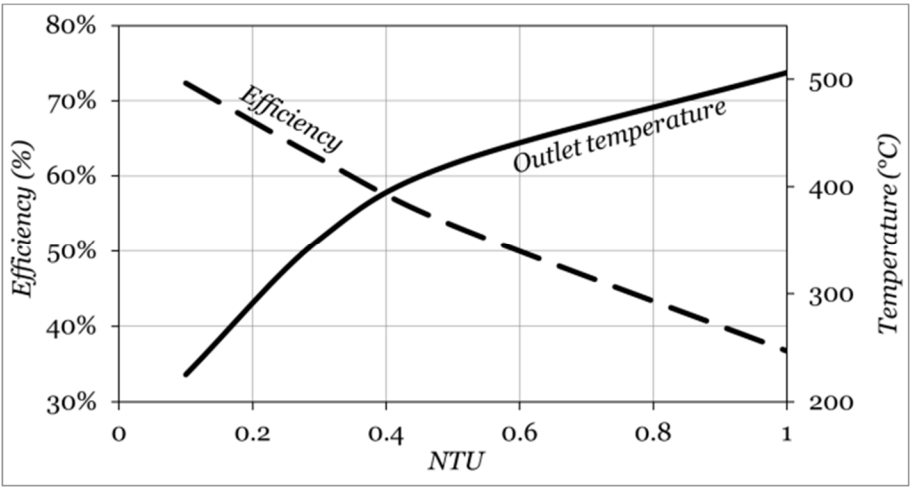

Figure 2.12. *Efficiency and outlet temperature according to the number of transfer unit*

This relationship indicates that an increase in the NTU, which typically suggests a greater capacity for heat transfer, may also be associated with a decrease in the thermal rate of heat exchange or a decrease in the overall thermal resistance within the system.

As the NTU increases, it becomes more challenging for the system to transfer heat effectively, leading to a reduction in efficiency. Simultaneously, the outlet temperature increases because the heat transfer fluid is unable to release as much thermal energy to the environment, resulting in a higher temperature upon exiting the receiver.

Importantly, the trends depicted in this figure are limited to the specific temperature range in which the heat transfer fluid operates. This operational temperature range is critical because it defines the boundaries within which the system can function effectively. In addition to this range, the behavior of the system may differ significantly because of changes in fluid properties, heat transfer mechanisms and the performance characteristics of the solar receiver. Therefore, understanding the relationships among the NTU, efficiency and outlet temperature is essential for optimizing the design and operation of solar thermal systems, ensuring that they operate within their most effective temperature ranges.

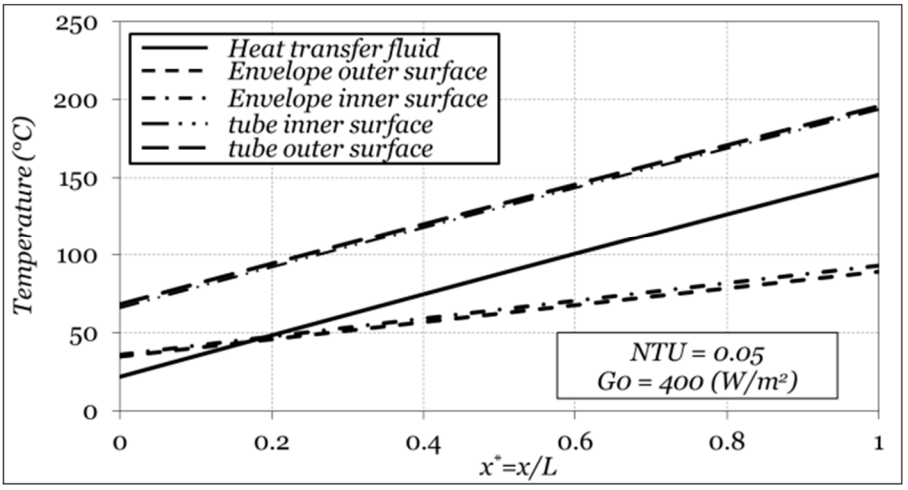

Figure 2.13. *Temperatures along the receiver with NTU = 0.05*

Figure 2.13 shows an example of the temperature variation along the length of the solar receiver, which extends from the inlet to the outlet. This particular figure is derived from a scenario in which the NTU is approximately 0.05, indicating a high

thermal flow rate in comparison with the overall heat transfer. As the heat transfer fluid moves through the inner tube of the receiver, the temperature significantly increases.

The progression of the temperature along the receiver is essential for understanding the thermal performance of the system. Analyzing this temperature profile can provide valuable insights into the effectiveness of heat transfer and help identify potential areas for optimization within the receiver design. These data are particularly important for ensuring that the receiver operates within its intended thermal range, maximizing efficiency and overall energy output.

Figure 2.14 presents the temperature distribution along the length of the tube for a scenario in which the NTUs is set to 0.5. As expected and in accordance with the trends shown in Figure 2.12, the temperatures within the tube increase as the NTU value increases. This increase is indicative of improved heat transfer efficiency within the system, as a higher NTU generally reflects a more effective transfer of thermal energy between the fluid and the surrounding environment.

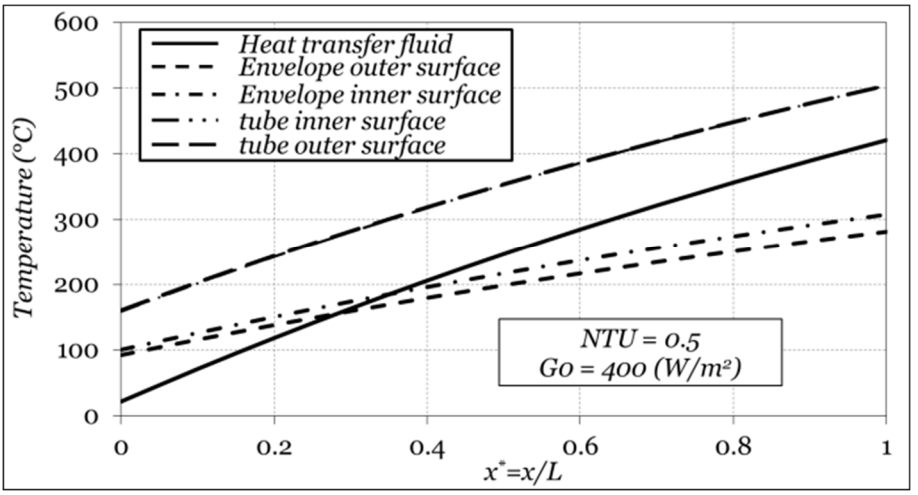

Figure 2.14. *Temperatures along the receiver with NTU = 0.5*

Figure 2.15 highlights the effects of the solar radiation intensity on both the outlet temperature and system efficiency. As solar irradiation increases, the outlet temperature increases accordingly because of the greater amount of energy available for heat transfer. This increase in temperature can enhance the system's thermal performance. The figure also indicates how system efficiency evolves with varying solar intensity, suggesting that while efficiency may improve with higher radiation,

it is influenced by factors such as the thermal capacity of the system and potential heat losses at higher operating temperatures.

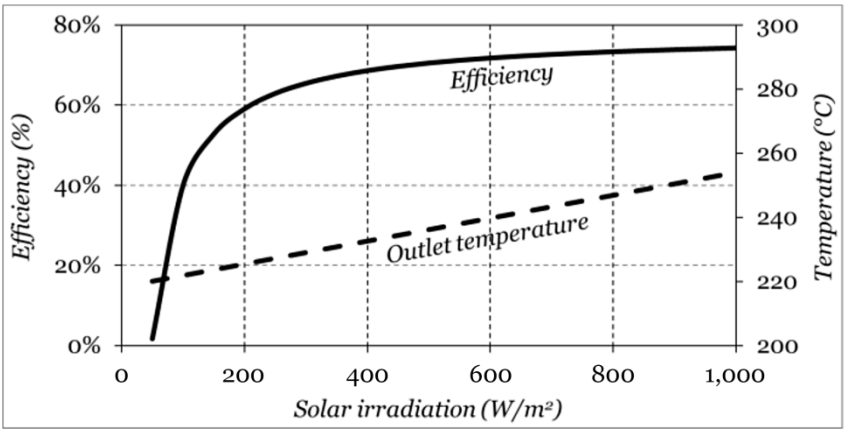

Figure 2.15. *Efficiency and outlet temperature according to solar irradiation*

Figure 2.16 illustrates the significant impact of the solar receiver length on both the efficiency and the outlet temperature of the heat transfer fluid, specifically under conditions where the NTUs is set at 0.05. As depicted in the figure, an increase in the length of the solar receiver correlates with an increase in both the system efficiency and the outlet temperature of the heat transfer fluid.

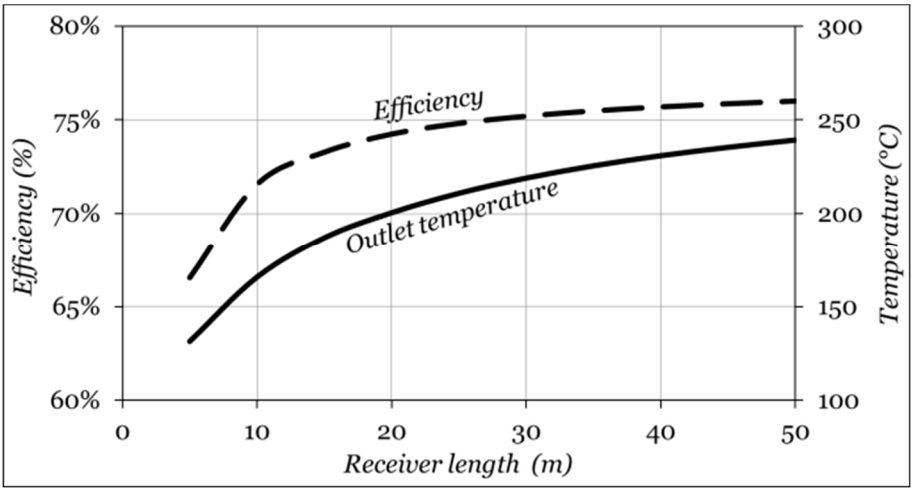

Figure 2.16. *Efficiency and outlet temperature as a function of the receiver length*

This phenomenon can be attributed to the extended surface area available for heat exchange within a longer receiver. As the heat transfer fluid traverses the increased length of the receiver, it has more opportunities to absorb thermal energy from the surrounding environment, resulting in higher outlet temperatures. This prolonged dwelling time with the heated surfaces enhances the thermal interaction between the fluid and the receiver walls, ultimately improving the ability of the fluid to capture heat. However, it is important to note that while the increase in efficiency and outlet temperature is obvious, this rise becomes less pronounced as the length of the receiver continues to increase. This observation suggests a diminishing return on performance gains, indicating that after a certain point, extending the receiver length yields progressively smaller improvements in thermal efficiency and fluid temperature.

The trend observed in this relationship provides valuable insights for the design and optimization of solar thermal systems. Understanding the diminishing returns associated with increased receiver length allows informed decisions to be made when sizing full-scale installations. These facts are essential for achieving an optimal balance between system performance and material costs, as excessively long receivers may lead to unnecessary expenditures without significantly increasing efficiency.

By analyzing this trend, the most effective length for the solar receiver can be determined, ensuring that it captures maximum thermal energy while remaining economically viable. Ultimately, this information contributes to the development of more efficient and cost-effective solar thermal systems, enhancing their overall performance in practical applications.

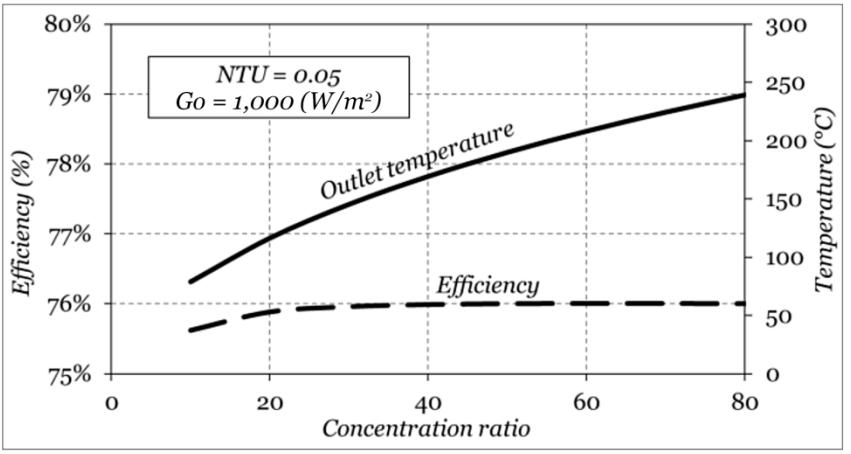

Figure 2.17. *Effect of the concentration ratio on the efficiency and outlet temperature of the receiver length*

Figure 2.17 illustrates the impact of the concentration ratio on the outlet temperature of the receiver, revealing a nonlinear relationship between these variables.

As the concentration ratio increases, the outlet temperature also increases but not at a constant rate. Initially, higher concentration ratios result in significant temperature increases because of intensified solar energy focused on the receiver, enhancing heat transfer to the working fluid. However, as the concentration ratio continues to rise, the rate of temperature increase slows. This nonlinear behavior is a result of complex thermal dynamics, including the growing influence of thermal radiative resistances and losses at elevated temperatures. As the receiver reaches higher temperature thresholds, additional energy input is increasingly offset by radiative heat losses, which dampen the efficiency of further temperature gains. This underscores the intricate interplay between the concentration ratio, thermal resistance and overall energy balance within the system.

In terms of efficiency, it remains nearly constant across a range of concentration ratios, demonstrating strong independence from changes in concentration. This suggests that the system operates at a stable efficiency level, regardless of the amount of solar energy being concentrated.

Notably, for low radiation, the efficiency should be more sensitive, as previously depicted in Figure 2.15.

The selection of an appropriate heat transfer fluid is crucial and largely dependent on the operating temperature range. Table 2.3 outlines three key fluids commonly used for transferring heat, each with distinct thermal properties suited to specific applications.

Heat transfer fluid	Range of temperature (°C)
Water/steam	0–550
Thermal oil (Therminol VP-1)	12–400
Molten salt	
HITEC	140–530
HITEC XL	130–550
Solar salt	260–600

Table 2.3. *Temperature range operation of the main heat transfer fluids*

Water, known for its relatively high thermal characteristics in the boiling phase, stands out as an efficient heat transfer medium at moderate temperatures. During this phase, the high heat capacity of water enables efficient energy transfer.

However, as water transitions into superheated steam, its performance as a heat transfer fluid diminishes significantly. The heat transfer coefficient, which governs the rate at which heat is transferred to receiving surfaces, decreases markedly, thereby reducing the overall efficiency of the system. Additionally, at high temperatures, steam can become corrosive, especially when in contact with metal surfaces, posing long-term challenges for the integrity and maintenance of piping systems, valves and heat exchangers. These corrosive effects necessitate the use of specialized materials and corrosion-resistant coatings, increasing system complexity and costs.

In contrast, molten salt eutectic mixtures are emerging as a preferred alternative, especially in high-temperature applications such as CSP plants. These salts, often composed of a mixture of sodium nitrate, potassium nitrate and other compounds, exhibit remarkable heat capacity, allowing them to store large amounts of thermal energy. This dual function, which serves both as a heat transfer fluid and as a medium for thermal energy storage, makes molten salts highly advantageous. They are capable of operating at much higher temperatures than water or steam without the risk of phase transition, thus maintaining consistent and efficient heat transfer. Furthermore, their chemical stability at elevated temperatures reduces the risk of corrosion and material degradation, making them ideal for long-term use in solar energy systems and other high-temperature industrial processes.

As CSP technology advances, molten salt systems are becoming more widespread because of their ability to support higher thermal efficiencies, improve energy storage capabilities and facilitate round-the-clock power generation by storing excess heat for use during periods of low solar activity. This shift toward molten salts underscores the growing demand for heat transfer fluids that not only operate efficiently across a broad temperature range but also contribute to the overall sustainability and reliability of energy systems.

Despite their many advantages, molten salts present two significant challenges that must be carefully managed:

– *High melting point*: molten salts have a relatively high melting point, often approximately 220–250°C, which requires additional engineering measures to prevent solidification. To maintain the salts in their liquid state, especially during periods of inactivity such as nighttime or unexpected drops in solar radiation due to cloud cover, heat-tracing systems are employed. This typically involves the installation of resistive heating elements, such as heating tape, along the entire network of pipes and ducts used for heat transfer circulation. These systems ensure that the temperature of the molten salts remains above their freezing point, preventing blockage and maintaining the continuous flow necessary for efficient plant operation. However, this adds complexity and increases operational costs, as it

requires constant monitoring and energy consumption, even when solar input is minimal.

– *Thermal decomposition at high temperatures*: another limitation of molten salts is their tendency to decompose when exposed to temperatures exceeding approximately 550°C. This decomposition not only degrades the salt mixture but also releases corrosive by-products that can damage the plant infrastructure over time. Consequently, this thermal limitation imposes a cap on the maximum operating temperature of systems utilizing molten salts. While modern CSP plants could theoretically achieve higher efficiency at elevated temperatures, the decomposition threshold of molten salts prevents them from reaching their full potential. This constraint necessitates a delicate balance between optimizing the thermal efficiency and preserving the integrity of the heat transfer medium, pushing the exploration of alternative salts or innovative solutions to overcome these challenges.

Despite these drawbacks, molten salts remain among the most viable solutions for high-temperature energy storage and heat transfer in solar power applications because of their excellent thermal capacity and relatively low cost. However, addressing these limitations is key to unlocking their full potential in future renewable energy technologies.

The following table presents the physical characteristics of the three main heat transfer fluids previously discussed.

	Water	**Thermal oil**	**Molten salt**
Density (kg/m^3)	1,000	1,060	2,000
Specific heat capacity (J/kg.K)	4,186	2,200	1,500 (at 300°C)
Thermal conductivity (W/m.K)	0.6 (at 25°C)	0.14	0.5
Viscosity (mPa.m)	0.89 (at 25°C)	1.18	2.65
Boiling point (°C)	100 (at 1 atm)	257	*
Freezing point (°C)	0 (at 1 atm)	12	221
Vapor pressure (kPa)	3.17	0.013	**

** Decomposes before boiling (typically > 550°C) - ** Negligible*

Table 2.4. *Heat transfer fluid characteristics*

The inner tubes used in high-temperature applications, such as solar thermal systems, are typically made from carbon steel, stainless steel or alloy steel.

The selection of a material is carefully based on a combination of thermal performance, mechanical properties and economic considerations.

Carbon steel, which is predominantly composed of iron and carbon with minor trace elements, is widely used because of its cost-effectiveness and satisfactory thermal conductivity, which is approximately 45 W/m·K. It offers a strong balance of good heat transfer capabilities and robust mechanical strength, making it an economical choice for many industrial applications. However, carbon steel is prone to corrosion, particularly in environments where high temperatures are combined with moisture or chemicals, limiting its long-term durability under harsh conditions. In such scenarios, protective coatings or additional maintenance measures may be required to prevent degradation.

Stainless steel, available in various grades, such as 304 and 316, presents a superior alternative because of its excellent corrosion resistance and stability at elevated temperatures. Although its thermal conductivity (~16 W/m·K) is notably lower than that of carbon steel, it compensates for this with its exceptional resistance to oxidation and chemical attack, even in highly corrosive or high-temperature environments. Furthermore, stainless steel maintains its mechanical integrity over a wide range of operating conditions, making it a reliable material for applications where durability is paramount. However, this enhanced performance comes at a higher price, making stainless steel a more expensive option than carbon steel, particularly when it is used in large-scale systems.

Alloy steel, which incorporates elements such as chromium, nickel and molybdenum, is designed for even greater strength and durability, especially at high temperatures. The addition of these alloying elements imparts improved thermal and mechanical properties, allowing alloy steel to perform remarkably well in demanding environments where high-temperature stability and resistance to mechanical stress are essential. Alloy steel has also enhanced resistance to oxidation and wear, making it ideal for long-term use in applications such as CSP systems. However, the advanced performance characteristics of alloy steel are associated with a significantly higher cost, limiting its use to applications where its specific advantages justify the added expense.

The choice of material for the inner tubes is crucial for balancing performance requirements with cost-effectiveness, ensuring the longevity and efficiency of systems. In addition to material selection, the inner tubes are coated with specialized layers designed to maximize solar energy absorption while minimizing thermal emissivity, a key factor in improving the overall efficiency of solar thermal systems. One commonly used coating is black chrome, which is known for its high solar absorptivity and low emissivity. This coating is highly effective at capturing solar

radiation and converting it into heat while minimizing energy loss through radiation, making it a popular choice for solar thermal collectors.

Cermet coatings, which are composites of ceramic and metallic materials, offer further flexibility by allowing precise tailoring of their optical properties. These coatings can be optimized to achieve high absorption of solar energy and low emissivity, making them suitable for applications requiring a fine balance between thermal capture and heat retention.

For even more demanding applications, titanium nitride (TiN) is also used because of its exceptional hardness, excellent thermal stability and resistance to high temperatures. TiN coatings are particularly useful in high-temperature solar applications where durability and thermal efficiency are of utmost importance.

As illustrated in Figure 2.18, the coating emissivity plays a pivotal role in the efficiency of solar receivers. The relationship between emissivity and efficiency is inversely proportional: as the emissivity increases, the efficiency of the solar receiver decreases. This highlights the importance of selecting appropriate coating materials that minimize emissivity while maximizing absorption, ultimately improving the overall energy conversion efficiency of solar thermal systems.

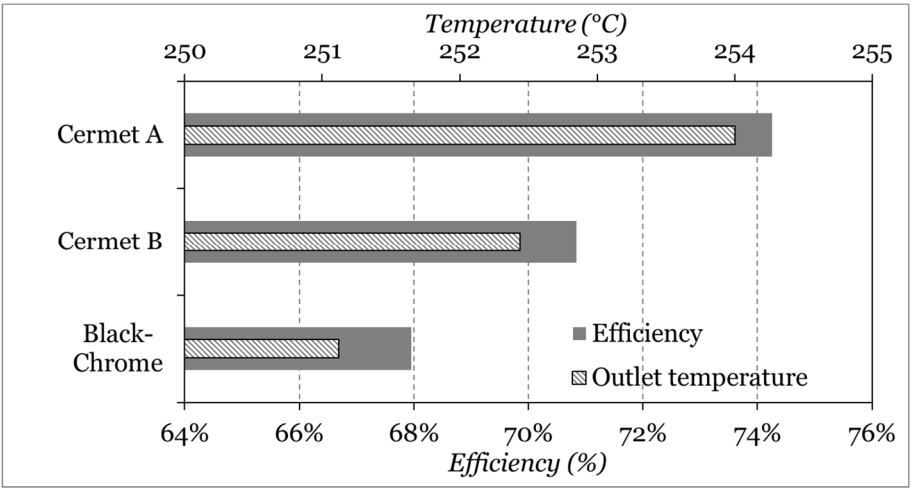

Figure 2.18. *Effect of the coating emissivity on the efficiency of the solar receiver*

The glass envelope of the absorber tube of a parabolic trough solar collector is an accurately designed component that plays a crucial role in the effective capture and conversion of solar energy. This specialized glass is made from high-purity,

low-iron materials, ensuring that it provides exceptional optical clarity. The choice of low-iron glass is important because it minimizes impurities that can interfere with the transmission of sunlight, allowing as much solar radiation as possible to pass through. This ensures maximum energy transfer to the absorber tube, which is the core of the system.

One of the key features of this glass envelope is its ability to transmit Sun rays with minimal reflection and absorption losses. This is achieved by maintaining a very low reflection coefficient, typically between 0.05 and 0.10. This efficient transmission is vital because the more solar energy that reaches the absorber tube, the more energy the system can harness and convert into heat.

Moreover, the glass envelope is designed to endure extreme conditions. It operates at high temperatures, sometimes reaching several hundred degrees Celsius, without losing its structural integrity or optical properties. This means that even after long-term exposure to intense solar heat, the glass does not warp, crack, or degrade in performance, ensuring the reliability and efficiency of the solar receiver over time.

To further improve the performance, the glass was treated with advanced antireflective coatings. These coatings play an essential role by reducing the amount of Sun radiation that is reflected off the glass surface. Without these coatings, a significant portion of the incoming solar radiation would be lost. By allowing more Sun rays to pass through, antireflective treatments help maximize the energy that enters the receiver, significantly increasing its overall efficiency.

However, despite these enhancements, receivers can still be affected by environmental factors, particularly dust accumulation. Dust particles settling on the glass can reduce its ability to transmit Sun rays effectively. The impact of dust on performance depends on two main factors. The first one corresponds to the size of the dust particles, which ranges from 5 to 100 μm. The second factor is related to the amount of dust that settles on the surface, which can reach 5 mg/cm^2. As more dust accumulates, the reflection coefficient increases, sometimes fluctuating between 0.05 and 0.5, meaning that more Sun rays are reflected and that fewer are absorbed by the system. Therefore, regular cleaning or protective measures are essential for maintaining optimal performance.

As the reflection coefficient increases, the energy efficiency of the receiver steadily and significantly decreases, as depicted in Figure 2.19. This figure displays the direct correlation between the rising reflection coefficient and the decreasing energy performance of the receiver, a relationship primarily due to dust accumulation on the glass envelope.

However, as dust particles accumulate on the glass surface, they scatter and reflect more incoming Sun rays, effectively increasing the reflection coefficient. This accumulation creates a physical barrier that prevents Sun radiation from fully entering the receiver, reducing the amount of energy it can convert.

The effect of dust accumulation is cumulative and progressive. Even small amounts of dust begin to disrupt the receiver efficiency, but as more dust settles over time, the reflection coefficient sharply increases. This results in a substantial drop in energy capture, limiting the receiver ability to maintain optimal performance. In essence, as the reflection coefficient increases, the energy efficiency of the receiver diminishes, directly impacting the overall performance of the solar system.

Figure 2.19 visually captures this decline in efficiency, underscoring the importance of maintaining a low reflection coefficient to maximize energy absorption. This highlights that without regular maintenance to reduce dust deposition, the receiver's ability to capture solar energy can be significantly compromised, emphasizing the need for solutions to mitigate dust accumulation for sustained energy efficiency.

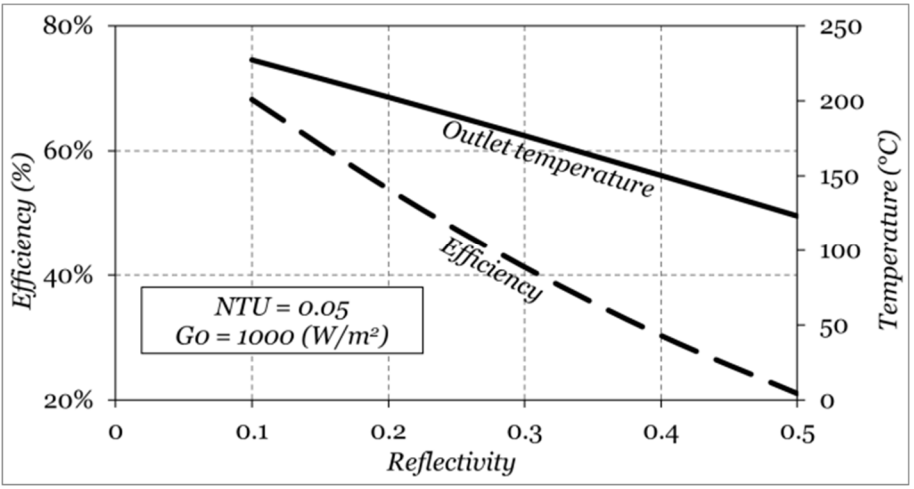

Figure 2.19. *Efficiency and outlet temperature as a function of the reflectivity*

The envelope durability is ensured by its resistance to thermal expansion and contraction, which are common in high-temperature environments. This robust design guarantees that the glass remains intact and functional over long periods,

even under fluctuating thermal conditions. The glass envelope is specifically sealed to create a vacuum or an inert gas-filled space. This sealing serves two primary purposes: providing superior thermal insulation to reduce heat loss and protecting internal components from contaminants such as dust and moisture, which could impair performance. The sealed environment within the envelope safeguards the receiver internal components from environmental factors such as humidity and particulate matter, thereby preserving efficiency and extending the lifespan of the solar receiver.

To ensure that most of the incident solar radiation is transmitted to the absorber tube, the glass envelope plays a crucial role in optimizing the efficiency of the solar receiver. The combination of high optical clarity, low reflection and antireflective coatings ensures that the solar energy system operates at peak performance.

The robust design of the glass envelope, which is capable of withstanding high temperatures and environmental stressors, ensures that the solar receiver remains reliable and effective over extended periods. This longevity is essential for the economic viability of solar energy systems. Additionally, the insulating properties of the vacuum or inert gas-filled space within the envelope help manage the thermal environment of the receiver. This thermal management is crucial for maintaining consistent performance and preventing overheating of internal components.

In terms of construction, parabolic trough power plants are often modular, enabling scalability from small installations to large-scale power plants. Each module consists of a series of parabolic troughs aligned in rows, with the heat transfer fluid flowing through interconnected receiver tubes. This modularity facilitates maintenance and allows for incremental capacity additions.

Moreover, the relatively straightforward design and operation of parabolic trough collectors contribute to their economic viability. The materials used for the reflectors and receiver tubes are readily available, and the technology has been refined over several decades, leading to cost reductions and efficiency improvements.

In examining the advancements and applications of parabolic trough technology, it is evident that there have been significant developments in solar power stations utilizing this technology. Table 2.5 lists several notable projects that demonstrate the evolution and implementation of parabolic trough collectors in large-scale solar power generation.

These projects highlight the versatility and scalability of parabolic trough systems, which can be deployed in various configurations to meet different energy demands.

Station	Country	Electrical capacity
Noor/Ouarzazate Solar Power Station*	Morocco	510 MW
Solar Energy Generating Systems (SEGS)	USA	310 MW
Solaben Solar Power Station	Spain	200 MW
Ashalim Power Station (Negev Energy)	Israel	121 MW
Kathu Solar Park	South Africa	100 MW
Shams Solar Power Station	UAE.	100 MW
Godawari Green Energy Limited	India	50 MW
Delingha Solar Plant	China	50 MW

Table 2.5. *List of major solar power stations based on a parabolic trough of at least 50 MW (*Combined solar parabolic through and solar tower plant)*

2.2. Low-temperature solar thermal

The foundations of low-temperature solar thermal technology, defined by operating temperatures below 120°C, can be traced to the groundbreaking experiments of Horace-Bénédict de Saussure in the late 18th century. De Saussure's work was fundamental in demonstrating the greenhouse effect, a phenomenon that would become a cornerstone in solar thermal design. In these experiments, de Saussure placed a layer of glass glazing above an absorber inside an insulated box. This setup allowed Sun rays to enter, trapping heat within the enclosure, and highlighted how heat retention could be achieved through strategic design. His innovative approach not only verified the greenhouse effect but also inspired future solar thermal concepts by illustrating the potential of controlled heat capture.

Despite the contributions of de Saussure, substantial progress was not made in making solar thermal systems practical for everyday use until the late 19th and early 20th centuries. A landmark development came with the Clarence Kemp invention with a patent for the first commercially viable solar water heater in the United States (Kemp 1891). Kemp's design has advanced in the utilization of solar energy for heating, offering a practical and efficient means of producing hot water directly from sunlight, a novel idea at the time.

The Kemp solar water heater, known as the "Climax" system, was both functional and ingeniously simple. The system consisted of four cylindrical iron pots, each with a 29-L capacity, arranged horizontally within a specially crafted wooden box. The choice of materials was intentional. The pots were coated with black paint to enhance solar absorption, whereas the wooden box was insulated and topped with glass glazing. The blackened iron pots absorbed Sun radiation

effectively, converting it into heat, and the insulation minimized heat loss to the surroundings. This configuration allowed the system to retain heat for prolonged periods, maximizing the water temperature and optimizing the heating efficiency.

Under favorable conditions, the Kemp Climax heater could reach water temperatures of up to 38°C, which is a remarkable feat for the period. This success demonstrated the practical viability of solar water heating and underscored the potential for renewable energy as a sustainable alternative to fossil fuels. The Climax heater soon gained popularity and became an emblem of innovation in renewable energy, providing a model for future solar thermal systems.

The simplicity and effectiveness of Kemp's design had far-reaching implications for the field of solar energy. The Climax heater demonstrated the importance of material choice, insulation and glazing in retaining solar heat, a combination that became foundational in solar technology. Its ability to capture, retain and utilize solar energy laid the groundwork for more advanced and efficient systems in the years that followed.

Kemp's invention did not just pave the way for practical applications of solar energy in households but also spurred further development in solar thermal technology. Inspired by the Climax heater success, inventors began refining and improving upon its design. These advances led to a new wave of solar water heating systems that were more efficient, accessible and reliable, fueling interest in the potential of solar energy for domestic use. As designs evolved, each iteration built on the principles that Kemp had established, cementing the role of solar thermal systems in renewable energy and promoting the gradual shift toward sustainable alternatives.

In 1909, Bailey revolutionized solar water heating with the invention of day–night solar water heaters, which operated on the thermosiphon principle (Bailey 1909; Butti and Perlin 1979). This principle relies on natural convection, where heated water rises and cooler water sinks, creating a continuous flow of water through the system without the need for pumps. Bailey's design featured a separation between the collector and the storage tank, which is a distinctive characteristic of thermosiphon systems. The collector, which is responsible for absorbing solar energy, is composed of a grid of pipes connected to a flat plate. This arrangement maximized the surface area exposed to solar radiation and facilitated efficient heat absorption. The collector was enclosed within a compact, glazed and insulated enclosure, optimizing heat retention and protecting the system from external elements.

These day–night solar water heaters, often referred to as flat plate collectors in modern terminology, represented a significant advancement in solar water heating

technology. By separating the collector and storage tank, the Bailey design minimized heat loss and improved the overall system efficiency. This separation allowed the storage tank to be placed in a well-insulated location, ensuring that the hot water remained hot for extended periods, thus providing a reliable supply of hot water, even during the night or on cloudy days.

In 1913, Bailey further enhanced his design by incorporating a coil of a pipe-type heat exchanger within the storage tank. This modification, known as a "closed-loop water heater", facilitated more effective heat transfer from the solar fluid to the water stored in the tank (Butti and Perlin 1981). The heat exchanger ensured that the solar energy captured by the collector was efficiently transferred to the water, providing a reliable source of hot water for various domestic and commercial applications. The closed-loop design also helped in maintaining the cleanliness and longevity of the system by preventing scaling and corrosion, which were common issues in earlier designs.

To address the issue of freezing during colder weather, Bailey introduced an innovative solution by using an alcohol–water mixture as an antifreeze solution within a heat exchanger. This antifreeze solution prevented the water from freezing, ensuring the continuous operation of the system, even at low temperatures. This crucial development has expanded the usability of solar water heaters to regions with colder climates, significantly broadening the market and potential applications for solar thermal technology.

Bailey's contributions marked a significant milestone in the development of solar water heating technology. His inventions laid the foundation for modern flat-plate collectors and closed-loop heat exchange systems, paving the way for the widespread adoption of solar water heating systems worldwide. His innovative approach not only improved the efficiency and reliability of solar water heaters but also demonstrated the potential for solar energy to be a viable and sustainable alternative to conventional water heating methods.

The impact of Bailey's work is still evident today, as modern solar water heaters continue to utilize principles and designs that he pioneered. The separation of the collector and storage tank, the use of flat-plate collectors and the implementation of closed-loop systems with antifreeze solutions are all standard features in contemporary solar water heating systems. These systems are now common in residential, commercial and industrial applications, contributing significantly to energy savings and the reduction of greenhouse gas emissions.

During the energy crisis of the 1970s, the solar thermal sector experienced a surge in growth, as governments and industries sought alternatives to fossil fuels. This period, spanning from 1973 to 1985, witnessed significant advancements and

investments in solar thermal technologies. However, this rapid expansion was not without its challenges. Issues such as substandard technologies and inexperienced installers led to widespread underperformance of solar thermal systems. Many systems failed to deliver the expected efficiency and reliability, causing disillusionment among consumers and slowing the initial momentum of the industry.

In response to these setbacks, the late 1990s saw a resurgence of interest in solar thermal energy, fueled by renewed commitments from governments and advancements in technology. This renewed interest was driven by a combination of environmental concerns, rising energy prices and a growing recognition of the importance of sustainable energy sources. Technological improvements have addressed many of the earlier issues, leading to more reliable and efficient solar thermal systems.

Countries such as Austria, Germany, China, Spain and Israel have spearheaded support programs aimed at revitalizing the solar thermal sector, recognizing its potential to contribute to sustainable energy solutions. These countries implemented policies and incentives to promote the adoption of solar thermal technologies. In Austria and Germany, government subsidies and research funding spurred innovation and deployment of advanced solar thermal systems. Given the vast potential of solar energy to meet its growing energy needs, China has invested heavily in manufacturing and large-scale deployment of solar thermal systems. With their abundant solar resources, Spain and Israel developed robust solar thermal industries that not only catered to domestic needs but also became significant exporters of solar thermal technology.

These support programs included financial incentives, such as grants, tax credits and low-interest loans for solar thermal installations. Additionally, public awareness campaigns and training programs for installers were launched to ensure high-quality installations and long-term performance of solar thermal systems. By addressing the previous issues of technology quality and installer expertise, these initiatives helped rebuild consumer confidence and drive the adoption of solar thermal energy.

The late 1990s and early 2000s also saw the introduction of innovative solar thermal technologies, such as evacuated tube collectors and advanced flat plate collectors, which offered higher efficiency and better performance under a variety of climatic conditions. These technological advancements made solar thermal systems more attractive to both residential and commercial users, further increasing sector growth.

The efforts of these pioneering countries not only revitalized their domestic solar thermal industries but also provided examples for other nations to follow. The success stories from Austria, Germany, China, Spain and Israel demonstrated the

viability and benefits of solar thermal energy, encouraging wider adoption and international collaboration in the field.

As a result, the solar thermal sector has become an integral part of the global renewable energy landscape. With continued innovation and support, solar thermal technology is poised to play a significant role in achieving sustainable energy goals worldwide.

As previously mentioned, solar thermal systems operate by harnessing heat from solar radiation through the use of fluid-filled collectors. These collectors, which may utilize air, water or other heat transfer fluids, capture and transfer solar energy to meet various heating needs. Among the primary applications of low-temperature solar thermal technologies are pool heating, space heating and domestic hot water production.

2.2.1. *Solar pool heating*

Pool heating is a straightforward and common application that effectively utilizes solar thermal energy to maintain comfortable swimming temperatures (de Winter 2014). When designing a solar heating system for a swimming pool, several technical aspects, sizing considerations and ratings need to be accurately evaluated to ensure optimal performance and efficiency.

The type of solar collector used is an essential factor and depends on various elements, such as available space and the local climate. Common types of solar collectors include unglazed collectors, typically made of rubber or plastic, which are well suited for warmer climates because of their cost-effectiveness and durability in mild weather. In contrast, glazed collectors, which are made of glass or metal, are more appropriate for colder climates, as they provide better insulation and higher efficiency in capturing and retaining heat.

The size of the collector involves calculating the total surface area required to effectively heat the pool. This calculation considers factors such as the pool size, desired temperature increase, solar radiation level and potential heat loss. Typically, the collector area is between 50% and 100% of the pool surface area, depending on these factors. For example, larger pools or those located in regions with lower solar radiation may require a larger collector area to achieve the desired heating effect.

In systems that incorporate a heat exchanger, selecting the appropriate type and size of exchanger is crucial. The heat exchanger must be capable of handling the heat transfer requirements and the flow rates of the circulating fluid. This ensures that the solar energy captured by the collectors is efficiently transferred to the pool

water. The heat exchanger should be designed to handle the specific thermal load and be resistant to the chemical composition of the pool water.

A circulation pump is essential for moving pool water through solar collectors or heat exchangers. The pump size is determined by the flow rate needed to achieve optimal heating efficiency. This involves calculating the head loss due to friction in the pipes, the height difference between the pool and the collectors, and the required flow rate through the collectors. An adequately sized pump ensures that water flows at a rate that maximizes heat absorption while minimizing energy consumption.

Figure 2.20 depicts a solar pool heating system equipped with an auxiliary heater designed to account for varying weather conditions and maintain a comfortable pool temperature, even when solar radiation is insufficient.

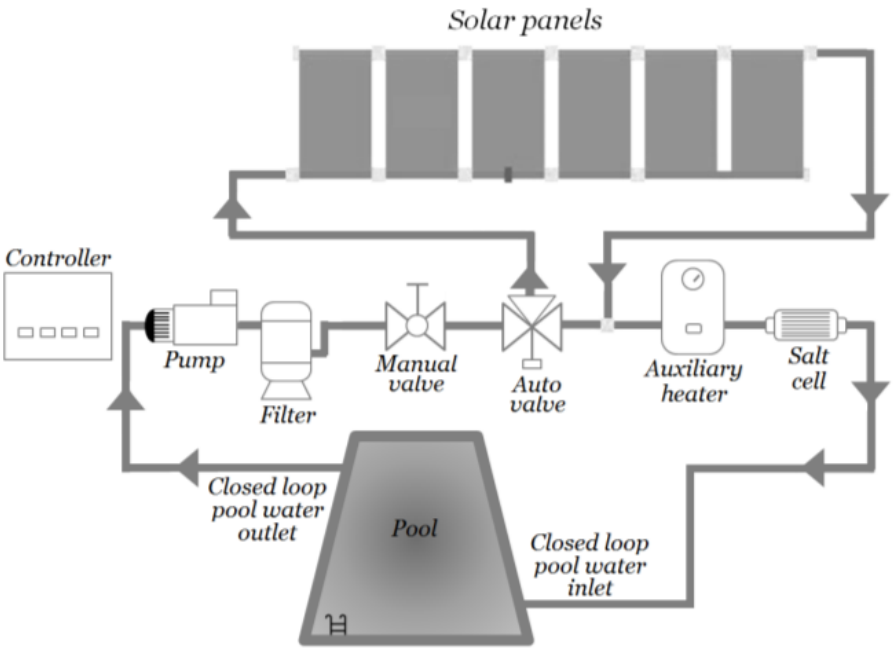

Figure 2.20. *Solar pool heater*

This dual-system approach allows for continuous temperature regulation: when solar energy alone cannot meet the heating demand, the auxiliary heater, powered by either electricity or gas, automatically activates to supplement the system. This feature optimizes energy consumption by relying primarily on solar energy and using the auxiliary heater only as needed.

A central controller manages the operation of the entire system, ensuring efficient function and temperature stability. This controller monitors the temperature differential between the solar collector and the pool water, turning the pump on or off accordingly. Temperature sensors, typically thermistors or thermocouples, track the temperatures of both the solar collector and the pool water. When the collector temperature is sufficiently high compared with the pool water, the pump is activated to circulate water through the collector, absorbing solar heat and transferring it to the pool. Conversely, if the temperature differential drops below a certain threshold, the pump turns off to prevent energy waste.

Importantly, solar heating systems can be seamlessly integrated with existing gas or electric heating systems, offering additional heating capacity during cloudy days or periods of high demand. This flexibility ensures that pools maintain a steady temperature regardless of weather, enhancing user comfort and extending the swimming season.

To further improve the system efficiency, insulating pipes and storage tanks are essential. Proper insulation minimizes heat loss during the circulation and storage of heated water. For example, in an uninsulated solar pool heating system, approximately 30% of heat can be lost during water transportation through pipes. However, by insulating these pipes, heat loss could be reduced to approximately 21%, representing a 30% reduction. This improvement results in a net energy saving of approximately 9%, which is directly attributable to the insulation. By minimizing heat loss, these adjustments make the system more cost-effective and sustainable, contributing to overall energy savings.

2.2.2. *Solar space heating*

Space heating can be achieved using either water or air collectors, offering eco-friendly heating solutions for both residential and commercial buildings. Solar space heating works by directly warming the air inside a building, providing comfort during colder periods. Solar collectors, typically mounted on rooftops, capture sunlight and convert it into heat. The choice of collectors depends on the specific design and efficiency requirements.

A heat transfer fluid, such as water or antifreeze, circulates through the solar collectors, converting sunlight into thermal energy. This heated fluid is then pumped through a network of pipes or heat exchangers to transfer heat into the building heating system. The heated fluid from the solar collectors can be utilized to directly warm the air in a forced-air heating system or transferred to a thermal storage system for later use. In some systems, the heated fluid may also be employed to heat a radiant floor system or baseboard heaters, offering versatile heating options, as

described in Figure 2.21. Solar space heating systems often incorporate a backup heating source, such as a conventional furnace or boiler, to provide additional heat during periods of low solar radiation or high heating demand. This backup ensures consistent comfort levels in the building throughout the year.

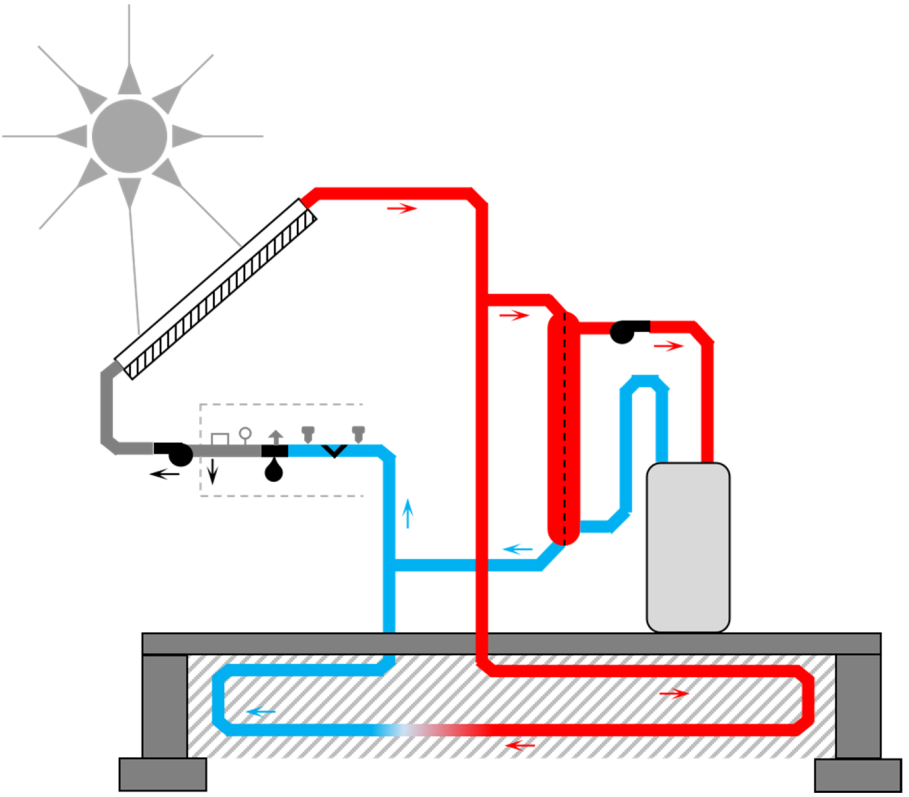

Figure 2.21. *Solar space heating*

Notably, buildings play a significant role in global energy consumption and carbon dioxide emissions. They account for approximately one-third of the world's energy consumption and contribute approximately one quarter of global dioxide carbon emissions.

This significant environmental footprint is particularly evident in some of the most energy-intensive nations. For example, buildings constitute 42% of energy consumption in Russia, 41% in the European Union, 37% in Japan and 34% in the United States, according to data from the International Energy Agency (IEA 2021).

Efforts to reduce energy consumption and carbon emissions in the building sector are crucial for mitigating climate change and promoting sustainability. Solar space heating systems offer a viable solution by harnessing renewable energy sources to meet heating needs while reducing reliance on fossil fuels and lowering greenhouse gas emissions.

The substantial impact of buildings on energy consumption and emissions has pushed them to the forefront of climate policies worldwide. Policymakers recognize the immense potential of buildings in mitigating climate change through improvements in energy efficiency and the adoption of renewable energy technologies.

Increasing the energy performance of buildings not only reduces greenhouse gas emissions but also contributes to energy security, economic competitiveness and improved indoor comfort and air quality.

Efforts to improve the energy efficiency of buildings involve implementing a range of measures, including better insulation, high-efficiency heating, ventilation and air conditioning (HVAC) systems, energy-efficient lighting and smart building technologies. Additionally, promoting the integration of renewable energy sources such as solar photovoltaics and solar thermal systems can further reduce reliance on fossil fuels and lower carbon emissions. Consequently, addressing the energy consumption and emissions associated with buildings is paramount in global efforts to combat climate change. By prioritizing energy efficiency improvements and renewable energy integration in the building sector, policymakers, industry stakeholders and communities achieve significant environmental, economic and social benefits.

2.2.3. *Domestic hot water*

Domestic hot water production is perhaps the most widespread application of low-temperature solar thermal energy. Domestic solar water heating systems are a sustainable and efficient way to meet the hot water needs of residential properties using solar energy. These systems utilize Sun radiation to heat water for various domestic purposes, such as bathing, cooking and cleaning.

The utilization of solar water heating systems is widespread across various sectors, including residential, hydraulic space heating installations, solar space heating, as well as commercial and industrial applications (Salunkhe and Krishna 2017). Despite its popularity, greenhouse gas emissions are particularly problematic in energy generation within the household sector. Studies have shown that household greenhouse gas emissions were as high as 20.4% in Spain, 7.5% in the

EU and 20% in the United States in 2014. Thus, selecting an appropriate water heating system for households can significantly reduce overall energy consumption and operational and maintenance costs and mitigate greenhouse gas emissions, benefiting the environment (Pomianowski et al. 2020; Vengadesan and Senthil 2020).

Currently, a substantial portion (84%) of the energy required for water heating and cooling applications is derived from fossil fuels, with only 16% originating from renewable sources (Ibrahim et al. 2014; Bellos and Tzivanidis 2017). In residential settings, solar water heating systems often serve as alternatives to fossil fuels and electricity, offering an economically viable and environmentally acceptable means of harnessing solar energy. These systems are particularly suitable for low-temperature applications below 80°C owing to their simplicity, low investment and operational costs (Ayompe et al. 2011).

Solar water heaters are widely adopted for their efficiency and cost-effectiveness in providing hot water for household needs, aligning closely with the focus of this book on analyzing a solar water heating system.

There are two primary types of solar water heating systems. The first type corresponds to passive solar water heaters that rely on evacuated tube collectors to harness solar energy. While passive systems may be simpler and more cost effective to install, they may also be less efficient in terms of heat capture, especially in areas with limited sunlight or fluctuating weather conditions.

2.2.3.1. *Passive solar water heaters*

As depicted in Figure 2.22, passive systems do not require mechanical components to circulate the heat transfer fluid; instead, they rely on natural convection or thermosiphon principles to move the heated fluid from the collector to the storage tank. This means that the heated water becomes less dense and naturally rises upward, whereas cooler, denser water descends downward to replace the heated water.

This process creates a continuous movement that circulates water through the storage tank and the solar collector. The thermosiphon effect relies on density differences in a fluid, typically caused by temperature gradients. As water is heated, its density decreases, creating buoyancy forces that drive circulation in the system. This natural circulation can be quantified by determining the pressure difference generated by the density variation and subsequently calculating the resultant flow rate using fluid dynamic equations. The thermosiphon current helps to accelerate the transfer of heat from the solar collector to the storage tank, thereby improving the overall efficiency of the solar water heating system (Jamar et al. 2016).

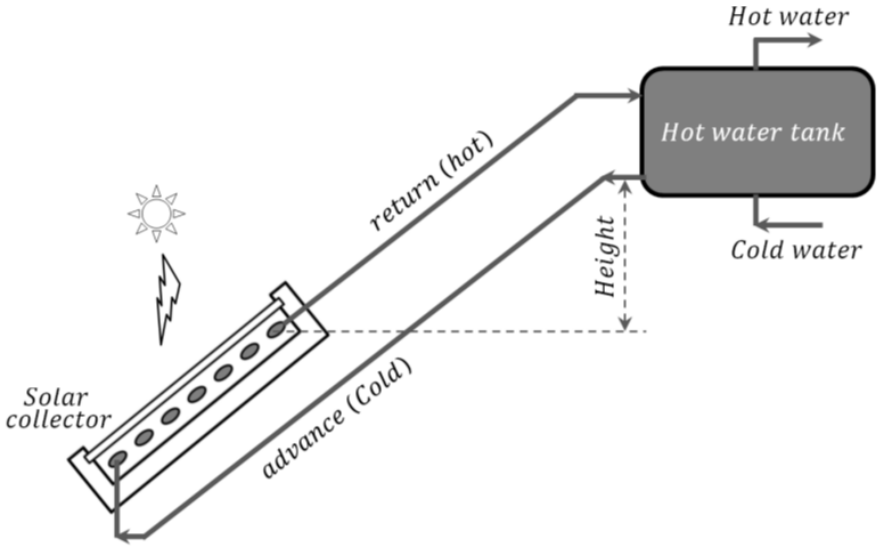

Figure 2.22. *Passive solar water heating systems*

The following figure illustrates the density variations in water according to the temperature. The pressure difference ΔP due to a density difference $\Delta\rho$ over a height H is calculated using the hydrostatic pressure formula:

$$\Delta P = g\, H\, \Delta\rho \qquad [2.78]$$

where g is the acceleration due to gravity.

The Darcy–Weisbach equation relates the pressure drop to the flow velocity in a pipe:

$$\Delta P = f\left(\frac{L}{D}\right)\left(\frac{\overline{\rho}\, V^2}{2}\right) \qquad [2.79]$$

In this context, f represents the friction factor, L denotes the length of the pipe and D corresponds to its diameter. The parameter $\overline{\rho}$ signifies the average fluid density, whereas V designates the flow velocity within the pipe.

The average density $\overline{\rho}$ is determined using the following mathematical relationship:

$$\overline{\rho} = \rho_0 - \frac{1}{2}\,\Delta\rho \qquad [2.80]$$

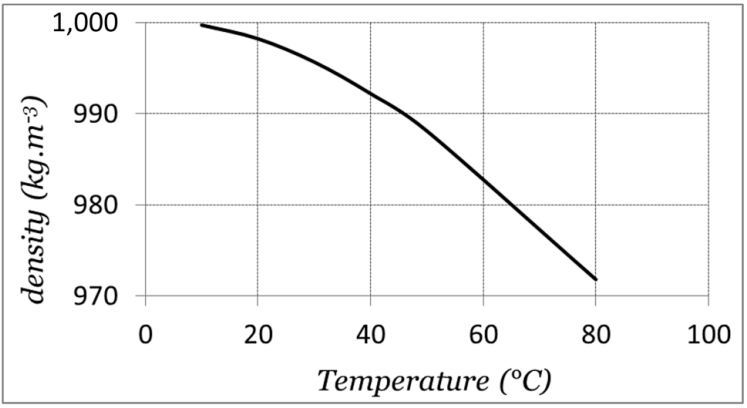

Figure 2.23. *Water density variation according to temperature*

The volumetric flow rate Q is then given by:

$$Q = \sqrt{\frac{2\,\Delta P\,D}{f\,\overline{\rho}\,L}}\,\pi\frac{D^2}{4} \qquad [2.81]$$

The friction factor can be determined using the Moody diagram or the Colebrook–White equation if the flow is turbulent according to a Reynolds number Re higher than 4,000:

$$\frac{1}{\sqrt{f}} = -2log\left(\frac{\frac{\varepsilon}{D}}{3.7} + \frac{2.51}{Re\,\sqrt{f}}\right) \qquad [2.82]$$

For laminar flow where the Reynolds number is less than 2,000, the friction factor is given by:

$$f = \frac{64}{Re} \qquad [2.83]$$

where ε is the relative roughness. The Reynolds number is given by:

$$Re = \frac{\overline{\rho}\,V\,D}{\mu} \qquad [2.84]$$

where μ is the dynamic viscosity.

2.2.3.2. *Active solar water heaters*

On the other hand, active solar water heaters utilize flat plate collectors as their main component. The absorbed heat is transferred to a heat transfer fluid that circulates in a closed loop through the collector and the storage tank of heat for later use (Hossain et al. 2011).

Figure 2.24 shows the active systems requiring a pump and other mechanical components to circulate the heat transfer fluid, making them more complex but often more efficient in terms of heat capture and distribution.

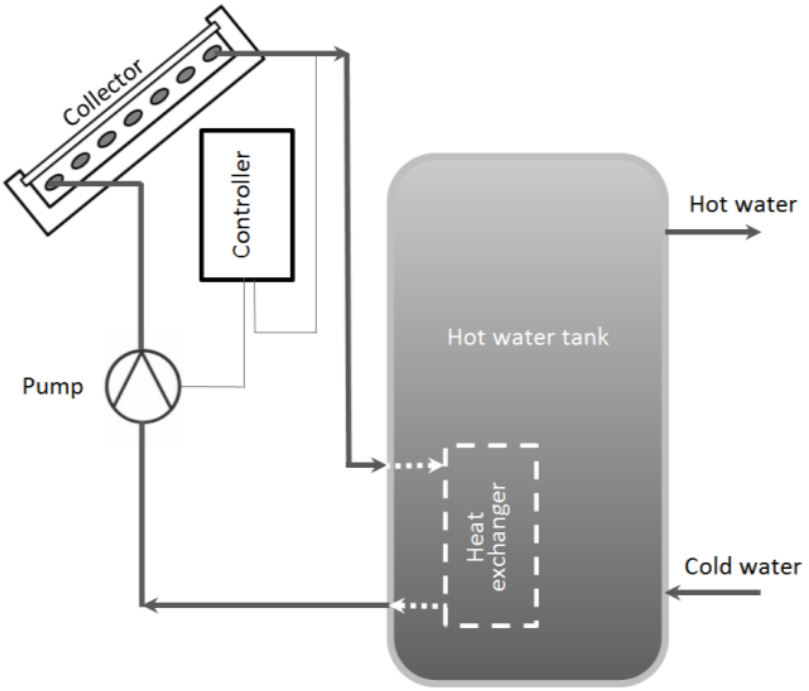

Figure 2.24. *Active solar water heating systems*

The active solar water heating can be in an open loop arrangement when the cold water is directly pumped to the collector. This configuration is suitable for areas that do not freeze for long periods. Otherwise, the incorporation of a heat exchanger allows separation of the unfreezing thermal fluid from the domestic water.

As described in Figures 2.22 and 2.24, the solar thermal system comprises several components, each of which plays an important role in harnessing solar

energy for thermal applications. The solar collectors are specialized panels, such as flat plate collectors, evacuated tube collectors, or concentrating collectors. They are used to capture Sun radiation and convert it into heat energy.

Flat plate collectors, for example, utilize dark absorber plates to absorb Sun energy and transfer the captured heat to a fluid passing through it. The thermal storage system ensures the continuous availability of heat, even when Sun radiation is unavailable. This system typically consists of insulated tanks or containers filled with heat transfer fluid or phase change materials that are capable of storing excess heat generated during sunny periods for later use.

Once solar energy is captured by the collectors, it is transferred through a heat transfer circuit to the intended applications. This circuit includes pipes or channels carrying the heat transfer fluid from the collectors to the heat exchangers or directly to the storage tanks, where the heat is either utilized directly or stored for future use.

The efficient operation of a solar thermal system relies on precise control and regulatory mechanisms. Automated control systems monitor various parameters, such as temperature, flow rates and solar radiation levels, to optimize system performance and ensure safety. A circulation pump is employed to flow the fluid to transfer heat through the system. This pump ensures a consistent flow of fluid, facilitating efficient heat transfer between the collectors, storage tanks and heat exchangers.

Safety features are essential for preventing system malfunctions or hazards. These components include pressure relief valves, temperature sensors and fail–safe mechanisms designed to mitigate risks such as overheating, excessive pressure buildup or fluid leaks.

As previously mentioned, a typical solar water heating system comprises four main components: a solar thermal collector, a heat storage tank, a heat exchanger with transferring fluid and an absorber plate with absorbing materials, each of which contributes to the system thermal performance (Al-Mamun et al. 2023). Furthermore, ancillary components such as a pump, piping unit and auxiliary heating units are necessary for the operation of the SWH system. Potential designs and modifications of these major components are discussed in their respective subsections.

2.3. Solar panels

2.3.1. *Types of solar panels*

There are three main types of solar panels: glazed flat-plate collectors, vacuum tube collectors and unglazed flat-plate collectors.

2.3.1.1. *Glazed flat-plate collector*

The glazed flat-plate collector is among the most prevalent types of solar panels. As illustrated in Figure 2.25, it consists of a flat, insulated metal box topped with a transparent cover, often made of glass or plastic. Inside this box lies a dark-colored absorber plate, typically made of metal, which is designed to capture solar radiation and convert it into heat.

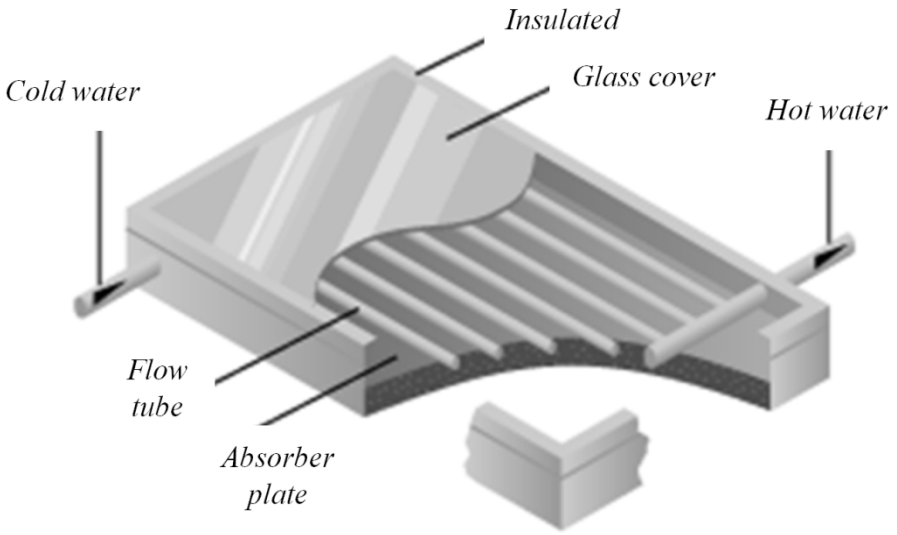

Figure 2.25. *Glazed flat plate solar collectors*

Running through the absorber plate is a network of tubes or channels filled with a heat transfer fluid, such as water or antifreeze. As the absorber plate heats up from the sun's radiation, it transfers this heat to the fluid circulating through the tubes.

Glazing plays a crucial role by trapping heat within the collector, thereby increasing its efficiency and protecting the absorber plate from environmental damage.

The construction and design of glazed flat-plate collectors make them highly versatile and suitable for a variety of applications. They are commonly used for domestic hot water heating, providing a renewable source of hot water for household use.

Additionally, they are employed in space heating systems, contributing to the heating of buildings by integrating with existing heating infrastructures.

Compared with other solar technologies, this type of solar collector is preferred because of its simplicity, effectiveness and relatively low cost. Its ability to provide substantial energy savings makes it a key component in sustainable building practices.

2.3.1.2. *Vacuum tube collector*

The vacuum tube collector, illustrated in Figure 2.26, also known as the evacuated tube collector, is a more advanced type of solar collector.

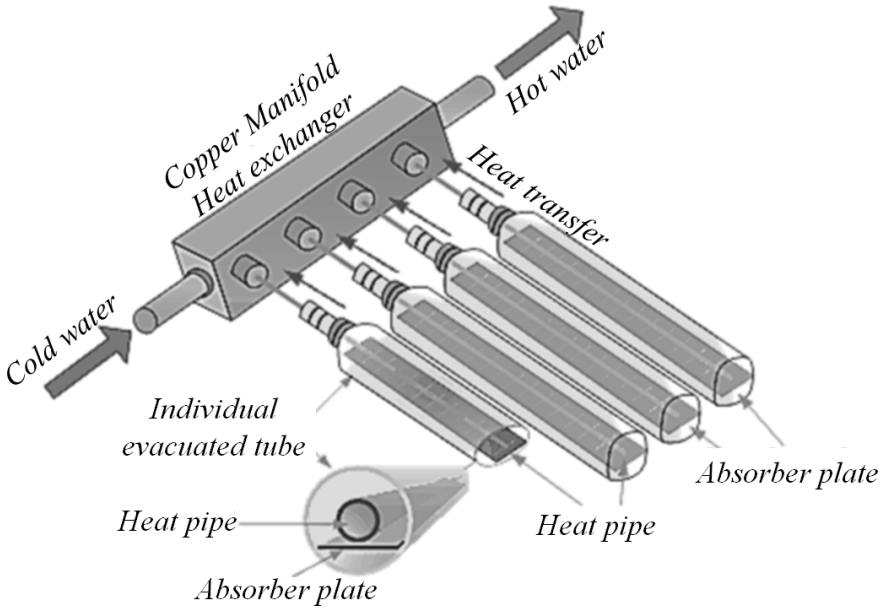

Figure 2.26. *Vacuum tube solar collector*

This consists of a series of parallel glass tubes, each containing an absorber tube inside. The air is evacuated from the space between the absorber tube and the outer glass tube, creating a vacuum that helps minimize heat loss. The absorber tube is coated with a selective coating that absorbs sunlight and converts it into heat. A heat transfer fluid flows through the absorber tubes, soaking up the heat and carrying it away.

Vacuum tube collectors are important components of solar energy systems, particularly because of their high efficiency and adaptability in a range of environmental conditions. The design of vacuum tube collectors is such that a vacuum is created between the glass layers, significantly reducing heat loss due to

convection and conduction. This makes them particularly effective even under cold and cloudy conditions, where other types of solar collectors might be less effective. In solar water heating systems, vacuum tube collectors can maintain high temperatures for extended periods, ensuring a consistent supply of hot water, regardless of the ambient weather conditions. Their ability to perform well in diffuse sunlight, which is common on cloudy days, enhances their overall efficiency and reliability. This makes them a preferred choice in regions with less sunlight or during winter months when the demand for heating is greater.

Moreover, vacuum tube collectors are increasingly used in solar thermal power plants, where their ability to capture and retain heat plays a crucial role. These systems can contribute to large-scale energy generation by heating a working fluid that drives turbines to produce electricity. The high efficiency of vacuum tube collectors ensures that the maximum amount of solar energy is harnessed, making solar thermal power plants more viable and competitive with conventional energy sources. Overall, their advanced design and versatility under various climatic conditions make vacuum tube collectors a key technology in the advancement of solar energy applications.

2.3.1.3. *Unglazed flat-plate collector*

Unglazed solar collectors are a simpler and more cost-effective alternative to glazed collectors and are designed specifically for applications where the demand for high-temperature output is lower and where exposure to these elements is less of a concern. Unlike glazed collectors, which incorporate a glass cover and insulation to minimize heat loss, unglazed collectors are built without these features, making them more affordable and easier to manufacture.

As indicated in Figure 2.27, the core component of an unglazed collector is the absorber plate, which is typically made from dark-colored materials such as metals or durable plastics.

The dark color enhances the ability of the plate to absorb solar radiation, converting it into heat. This heat is then directly transferred to a heat transfer fluid, usually water or a water–glycol mixture, which flows through channels or pipes attached to the back of the plate. The simplicity of this design allows for efficient heat transfer with minimal thermal barriers.

Unglazed collectors are particularly well suited for applications where moderate temperatures are sufficient, such as swimming pool heating. In this context, the relatively lower operating temperature of the unglazed collector is not a drawback but an advantage, as it aligns perfectly with the needs of pool heating systems. These systems typically require temperatures only slightly above ambient temperature, making unglazed collectors an ideal, energy-efficient solution. One of the main

benefits of unglazed collectors is their ability to withstand harsh environmental conditions without the need for protective glazing. The absence of glass or insulation reduces the risk of damage from environmental factors such as hail or debris, contributing to the durability and longevity of these systems.

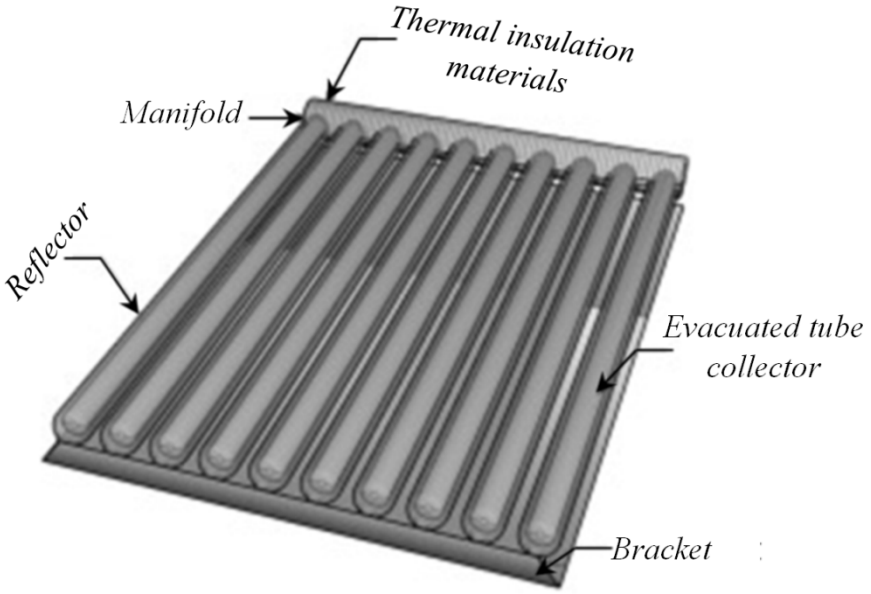

Figure 2.27. *Unglazed solar collector*

Additionally, their lower manufacturing costs make them an attractive option for large-scale installations, such as those needed for heating commercial or residential swimming pools.

2.3.2. *Solar collector efficiency*

The efficiency of solar collectors is a measure of how effectively they convert the solar energy incident on their surface into usable thermal energy. It is calculated as the ratio of the thermal power recovered by the heat transfer fluid circulating within the collector to the total solar energy reaching the collector surface. The thermal power captured by the heat transfer fluid is determined by subtracting the thermal losses that occur within the collector. By accounting for these losses, the net surface thermal power φ_{th} available for utilization within the system can be approximated by a linear expression:

$$\varphi_{th}(W.m^{-2}) = \eta_0 I - U_c\left(T_{c,m} - T_a\right) \quad [2.85]$$

where $T_{c,m}$ and T_a represent the collector mean temperature and the ambient temperature, respectively. I represents the solar radiation intensity on the collector surface. U_c is the overall heat transfer coefficient between the collector and its ambient environment. η_0 is related to the efficiency when the collector is at ambient temperature.

The efficiency can be approximated by a linear approach by taking the mean temperature:

$$\eta = \eta_0 - \frac{U_c\, \Delta T_{c,m}}{I} \quad [2.86]$$

The assessment of U_c was suggested by Klein (1975), who considered the top side and the rear side. The rear heat loss coefficient is typically assumed to remain constant and is determined by the inverse of the thermal resistance of the insulation. Moreover, the top coefficient considers both convection and irradiation effects. More details of this theoretical calculation and the underlying assumptions are reported by Kalogirou (2004).

The determination of efficiency has been standardized in Europe through a second-order approximation method to test collectors. This approach involves a mathematical method that accounts for various factors and complexities discussed above to provide a more accurate estimation of efficiency. By employing a second-order approximation, European standards ensure robust and reliable methods for evaluating efficiency across different systems and applications.

$$\eta = \eta_0 - a_1 \Delta T_{c,m} - a_2\left(\Delta T_{c,m}\right)^2 \quad [2.87]$$

The coefficient a_1 corresponding to the linear heat loss and a_2 relative to the quadratic heat loss represent the thermal losses in solar collectors due to conduction, convection and radiation. These coefficients are derived on the basis of the physical properties of the collector and its surrounding environment.

This approach is based on energy balance by considering radiative losses as well as convective and conductive losses. The useful energy corresponds to the difference between the solar energy absorbed by the collector and the heat loss.

The amount of solar energy absorbed depends on the solar radiation and the optical properties of the collector and can be expressed as:

$$\phi_{abs} = \tau\, \alpha\, A_c\, G \quad [2.88]$$

where τ and α correspond to the transmittance of the glazing plate and the absorptance of the absorber plate, respectively.

The linear heat loss coefficient accounts for heat losses due to convection from the collector surface A_c combined with conduction through the thickness. It is expressed as:

$$\phi_{loss,conv} = h_a A_c (T_m - T_a) \quad [2.89]$$

The convective heat transfer coefficient reflects the combined effects of natural convection and forced convection, with the latter typically influenced by wind. The role of wind in convective heat transfer has been the focus of numerous studies in the scientific literature. One of the earliest experimental investigations into wind-induced forced convective heat transfer was conducted by Jurges (1924), as cited by McAdams (1954). In this seminal work, experiments were performed on a heated copper plate with a surface area of 0.5 m² mounted vertically within a wind tunnel. McAdams subsequently reported a correlation between the convective heat transfer coefficient and wind speed on the basis of Jurges' experimental findings. This research provides foundational insights into the interaction between wind and surface heat transfer. Building on this early work, Wattmuff et al. (1977) conducted similar wind tunnel experiments, which led to the development of their own empirical correlation. However, these pioneering studies were limited in scope and could not be readily generalized to all surface sizes or environmental conditions.

To address these limitations, Sharples and Charlesworth (1998) carried out a series of full-scale measurements under real-world conditions. Their objective was to quantify the magnitude and variability of wind-induced convective heat transfer from a heated surface raised above the pitched roof of a residential-sized building. The dimensions of the test surface were chosen to resemble those of a typical flat-plate solar collector, making the results directly relevant to solar thermal applications. In their experiments, the wind speed was measured at a height of approximately 1.5 m above the surface, simulating the conditions experienced by actual rooftop installations. The researchers derived a correlation between the forced convective heat transfer coefficient h_w and the wind speed V_w, specifically for scenarios where the wind flow was parallel to the surface. This correlation is expressed as:

$$h_w = 6.5 + 3.3\, V_w \quad f \ or \ V_w \leq 6\, m/s \quad [2.90]$$

This study (Sharples and Charlesworth 1998) not only validated the dependence of convective heat transfer on wind speed but also highlighted the influence of wind direction and environmental variability. These findings advanced the understanding

of convective heat transfer in practical applications, particularly for solar collectors and other rooftop-mounted systems.

For natural convective heat transfer over a plate surface, the heat transfer coefficient is determined using formulae that incorporate a combination of dimensionless numbers, including the Nusselt number, the Rayleigh number and the Prandtl number. These dimensionless quantities capture the interplay between the thermal and physical properties of the system, as well as the effects of buoyancy and diffusion processes in the surrounding air. The fundamental principle governing natural convection lies in the temperature difference between the plate surface and the surrounding ambient air. This temperature gradient causes variations in the air density near the plate, setting the stage for convective movement. Warmer, less dense air near the heated plate rises, whereas cooler, denser air from the surroundings descends to replace it. This continuous exchange of air molecules, driven by buoyancy forces, establishes the convective flow that facilitates heat transfer. For purely buoyancy-driven flows, correlations have been developed to relate the Nusselt number – which represents the convective heat transfer relative to conductive heat transfer – to the Rayleigh number and the Prandtl number. These relationships account for the complex interplay of thermal and viscous forces in natural convection systems. Typically, the Nusselt number is expressed as a function of the Rayleigh number, which quantifies the relative influence of buoyancy and thermal diffusivity, and the Prandtl number, which characterizes the ratio of momentum diffusivity to thermal diffusivity.

The specific form of this correlation depends on the geometry of the plate, its orientation and the boundary conditions. For example, a vertical plate may exhibit different convective behavior to a horizontal plate because of variations in buoyancy-driven flow patterns. These empirical and theoretical correlations provide a critical framework for accurately estimating the natural convective heat transfer coefficient in various applications. For a horizontal plate, the Nusselt number can be expressed in two distinct forms, depending on the specific range of the Rayleigh number. The mathematical formulation varies to account for different convective heat transfer regimes, ensuring accurate representation of thermal behavior under varying conditions of natural convection.

$$\begin{cases} Nu = 0.54\, Ra^{1/4} & (10^4 \leq Ra \leq 10^7) \\ Nu = 0.15\, Ra^{1/3} & (10^7 \leq Ra \leq 10^{11}) \end{cases} \quad [2.91]$$

The Rayleigh number is defined as the product of the Grashof number and the Prandtl number, $Ra = Gr\, Pr$.

$$Ra = Gr\, Pr \quad [2.92]$$

The Grashof number is a quantity that describes the relationship between buoyant and viscous forces acting on a fluid and is defined as:

$$Gr = \frac{g\beta(T_s - T_\infty)\, L^3}{\nu^2} \quad [2.93]$$

where g is gravitational acceleration, β is the thermal expansion coefficient, T_s is the surface temperature, T_∞ is the bulk temperature and ν is the kinematic viscosity. L is the characteristic length and can be considered the ratio of the surface and the perimeter of the plate.

The Prandtl number describes the relationship between momentum diffusivity and thermal diffusivity and is defined as:

$$Pr = \frac{\nu}{\alpha} = \frac{C_p\, \mu}{k} \quad [2.94]$$

where α is the thermal diffusivity and μ is the dynamic viscosity.

$$\alpha = \frac{k}{\rho\, C_p} \quad [2.95]$$

For vertical plates, Churchill and Chu (1975) proposed a widely accepted correlation that applies to the entire range of Rayleigh numbers (RaRa), encompassing both laminar and turbulent natural convection regimes (Churchill and Chu 1975). The correlation is given as:

$$Nu = \left[0.825 + \frac{0.387\, Ra^{1/6}}{(1 + (0.492/Pr)^{8/27})}\right]^2 \quad [2.96]$$

For inclined surfaces, the dynamics of the boundary layer are influenced by the inclination angle θ, as the component of the gravitational force driving the buoyancy changes with orientation. This dependency makes the convective behavior sensitive to the angle of inclination, such as inclined solar panels. However, most studies in the literature suggest that for surfaces inclined at angles less than 60°, the correlation for a vertical plate remains valid with a minor modification by replacing the gravitational acceleration g with its component normal to the surface, g cos θ. This adjustment accounts for the reduced buoyancy force acting along the inclined surface while preserving the underlying assumption of the boundary layer flow.

The heat loss due to radiation is given by:

$$\phi_{loss,rad} = \epsilon\, \sigma\, A_c \left({T_m}^4 - {T_a}^4\right) \quad [2.97]$$

For the range temperature differences in the case of solar water heating, this expression can be approximated using a Taylor series expansion:

$$\phi_{loss,rad} \approx \epsilon\, \sigma\, A_c \left\{4{T_a}^3\, (T_m - T_a) + 6{T_a}^2 (T_m - T_a)^2\right\} \quad [2.98]$$

where ε is the radiative emissivity and where σ is the Stephan–Boltzmann constant:

$$\sigma = 5.670374419 \times 10^{-8}\ (\mathrm{W/m^2K^4}) \quad [2.99]$$

The efficiency can be expressed as the ratio of the rates of useful energy and solar energy:

$$\eta = \frac{\phi_{abs} - \phi_{loss,conv} - \phi_{loss,rad}}{\phi_{sol}} \quad [2.100]$$

By reporting the different fluxes, the efficiency is given as:

$$\eta = \frac{\left[\tau\, \alpha G - \left(h_a + 4\epsilon\, \sigma {T_a}^3\right)(T_m - T_a) - 6\epsilon\, \sigma {T_a}^2 (T_m - T_a)^2\right] A_c}{A_c\, G} \quad [2.101]$$

Finally, the second-order expression of the efficiency is obtained:

$$\eta = \eta_0 - a_1 (T_m - T_a) - a_2 (T_m - T_a)^2 \quad [2.102]$$

The different parameters are as follows:

– the efficiency at ambient temperature

$$\eta_0 = \tau\, \alpha \quad [2.103]$$

– the first-order coefficient is given as:

$$a_1 = \frac{\left(h_a + 4\, \epsilon\, \sigma {T_a}^3\right)}{G} \quad [2.104]$$

– the second-order coefficient is given as:

$$a_2 = \frac{6\, \epsilon\, \sigma\, {T_a}^2}{G} \quad [2.105]$$

Here, η_0 is approximately 0.8. a_1 is approximately 1.5 (K^{-1}) for vacuum tubes and 4 (K^{-1}) for flat plates. a_2 exhibits a wide range of variation, ranging from 0.001 (K^{-2}) to 0.15 and beyond, for both vacuum tubes and flat plates.

An example of the efficiency of these three collectors is represented in Figure 2.28, which describes their performance across a range of applications, as previously discussed. This graphical depiction offers a view of how each collector performs in different scenarios according to the range of temperatures.

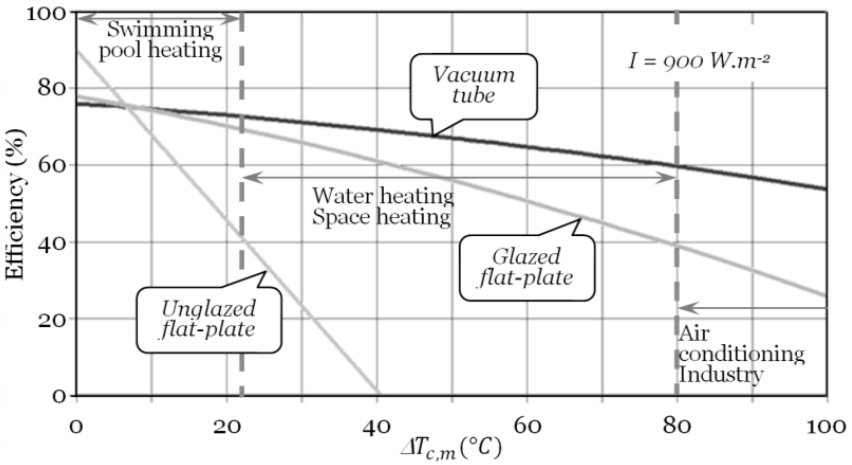

Figure 2.28. *Solar collector efficiency according to temperature*

A comparative analysis of the energy cost savings between unglazed and glazed collectors for domestic water heating was conducted (Burch et al. 2004). This analysis revealed that for a collector area of 3.72 m², glazed collectors with selective coatings achieved an average annual efficiency of approximately 38%, whereas unglazed collectors demonstrated a lower average efficiency of 21%.

The study highlighted a key difference in the conditions under which the two types of collectors performed optimally. Unglazed collectors were most effective under conditions of higher ambient temperature and solar irradiance, harvesting the greatest amount of energy when the temperature differential between the inlet water and ambient water, divided by the solar irradiance, was approximately 0.2°C·m²/W. In contrast, the glazed collectors delivered peak energy efficiency at a ratio of approximately 0.4°C·m²/W. These results suggest that while glazed collectors may generally outperform their unglazed counterparts in terms of efficiency, unglazed collectors could offer a competitive advantage in environments with relatively high ambient temperatures. Additionally, the study indicates that the overall efficiency of

these systems might be enhanced by integrating them into low-temperature space heating applications alongside medium-temperature water heating.

Furthermore, glazed collectors can be configured in two distinct ways. The first configuration involves a single-glazed collector, whereas the second configuration pertains to a double-glazed collector. Figure 2.29 illustrates these two configurations, where the schematic labeled (a) represents the single-glazed collector and (b) corresponds to the double-glazed version.

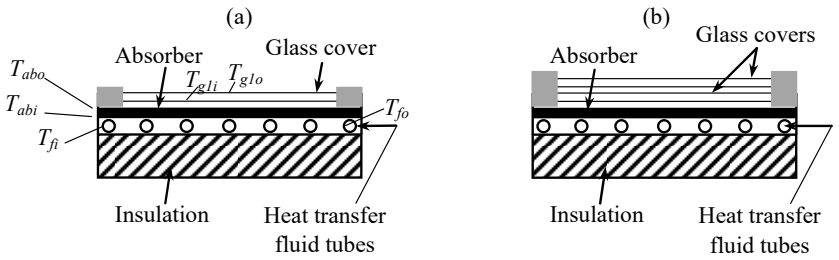

Figure 2.29. *Solar plate collector: (a) single glazed; (b) double glazed*

These two types of collectors differ primarily in the number of glazing layers, each affecting their thermal performance and efficiency in distinct ways.

2.3.2.1. *Single-glazed flat-plate collector*

This type of collector features a single transparent cover, typically made of glass or a durable plastic material, which is placed above the absorber plate. The purpose of glazing is to reduce heat loss from the absorber plate while allowing Sun radiation to penetrate efficiently. As illustrated in the schematic (a) of Figure 2.29, the single layer of glazing forms a protective barrier over the absorber plate. The single-glazed design is simpler and more cost-effective, offering moderate thermal insulation. It is often used in applications where heat retention requirements are not extremely high, such as in regions with mild climates or for lower-temperature heating systems.

A single-glazed solar collector consists of an absorber plate and a single layer of glass above it to reduce heat loss. The useful energy rate is defined by the heat transfer fluid thermal rate, which is given as:

$$\phi_{th} = \dot{m}_f \, Cp_f \left(T_{fo} - T_{fi}\right) \qquad [2.106]$$

where $\dot{m}_f$ is the mass flow rate of the heat transfer fluid, and Cp_f is its specific heat capacity. As depicted in Figure 2.29, T_{fo} and T_{fi} are the outlet and inlet temperatures of the heat transfer fluid, respectively.

The useful thermal rate corresponds to the heat exchange between the heat transfer fluid at the boundary with the absorber and is expressed as:

$$\phi_{th} = U_{f,ab}\, A_f \left(T_{abi} - T_f\right) \quad [2.107]$$

T_f is considered the mean temperature of the heat transfer fluid:

$$T_f = \frac{T_{fi} + T_{fo}}{2} \quad [2.108]$$

A_f is considered equivalent to the lateral surface of the tube through which the fluid circulates. $U_{f,ab}$ represents the heat transfer coefficient between the fluid and the absorber with consideration of the mean temperature of the heat transfer fluid. This coefficient is related to the convective heat transfer of the fluid with the absorber and can be obtained from the Nusselt number. The most commonly used formula corresponds to the Colburn correlation, which is given as:

$$Nu = 0.023\, Re^{4/5} Pr^{4/5} \quad [2.109]$$

where Re represents the Reynolds number:

$$Re = \frac{V\, d_H}{\nu} = \frac{\rho\, V\, d_H}{\mu} \quad [2.110]$$

V corresponds to the velocity, d_H denotes the hydraulic diameter and μ is the fluid dynamic viscosity. The Prandtl number Pr was previously defined.

The temperature difference between the heat transfer fluid and the absorber can be expressed according to the thermal resistance as:

$$\left(T_{abi} - T_f\right) = R_{thf}\, \phi_{th} \quad [2.111]$$

where

$$R_{thf} = \frac{1}{U_{f,ab}\, A_f} \quad [2.112]$$

The boundary energy rate conservation at the lower frontier of the absorber can be expressed as:

$$-k_{ab} A_c \left.\frac{dT_{ab}}{dz_{ab}}\right|_{z_{ab}=0} + \phi_{th} = 0 \quad [2.113]$$

The absorber is internally heated by the volumetric absorbed solar flux $q_{ab,sol}$.

$$q_{ab,sol} = \frac{\tau_{g1}\, G\, A_c}{V_{ab}} \qquad [2.114]$$

where τ_{g1} is the transmittance of the glass, G is the solar irradiance and V_{ab} is the absorber volume.

With a single glass, the transmittance is given as a function of the reflection coefficient R_1, its thickness and the absorption coefficient α_1.

When accounting for multiple reflections, the overall reflection and transmission of radiation through the glass can be determined by considering the interactions of light waves as they reflect back and forth between the upper and lower surfaces of the glass. These repeated reflections influence the total amount of light that is ultimately reflected or transmitted, creating a complex interplay that must be analyzed to accurately describe the optical behavior of the glass.

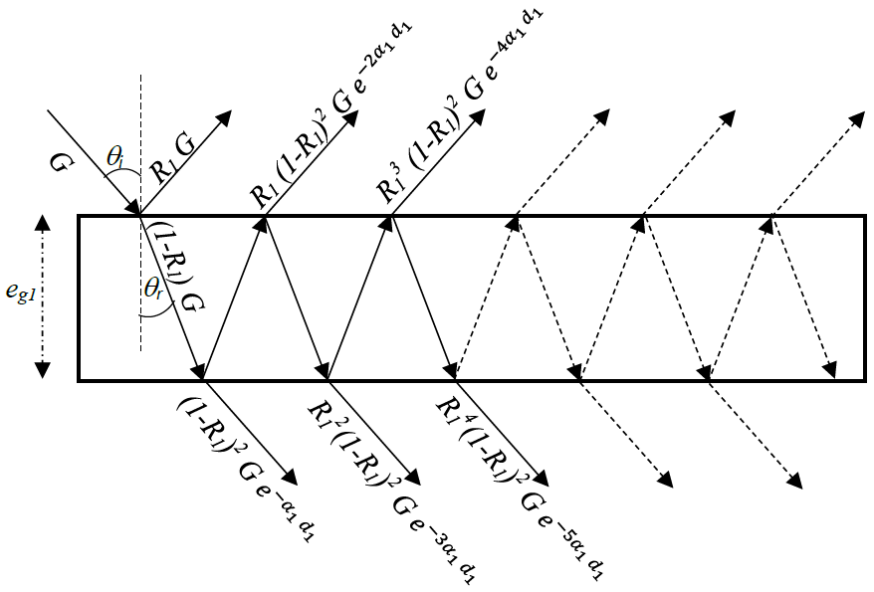

Figure 2.30. *Multiple reflections in the glass thickness*

Figure 2.30 illustrates the multiple reflections in the thickness of the glass. The reflection coefficient is supposed to be similar at the outer and inner surfaces of the glass. The solar panel receives incident radiation at an angle of incidence, denoted

as θ_i. As the radiation enters the glass, it refracts, changing direction to form a refracted angle, θ_r. The relationship between these two angles is governed by the Snell–Fresnel law.

This law is expressed mathematically as follows:

$$n_a \, sin(\theta_i) = n_{g1} \, sin(\theta_r) \qquad [2.115]$$

where n_{g1} and n_a represent the glass and air refractive indices, respectively. The glass has an index of approximately 1.5, and the air has an index of 1.

The refractive index is a key optical property of a material that quantifies how much radiation slows down and bends when it transitions from one medium, such as air, into glass. This relationship is fundamental for understanding how radiation interacts with a solar panel, affecting its efficiency in capturing solar energy.

d_l denotes the radiation path in the glass after refraction. It can be derived as a function of the glass thickness, refractive index and angle of incidence:

$$d_1 = \frac{n_{g1} \, e_{g1}}{\sqrt{n_{g1}^2 - sin^2(\theta_i)}} \qquad [2.116]$$

The reflection coefficient is expressed as a function of the refractive indices of the two media:

$$R_1 = \left(\frac{n_{g1} - 1}{n_{g1} + 1}\right)^2 \qquad [2.117]$$

The overall reflection coefficient can be obtained by the following expression derived from the external reflection $(R_1 G)$ added to the multiple reflections of the crossing that share radiation $\left((1 - R_1)G\right)$ through the two internal sides after absorption:

$$R_{g1} = R_1 + (1 - R_1)[R_1(1 - R_1) \, e^{-2\alpha_1 \, d_1} + R_1^3(1 - R_1) \, e^{-4\alpha_1 \, d_1} + \cdots] \qquad [2.118]$$

The reflection coefficient can be formulated as a geometrical series with a ratio of $(R_1^2 \, e^{-2\alpha_1 \, d_1})$:

$$R_{g1} = R_1 + \frac{(1 - R_1)^2}{R_1} \sum_{i=1}^{\infty} (R_1^2 \, e^{-2\alpha_1 \, d_1})^i \qquad [2.119]$$

This formula accounts for an infinite number of internal reflections within the glass, under the assumption that the glass thickness is negligible compared with the overall dimensions of the solar panel. The infinite series reflects the cumulative effects of radiation reflecting back and forth between the surfaces of the glass layer.

By simplifying the previous arithmetic expression, an analytical form of the reflection coefficient can be derived:

$$R_{g1} = R_1 + \frac{(1 - R_1)^2 \, R_1 \, e^{-2\alpha_1 \, d_1}}{1 - R_1^2 e^{-2\alpha_1 \, d_1}} \qquad [2.120]$$

This simplified expression considers the combined effect of the initial external reflection on the glass surface and the contributions from the subsequent internal reflections, which are attenuated exponentially by the factor $e^{-2\alpha_1 \, d_1}$. This analytical form is particularly useful for accurately modeling the reflective behavior of thin glass layers in solar panel applications.

The reflection coefficient can be expressed as the sum of the first external reflections added to the multiple internal reflections of both sides:

$$R_{g1} = R_1 + (1 - R_1) R_{g1_m} \qquad [2.121]$$

where R_{g1_m} denotes the multiple reflections coefficient inside the glass:

$$R_{g1_m} = \frac{(1 - R_1) \, R_1 \, e^{-2\alpha_1 \, d_1}}{1 - R_1^2 e^{-2\alpha_1 \, d_1}} \qquad [2.122]$$

The radiation transmitted by the glass is given as:

$$\tau_{g_1} = (1 - R_1)[(1 - R_1) \, e^{-\alpha_1 \, d_1} + R_1^2 (1 - R_1) \, e^{-3\alpha_1 \, d_1} + \cdots] \qquad [2.123]$$

Similar to the reflectance, the transmittance due to multiple internal reflections can be written as a geometrical series with a common ratio of $R_1^2 e^{-2\alpha_1 \, d_1}$:

$$\tau_{g_1} = (1 - R_1)^2 e^{-\alpha_1 \, d} \sum_{i=0}^{\infty} (R_1^2 \, e^{-2\alpha_1 \, d_1})^i \qquad [2.124]$$

The analytical expression of the transmittance of solar radiation is given as:

$$\tau_{g_1} = \frac{(1 - R_1)^2 \, e^{-\alpha_1 \, d_1}}{1 - R_1^2 e^{-2\alpha_1 \, d_1}} \qquad [2.125]$$

The share of radiation crossing the upper surface of the glass corresponds to $(1 - R_1)\, G$ and is subjected to multiple reflections by transmitting a part of the radiation through the lower side. The transmission coefficient is expressed as a function of the multiple transmissions coefficient:

$$\tau_{g_1} = (1 - R_1)\, \tau_{g_1 m} \qquad [2.126]$$

where

$$\tau_{g_1 m} = \frac{(1 - R_1)\, e^{-\alpha_1\, d_1}}{1 - R_1^2 e^{-2\alpha_1\, d_1}} \qquad [2.127]$$

Figure 2.31 illustrates the influence of the intrinsic reflection coefficient of glass on its overall transmittance and reflectance properties.

As the intrinsic reflection coefficient increases, the proportion of radiation reflected by the glass increases, resulting in a higher overall reflectance. Conversely, this increase in reflectance reduces the amount of light that can pass through the glass, leading to a corresponding decrease in overall transmittance. This relationship highlights the critical role of the reflective characteristics of glass in determining its optical performance, particularly in applications where controlling radiation transmission and reflection is essential.

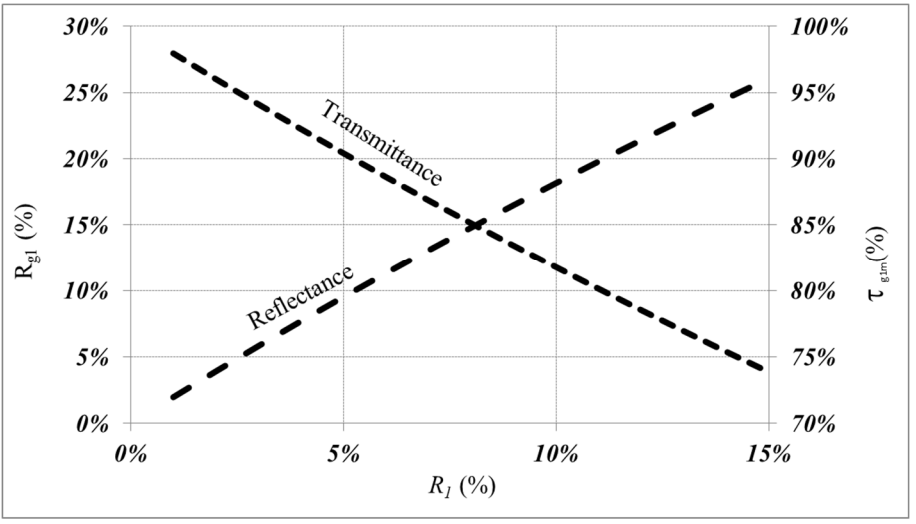

Figure 2.31. *Effect of the intrinsic reflection coefficient on the overall reflectance and transmittance of solar panel glass*

The boundary energy rate conservation is obtained as:

$$\frac{k_{ab}}{e_{ab}} A_c \, (T_{abo} - T_{abi}) + \frac{1}{2} V_{ab} q_{ab,sol} = \phi_{th} \quad [2.128]$$

The temperature difference between the upper and lower sides of the absorber can be expressed as a function of its thermal resistance:

$$(T_{abo} - T_{abi}) = R_{th,ab} \left(\phi_{th} - \frac{1}{2} V_{ab} q_{ab,sol} \right) \quad [2.129]$$

where

$$R_{th,ab} = \frac{e_{ab}}{k_{ab} \, A_c} \quad [2.130]$$

The absorbed volumetric energy rate is given as:

$$q_{ab,sol} = \frac{G \, A_c (1 - R_1)^2 \, e^{-\alpha_1 \, d_1}}{V_{ab} \, (1 - R_1^2 e^{-2\alpha_1 \, d_1})} \quad [2.131]$$

Similarly, the energy balance at the upper surface of the absorber is governed by the conservation of energy, which accounts for the conductive heat transfer within the absorber itself as well as the conductive heat exchange between the absorber and the glass through the intervening air. Furthermore, the radiative heat exchange at the boundary leads to the following:

$$-k_{ab} A_c \left. \frac{dT_{ab}}{dz_{ab}} \right|_{z_{ab}=e_{ab}} + \frac{k_{air1}}{e_{air1}} A_c \left(T_{g1i} - T_{abo} \right) + \epsilon_{eff} \, \sigma \, A_c \left({T_{g1i}}^4 - {T_{abo}}^4 \right) = 0 \quad [2.132]$$

This relation leads to the following expression after linearization of the radiative flux:

$$\frac{k_{ab}}{e_{ab}} A_c (T_{abo} - T_{abi}) - \frac{1}{2} V_{ab} q_{ab,sol} - \frac{(k_{air1} + k_{rad1})}{e_{air1}} A_c \left(T_{g1i} - T_{abo} \right) = 0 \quad [2.133]$$

where k_{rad} is the equivalent thermal conductivity for radiative heat exchange:

$$k_{rad1} = 4 \, \epsilon_{eff_1} \, \sigma \, A_c \, T_{g,ab_m}^3 \, e_{air1} \quad [2.134]$$

ϵ_{eff_1} is the effective radiative emissivity between the glass and the absorber.

$$\frac{1}{\epsilon_{eff_1}} = \frac{1}{\epsilon_g} + \frac{1}{\epsilon_{ab}} - 1 \quad [2.135]$$

$T_{g,ab,m}$ is the mean surface temperature of the lower side of the glass and the absorber temperature.

$$\frac{k_{ab}}{e_{ab}} A_c (T_{abo} - T_{abi}) - \frac{1}{2} V_{ab} q_{ab,sol} = \frac{k_{air1,t}}{e_{air1}} A_c (T_{g1i} - T_{abo}) \quad [2.136]$$

where

$$k_{air1,t} = k_{air1} + k_{rad1} \quad [2.137]$$

The temperature difference between the glass lower side and the upper side of the absorber can be obtained in terms of the thermal resistance:

$$(T_{g1i} - T_{abo}) = R_{th,air1,t} \left(\frac{(T_{abo} - T_{abi})}{R_{th,ab}} - \frac{1}{2} V_{ab} q_{ab,sol} \right) \quad [2.138]$$

where

$$R_{th,air1,t} = \frac{e_{air1}}{k_{air1,t}\, A_c} \quad [2.139]$$

On the lower side of the glass, the energy rate conservation leads to the following expression:

$$-k_{g1} A_c \left. \frac{dT_{g1}}{dz_{g1}} \right|_{z_{g1}=0} + \frac{(k_{air1} + k_{rad1})}{e_{air1}} A_c (T_{g1i} - T_{abo}) = 0 \quad [2.140]$$

Considering the share of solar energy absorbed by the glass, the following expression is obtained:

$$-\frac{k_{g1}}{e_{g1}} A_c (T_{g1o} - T_{g1i}) + \frac{1}{2} V_{g1}\, q_{g1,sol} = -\frac{k_{air1,t}}{e_{air1}} A_c (T_{g1i} - T_{abo}) \quad [2.141]$$

The temperature difference between the upper and lower sides of the glass can be written in terms of the thermal resistance:

$$\left(T_{g1o} - T_{g1i}\right) = R_{th,g1}\left(\frac{\left(T_{g1i} - T_{abo}\right)}{R_{th,air1,t}} - \frac{1}{2}V_{g1}q_{g1,sol}\right) \quad [2.142]$$

where

$$R_{th,g1} = \frac{e_{g1}}{k_{g1}\,A_c} \quad [2.143]$$

Similar to the analysis of the reflectance and transmittance of the glass, the absorbed share is given as:

$$Ab_{g1} = 1 - R_{g_1} - \tau_{g_1} \quad [2.144]$$

The absorbed part also considers the multiple reflections into the glass as described previously and is given, after rearrangement, as:

$$Ab_{g1} = \frac{(1 - R_1)(1 - e^{-\alpha_1 d_1})(1 + R_1 e^{-\alpha_1 d_1})}{1 - R_1^2 e^{-2\alpha_1 d_1}} \quad [2.145]$$

The mean volumetric energy flux absorbed by the glass is as follows:

$$q_{g1,sol} = Ab_{g1}\frac{G\,A_c}{V_{g1}} \quad [2.146]$$

where V_{g1} denotes the glass volume.

The volumetric solar energy absorbed by the glass is expressed as a function of the thickness, reflection coefficient and absorption coefficient:

$$q_{g1,sol} = \frac{G\,(1 - R_1)(1 - e^{-\alpha_1 d_1})}{e_{g1}(1 - R_1 e^{-\alpha_1 d_1})} \quad [2.147]$$

The energy rate conservation at the upper side of the glass corresponds to the balance of the conductive heat transfer and the convective exchange, combined with radiative exchange with the external environment:

$$-k_{g1}A_c\left.\frac{dT_{g1}}{dz_{g1}}\right|_{z_{g1}=e_{g1}} + h_a\,A_c\left(T_a - T_{g1o}\right) + \varepsilon_g\sigma A_c\left(T_a^4 - T_{g1o}^4\right) = 0 \quad [2.148]$$

where h_a is the convective heat exchange coefficient with the upper side of the solar glass. By linearizing the radiative heat exchange, the following expression is obtained:

$$-k_{g1}A_c \left.\frac{dT_{g1}}{dz_{g1}}\right|_{z_{g1}=e_{g1}} + h_{a,t}\, A_c\left(T_a - T_{g1o}\right) = 0 \qquad [2.149]$$

where $h_{a,t}$ is the total heat transfer coefficient taking into account the convective and radiative exchanges with the environment. This is expressed as:

$$h_{a,t} = h_{a,conv} + h_{a,rad} \qquad [2.150]$$

As previously discussed, the convective heat transfer coefficient with the external environment considers natural convection and the component linked to forced wind convection. The natural convective heat transfer coefficient over a plate surface is determined using a combination of dimensionless numbers such as the Nusselt number, the Rayleigh number and the Prandtl number.

For radiative exchange, it can be approximated as linear for the low-temperature operating range of solar panels, simplifying the analysis of thermal interactions. This linearization is particularly valid when the temperature differences involved remain moderate, ensuring that the radiative heat transfer remains proportional to the temperature difference.

$$h_{a,rad} \approx 4\,\sigma\,\varepsilon_g\,T_{mg}^3 \qquad [2.151]$$

T_{mg} represents the mean temperature of the upper side of the glass envelope and the ambient environment.

Considering the solar absorbed energy, the following expression is related to the boundary condition at the upper side of the glass:

$$-\frac{k_{g1}}{e_{g1}}A_c\left(T_{g1o} - T_{g1i}\right) + \frac{1}{2}V_{g1}\, q_{g1,sol} + h_{a,t}\, A_c\left(T_a - T_{g1o}\right) = 0 \qquad [2.152]$$

The temperature difference between the ambient environment and the upper side of the glass is given in terms of the thermal resistance as follows:

$$\left(T_a - T_{g1o}\right) = R_{th_{a,t}}\left(\frac{\left(T_{g1o} - T_{g1i}\right)}{R_{th_{g1}}} - \frac{1}{2}V_{g1}\, q_{g1,sol}\right) \qquad [2.153]$$

where

$$R_{th_{a,t}} = \frac{1}{h_{a,t}\, A_c} \quad [2.154]$$

The different relationships between temperatures lead to the following expression of the thermal useful energy rate:

$$\phi_{th} = \frac{1}{R_{th_{T1}}} \left(\Delta T_{ab,sol} + \Delta T_{g1,sol} + T_a - T_f\right) \quad [2.155]$$

where

$$R_{th_{T1}} = \left(R_{th_f} + R_{th_{ab}} + R_{th_{air1,t}} + R_{th_{g1}} + R_{th_{a,t}}\right) \quad [2.156]$$

and

$$\Delta T_{ab,sol} = q_{ab,sol}\, V_{ab} \left(\frac{1}{2} R_{th_{ab}} + R_{th_{air1,t}} + R_{th_{g1}} + R_{th_{a,t}}\right) \quad [2.157]$$

$$\Delta T_{g1,sol} = q_{g1,sol}\, V_{g1} \left(\frac{1}{2} R_{th_{g1}} + R_{th_{a,t}}\right) \quad [2.158]$$

The thermal useful energy rate can be written as a function of the number of transfer units:

$$\phi_{th} = \dot{m}_f\, Cp_f \left(\frac{NTU_1}{1 + 2\, NTU_1}\right) \left(\Delta T_{ab,sol} + \Delta T_{g1,sol} + T_a - T_{fi}\right) \quad [2.159]$$

where

$$NTU_1 = \frac{1}{\dot{m}_f\, Cp_f\, R_{th_{T1}}} \quad [2.160]$$

The temperature difference between the outlet and inlet temperatures of the heat transfer fluid is given as:

$$T_{fo} - T_{fi} = \left(\frac{NTU_1}{1 + 2\, NTU_1}\right) \left(\Delta T_{ab,sol} + \Delta T_{g1,sol} + T_a - T_{fi}\right) \quad [2.161]$$

The efficiency of the single-glazed collector, η_{sg}, is then:

$$\eta_{sg} = \frac{\varphi_{th}}{G} = \frac{\Delta T_{ab,sol} + \Delta T_{g1,sol} + T_a - T_{fi}}{G\, R_{th_{T_1}}\,(1 + 2\, NTU_1)} \quad [2.162]$$

2.3.2.2. *Double-glazed flat-plate collector*

A double-glazed solar collector adds an additional glass layer to reduce heat loss further. This additional layer creates an air gap, which acts as additional insulation. Indeed, the overall heat loss coefficient for a double-glazed collector generally accounts for the heat resistance from the air gap.

When considering the double-glazed solar panel, the thermal exchanges occurring through the external layer of glazing play a significant role in influencing the overall thermal performance of the panel. These exchanges, which involve the transfer of heat between the glazing and its surrounding, define the panel's thermal behavior.

The thermal analysis of the double-glazed panel is similar to that described previously for a single-glazed panel. The thermal effect of the second glass is added to describe the double-glazed thermal behavior.

The energy rate conservation at the boundary between the upper side of the internal glass and the air layer between the two glasses is expressed as:

$$-k_{g1} A_c \left.\frac{dT_{g1}}{dz_{g1}}\right|_{z_{g1}=e_{g1}} + \frac{k_{air2}}{e_{air2}} A_c \left(T_{g2i} - T_{g1o}\right) + \epsilon_{eff2}\, \sigma\, A_c \left(T_{g2i}^4 - T_{g1o}^4\right) = 0 \quad [2.163]$$

By considering the thermal conductive energy rate at the boundary, the following expression is derived, accounting for the transfer of heat through the material interface.

This expression encapsulates the relationship between the temperature gradient and the internal energy source generated by the solar radiation at the specified boundary.

$$\frac{k_{g1}}{e_{g1}} A_c \left(T_{g1o} - T_{g1i}\right) - \frac{1}{2} V_{g1} q_{g1,sol} = \frac{k_{air2,t}}{e_{air2}} A_c \left(T_{g2i} - T_{g1o}\right) \quad [2.164]$$

where T_{g2i} denotes the inner surface temperature of the lower side of the external glass layer. $k_{air2,t}$ is given as:

$$k_{air2,t} = k_{air2} + k_{rad2} \quad [2.165]$$

where k_{rad2} is an equivalent thermal conductivity for radiative heat exchange:

$$k_{rad2} \approx 4\, \epsilon_{eff2}\, \sigma\, A_c\, T_{air2,m}^3\, e_{air2} \quad [2.166]$$

ϵ_{eff_2} is the effective radiative emissivity between the two parallel glasses.

$$\frac{1}{\epsilon_{eff_2}} = \frac{1}{\epsilon_{g1}} + \frac{1}{\epsilon_{g2}} - 1 \quad [2.167]$$

The temperature difference between the lower side of the external glass and the upper side of the internal glass can be obtained in terms of the thermal resistance:

$$\left(T_{g2i} - T_{g1o}\right) = R_{th,air2,t}\left(\frac{\left(T_{g1o} - T_{g1i}\right)}{R_{th,g1}} - \frac{1}{2} V_{g1}\, q_{g1,sol}\right) \quad [2.168]$$

With a double-glazed panel, the solar energy rate absorbed by the internal glass is as follows:

$$q_{g1,sol} = Ab_{g1} \frac{G\, A_c}{V_{g1}} \quad [2.169]$$

In this case, Ab_{g1} represents the share of radiation absorbed after accounting for the multiple reflections and transmissions that occur within the various layers of the system. This includes reflections and absorptions through the upper glass layer, the air interface above the glass, the lower glass layer and the air interface below the glass.

Each of these layers contributes to the overall behavior of radiation as it interacts with the material, with energy being reflected, absorbed or transmitted at each interface. The calculation of Ab_{g1} incorporates the cumulative effects of these processes, ensuring that the absorption is accurately determined after considering all potential reflection and transmission pathways.

To determine the overall reflection, transmission and absorption, these parameters are evaluated iteratively in three stages. First, multiple reflections within the upper glass layer are considered, treating it as a single glass medium. Second, the interaction between the upper glass and the adjacent air layer is analyzed,

accounting for multiple reflections of the radiation transmitted from the glass. In the third stage, this combined glass–air system is treated as an equivalent medium bordering the second glass layer, through which energy must pass before reaching the absorber, which is separated by the lower air layer. The absorber is assumed to capture all of the solar energy transmitted through the lower air layer, meaning that no further reflection or transmission occurs beyond this point.

To consider multiple reflections, the upper glass is defined by its reflectance, absorbance and transmittance. They are defined similarly to the case of a single glassed solar panel that was previously presented.

The reflectance of the upper glass is a combination of the external reflection with multiple reflections and is given as:

$$R_{g_2} = R_2 + (1 - R_2)R_{g_{2m}} \quad [2.170]$$

where the multiple reflection coefficient inside the glass thickness is given as:

$$R_{g_{2m}} = \frac{(1 - R_2)\, R_2\, e^{-2\alpha_2\, d_2}}{1 - R_2^2 e^{-2\alpha_2\, d_2}} \quad [2.171]$$

The transmission coefficient due to multiple reflections in the thickness of the upper glass plate is defined as:

$$\tau_{g2} = (1 - R_2)\tau_{g_{2m}} \quad [2.172]$$

where

$$\tau_{g_{2m}} = \frac{(1 - R_2)\, e^{-\alpha_2\, d_2}}{1 - R_2^2 e^{-2\alpha_2\, d_2}} \quad [2.173]$$

The entire transmitted radiation to the lower bordering air layer is also subjected to multiple reflections, as illustrated in Figure 2.32.

In this case, the radiation enters the glass and, after multiple reflections, transmits a share through the boundary to the air layer, which also subjects the radiation to multiple reflections and reflects up a part to the upper glass and transmits down a share of radiation.

The upward reflected radiation returns to the glass and reflects again in the glass several times. This process is repeated infinitely between the upper glass layer and the air layer.

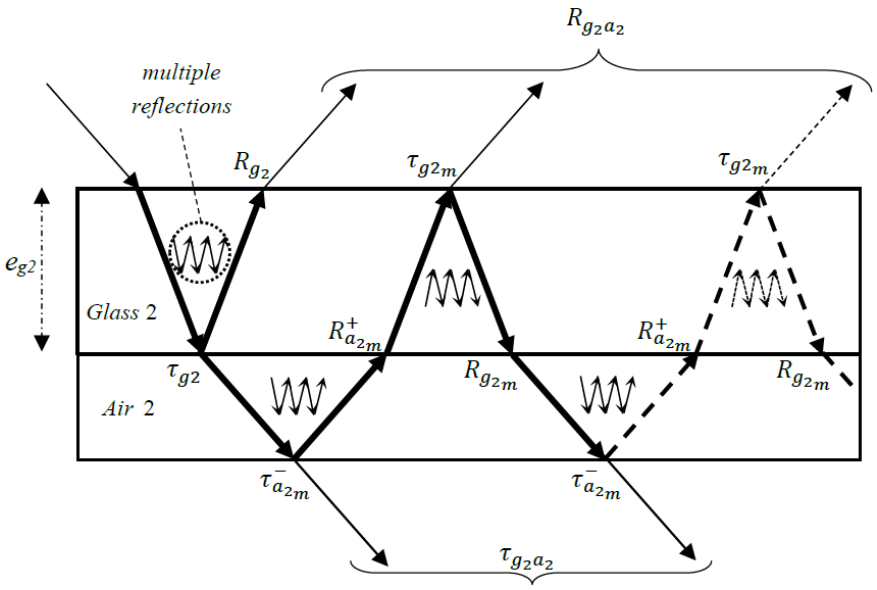

Figure 2.32. *Multiple reflections in both the glass thickness and the air layer*

When accounting for multiple reflections through both the upper glass and the adjacent air layer, the total double multiple reflectance can be determined similarly to a series with a ratio of $R^+_{a_{2m}}\ R_{g_{2m}}$:

$$R_{g_2a_2} = R_{g_2} + \tau_{g_2} R^+_{a_{2m}} \tau_{g_{2m}} \sum_{i=0}^{\infty} \left(R^+_{a_{2m}}\ R_{g_{2m}} \right)^i \qquad [2.174]$$

The overall reflection coefficient of the upper glass combined with its bordering air layer results from the following series expression:

$$R_{g_2a_2} = R_{g_2} + \frac{\tau_{g_2} R^+_{a_{2m}} \tau_{g_{2m}}}{1 - R^+_{a_{2m}}\ R_{g_{2m}}} \qquad [2.175]$$

The signs (+/–) indicate, particularly for the intermediate air layer, the direction of radiation propagation, with (+) representing upward propagation and (–) representing downward propagation. The upper air layer is located between the two glasses. Indeed, the reflection coefficients of the boundaries of the high and low sides are different. Its upper boundary has a reflection coefficient R_2, associated

with the upper glass, whereas its lower boundary has a reflection coefficient R_1, corresponding to the lower glass. $R^+_{a_{2m}}$ represents the multiple reflectances of the air layer for radiation traveling upward, and $\tau^-_{a_{2m}}$ denotes the downward transmission coefficient of the air layer.

The reflection coefficient of the joined glass–air layer can be expressed by reporting the expression of R_{g_2} and τ_{g_2} as:

$$R_{g_2a_2} = R_2 + (1 - R_2)R_{g_{2m}} + (1 - R_2)\frac{\tau^2_{g_{2m}} R^+_{a_{2m}}}{1 - R^+_{a_{2m}} R_{g_{2m}}} \quad [2.176]$$

Analogous to the single-glass scenario, the double multiple reflectance is determined using a formulation that combines the effects of external reflection with those of multiple internal reflections. In this approach, the reflectance at the outer interface is relative to the upper surface reflection, and then the contribution from successive reflections occurring within the two media is added.

$$R_{g_2a_2} = R_2 + (1 - R_2)R_{g_2a_{2m}} \quad [2.177]$$

where

$$R_{g_2a_{2m}} = R_{g_{2m}} + \frac{\tau^2_{g_{2m}} R^+_{a_{2m}}}{1 - R^+_{a_{2m}} R_{g_{2m}}} \quad [2.178]$$

The overall double multiple transmission of the upper glass–air layer is expressed as a series with a common ratio of $R^+_{a_{2m}} R_{g2_m}$:

$$\tau_{g_2a_2} = \tau_{g_2}\tau^-_{a_{2m}} \sum_{i=0}^{\infty} \left(R^+_{a_{2m}} R_{g_{2m}}\right)^i \quad [2.179]$$

where $\tau^-_{a_{2m}}$ is the downward multiple reflectance of the upper air layer.

The double overall multiple transmittance can be expressed as:

$$\tau_{g_2a_2} = \frac{\tau_{g_2}\tau^-_{a_{2m}}}{1 - R_{g_{2m}} R^+_{a_{2m}}} \quad [2.180]$$

This expression can also be expressed by the same analogy of a single layer with multiple reflections:

$$\tau_{g_2a_2} = (1 - R_2)\tau_{g_2a_{2m}} \quad [2.181]$$

where

$$\tau_{g_2 a_{2m}} = \frac{\tau_{g_{2m}} \tau^{-}_{a_{2m}}}{1 - R_{g_{2m}} R^{+}_{a_{2m}}} \quad [2.182]$$

In these formulations, the different multiple reflection and transmission coefficients are defined as follows for the upper glass:

$$\begin{cases} R_{g_{2m}} = \dfrac{(1 - R_2)\, R_2\, e^{-2\alpha_2\, d_2}}{1 - R_2^2 e^{-2\alpha_2\, d_2}} \\ \tau_{g_{2m}} = \dfrac{(1 - R_2)\, e^{-\alpha_2\, d_2}}{1 - R_2^2 e^{-2\alpha_2\, d_2}} \end{cases} \quad [2.183]$$

The same formulations are given for the upper air layer, where there is no absorption:

$$\begin{cases} R^{+}_{a_{2m}} = \dfrac{R_1(1 - R_2)}{1 - R_1 R_2} \\ R^{-}_{a_{2m}} = \dfrac{R_2(1 - R_1)}{1 - R_1 R_2} \\ \tau^{+}_{a_{2m}} = \dfrac{1 - R_2}{1 - R_1 R_2} \\ \tau^{-}_{a_{2m}} = \dfrac{1 - R_1}{1 - R_1 R_2} \end{cases} \quad [2.184]$$

Note that

$$\begin{cases} R^{+}_{a_{2m}} + \tau^{-}_{a_{2m}} = 1 \\ R^{-}_{a_{2m}} + \tau^{-}_{a_{2m}} = 1 \end{cases} \quad [2.185]$$

The lower reflectance and transmittance of the lower glass should also be considered when accounting for multiple reflections within the system.

Since the absorber is assumed to capture all of the solar energy that reaches it after passing through the various layers, any downward reflectance of the absorber is deemed negligible and is therefore not taken into account.

The upward and downward reflection coefficients of the lower glass are identical because the first rays are considered for both from the inside.

$$\begin{cases} R_{g_1 m} = \dfrac{(1-R_1)\,R_1\,e^{-2\alpha_1\,d_1}}{1-R_1^2 e^{-2\alpha_2\,d_2}} \\ \tau_{g_1 m} = \dfrac{(1-R_1)\,e^{-\alpha_1\,d_1}}{1-R_1^2 e^{-2\alpha_1\,d_1}} \end{cases} \qquad [2.186]$$

The overall three-layered multiple reflectance, considering the upper and lower glasses separated by the upper air layer, is illustrated in Figure 2.33.

As shown in this figure, the upper glass combined with the adjacent air layer can be considered an equivalent medium because of its overall multiple reflection and transmission coefficients.

In this case, the overall reflection coefficient of the three-layered media can be expressed as:

$$R_{g_2 a_2 g_1} = R_{g_2 a_2} + \tau_{g_2 a_2} R_{g_1 m} \tau_{g_2 a_2 m} \sum_{i=0}^{\infty} \left(R_{g_2 a_2 m}\, R_{g_1 m}\right)^i \qquad [2.187]$$

The overall reflection coefficient is written as:

$$R_{g_2 a_2 g_1} = R_{g_2 a_2} + \frac{\tau_{g_2 a_2} R_{g_1 m} \tau_{g_2 a_2 m}}{1 - R_{g_2 a_2 m}\, R_{g_1 m}} \qquad [2.188]$$

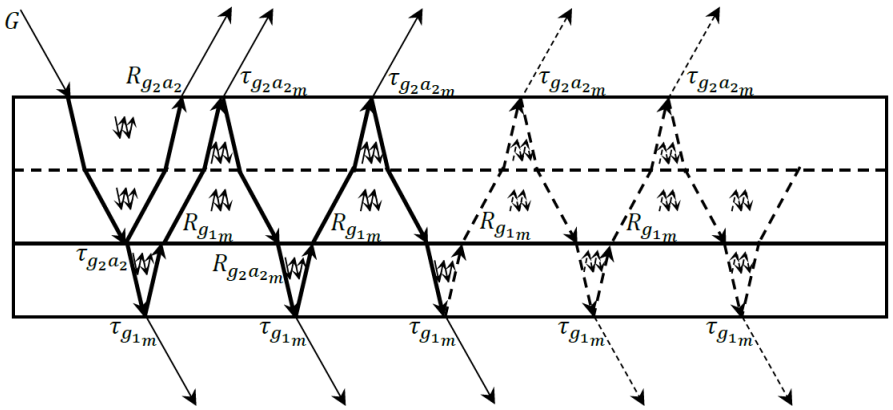

Figure 2.33. *Multiple reflections in three-layered glasses and the mid-air layer*

By reporting the expressions of $R_{g_2a_2}$ and $\tau_{g_2a_2}$, the overall reflection coefficient can be expressed similarly to the sum of the external reflection and the internal multiple reflections:

$$R_{g_2a_2g_1} = R_2 + (1 - R_2)\, R_{g_2a_2g_{1m}} \quad [2.189]$$

where

$$R_{g_2a_2g_{1m}} = R_{g_2a_{2m}} + \frac{\tau^2_{g_2a_{2m}} R_{g_{1m}}}{1 - R_{g_2a_{2m}}\, R_{g_{1m}}} \quad [2.190]$$

The transmission coefficient is given by the following expression:

$$\tau_{g_2a_2g_1} = \tau_{g_2a_2}\tau_{g_{1m}} \sum_{i=0}^{\infty} \left(R_{g_2a_{2m}}\, R_{g_{1m}}\right)^i \quad [2.191]$$

By reporting the expression of the series, the transmission coefficient results as:

$$\tau_{g_2a_2g_1} = \frac{\tau_{g_2a_2}\tau_{g_{1m}}}{1 - R_{g_2a_{2m}}\, R_{g_{1m}}} \quad [2.192]$$

Similarly, the overall transmittance coefficient is given as:

$$\tau_{g_2a_2g_1} = (1 - R_2)\tau_{g_2a_2g_{1m}} \quad [2.193]$$

where

$$\tau_{g_2a_2g_{1m}} = \frac{\tau_{g_2a_{2m}}\, \tau_{g_{1m}}}{1 - R_{g_2a_{2m}}\, R_{g_{1m}}} \quad [2.194]$$

The energy absorbed by the lower glass corresponds to the difference between the energy received from the upper air layer and the sum of the energies transmitted downward and reflected upward.

As illustrated in Figure 2.33, the absorption coefficient of the lower glass becomes:

$$Ab_{g1} = \tau_{g_2a_2}\left(1 - R_{g_{1m}} - \tau_{g_{1m}}\right) \sum_{i=0}^{\infty} \left(R_{g_2a_{2m}}\, R_{g_{1m}}\right)^i \quad [2.195]$$

The part of the energy absorbed by the lower glass is obtained by reporting the expression of the geometrical series:

$$Ab_{g1} = \tau_{g_2 a_2} \left(\frac{1 - R_{g_{1m}} - \tau_{g_{1m}}}{1 - R_{g_2 a_{2m}} R_{g_{1m}}} \right) \quad [2.196]$$

By replacing the expression of $\tau_{g_2 a_2}$, the absorptance is given as:

$$Ab_{g1} = (1 - R_2)\, \tau_{g_2 a_{2m}} \left(\frac{1 - R_{g_{1m}} - \tau_{g_{1m}}}{1 - R_{g_2 a_{2m}} R_{g_{1m}}} \right) \quad [2.197]$$

This can be written in the following form:

$$Ab_{g1} = (1 - R_2)\, Ab_{g1_m} \quad [2.198]$$

where Ab_{g1_m} is the absorption coefficient due to the multiple reflections of the transmitted radiation by the upper glass combined with its adjacent air layer:

$$Ab_{g1_m} = \tau_{g_2 a_{2m}} \left(\frac{1 - R_{g_{1m}} - \tau_{g_{1m}}}{1 - R_{g_2 a_{2m}} R_{g_{1m}}} \right) \quad [2.199]$$

The energy absorbed by the upper glass can also be obtained from the following relation:

$$R_{g_2 a_2 g_1} + \tau_{g_2 a_2 g_1} + Ab_{g1} + Ab_{g2} = 1 \quad [2.200]$$

By replacing the different expressions, the absorptance coefficient of the upper glass is given as:

$$Ab_{g2} = (1 - R_2)\, Ab_{g2_m} \quad [2.201]$$

where

$$Ab_{g2_m} = 1 - R_{g_2 a_{2m}} - \tau_{g_2 a_{2m}} \left(\frac{1 - R_{g_{1m}} \left(1 - \tau_{g_{1m}}\right)}{1 - R_{g_2 a_{2m}} R_{g_{1m}}} \right) \quad [2.202]$$

The energy rate conservation at the boundary between the lower side of the external glass and the air layer between the two glasses is expressed as:

$$-k_{g2} A_c \left. \frac{dT_{g2}}{dz_{g2}} \right|_{z_{g2}=0} + \frac{k_{air2}}{e_{air2}} A_c \left(T_{g2i} - T_{g1o} \right) + \epsilon_{eff2}\, \sigma\, A_c \left(T_{g2i}^4 - T_{g1o}^4 \right) = 0 \quad [2.203]$$

This boundary energy conservation results in an expression for the temperature difference between the upper and lower surfaces of the external glass:

$$\left(T_{g2o} - T_{g2i}\right) = R_{th_{g2}} \left(\frac{\left(T_{g2i} - T_{g1o}\right)}{R_{th_{air2,t}}} - \frac{1}{2} V_{g2}\, q_{g2,sol} \right) \quad [2.204]$$

where

$$R_{th_{g2}} = \frac{e_{air2}}{k_{air2}\, A_c} \quad [2.205]$$

V_{g2} is the volume of the external glass, and $q_{g2,sol}$ is the amount of solar energy absorbed by the external glass.

Similar to the case of a single-glazed panel, the average absorbed volumetric energy rate is taken into account.

$$q_{g2,sol} = (1 - R_2)\, Ab_{g2_m} \frac{G}{e_{g_2}} \quad [2.206]$$

By replacing the expression of Ab_{g2_m}, the volumetric energy rate is given by relation [2.207]. This equation quantifies the volumetric energy rate by accounting for the multiple reflection and transmission interactions within the system. The formulation highlights the impact of surface reflectivity, transmissivity and absorption characteristics, ensuring an accurate representation of energy transfer dynamics.

$$q_{g2,sol} = (1 - R_2) \left\{ 1 - R_{g_2 a_{2_m}} - \tau_{g_2 a_{2_m}} \left(\frac{1 - R_{g_{1_m}} \left(1 - \tau_{g_{1_m}}\right)}{1 - R_{g_2 a_{2_m}} R_{g_{1_m}}} \right) \right\} \frac{G}{e_{g_2}} \quad [2.207]$$

Next, the heat exchange between the external glass and the surrounding environment is analyzed. The conservation of energy at the boundary on the upper surface of the external glass is expressed as:

$$-k_{g2} A_c \left. \frac{dT_{g2}}{dz_{g2}} \right|_{z_{g2}=e_{g2}} + h_a A_c \left(T_a - T_{g2o}\right) + \epsilon_{g2}\, \sigma\, A_c \left(T_a^4 - T_{g2o}^4\right) = 0 \quad [2.208]$$

Substituting the expression of the conductive heat flux through the external glass at the interface with the ambient environment, the following expression is obtained:

$$\left(T_a - T_{g2o}\right) = R_{th_{a,t}}\left(\frac{\left(T_{g2o} - T_{g2i}\right)}{R_{th_{g2}}} - \frac{1}{2}V_{g2}\, q_{g2,sol}\right) \quad [2.209]$$

The energy absorbed by the absorber is given as the energy transmitted through the lower air layer from the lower glass:

$$q_{ab,sol} = \frac{\tau_{g_2 a_2 g_1}\, G\, A_c}{V_{ab}} \quad [2.210]$$

By substituting the expression of the transmittance, the energy rate is given as:

$$q_{ab,sol} = \frac{G\, A_c (1 - R_2)\, \tau_{g_2 a_{2m}} \tau_{g_{1m}}}{V_{ab}\left(1 - R_{g_2 a_{2m}}\, R_{g_{1m}}\right)} \quad [2.211]$$

The useful thermal energy rate is derived as a function of the thermal resistance and the absorbed solar energy:

$$\phi_{th} = \frac{1}{R_{th_{T2}}}\left(\Delta T_{ab,sol} + \Delta T_{g1,sol} + \Delta T_{g2,sol} + T_a - T_f\right) \quad [2.212]$$

where

$$R_{th_{T2}} = \left(R_{th_f} + R_{th_{ab}} + R_{th_{air1,t}} + R_{th_{g1}} + R_{th_{air2,t}} + R_{th_{g2}} + R_{th_{a,t}}\right) \quad [2.213]$$

and

$$\Delta T_{ab,sol} = q_{ab,sol}\, V_{ab}\left(\frac{1}{2}R_{th_{ab}} + R_{th_{air1,t}} + R_{th_{g1}} + R_{th_{air2,t}} + R_{th_{g2}} + R_{th_{a,t}}\right) \quad [2.214]$$

$$\Delta T_{g1,sol} = q_{g1,sol}\, V_{g1}\left(\frac{1}{2}R_{th_{g1}} + R_{th_{air2,t}} + R_{th_{g2}} + R_{th_{a,t}}\right) \quad [2.215]$$

$$\Delta T_{g2,sol} = q_{g2,sol}\, V_{g2}\left(\frac{1}{2}R_{th_{g2}} + R_{th_{a,t}}\right) \quad [2.216]$$

The useful thermal energy rate can also be expressed as a function of the number of transfer units:

$$\phi_{th} = \dot{m}_f \, Cp_f \left(\frac{NTU_2}{1 + 2\, NTU_2} \right) \left(\Delta T_{sol} + T_a - T_{fi} \right) \quad [2.217]$$

where

$$\Delta T_{sol} = \Delta T_{ab,sol} + \Delta T_{g1,sol} + \Delta T_{g2,sol} \quad [2.218]$$

and

$$NTU_2 = \frac{1}{\dot{m}_f \, Cp_f \, R_{th_{T2}}} \quad [2.219]$$

The difference between the outlet and inlet temperatures of the heat transfer fluid is expressed as:

$$T_{fo} - T_{fi} = \left(\frac{NTU_2}{1 + 2\, NTU_2} \right) \left(\Delta T_{sol} + T_a - T_{fi} \right) \quad [2.220]$$

The efficiency of the double-glazed collector, η_{dg}, is then:

$$\eta_{dg} = \frac{\varphi_{th}}{G} = \frac{\Delta T_{sol} + T_a - T_{fi}}{G \, R_{th_{T2}} \, (1 + 2\, NTU_2)} \quad [2.221]$$

As previously described, heat exchange plays a crucial role in these types of devices. Heat exchangers are widely used in refrigeration, air conditioning, space heating, power generation and chemical processing. Common types of heat exchanger flows include parallel flow, counter flow and cross flow. In parallel flow, both fluids move in the same direction while transferring heat; in counter flow, the fluids move in opposite directions; and in cross flow, the fluids move at right angles to each other. Common types of heat exchangers include shell and tube, double pipe, extruded finned pipe, spiral fin pipe, u-tube and stacked plate. Each type has certain advantages and disadvantages over other types.

Typically, the design of heat exchangers relies on assessing their properties under steady-state conditions. In the academic literature, steady-state solutions are commonly derived using the global heat transfer coefficient (Kakaç and Liu 2002; Shah 2006; Serth 2014). The logarithmic mean temperature difference (LMTD) method is straightforward when inlet temperatures are given and outlet temperatures are specified, as presented by Claesson (2005). To examine indirect evaporative heat

exchangers, Cui et al. (2014) introduced a modified LMTD method. When the outlet temperatures are unspecified, the effectiveness-number of transfer unit (ε -NTU) method should be used (Ranong and Roetzel 2002; Noie 2006). This method relies on identifying the maximum achievable heat transfer rate and the number of transfer units. On the other hand, a streamlined concept based on heat exchanger efficiency derived from a singular algebraic expression was proposed (Fakheri 2007, 2014). These methodologies collectively offer a comprehensive framework for the analysis of heat exchangers. Additionally, an approach based on the thermal convexity of steady-state heat exchangers was proposed for their characterization (Abdelghani-Idrissi et al. 2015).

Numerous researchers have delved into the transient behavior of heat exchangers. An analytical approach employing the Laplace-transform technique was proposed by Malinowski and Bielski (2004). However, this method is applicable only under specific conditions, where the thermal capacities and velocities of fluids are identical in both channels. The temporal dynamics of heat exchangers can be characterized through two key parameters, namely, the delay time and rising time (Pierson and Padet 1988; Lachi et al. 1995). Pierson and Padet proposed an analytical formulation of this strategy, and a generalization of the method was provided (Pierson and Padet 1985). Similarly, Göğüs and Ataer (1997) suggested a comparable approach, summarizing the dynamic characteristics of heat exchangers via a first-order approximation, incorporating its gain, time constant and delay time (Göğüs and Ataer 1997; Ataer 2004). A novel methodology to investigate the distributed transient behavior along tubular heat exchangers was introduced (Abdelghani-Idrissi et al. 2001). These findings were further corroborated by Ansari and Mortazavi (2006), who validated the results through a comparison with numerical solutions combined with analytical solutions of the energy equation.

This book addresses the steady and unsteady state of the thermal convexity of heat exchanges. This method, which is based on the assessment of the thermal convexity coefficients for both exchanging fluids, is used for analyzing solar water heating.

3

Thermal Convexity Principle

3.1. Single-phase fluid mixing

For example, we consider two identical hot and cold fluids, each flowing through its own pipe, with different flow rates ($\dot{m}_h, \dot{m}_c$) and temperatures ($T_{h,in}, T_{c,in}$). They mix into a single pipe with a mix flow rate ($\dot{m}$) and resulting temperature (T_{out}) through a valve, as depicted in Figure 3.1, which represents a mixing valve used in heating systems. This allows mixing of hot fluid from the heating generator with cooled return fluid from the circuit. This enables achieving an optimal hot fluid temperature for heating or cooling. Typically, a servo motor controlled by a regulator system operates this kind of valve.

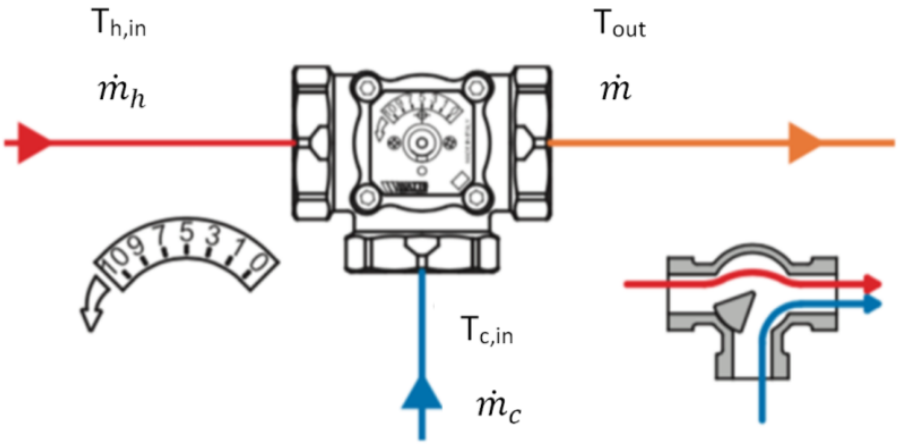

Figure 3.1. *Single fluid-phase mixing valve. For a color version of this figure, see www.iste.co.uk/abdelghani-idrissi/solarwaterheating.zip*

Figure 3.2 shows the characteristics of the mixing valve, which obey the principle of mass conservation. The outlet mass flow rate corresponds to the sum of the flow rates of each fluid:

$$\dot{m} = \dot{m}_h + \dot{m}_c \quad [3.1]$$

As depicted in this figure:

$$\dot{m}_h(\%) + \dot{m}_c(\%) = 100\% \quad [3.2]$$

The conservation of thermal energy between the inlets and outlet gives rise to the thermal convexity expression [3.3].

$$T_{out} = \gamma\, T_{h,in} + (1-\gamma) T_{c,in} \quad [3.3]$$

where γ is given as:

$$\gamma = \frac{1}{1 + \frac{\dot{m}_c}{\dot{m}_h}} \quad [3.4]$$

Note that

$$0 \leq \gamma \leq 1 \quad [3.5]$$

The mathematical expression given in equation [3.3] remains valid for any flow rate values. The thermal convexity coefficient γ is nonlinearly dependent on the flow rate, whereas the outlet temperature, T_{out}, varies linearly with respect to the inlet temperatures, $T_{h,in}$ and $T_{c,in}$. The outlet temperature maintains a convex relationship with the inlet temperature, provided that the thermal convexity coefficient γ remains constrained within the range of 0–1, as defined by equation [3.5].

Figure 3.3 illustrates the variation in the thermal convexity coefficient as a function of the flow rate ratio.

The coefficient γ gradually decreases from 1 to 0, following a hyperbolic trend. This behavior underscores the influence of flow rate variations on the thermal mixing and energy distribution within the system.

Importantly, the fundamental principle governing the single-phase mixing of two distinct fluids follows a similar trend, characterized by an analogous thermal convexity coefficient.

This coefficient is mathematically expressed as a hyperbolic function of the thermal rate ratio:

$$\gamma = \frac{1}{1 + \frac{\dot{m}_c \, C_{pc}}{\dot{m}_h \, C_{ph}}} = \frac{1}{1 + \frac{C_c}{C_h}} \qquad [3.6]$$

where C_{ph} and C_{pc} represent the hot and cold fluid heat capacities, respectively.

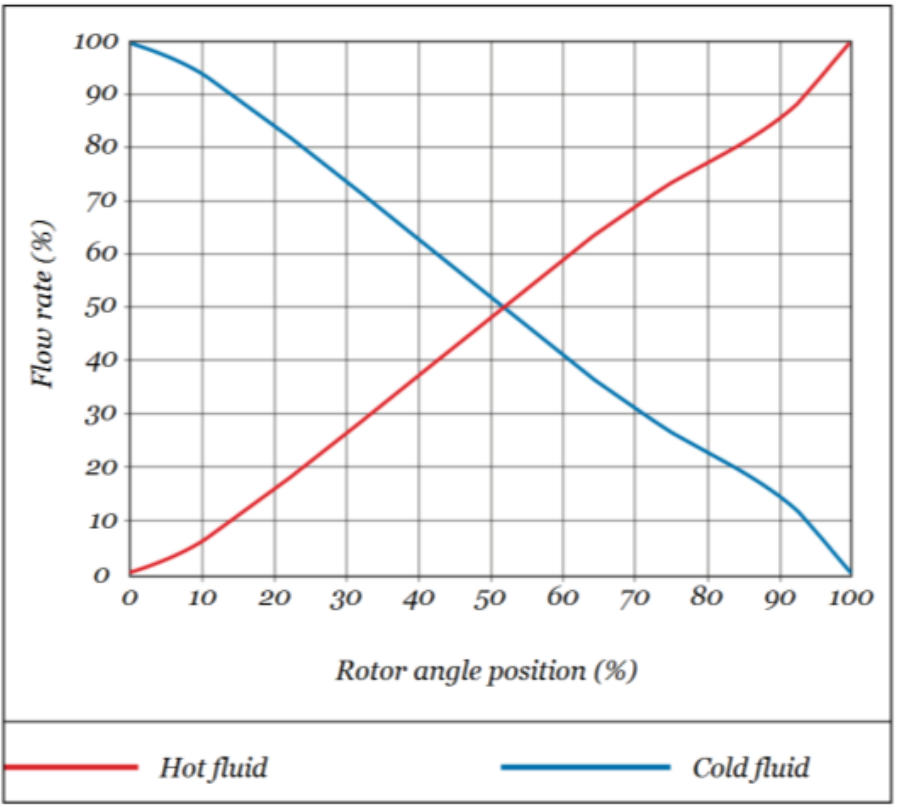

Figure 3.2. *Characteristic of a single fluid phase mixing valve. For a color version of this figure, see www.iste.co.uk/abdelghani-idrissi/solarwaterheating.zip*

Note that C_h and C_c are the thermal rates. The plot of γ as a function of the thermal rates ratio is similar to that in Figure 3.3.

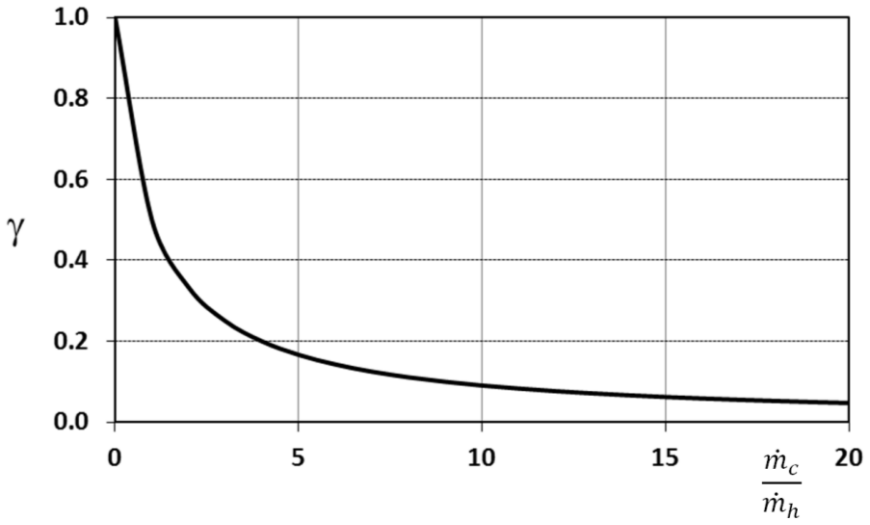

Figure 3.3. *Thermal convexity coefficient as a function of the flow rates ratio*

3.2. Fluid heat exchange through an isotherm surface

Now, let us investigate the heat transfer process occurring from a fluid through an isotherm surface A with a given flow rate $\dot{m}_h$. Here, U represents the overall heat transfer coefficient. The fluid, characterized by a thermal capacity of C_{ph}, enters the system at an inlet temperature of $T_{h,in}$ and exits after exchanging heat with the surroundings, attaining an outlet temperature of $T_{h,out}$. The opposite side of the surface is assumed to be at a uniform temperature denoted as T_c. The conventional depiction of a single compartment (Incropera and DeWitt 1996; Kays and London 1998) yields:

$$U\,A\left(T_c - T_{h,out}\right) + \dot{m}_h\,C_{ph}\left(T_{h,in} - T_{h,out}\right) = 0 \qquad [3.7]$$

Equations [3.7] can be rearranged in the following form:

$$T_{h,out} = \gamma\,T_{h,in} + (1-\gamma)T_c \qquad [3.8]$$

The thermal convexity coefficient is given in this case as a function of the number of transfer units NTU:

$$\gamma = \frac{1}{1 + \text{NTU}} \qquad [3.9]$$

where

$$\text{NTU} = \frac{U\ A}{\dot{m}_h\ C_{ph}} \qquad [3.10]$$

The relationship between the thermal convexity coefficient and the number of transfer units looks like the curve depicted in Figure 3.3, showing a hyperbolic decrease in γ.

3.3. Heat exchange along a pipe crossing an isotherm compartment

We consider now heat exchange along a pipe crossing a compartment with uniform temperature, as represented in Figure 3.4. The incompressible hot fluid characterized by its heat capacity C_{ph} enters with a mass flow rate $\dot{m}_h$ and its inlet temperature $T_{h,in}$ and exits at its outlet temperature $T_{h,out}$ after exchanging heat with the compartment. As the fluid passes through the compartment, it gradually loses its energy due to heat exchange with the compartment through the separating lateral pipe surface A, leading to a progressive decrease in temperature along the flow path $(T_h(x))$.

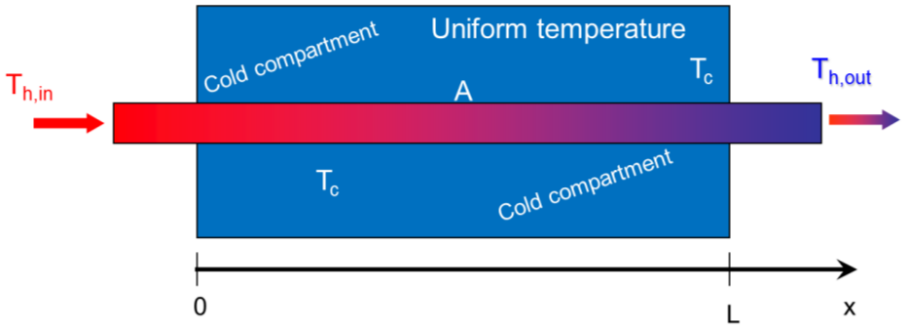

Figure 3.4. *Heat exchange along a hot pipe crossing a cold compartment with uniform temperature. For a color version of this figure, see www.iste.co.uk/abdelghani-idrissi/solarwaterheating.zip*

The steady-state thermal balance applied at position x to an infinitesimal volume over a length dx leads to the following relationship:

$$\dot{m}_h\ C_{ph}(T_h(x) - T_h(x+dx)) + U\ A\ \frac{dx}{L}(T_c - T_h(x)) = 0 \qquad [3.11]$$

Relation [3.11] leads to the differential equation when dx tends to 0:

$$L\,\frac{dT}{dx}(x) + \mathrm{NTU}(T_c - T_h(x)) = 0 \qquad [3.12]$$

L is the pipe length in the compartment, and the NTU is defined by the same expression [3.10].

The solution of equation [3.12] expresses the temperature $T_h(x)$ along the pipe with respect to the thermal convexity principle at any longitudinal position of the pipe:

$$T_h(x) = \gamma(x)\,T_{h,in} + (1 - \gamma(x))T_c \qquad [3.13]$$

where

$$\gamma(x) = e^{-\mathrm{NTU}\frac{x}{L}} \qquad [3.14]$$

Figure 3.5 shows the exponential decrease in the thermal convexity coefficient for different positions along the pipe crossing the compartment with uniform temperature.

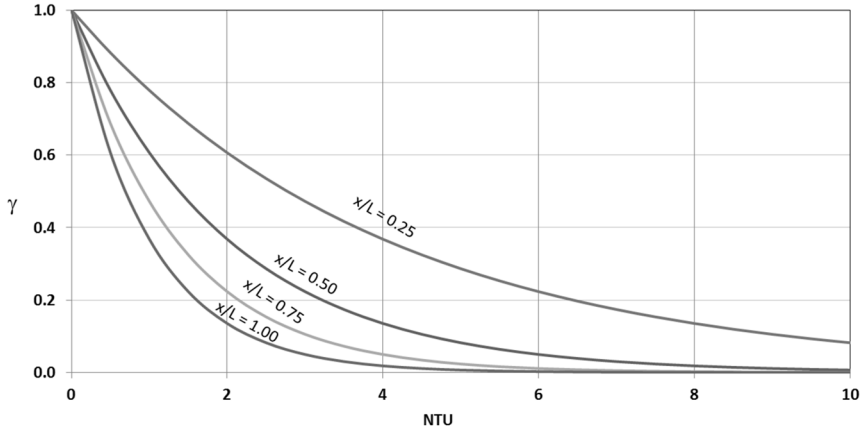

Figure 3.5. *Thermal convexity coefficient along a pipe crossing a tank with uniform temperature*

The variation in the thermal convexity coefficients across the longitudinal position of the heat pipe is expressed by a spatial relationship. Specifically, as the

pipe extends along its length, the thermal convexity coefficients exhibit exponential changes.

The outlet temperature is expressed as follows:

$$T_{h,out} = \gamma\, T_{h,in} + (1-\gamma) T_c \qquad [3.15]$$

where

$$\gamma = e^{-\mathrm{NTU}} \qquad [3.16]$$

When $U\,A \ll \dot{m}_h\, C_{ph}$, the thermal convexity coefficient is similar to that expressed by relation [3.9].

3.4. Solar receiver

In the previous chapter, a thermal analysis of a parabolic solar trough receiver was presented. The outlet temperature along the tubular receiver was obtained as a function of solar irradiation and is calculated as follows:

$$T_r(x) = T_a + \left(T_{r,in} - T_a - \Delta T_{sol}\right) e^{-\mathrm{NTU}\frac{x}{L}} + \Delta T_{sol} \qquad [3.17]$$

The heat transfer fluid can be written in the following convex form:

$$T_r(x) = \gamma_r(x)\, T_{r,in} + \left(1-\gamma_r(x)\right) T_a + \Delta T_{sol}\left(1-\gamma_r(x)\right) \qquad [3.18]$$

The heat transfer fluid obeys the principle of thermal convexity with regard to the inlet temperature of the heat transfer fluid and the ambient environment.

The thermal convexity coefficient is the same as that given by expression [3.14].

The outlet temperature is obtained as:

$$T_{r,out} = \gamma_{r,out}\, T_{r,in} + \left(1-\gamma_{r,out}\right) T_a + \Delta T_{sol}\left(1-\gamma_{r,out}\right) \qquad [3.19]$$

where $\gamma_{r,out}$ is similar to that given by relation [3.16] with a number of transfer unit NTU specific to the solar receiver defined in the previous chapter.

With this definition, the thermal efficiency of the receiver is given as:

$$\eta_{th} = \left(1-\gamma_{r,out}\right) \frac{L}{R_{th}\,\mathrm{NTU}} \frac{\left(T_a - T_{r,in} + \Delta T_{sol}\right)}{C\; G_0\; A_{go}} \qquad [3.20]$$

3.5. Heat exchange along a tubular heat exchanger

In this section, a double-pipe heat exchanger is considered to extend the analysis of the thermal convexity. This type of heat exchangers consists of one pipe concentrically placed within another. The cold fluid flows inside the inner pipe, whereas the other fluid flows in the annular space between the inner and outer pipes. As depicted in Figure 3.6, the double pipe heat exchanger is considered in the cocurrent and countercurrent flows in arrangements (a) and (b), respectively. The hot fluid, entering the inner tube at an inlet temperature of $T_{h,in}$, flows with a mass flow rate denoted as $\dot{m}_h$. Simultaneously, the cold fluid passes through the annular space at an inlet temperature of $T_{c,in}$ with a mass flow rate denoted as $\dot{m}_c$. Their thermal capacities are C_{ph} and C_{pc}, respectively.

A counterflow heat exchanger is a type of heat exchanger where the two fluids flow parallel to each other but in opposite directions. This arrangement maximizes the temperature gradient between the fluids along the entire length of the exchanger, allowing for the most efficient heat transfer. In this setup, the hottest fluid entering the exchanger transfers heat to the coldest fluid exiting the exchanger and vice versa. This continuous temperature differential ensures that the largest possible temperature change occurs in both fluids. As a result, counterflow heat exchangers achieve higher thermal efficiency compared to other configurations, such as parallel flow or crossflow exchangers, making them ideal for applications requiring efficient thermal management.

In cocurrent flow heat exchangers, the streams flow parallel to each other and in the same direction. This configuration means that both the hot and cold fluids enter the heat exchanger at the same end and flow side by side toward the opposite end. Because the temperature difference between the two fluids is greatest at the inlet and decreases along the length of the exchanger, the rate of heat transfer diminishes as the fluids move through the exchanger. This results in a less efficient overall heat transfer compared to counterflow arrangements.

However, the cocurrent flow configuration does offer the advantage of more uniform wall temperatures. Since both fluids enter and exit the heat exchanger together, the temperature gradient between the fluids and the exchanger walls remains relatively constant along the length of the exchanger. This can be beneficial in applications where maintaining consistent wall temperatures is critical, such as in processes where thermal stresses must be minimized to prevent material fatigue or damage.

To derive the equations governing thermal behavior, the heat exchanger is divided into multiple small volumes with a length of *dx*, following a similar approach to the previous case.

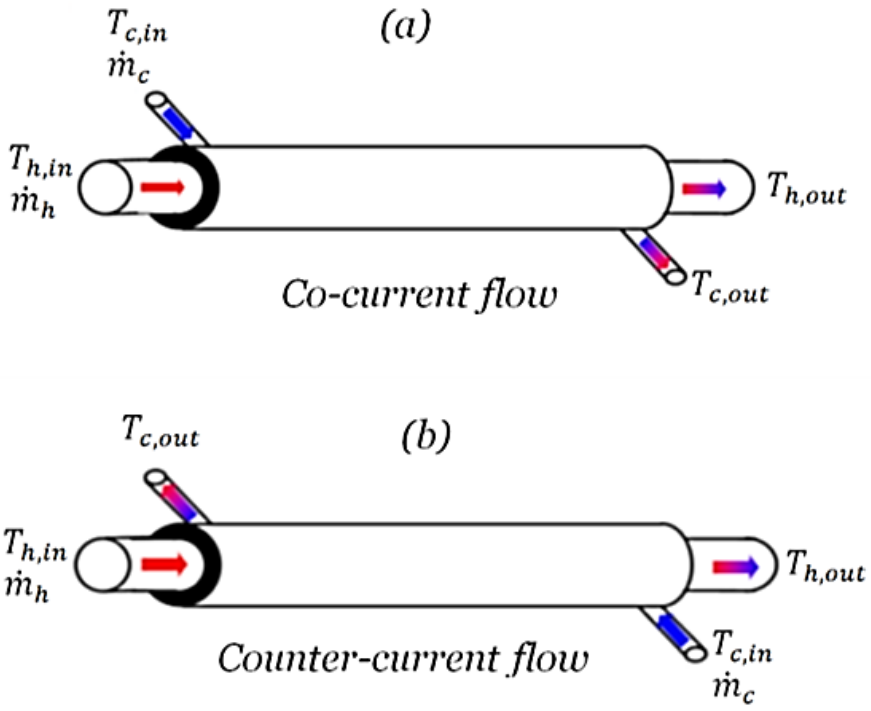

Figure 3.6. *Double pipe heat exchangers: (a) cocurrent flow and (b) countercurrent flow. For a color version of this figure, see www.iste.co.uk/abdelghani-idrissi/solarwaterheating.zip*

As the hot fluid passes through each elementary volume, heat is transferred to the wall via convection, resulting in a decrease in its outlet enthalpy and stored thermal energy. By applying an energy balance to each differential volume of the hot fluid and simplifying and rearranging, we obtain the first equation of system [3.21].

$$\begin{cases} \pm\dot{m}_h C_{ph} L \dfrac{dT_h}{dx}(x) + h_h A_h\big(T_w(x) - T_h(x)\big) = 0 \\ \dot{m}_c C_{pc} L \dfrac{dT_c}{dx}(x) + h_c A_c\big(T_w(x) - T_c(x)\big) = 0 \\ h_h A_h\big(T_h(x) - T_w(x)\big) + h_c A_c\big(T_c(x) - T_w(x)\big) = 0 \end{cases} \quad [3.21]$$

Similarly, applying an energy balance to the cold fluid and the separating wall yields the second and third equations of system [3.21].

The symbol ± signifies the potential for either a cocurrent or countercurrent flow arrangement, where h_h and h_c correspond to the convective heat transfer coefficients associated with the hot and cold fluids, respectively.

Additionally, A_h and A_c specify the lateral exchange areas dedicated to facilitating heat transfer between the respective hot and cold fluids and the separating wall. L represents the length of the heat exchanger.

Now, let us establish definitions for the following parameters:

– dimensionless axial position

$$x^* = \frac{x}{L} \qquad [3.22]$$

– thermal rates ratio

$$C^* = \frac{\dot{m}_h C_{ph}}{\dot{m}_c C_{pc}} \qquad [3.23]$$

– dimensionless numbers

$$N_h = \frac{h_h A_h}{\dot{m}_h C_{ph}} \qquad [3.24]$$

$$N_c = \frac{h_c A_c}{\dot{m}_c C_{pc}} \qquad [3.25]$$

By incorporating the previously defined parameters, the system of equations [3.21] can be reexpressed in terms of the following dimensionless variables, providing a more generalized and scalable representation of the underlying physical relationships:

$$\begin{cases} \pm \dfrac{dT_h}{dx^*}(x^*) + N_h\big(T_w(x^*) - T_h(x^*)\big) = 0 \\ \dfrac{dT_c}{dx^*}(x^*) + N_c\big(T_w(x^*) - T_c(x^*)\big) = 0 \\ C^* N_h\big(T_h(x^*) - T_w(x^*)\big) + N_c\big(T_c(x^*) - T_w(x^*)\big) = 0 \end{cases} \qquad [3.26]$$

The following boundary conditions are specified for the cocurrent and countercurrent arrangements:

– in the cocurrent flow configuration:

$$\begin{cases} T_h(x^* = 0) = T_{h,in} \\ T_c(x^* = 0) = T_{c,in} \end{cases} \quad [3.27]$$

– in the countercurrent flow configuration:

$$\begin{cases} T_h(x^* = 1) = T_{h,in} \\ T_c(x^* = 0) = T_{c,in} \end{cases} \quad [3.28]$$

In the formulation [3.26], the groups N_h and N_c closely look like the number of transfer units utilized in the steady-state NTU method (Rohsenowet al. 1985; Kakaç and Liu 2002). The NTU is associated with the overall heat transfer coefficient, whereas N_h and N_c depend upon the convective heat transfer coefficients. The convective heat transfer coefficients, h_h and h_c, can be determined in two ways. The first method involves finding the optimal fit between the experimental and theoretical steady-state results to obtain suitable values. The second method consists of utilizing Nusselt number correlations that are associated with the heat transfer coefficients.

As described in the case of a pipe crossing a compartement with uniform temperature, the thermal convexity coefficients vary across the longitudinal position of the heat exchanger. Notably, each fluid involved in the heat exchange process is characterized by its distinct thermal convexity coefficient. This emphasizes the individuality of the thermal behavior exhibited by each fluid within the system. Then, the steady-state solutions of equation system [3.26] can be derived, upon rearrangement, through the expressions [3.29]. These relationships constitute an analogous framework for describing the fundamental thermal convexity of heat exchangers. This relationship remains consistent regardless of location within the heat exchanger.

$$\begin{cases} T_h(x^*) = \gamma_h(x^*)\, T_{h,in} + (1 - \gamma_h(x^*))\, T_{c,in} \\ T_c(x^*) = \gamma_c(x^*)\, T_{h,in} + (1 - \gamma_c(x^*))\, T_{c,in} \end{cases} \quad [3.29]$$

Cocurrent	**Countercurrent**
$\boldsymbol{\gamma_h(x^*) = \dfrac{e^{-\alpha x^*} + C^*}{1 + C^*}}$ $\boldsymbol{\gamma_c(x^*) = C^*\left(\dfrac{e^{-\alpha x^*} - 1}{1 + C^*}\right)}$	$\gamma_h(x^*) = \dfrac{e^{-\alpha x^*} - C^*}{e^{-\alpha} - C^*}$ $\gamma_c(x^*) = C^*\left(\dfrac{e^{-\alpha x^*} - 1}{e^{-\alpha} - C^*}\right)$
$\boldsymbol{\alpha = N(C^* \pm 1)}$	
$\boldsymbol{N = \dfrac{N_h N_c}{N_h + N_c}}$	

Table 3.1. *Thermal convexity coefficients along a double-pipe heat exchanger*

The thermal convexity coefficients are given according to the heat exchanger configuration in Table 3.1.

Figure 3.7 shows the steady-state convexity coefficients of the hot fluid along the length of the heat exchanger. This graph is obtained under a cocurrent flow configuration with N = 1, considering different thermal rate ratios. Similarly, Figure 3.8 presents the corresponding steady-state convexity coefficients of the cold fluid along the heat exchanger, in the cocurrent flow setup and for varying thermal rate ratios.

A critical observation from these figures is that the convexity coefficients of both the hot and cold fluids exhibit an increasing trend as the thermal rate ratio increases. This behavior reflects the influence of heat transfer dynamics on the thermal profile evolution within the exchanger. Specifically, when the dimensionless thermal capacity rate ratio, C^*, reaches high values, the convexity coefficient of the hot fluid asymptotically approaches unity.

Conversely, in the limiting case where C^* becomes negligible, the convexity coefficient of the cold fluid approaches zero, signifying minimal curvature in its thermal profile, whereas the convexity coefficient of the hot fluid converges toward a characteristic limiting profile. This behavior highlights the diminishing influence of heat capacity variations on hot fluid thermal evolution when the thermal rate ratio is significantly reduced.

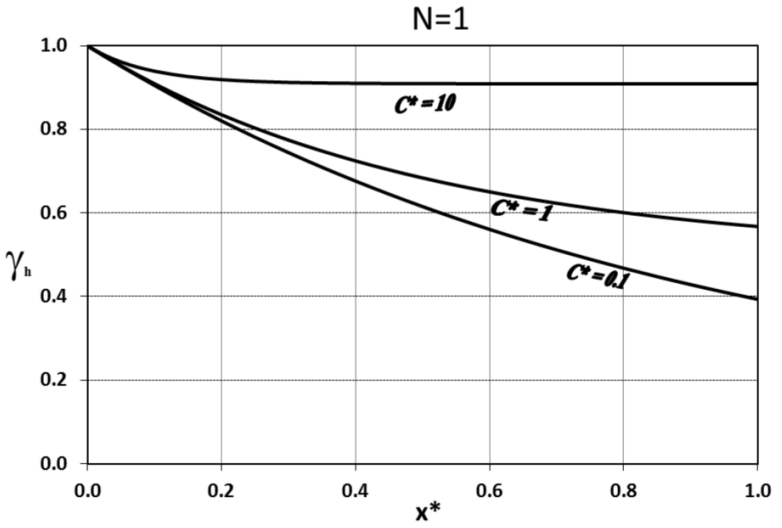

Figure 3.7. *Thermal convexity coefficients of hot inner fluid in a double-pipe heat exchanger in cocurrent flow*

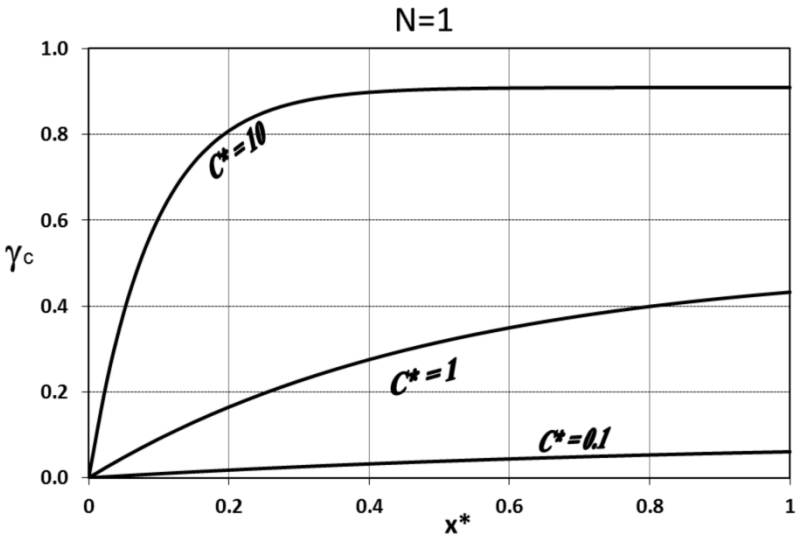

Figure 3.8. *Thermal convexity coefficients of cold outer fluid in a double-pipe heat exchanger in cocurrent flow*

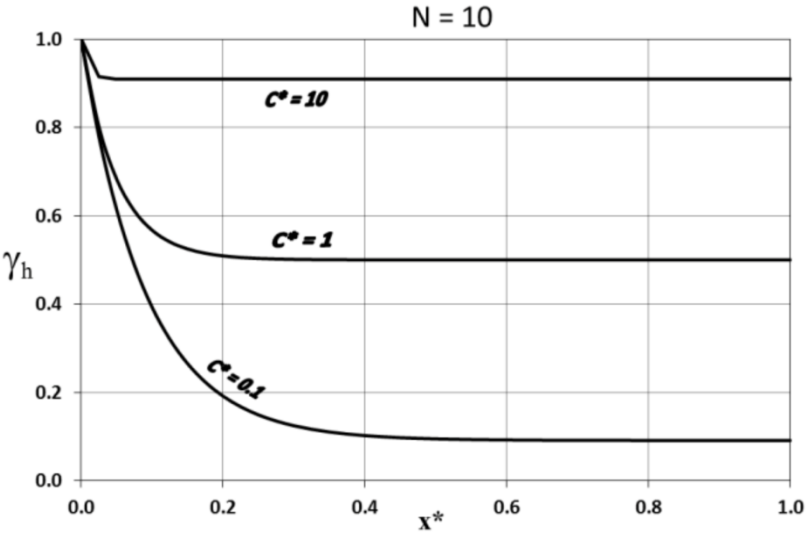

Figure 3.9. *Thermal convexity coefficients of the hot inner fluid in a double-pipe heat exchanger in cocurrent flow with N = 10*

To further investigate the impact of increasing the number of thermal transfer units, Figure 3.9 presents the thermal convexity distribution of the hot inner fluid along the heat exchanger for different thermal rate ratios but with a higher parameter value of N = 10. The results indicate a pronounced influence of increased heat exchanger effectiveness on the convexity behavior of the hot fluid.

Similarly, Figure 3.10 depicts the thermal convexity coefficient of the cold outer fluid along the heat exchanger under the same conditions applied in Figure 3.9. A comparative analysis of these figures provides valuable insight into the evolution of the thermal curvature across different operating regimes, reinforcing the fundamental relationships among the thermal rate ratio, heat exchanger efficiency, and flow configuration.

Across the two figures, how the thermal convexity coefficients behave over the depicted curves is discernible. They provide a visual representation of the fluctuating trends and patterns exhibited by the coefficients, as they vary under different conditions and parameters.

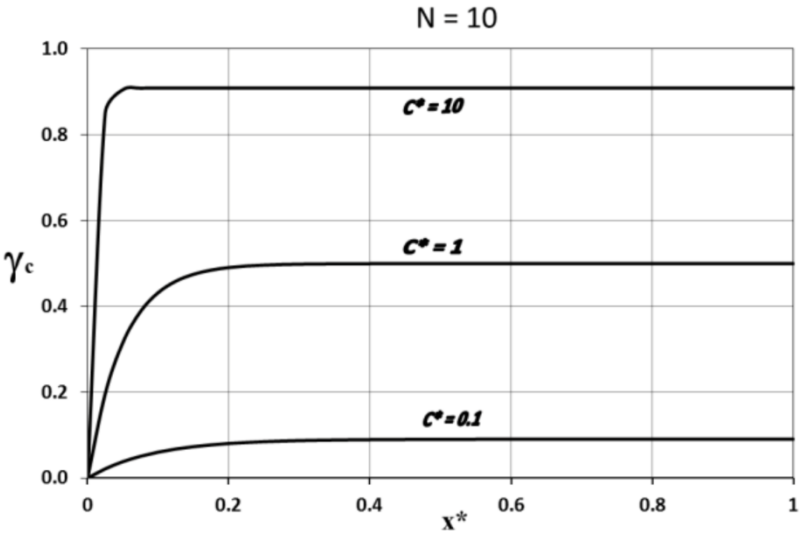

Figure 3.10. *Thermal convexity coefficients of cold outer fluid in a double-pipe heat exchanger in cocurrent flow with N = 10*

By considering the countercurrent flow configuration, Figures 3.11 and 3.12 depict the thermal convexity coefficients in tubular heat exchangers operating across

various values of C^* with N = 1. Figure 3.11 shows the hot fluid flowing through the inner tube, whereas Figure 3.12 shows the cold fluid circulating through the annular space.

The thermal convexity coefficients increase with increasing thermal rate ratio, similar to what is obtained in cocurrent flow. In the countercurrent flow, a singularity occurs at $C^* = 1$, resulting in the thermal convexity coefficients showing linearity along the axial position of the heat exchanger.

As C^* approaches very high values ($C^* >> 1$), the convexity coefficient of the hot fluid uniformly converges toward 1 along the heat exchanger. The hot fluid enters at the inlet temperature and quasi maintains this temperature almost uniformly throughout the heat exchanger. Moreover, the convexity coefficient of the cold fluid reaches its peak profile.

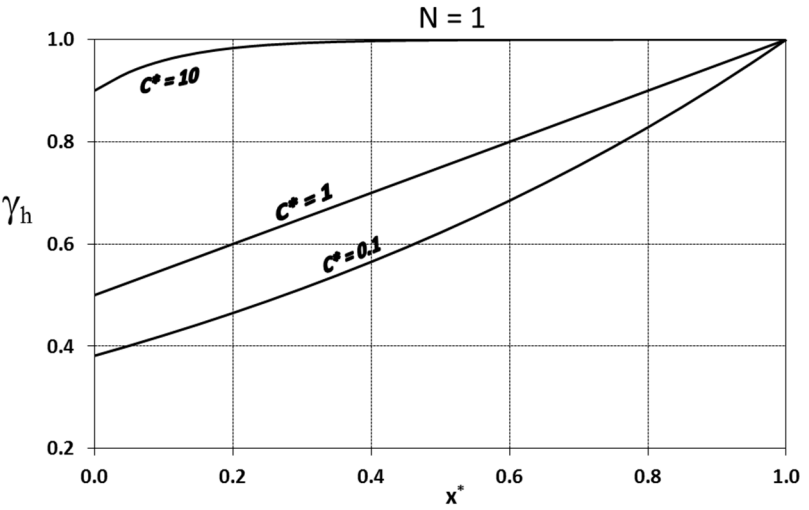

Figure 3.11. *Thermal convexity coefficients of the inner hot fluid in a double-pipe heat exchanger in countercurrent flow with N = 1*

By increasing the dimensionless number N to 10, the results displayed in Figures 3.13 and 3.14 are obtained.

The curves in Figure 3.13 are related to the hot fluid flowing through the inner tube, and those in Figure 3.14 correspond to the cold fluid circulating through the outer annular space.

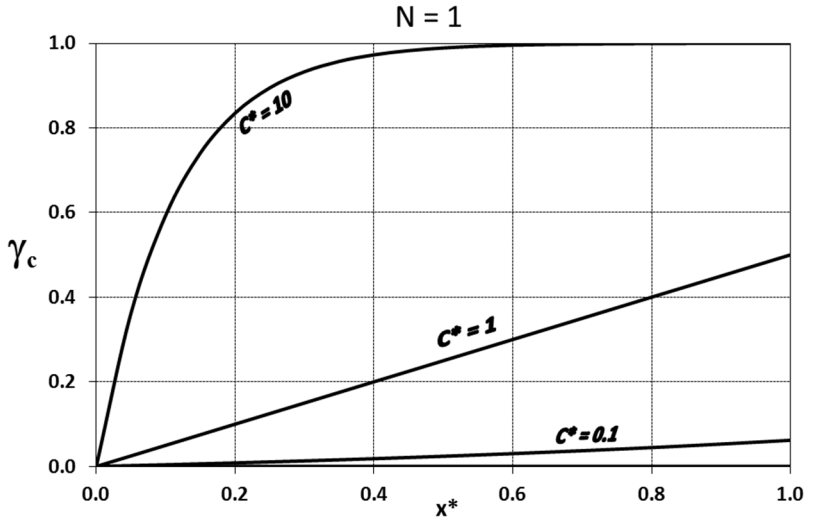

Figure 3.12. *Thermal convexity coefficients of cold outer fluid in a double-pipe heat exchanger in countercurrent flow with N = 1*

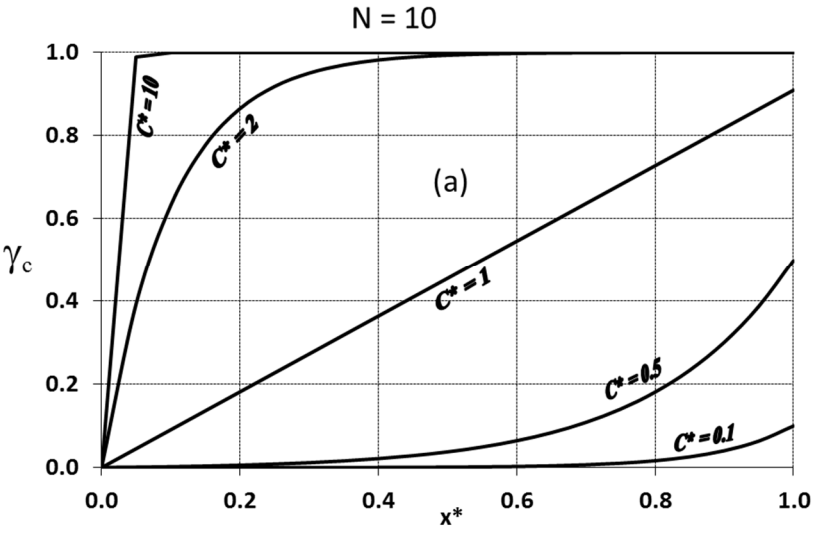

Figure 3.13. *Thermal convexity coefficients of the hot inner fluid in a double-pipe heat exchanger in countercurrent flow with N = 10*

The figures provide a detailed representation of the results, highlighting the impact of this parameter change on the heat exchanger behavior. They underline the comprehensive data trends and variations resulting from this increment, offering a clear visualization of how increasing N influences the overall performance and characteristics of the model under study.

The sensitivity of the convexity coefficient to variations in the thermal rate ratio becomes more pronounced as the parameter N increases. This heightened sensitivity suggests that larger values of N amplify the influence of thermal rate disparities on the convexity behavior of both fluids. To provide a more detailed quantitative analysis, Table 3.2 presents the approximated mathematical expressions for the convexity coefficients corresponding to both fluids in the limiting cases of high and low thermal rate ratios.

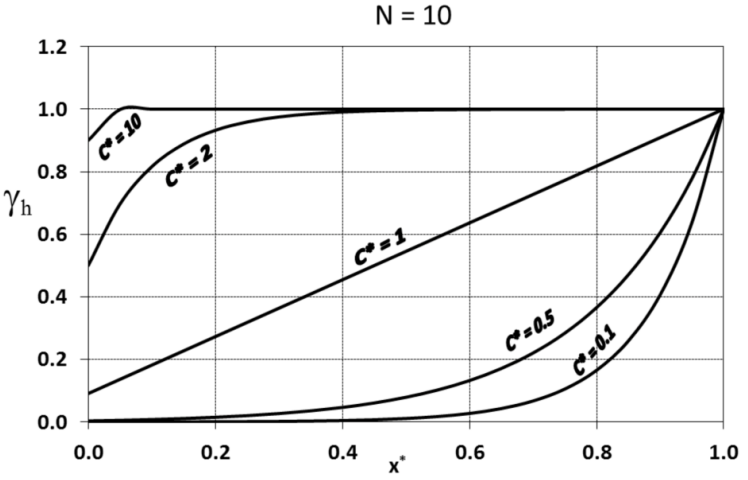

Figure 3.14. *Thermal convexity coefficients of the cold outer fluid in a double-pipe heat exchanger in countercurrent flow with N = 10*

	$C^* >> 1$	$C^* << 1$
Cocurrent	$\begin{cases}\gamma_h(x^*) \approx 1 \\ \gamma_c(x^*) \approx e^{-NC^*x^*} - 1\end{cases}$	$\begin{cases}\gamma_h(x^*) \approx e^{-N\,x^*} \\ \gamma_c(x^*) \approx 0\end{cases}$
Countercurrent	$\begin{cases}\gamma_h(x^*) \approx 1 \\ \gamma_c(x^*) \approx 1 - e^{-NC^*x^*}\end{cases}$	$\begin{cases}\gamma_h(x^*) \approx e^{N(x^*-1)} \\ \gamma_c(x^*) \approx 0\end{cases}$

Table 3.2. *Thermal convexity coefficients approximation for high and small thermal rates ratio*

This method introduces a paradigm shift in how the sizing and rating of heat exchangers are considered within industrial settings, particularly compared with the prevalent ε-NTU and log mean temperature difference (LMTD) methods.

While the latter techniques rely expressively on overall heat transfer coefficients, the steady-state approach in question focuses instead on the average convective heat transfer coefficients of both fluid streams involved.

By doing so, it offers a nuanced understanding of heat transfer that goes beyond conventional methods. Central to this approach is the concept of thermal convexity, which exposes a crucial linear relationship between inlet and outlet temperatures and states a more intricate nonlinear correlation, particularly with respect to flow rates through thermal convexity coefficients. This exposure not only enhances the comprehension of heat transfer processes but also provides a more accurate basis for the optimization and analysis of heat exchanger networks. Moreover, what sets this formulation apart is its adaptability to various types of heat exchangers. Through the incorporation of the fin analogy number, a well-defined parameter is established in the literature. This method can seamlessly extend its applicability to multipass shell-and-tube and cross-flow heat exchangers. This flexibility is invaluable, given the diverse range of applications and configurations encountered in industrial settings.

Indeed, as defined by the LMTD method, the introduction of the correction factor allows for a more comprehensive analysis of heat exchangers. This correction factor, often denoted as F, is used to adjust the LMTD for heat exchangers that do not operate in ideal counterflow or cocurrent flow configurations, such as crossflow or multipass arrangements.

The total heat exchanged is defined as follows:

$$\dot{Q} = \dot{m}_h C_{ph}\left(T_{h,in} - T_{h,out}\right) = \dot{m}_c C_{pc}\left(T_{c,out} - T_{c,in}\right) \quad [3.30]$$

$$\dot{Q} = UA \int_0^1 \left(T_h(x^*) - T_c(x^*)\right) dx^* \quad [3.31]$$

where U is the overall heat transfer coefficient and A is the heat transfer area.

$$\dot{Q} = UA\left(T_{h,in} - T_{c,in}\right) \int_0^1 \left(\gamma_h(x^*) - \gamma_c(x^*)\right) dx^* \quad [3.32]$$

The mean temperature difference can be defined as:

$$\Delta T_m = \left(T_{h,in} - T_{c,in}\right) \int_0^1 \left(\gamma_h(x^*) - \gamma_c(x^*)\right) dx^* \quad [3.33]$$

In countercurrent flow, the mean temperature is given as follows:

$$\Delta T_m = \left(T_{h,in} - T_{c,in}\right) \frac{(1 - C^*)(1 - e^{-\alpha})}{\alpha(e^{-\alpha} - C^*)} \quad [3.34]$$

where α and C^* are specified previously.

ΔTm can be rearranged as follows:

$$\Delta T_m = \Delta T_{in} \frac{1}{N} \frac{\left(1 - exp\left(-N(C^* - 1)\right)\right)}{\left(C^* - exp\left(-N(C^* - 1)\right)\right)} \quad [3.35]$$

where ΔT_{in} represents the gap between the inlet temperatures of the hot and cold fluids.

The mathematical derivation of the exact mean temperature difference becomes highly intricate when dealing with heat exchanger configurations that deviate from simple parallel-flow or counterflow arrangements. While these basic configurations allow for a straightforward analytical approach, more complex flow patterns, such as those found in crossflow or multipass heat exchangers, introduce significant variations in local temperature differences, making direct calculations considerably more challenging.

For example, in crossflow heat exchangers, hot and cold fluids move perpendicularly to each other rather than in parallel or opposite directions. This orthogonal interaction results in spatially nonuniform temperature gradients across the exchanger, as different sections of the working fluids experience varying levels of heat transfer efficiency. Unlike counterflow configurations, where there is a well-defined and predictable temperature distribution along the flow path, crossflow systems exhibit local temperature disparities, necessitating the use of advanced correction techniques.

Similarly, in multipass heat exchangers, the fluids are designed to traverse the exchanger multiple times, following distinct paths that may alternate direction. These multiple passes introduce intermittent mixing zones, where temperature variations become even more complex because of repeated interactions between heated and cooled regions.

The fluid redistribution occurring at each pass alters the overall thermal performance, creating a challenge for accurately determining the logarithmic mean temperature difference using conventional formulas.

Owing to these complexities, a correction factor is introduced to modify the standard LMTD equation, ensuring that it accurately reflects the true temperature behavior in nonideal flow arrangements. This correction factor is derived based on the principles of counterflow heat exchange, which is considered the most thermodynamically efficient arrangement owing to its ability to maintain a larger temperature difference between the fluids over a greater portion of the exchanger.

To facilitate the determination of appropriate correction factors, extensive charts and empirical formulas have been developed for each type of nonideal heat exchanger. These resources are built upon a foundation of experimental data, computational fluid dynamics simulations and theoretical analysis, allowing for accurate and reliable adjustments to thermal performance calculations. By incorporating these correction factors, the gap between idealized mathematical models and the actual performance of complex heat exchangers can be bridged.

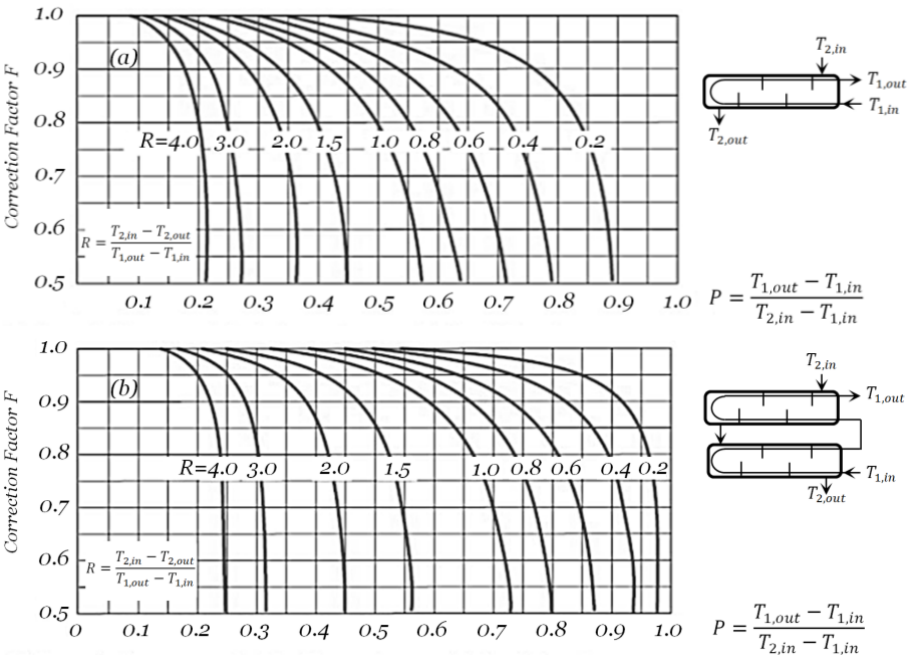

Figure 3.15. *Correction factor F of the shell-and-tube heat exchanger: (a) one shell pass and two, four or any multiple tube passes; (b) two shell passes and four, eight or any multiple tube passes*

The charts presented in Figure 3.15 depict the correction factors for commonly used shell-and-tube heat exchangers, as proposed by the Tubular Exchanger

Manufacturers Association (TEMA). Chart (a) is associated with configurations featuring one shell pass and two, four or multiple tube passes, whereas chart (b) pertains to systems with two shell passes and four, eight or other multiples of tube passes. These charts provide a means of adjusting the performance predictions of heat exchangers based on the specific design of the flow arrangement.

In addition, the correction factor (F) charts for typical cross-flow heat exchangers are presented in Figure 3.16, offering similar adjustments for this type of heat exchanger configuration, which is prevalent in various industrial applications.

Importantly, both boilers and condensers typically operate under phase change conditions, which profoundly affect the temperature profiles within the system. These phase transitions significantly influence the determination of the mean temperature difference, a key parameter in heat exchanger calculations.

In such cases, the correction factor often approaches unity because the temperature difference remains relatively stable throughout the phase change process.

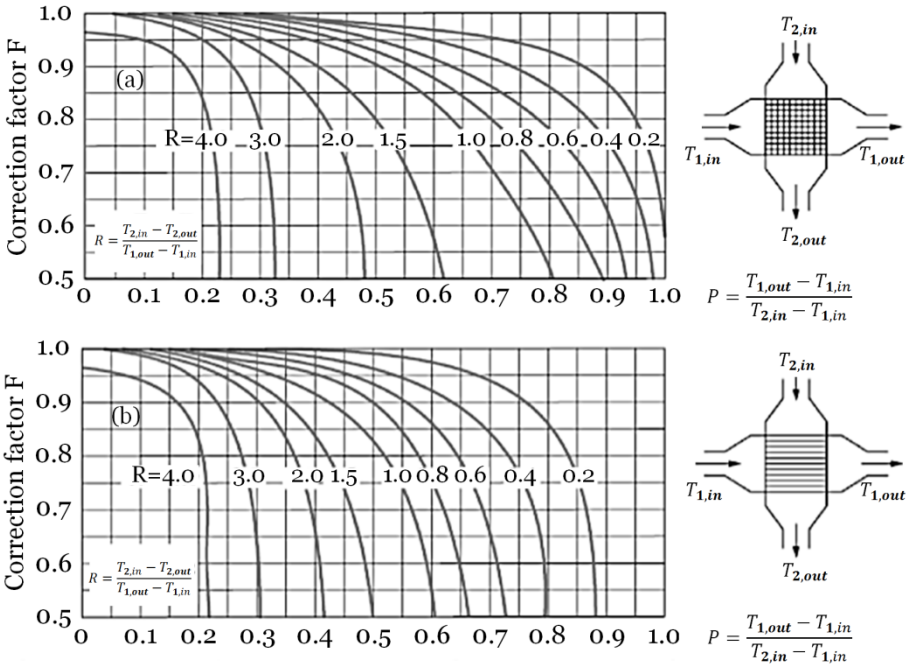

Figure 3.16. *Correction factor F of common cross-flow heat exchangers: (a) single-pass cross-flow with both fluids unmixed and (b) single-pass cross-flow with one fluid mixed and the other unmixed*

In boilers, the transformation from liquid to vapor generally occurs at an almost constant temperature, simplifying the computation of the logarithmic mean temperature difference. This stability eliminates the complexities associated with temperature variations that typically arise in sensible heat exchange processes.

However, despite this simplification, the use of a correction factor remains necessary, particularly when the boiler design deviates from ideal conditions. Variations in flow configurations, heat transfer surfaces and operating pressures can introduce temperature gradients, which require adjustments to ensure accurate thermal performance assessments.

In a similar manner, the concept of thermal convexity plays a crucial role in further refining heat transfer predictions. The thermal convexity coefficients of both working fluids can also be adjusted using the correction factor, thereby improving the precision of temperature modeling in complex heat exchange scenarios. By integrating thermal convexity principles into the analysis, it becomes possible to achieve a more refined and predictive understanding of heat exchanger behavior under varying operational conditions.

This approach is particularly valuable in systems where fluid properties, flow rates and heat transfer coefficients vary dynamically, as it enables the development of more efficient heat exchanger designs with optimized energy utilization. Whether in industrial power plants, chemical processing facilities or renewable energy applications, the combination of LMTD correction factors and thermal convexity analysis provides an essential framework for enhancing the performance and reliability of advanced heat exchanger systems.

The thermal convexity coefficients of both fluids can be corrected with the factor F:

$$\dot{Q} = UA \int_0^1 F\left(T_{h,in} - T_{c,in}\right)\left(\gamma_h(x^*) - \gamma_c(x^*)\right) dx^* \qquad [3.36]$$

$$\Delta T_m = F\ \Delta T_{in}\ \frac{1}{N}\frac{\left(1\ - exp\left(-N(C^* - 1)\right)\right)}{\left(C^* - exp\left(-N(C^* - 1)\right)\right)} \qquad [3.37]$$

$$\begin{cases} \gamma_{h,out} = F\left(\dfrac{C^* - 1}{C^* - exp\left(-N(C^* - 1)\right)}\right) \\ \gamma_{c,out} = F\ C^*\left(\dfrac{1\ - exp\left(-N(C^* - 1)\right)}{C^* - exp\left(-N(C^* - 1)\right)}\right) \end{cases} \qquad [3.38]$$

4

Solar Water Heating Analysis

4.1. Thermal modeling of solar water heating

The modeling process should consider unsteady-state conditions because of the dynamic nature of solar irradiance variations throughout the day. As the Sun position changes and atmospheric conditions evolve, the intensity of the incident solar radiation on the surface continuously fluctuates. This variability is influenced by factors such as cloud cover, time of day and seasonal changes. Consequently, a modeling approach that incorporates these dynamic aspects is essential for accurately simulating the performance of solar energy systems. By accounting for the temporal variations in solar irradiance, the model can provide more realistic and reliable predictions of system behavior and performance under real-world operating conditions.

For this purpose, the examination of each component within the thermal solar system will be carried out separately, allowing for a thorough evaluation of their specific thermal characteristics and energy balances. This entails assessing factors such as solar radiation absorption, heat retention, and energy transfer for each component. Following this individual analysis, a functional and systemic approach will be implemented to establish cohesive connections among these different components. This approach was also presented in Khalfallaoui et al. (2011).

4.1.1. *Collector model*

In the domain of solar energy research, numerous collector models have been developed and documented. Among these, the Hottel–Whilliere–Bliss model stands out as one of the earliest and most influential. This model, introduced in seminal work (Hottel and Woertz 1942), has persisted as a cornerstone in the field and continues to be extensively cited and utilized in recent studies (Góngora-Gallardo

et al. 2013). This model provides a comprehensive framework for analyzing the thermal performance of solar collectors. It considers various physical phenomena, including heat transfer mechanisms such as convection, radiation and absorption, as well as factors such as collector geometry, fluid flow dynamics and environmental conditions. By incorporating these elements, the model offers valuable insights into the behavior and efficiency of solar collectors under different operating conditions.

Over the years, researchers have built upon this basis model, refining its formulations and extending its applicability to diverse collector designs and configurations. Despite the emergence of newer models, the enduring relevance of the pioneer model underscores its robustness and significance in the field of solar energy research and engineering.

For the flat-plate collector, the same analysis is applied (Buzás and Kicsiny 2014), and the transfer functions of the solar collectors are considered for dynamical analysis and control design.

Figure 4.1 shows the collector receiving solar energy through its top area.

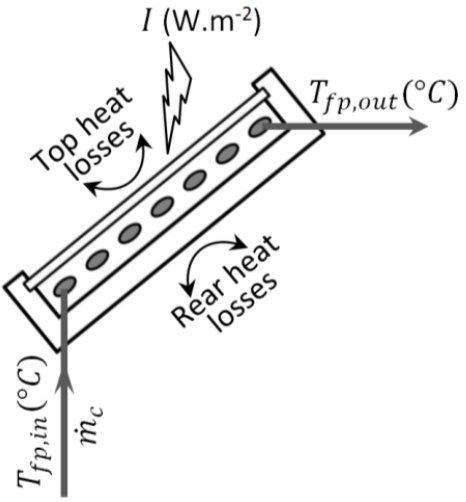

Figure 4.1. *Solar flat-panel collector*

The calorific fluid, specified by its thermal capacity C_{p_c}, flows through the flat panel with a mass flow rate $\dot{m}_c$ at an inlet temperature $T_{fp,in}$ and exits at an outlet temperature $T_{fp,out}$.

The solar collector receives solar radiation $I(t)$ with an efficiency of η_0. The heat losses through the top and rear areas are characterized by the global heat transfer coefficient U_{fp}. The latter considers thermal losses occurring at the insulated rear side and the upper area, which is exposed to convective heat transfer with the surrounding environment and solar radiation. It can be obtained as previously described (Klein 1975; Tagliafico et al. 2014). As the fluid circulates through the solar collector, it interacts with the absorber surface, where solar radiation is converted into heat. This thermal convection causes the fluid to heat up, resulting in a change in its enthalpy as it exits the collector.

To account for the thermal dynamics within the solar collector, an energy balance analysis is conducted considering various factors. These include the heat rate transferred to the fluid, which depends on its flow rate $\dot{m}_c$ and the temperature difference between the fluid and the effective flat-panel surface A_{fp}. Furthermore, the heat exchange between the solar panel and the surrounding environment, influenced by factors such as the external temperature $T_{ext}(t)$ and wind speed, is also considered. This leads to the following equation:

$$\begin{aligned} m_{c,fp} C_{p_c} \frac{dT_{fp,out}}{dt}(t) &= \dot{m}_c C_{p_c} \left(T_{fp,in}(t) - T_{fp,out}(t)\right) \\ &+ \eta_0 I(t) A_{fp} \\ &+ U_{fp} A_{fp} \left(T_{ext}(t) - T_{fp,out}(t)\right) \end{aligned} \quad [4.1]$$

where

$$m_{c,fp} = \rho_c \, V_{c,fp} \quad [4.2]$$

Here, $m_{c,fp}$ represents the calorific fluid mass of the instantaneous occupied volume $V_{c,fp}$ in the flat-panel collector. ρ_c is relative to the calorific fluid density.

To effectively identify the intrinsic connections in a functional manner, such as that described in the literature (Buzás and Kicsiny 2014), equation [4.1] can be restated using the Laplace transform to illustrate the causal links among the different parameters involved in analyzing the transient thermal behavior of the solar collector. The outlet temperature of the solar flat-panel collector can then be obtained as:

$$\begin{aligned} T_{fp,out}(s) = \Big(\big(\gamma_{fp} T_{fp,in}(s) + (1 - \gamma_{fp}) T_{ext}(s)\big) \\ + \alpha_s I(s)\Big)\left(\frac{1}{1 + \tau_{fp}\, s}\right) \end{aligned} \quad [4.3]$$

The thermal convexity coefficients are defined as:

$$\gamma_{fp} = \frac{\dot{m}_c C_{p_c}}{\dot{m}_c C_{p_c} + U_{fp} A_{fp}} = \frac{1}{1 + NTU_{fp}} \quad [4.4]$$

$$\gamma_{fp} = \frac{\dot{m}_c C_{p_c}}{\dot{m}_c C_{p_c} + U_{fp} A_{fp}} = \frac{1}{1 + NTU_{fp}} \quad [4.5]$$

and

$$\alpha_s = \frac{\eta_0 \, A_{fp}}{\dot{m}_c C_{p_c} + U_{fp} A_{fp}} \quad [4.6]$$

The time constant reflecting the thermal dynamics of the collector is given as:

$$\tau_{fp} = \frac{m_{c,fp} C_{p_c}}{\dot{m}_c C_{p_c} + U_{fp} A_{fp}} \quad [4.7]$$

The dwelling time of the calorific fluid in the solar collector is given by the ratio between the calorific fluid mass of the instantaneous volume in the solar collector and its mass flow rate:

$$\tau_{dw,fp} = \frac{m_{c,fp}}{\dot{m}_c} \quad [4.8]$$

This leads to a simple expression of the time constant of the solar collector as a function of the thermal convexity coefficient:

$$\tau_{fp} = \tau_{dw,fp} \; \gamma_{fp} \quad [4.9]$$

When there is no solar radiation ($I = 0$), the outlet temperature of the collector obeys the thermal convexity principle governing heat exchange. This property essentially implies that the temperature behaves in a certain manner, likely increasing or decreasing in a convex fashion in response to changes in environmental conditions. Notably, the coefficient governing this convex behavior, referred to as the thermal convexity coefficient γ_{fp}, must satisfy the following condition: $0 \leq \gamma_{fp} \leq 1$. This condition ensures that the coefficient remains within a reasonable range, reflecting the physical constraints of the system.

Expression [4.3] leads to a schematic presentation reflecting the link between the different inputs and outputs of the solar flat-panel collector. Figure 4.2 depicts the transfer functions.

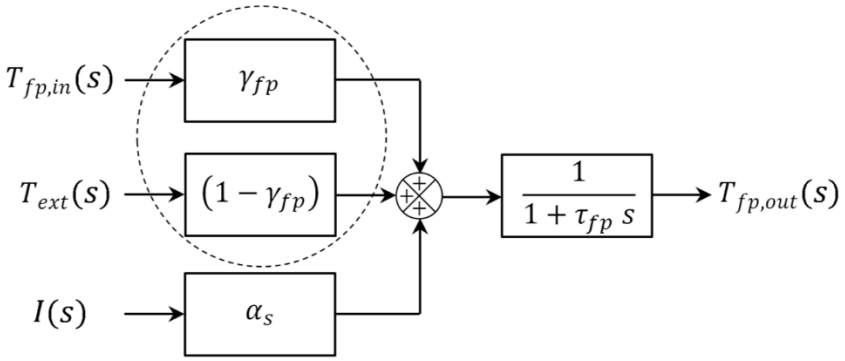

Figure 4.2. *Functional link between the input parameters and the solar panel outlet temperature*

Note that the heat exchange between a solar panel and its environment is described by the thermal convexity principle.

4.1.2. *Heat exchanger*

When the calorific fluid exits the solar collector, it flows through the heat exchanger at the inlet temperature $T_{he,in}(t)$ with the same flow rate $\dot{m}_c$ and closes the loop back to the solar collector at its outlet temperature $T_{he,out}(t)$. The calorific fluid transfers its thermal energy to the water within the storage system being at temperature T_w. This transfer of energy occurs across the separating surface A_{he} between the calorific fluid and the water with a heat transfer coefficient U_{he}.

Figure 4.3 shows the heat exchanger integrated into the storage tank. By neglecting losses through the pipes connecting the solar collector and the heat exchanger, the temperatures at the inlet and outlet of the heat exchanger align with the outlet and inlet temperatures of the solar collector, respectively.

The mixing of hot water in a storage tank typically occurs through natural convection. As water is heated at the bottom of the tank with a heat exchanger, it tends to rise to the top of the tank because of its lower density than cold water. Moreover, the cooler water flows down to the tank bottom. This natural convection is enhanced by the use of an open vertical tubular system, which incorporates a reduction in diameter. This reduction in diameter facilitates the movement of hot water upward and cooler water downward within the system, which results in efficient mixing and temperature uniformity throughout the storage tank.

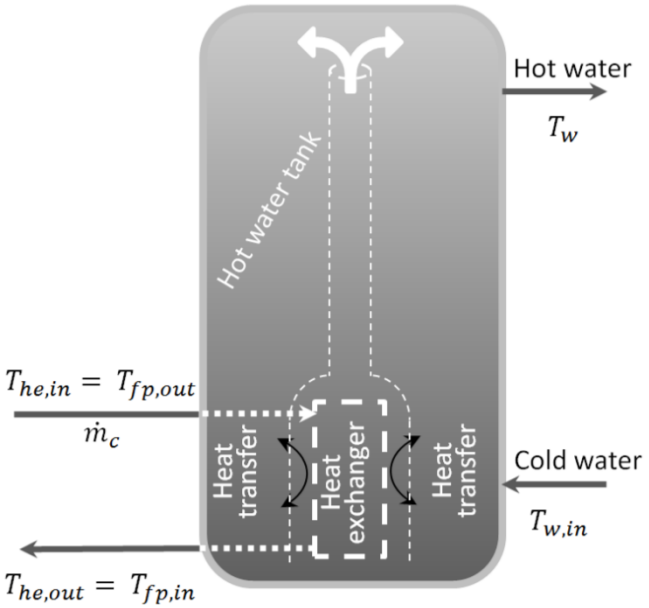

Figure 4.3. *Heat exchange with the water tank via the heat exchanger*

With the same equation [4.1], the energy balance applied to the calorific fluid circulating through the heat exchanger located within the storage system results in the derivation of the following equation:

$$m_{c,he} C_{p_c} \frac{dT_{he,out}}{dt} = \dot{m}_c C_{p_c} \left(T_{he,in}(t) - T_{he,out}(t)\right) + U_{he} A_{he} \left(T_w(t) - T_{he,out}(t)\right) \quad [4.10]$$

$$m_{c,he} = \rho_c \, V_{c,he} \quad [4.11]$$

where $m_{c,he}$ is the calorific fluid mass of the instantaneous occupied volume $V_{c,he}$ in the heat exchanger.

The term $U_{he} A_{he} \left(T_w(t) - T_{he,out}(t)\right)$ represents the heat exchange between the heat exchanger and the water tank through the separating area A_{he}.

The outlet temperature could be replaced by the mean temperature of the heat exchanger.

As mentioned above, the inlet and outlet temperatures are as follows:

$$\begin{cases} T_{he,in}(t) = T_{fp,out}(t) \\ T_{he,out}(t) = T_{fp,in}(t) \end{cases} \quad [4.12]$$

Equation [4.10] becomes:

$$m_{c,he} C_{p_c} \frac{dT_{fp,in}}{dt}(t) = \dot{m}_c C_{p_c} \left(T_{fp,out}(t) - T_{fp,in}(t)\right) + U_{he} A_{he} \left(T_w(t) - T_{fp,in}(t)\right) \quad [4.13]$$

In the same manner, the Laplace transform applied to differential equation [4.13] leads to the following expression:

$$T_{fp,in}(s) = \left(\gamma_{he} T_{fp,out}(s) + (1 - \gamma_{he}) T_w(s)\right)\left(\frac{1}{1 + \tau_{he}\, s}\right) \quad [4.14]$$

where

$$\gamma_{he} = \frac{\dot{m}_c C_{p_c}}{\dot{m}_c C_{p_c} + U_{he} A_{he}} = \frac{1}{1 + NTU_{he}} \quad [4.15]$$

and

$$\tau_{he} = \frac{m_{c,he} C_{p_c}}{\dot{m}_c C_{p_c} + U_{he} A_{he}} \quad [4.16]$$

Expression [4.14] establishes a construction with the thermal convexity previously discussed, ensuring its validity within the range of $0 \leq \gamma_{he} \leq 1$. This convexity condition remains fulfilled, as indicated by relation [4.15], given that $NTU_{he} \geq 0$.

The time constant τ_{he} represents the heat exchanger dynamic behavior. It can be calculated as the product of the thermal convexity coefficient and the residence time of the fluid within the heat exchanger. This relationship provides insight into how the heat exchanger responds to changes in operating conditions.

$$\tau_{he} = \gamma_{he} \quad \tau_{dw,he} \quad [4.17]$$

With expression [4.14], a functional diagram can be obtained to link the inputs and outputs of the heat exchanger, as presented in Figure 4.4.

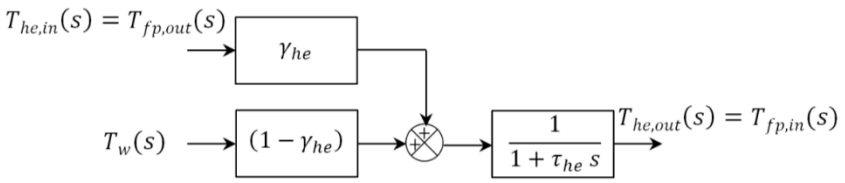

Figure 4.4. *Functional diagram of the heat exchanger*

4.1.3. *Storage tank*

As previously discussed, the proper mixing of hot water within the storage tank of a solar water heating system plays a crucial role in ensuring a reliable and consistent supply of heated water for domestic applications. The thermal energy required to maintain the desired water temperature is acquired through the operation of a heat exchanger, which serves as the intermediary for energy transfer within the system.

This heat exchanger facilitates the transfer of thermal energy that originates from the solar panel, enabling convective heat exchange across the separating surface between the two fluid streams. This process ensures the efficient transfer of absorbed solar energy to the water stored within the tank, thereby sustaining the overall thermal performance of the system.

Although the storage tank is specifically designed with thermal insulation to minimize heat losses and enhance energy retention, it is not entirely isolated from external influences.

Inevitably, thermal interaction occurs between the stored water and the surrounding environment. This exchange takes place through the external surface area of the storage tank, denoted as A_{ws}, where heat is transferred to or from the ambient environment at a temperature $T_a(t)$. The rate of this heat exchange is governed by the heat transfer coefficient U_{ws}, which characterizes the extent of the thermal interaction between the tank and its surroundings.

The energy balance applied to hot water leads to relation [4.18]:

$$m_w C_{p_w} \frac{dT_w}{dt}(t) = \dot{m}_w C_{p_w} \left(T_w(t) - T_{w,in}(t)\right) + U_{he} A_{he} \left(T_{fp,in}(t) - T_w(t)\right) + U_{ws} A_{ws} \left(T_a(t) - T_w(t)\right) \quad [4.18]$$

where

$$m_w = \rho_w V_w \quad [4.19]$$

where V_w represents the hot water tank volume.

Equation [4.18] can be written by applying the Laplace transform:

$$T_w(s) = \left(\gamma_w T_{w,in}(s) + (1 - \gamma_w - \gamma_{ws})T_{fp,in}(s) + (1 - \gamma_w - \gamma_{whe})T_a(s)\right) \quad [4.20]$$

where

$$\gamma_w = \frac{\dot{m}_w C_{p_w}}{\dot{m}_w C_{p_{cw}} + U_{he}A_{he} + U_{ws}A_{ws}} = \frac{1}{1 + NTU_{whe} + NTU_{ws}} \quad [4.21]$$

$$\gamma_{whe} = \frac{U_{he}A_{he}}{\dot{m}_w C_{p_{cw}} + U_{he}A_{he} + U_{ws}A_{ws}} = \frac{NTU_{whe}}{1 + NTU_{whe} + NTU_{ws}} \quad [4.22]$$

$$\gamma_{ws} = \frac{U_{ws}A_{ws}}{\dot{m}_w C_{p_{cw}} + U_{he}A_{he} + U_{ws}A_{ws}} = \frac{NTU_{ws}}{1 + NTU_{whe} + NTU_{ws}} \quad [4.23]$$

and

$$\tau_w = \frac{m_w C_{p_w}}{\dot{m}_w C_{p_w} + U_{he}A_{he} + U_{ws}A_{ws}} \quad [4.24]$$

τ_w can also be written as a function of the dwell time of water in the storage tank:

$$\tau_w = \gamma_w \quad \tau_{dw,w} \quad [4.25]$$

Note that:

$$\gamma_w + \gamma_{whe} + \gamma_{ws} = 1 \quad [4.26]$$

The thermal convexity is expressed here with three parameters and remains valid when their sum is equal to unity.

The functional diagram depicted in Figure 4.5 is obtained from expression [4.20].

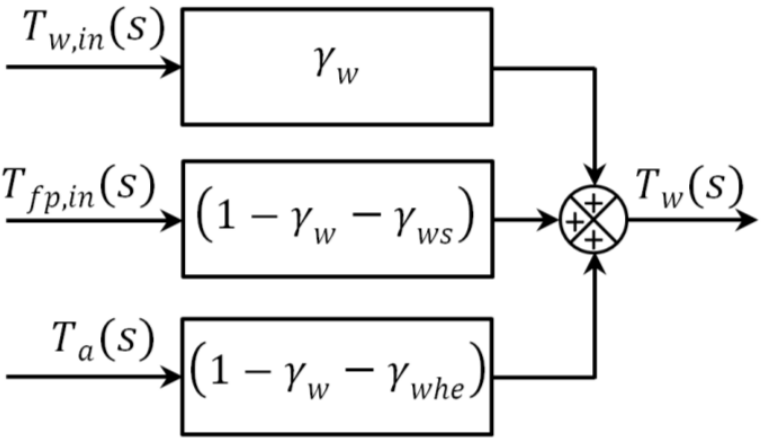

Figure 4.5. *Functional diagram of the hot water tank*

This figure shows the functional link between the inputs, such as the water inlet temperature, the calorific fluid input and the ambient temperature, and the output, representing the water tank temperature.

4.1.4. *Solar water heating global model*

With Figures 4.2, 4.4 and 4.5, the global functional diagram of solar water heating is shown in Figure 4.6, representing the overall links between the different parameters.

The figure presented here illustrates the relationship between the four key inputs of the solar water heating system and the resulting output. This functional diagram is incorporated into the Simulink® software, which serves as a powerful tool for analyzing and assessing various parameters, such as temperatures, thermal power, and the total amount of energy within the system. By employing this modeling approach, a comprehensive evaluation of system performance is possible, allowing for the optimization of energy efficiency and operational characteristics.

The thermal power absorbed by the solar panel can be determined through the following equation, which takes into account the specific heat exchange mechanisms at play within the system. This equation provides a quantitative means to measure

the energy input into the system, which is critical for assessing the overall efficiency and effectiveness of the solar water heating setup.

$$P_{th,fp}(t) = \dot{m}_c C_{p_c} \left(T_{fp,out}(t) - T_{fp,in}(t) \right) \quad [4.27]$$

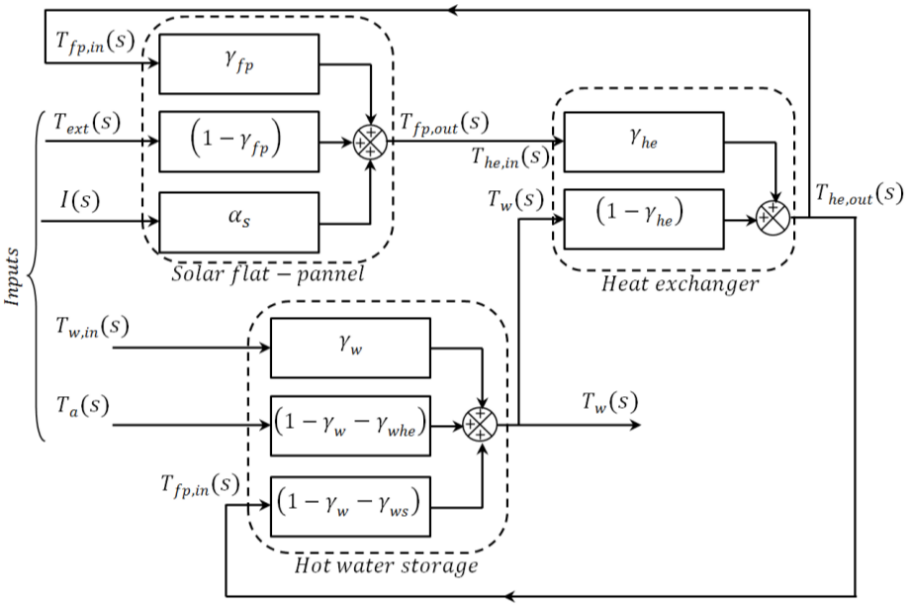

Figure 4.6. *Global functional diagram of the solar water heating*

4.2. Solar position and radiation

The amount of solar radiation received by a solar panel is influenced by several key factors, including its inclination angle, its orientation with respect to the Sun and its specific geographical location on Earth.

First, the inclination angle of a solar panel refers to the angle at which it is positioned relative to the horizontal plane. This angle plays a crucial role in determining how effectively the panel can capture solar energy. The optimal inclination angle varies depending on factors such as the season, latitude and intended use of the solar panel. Adjusting the inclination angle allows maximizing exposure to sunlight throughout the year.

Second, the orientation of a solar panel refers to its alignment relative to the position of the Sun in the sky. Panels are typically oriented to face south in the

northern hemisphere and north in the southern hemisphere to receive the maximum amount of sunlight over the course of the day.

However, slight adjustments may be made based on local conditions and specific energy needs.

Furthermore, the geographical location of a solar panel also plays a significant role in determining the amount of solar radiation it receives. Regions closer to the Equator generally receive more direct sunlight throughout the year, whereas areas farther from the Equator may experience variations in sunlight intensity due to seasonal changes and atmospheric conditions.

4.2.1. *Sun position*

Kepler laws of planetary motion provide insight into the orbit of the Earth around the Sun. According to Kepler's first law, the Earth moves along an elliptical orbit with the Sun at one of the focal points. This orbit lies within a plane known as the ecliptic. As the Earth travels along its orbital path, its relative position with respect to the Sun changes, resulting in variations in the amount of solar radiation received at different times of the year.

Visualizing the relationship between the Sun and the Earth position can be facilitated by imagining a celestial sphere surrounding the Earth, as presented in Figure 4.7. This celestial sphere serves as a reference frame, allowing observers to track the apparent motion of celestial bodies such as the Sun across the sky. The changing positions of the Sun relative to this celestial sphere throughout the year illustrate the seasonal variations in solar radiation that impact the performance of solar panels. The position of the Sun in the sky is commonly defined by two key parameters: the azimuth angle and solar elevation.

As depicted in Figure 4.7, the azimuth angle indicates the horizontal position of the Sun compared with a fixed point, measured in degrees clockwise from true north. It provides information about the position of the Sun relative to an observer's location on Earth.

For example, an azimuth angle of 0° means that the Sun is directly north, whereas 90° signifies that it is directly east. Monitoring the azimuth angle fluctuations throughout the day helps trace the Sun's trajectory across the sky.

The solar height, also known as the solar elevation angle or solar altitude angle, is a fundamental concept in solar geometry that quantifies the angle between the horizontal plane and the direction of the Sun's rays, as observed from a specific location on the Earth's surface.

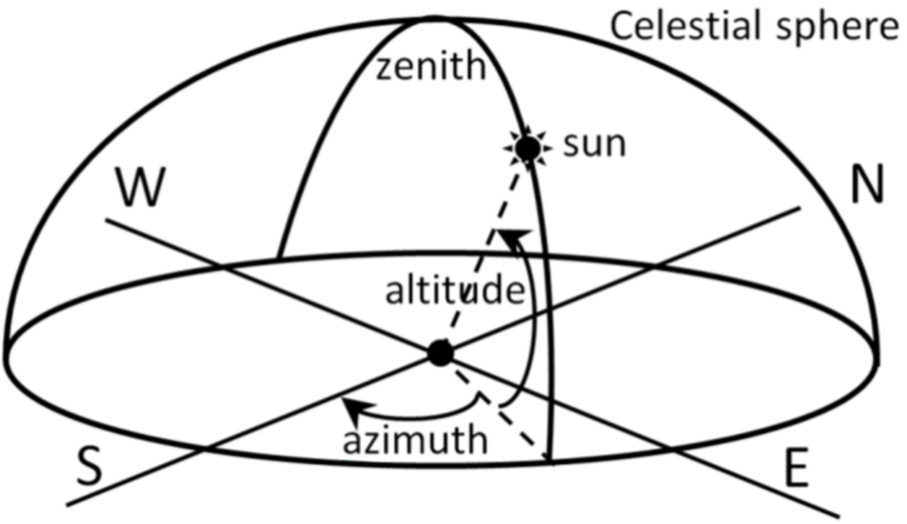

Figure 4.7. *Solar position observed from the Earth*

This angle determines how high the Sun appears to be in the sky at a given time relative to an observer position. The solar height angle is necessary for assessing the intensity and distribution of solar radiation reaching a particular spot on the Earth's surface. This angle varies throughout the day because of the rotation of the Earth and the tilt of its axis relative to the Sun. Considering these variations helps in optimizing the design and placement of solar energy systems, such as solar panels and solar thermal collectors, to maximize their efficiency and output.

During sunrise and sunset, when the Sun is near the horizon, the solar elevation angle is relatively low, resulting in oblique sunlight that covers a larger area and tends to be less intense. As the day progresses and the Sun rises higher in the sky, the solar elevation angle increases, leading to more direct sunlight concentrated over a smaller area, which results in higher solar radiation levels.

The solar elevation angle is influenced by factors such as the time of day, season, latitude, and atmospheric conditions such as clouds, haze and pollution. At noon on a clear day at the Equator, when the Sun is directly overhead, the solar elevation angle is at its maximum, resulting in the most intense solar radiation.

Figure 4.8 also illustrates the relationship between geographic latitude and solar height. Geographic latitude is the angular distance of a location north or south of the Earth Equator, measured in degrees.

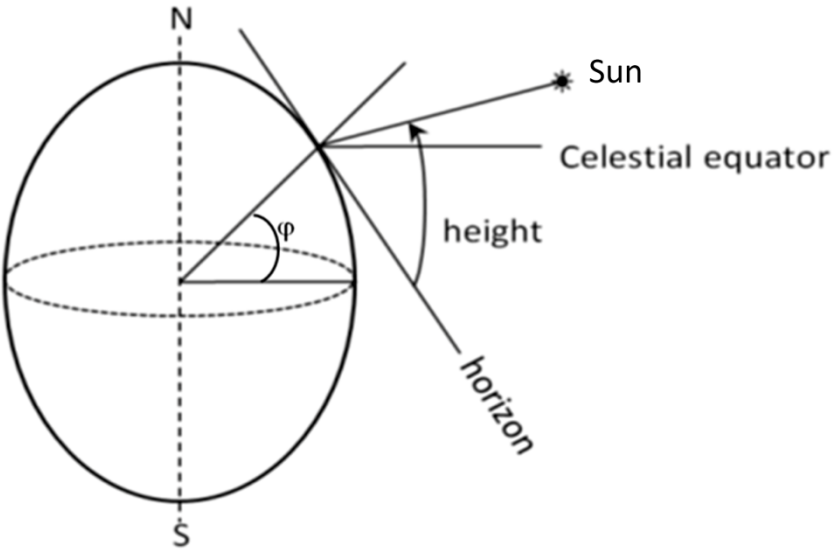

Figure 4.8. *Solar azimuth, altitude and height*

The angle of solar elevation varies with latitude because of the axial tilt of the Earth and its orbit around the Sun. At higher latitudes, such as those closer to the poles, the Sun's elevation angle tends to be lower, resulting in fewer days and less direct sunlight, especially during certain seasons. On the other hand, locations closer to the Equator are characterized by higher solar elevation angles and more consistent Sun radiation throughout the year.

Considering the interplay between the azimuth angle, solar height and geographic latitude is essential for optimizing the design and placement of solar energy systems, as it influences the efficiency and performance of solar panels and other solar technologies. By considering these factors, solar energy capture and utilization in various applications can be optimized, from residential rooftop installations to large-scale solar farms.

4.2.1.1. *Solar declination*

The solar declination delineates the angle between the line connecting the centers of the Sun and the Earth and its projection onto the equatorial plane. This angle undergoes significant variation throughout the year, ranging from a maximum of +23°260′ to a minimum of −23°260′. The equatorial plane, a surface aligned with the Earth Equator, intersects the celestial sphere, defining both the celestial Equator and the celestial axis poles. The celestial Equator serves as the projection of Earth's

Equator onto the celestial sphere, whereas the celestial axis poles represent the points where Earth's polar axis intersects the celestial sphere. The equinoxes are the two dates of the year during which the Sun crosses the equatorial plane. In this case, its declination is 0, which means that day and night have the same duration. The daily declination value can be obtained as a function of the day number of the year n with good accuracy by the following relation (Duffie and Beckman 2013):

$$\delta = 23.45\ sin\left(\frac{360}{365}(n - 81)\right) \quad [4.28]$$

The Sun's celestial positioning is intricately linked to the true solar time (TST). This association stems from the Earth's rotation, which maintains a consistent velocity, completing one full revolution per diurnal cycle around its polar axis. During this rotation, the Earth effectively transports the celestial sphere, the backdrop against which both stars and the Sun seem to traverse. The trajectory of the Sun across this celestial sphere throughout the course of a day is delineated by the hour angle ω. This angular measurement quantifies the deviation of the Sun from the observer meridian, a line extending from the observer location to the celestial poles. Essentially, the hour angle denotes the angular displacement of the Sun from its zenith, the point directly overhead, particularly significant at noon. This parameter serves as a crucial determinant in the computation of solar time, as it intimately correlates with the spatial orientation of the Sun in the sky at any given juncture.

The following relation expresses the hour angle as a function of solar time:

$$\omega = \dot{\theta}(TST - 12) \quad [4.29]$$

The parameter $\dot{\theta}$ signifies the angular velocity of the Earth's rotation, indicating the rate at which the Earth's surface traverses through its complete cycle of rotation. This angular velocity is observed to be approximately 15° per hour, reflecting the swift movement of the Earth's surface across its axis. Moreover, the hour angle attains a value of zero precisely when the Sun intersects the plane defined by the local meridian. This alignment signifies the moment of solar noon, where the Sun reaches its highest point in the sky for the day. At this juncture, the Sun directly faces the observer meridian line, casting no angular displacement from it. Thus, the hour angle serves as an important metric for discerning the Sun's relative position in the sky relative to the observer location and the solar noon reference point.

4.2.1.2. *Latitude*

The latitude, denoted by the symbol φ, serves as a fundamental angular parameter defining the geographical position of a specific point on Earth relative to the equatorial plane, as depicted in Figure 4.8. This angular measure delineates the

angle formed between the equatorial plane and the line connecting the point to the Earth center. With values ranging from –90° at the South Pole to +90° at the North Pole, latitude comprehensively characterizes the spatial positioning of locations across the globe. In the context of the analysis presented in this chapter, the experimental site under consideration is positioned at a latitude of 49°23'. This precise measurement pinpoints the site location in relation to the Equator, providing crucial geographic context for these investigations.

Importantly, this analytical framework extends beyond a specific experimental site and remains universally applicable to any geographical location on Earth. By evaluating the intersection of longitudinal and latitudinal angles, the latitude of any given point can be accurately determined, facilitating comprehensive spatial referencing and geographic analysis across diverse regions and contexts.

4.2.1.3. *Solar height*

The solar height, a key astronomical parameter, describes the angular elevation of the Sun above or below the horizontal plane relative to a specific location and time. This study provides valuable insight into the position of the Sun in the sky and its impact on local conditions such as solar radiation. The Gauss relation, as expressed by equations [4.30], offers a mathematical outline that shows the relationships among the solar height, declination, hour angle and latitude.

$$sin(h) = cos(\delta)cos(\omega)cos(\varphi) + sin(\delta)sin(\varphi) \quad [4.30]$$

By incorporating these variables, the Gauss relation enables precise calculations of the instantaneous solar height, considering the Earth axial tilt, the apparent motion of the Sun throughout the day and the geographical coordinates of the observer.

To achieve the highest energy output, the inclination angle $i(t)$ of the solar panels needs to adapt in accordance with the fluctuating solar height $h(t)$. This dynamic adjustment ensures that the plane of the solar panels consistently faces the Sun, maximizing the absorption of radiation. As a result, the instantaneous inclination of the solar panels can be determined by the following expression:

$$i(t) = 90° - h(t) \quad [4.31]$$

4.2.1.4. *Solar azimuth*

As illustrated in Figure 4.7, the solar azimuth a serves as an angular measure defining the clockwise angle from either the southern cardinal point (in the northern hemisphere) or the northern cardinal point (in the southern hemisphere) to the

horizontal projection of the Sun's rays. During the morning hours, the solar azimuth assumes negative values, indicating the Sun's position in the eastern direction relative to the observer. At solar noon, the azimuth angle becomes either null or reaches 180°, depending on the hemisphere. In the northern hemisphere, it signifies the Sun's alignment due south, whereas in the southern hemisphere, it represents the Sun's alignment due north. In the afternoon, the solar azimuth is positive, indicating the Sun's movement toward the western direction. The definition of the azimuthal angle is formally expressed by the following relation:

$$tg(a) = \frac{sin(\omega)}{sin(\varphi)\, cos(\omega) - cos(\varphi)\, tg(\delta)} \quad [4.32]$$

4.2.2. *Solar radiation*

Solar radiation comprises both direct radiation and that scattered by the atmosphere and surrounding environment. The intensity of sunlight received by a surface is contingent upon the orientation of that surface relative to the incoming solar rays. Pucar and Despic (2005) delved into the energy dynamics associated with indirect solar radiation. Their analysis revealed that the energy gain resulting from diffuse radiation is generally weak, with noticeable benefits primarily observed under specific atmospheric conditions, notably when the sky is heavily cloudy. During such instances of complete cloud cover, the scattering of sunlight by clouds facilitates a more uniform distribution of light, consequently leading to an increase in the amount of diffuse radiation reaching the Earth's surface. However, despite this augmentation, the overall energy gain remains relatively modest.

4.2.2.1. *Direct radiation*

The orientation of a solar panel with respect to the Sun's position is determined by two fundamental angles: the inclination angle (i), which describes the tilt of the panel relative to the horizontal plane, and the azimuth angle (β), which indicates the deviation of the panel orientation from the southern direction. Direct radiation I_{DR} refers specifically to the portion of solar radiation that impinges directly onto the surface of the solar panel perpendicular to its plane. This direct component of solar radiation is critical for maximizing the energy capture efficiency of solar panels, as it represents the most potent source of energy available for conversion into heat.

The relationship between the hour angle of the day and the elevation angle of the Sun plays an essential role in determining the intensity of direct solar radiation received by a surface. This relationship, encapsulated by a mathematical expression,

describes how the changing position of the Sun throughout the day influences the direct solar radiation incident at a particular location.

$$I_{Direct} = I\,\vec{k}.\vec{n} \qquad [4.33]$$

In this context, the unit vector $\vec{k}$ precisely defines the direction from which the Sun's rays are arriving, effectively pointing toward the position of the Sun in the sky. On the other hand, $\vec{n}$ serves as the unit vector perpendicular to the surface of the solar panels, indicating the orientation of the panel relative to its surroundings.

These vectors can be formulated as mathematical functions dependent on various angles that outline the precise orientation and spatial alignment of the solar panel with respect to the trajectory of the Sun.

$$\begin{cases} \vec{k} = \begin{pmatrix} cos(h)\ sin(a) \\ cos(h)\ cos(a) \\ sin(h) \end{pmatrix} \\ \vec{n} = \begin{pmatrix} sin(\beta)\ sin(i) \\ cos(\beta)\ sin(i) \\ cos(i) \end{pmatrix} \end{cases} \qquad [4.34]$$

Given these defined parameters, direct solar radiation can be expressed as follows:

$$I_{Direct} = I\left(sin(i)\ cos(h)\ cos(a-\beta)\ + cos(i)\ sin(h)\right) \qquad [4.35]$$

4.2.2.2. *Diffuse radiation*

The total diffuse solar radiation, which is assumed to exhibit isotropic behavior, comprises contributions from both atmospheric scattering and ground reflection, symbolized as I_{Datm} and I_{DGr}, respectively. When the solar panel is positioned horizontally, the entirety of the diffuse radiation is derived solely from atmospheric sources. However, upon inclination of the panel at an angle i relative to the horizontal plane, a fraction of the diffuse radiation originates from ground reflection in addition to atmospheric scattering.

Consequently, in this configuration, the diffuse radiation I_{atm} attributable to atmospheric scattering alone can be calculated as follows:

$$I_{atm}(i) = I_{Datm}\left(\frac{1+cos(i)}{2}\right) \qquad [4.36]$$

Concerning the radiation from reflection on the ground, the proportion intercepted by the solar panels can be expressed as follows:

$$I_{Gr}(i) = I_{DGr}\left(\frac{1 - cos(i)}{2}\right) a^* \quad [4.37]$$

The term a^* signifies the albedo, a measure of the reflectivity of a surface, representing the fraction of incident radiation that is reflected away. In this context, the albedo is approximated to be around 30%.

When the solar panel is inclined at an angle i, the manner in which it intercepts diffuse radiation differs. This change in inclination affects the surface exposure to diffuse radiation, consequently influencing the total amount of diffuse radiation received by the panel, as given by the following formulation:

$$I_{Diffuse}(i) = I_{Datm}\left(\frac{1 + cos(i)}{2}\right) + I_{DGr}\left(\frac{1 - cos(i)}{2}\right) a^* \quad [4.38]$$

4.2.2.3. *Total radiation*

The total radiation incident upon the solar panels represents the culmination of both direct solar radiation and diffuse solar radiation from the atmosphere and surrounding environment. This combined radiation constitutes the entirety of the solar energy reaching the panels and is given as:

$$I_t(i) = I_{Direct} + I_{Diffuse} \quad [4.39]$$

with

$$I_{Datm} = I_{DGr} - I\ sin(h) \quad [4.40]$$

A comprehensive examination of weather data conducted over an extended period of time enabled the formulation of empirical formulas to quantify both direct and diffuse radiation levels (Brichambaut and Vauge 1982). This data-driven approach was instrumental in understanding the intricate dynamics of solar radiation and its interaction with the Earth's atmosphere. By analyzing a wide range of meteorological variables, including cloud cover, atmospheric composition and seasonal fluctuations, these empirical relationships were developed to offer accurate predictions of solar radiation patterns.

These formulas not only quantify the direct light received from the Sun but also account for the diffuse radiation that is scattered by the atmosphere and clouds.

The ability to differentiate between these two components of Sun radiation is critical for solar energy applications, as direct radiation provides higher energy intensity, whereas diffuse radiation is often more uniform and can contribute to energy generation even under cloudy or overcast conditions.

Moreover, the empirical relationships derived from this study provide essential insights into the characterization of direct solar radiation emitted from the sky. These methods allow for a more refined understanding of how solar radiation varies throughout the day, across different seasons, and in response to geographical location. By applying these formulas, engineers and researchers can improve the modeling and forecasting of solar energy potential, helping to enhance the design, efficiency and optimization of solar energy systems, particularly in regions where sunlight is highly variable.

This detailed understanding of solar radiation is fundamental to improving solar collector efficiency, designing more effective solar thermal systems and accurately predicting energy output. In turn, these empirical relationships contribute to the broader field of renewable energy by facilitating more accurate energy harvesting and energy management in solar technologies.

This analysis is reported in Table 4.1.

	Very clear sky	**Fairly disturbed sky**	**Turbid sky**
Solar radiation	$I = 1{,}210\, e^{-\frac{1}{6\,sin(h+1)}}$	$I = 1{,}230\, e^{-\frac{1}{3.8\,sin(h+1.6)}}$	$I = 1{,}260\, e^{-\frac{1}{2.3\,sin(h+3)}}$
Total ground diffused radiation	$I_{DGr} = 1{,}130\,\left(sin(h)\right)^{1.15}$	$I_{DGr} = 1{,}080\,\left(sin(h)\right)^{1.22}$	$I_{DGr} = 995\,\left(sin(h)\right)^{1.25}$

Table 4.1. *Solar radiation and ground diffused radiation*

4.3. Simulation and discussion

Multiple simulations are conducted using a comprehensive set of parameters that closely correspond to the specifications governing the design and operational settings of the solar water heating experimental device. Upon completion of the simulations, the resulting data are analyzed and compared with observations obtained from experimental measurements. This comparative analysis serves to validate the accuracy and reliability of the thermal convexity method applied to a solar water heating system.

4.3.1. *Daily response to variation in solar radiation*

Figure 4.9 illustrates the diurnal variation in solar flux observed on a clear, sunlit day, providing a visual representation of how solar energy availability changes over the course of the day. The temporal progression of solar flux shown in the figure closely mirrors the typical solar radiation pattern, where solar energy gradually increases from sunrise, peaks at solar noon and then decreases toward sunset. This pattern is consistent with established solar flux data, such as that presented by Esen (2004), which helps ensure that the depiction of solar energy dynamics is both accurate and reliable.

The fluctuation in solar flux throughout the day is a crucial input parameter for various simulation frameworks. By incorporating these variations, the simulation can more accurately predict the dynamic evolution of temperatures within the system being modeled. For example, in solar thermal systems, the changing solar flux directly influences the temperature of the working fluids, heat storage materials or other components over time. Accurately capturing this diurnal fluctuation is essential for understanding the thermal performance of the system, optimizing its design and improving energy efficiency. Thus, the solar flux profile depicted in Figure 4.9 serves not only as a reference for understanding solar energy availability but also as a critical factor in the dynamic modeling of thermal systems.

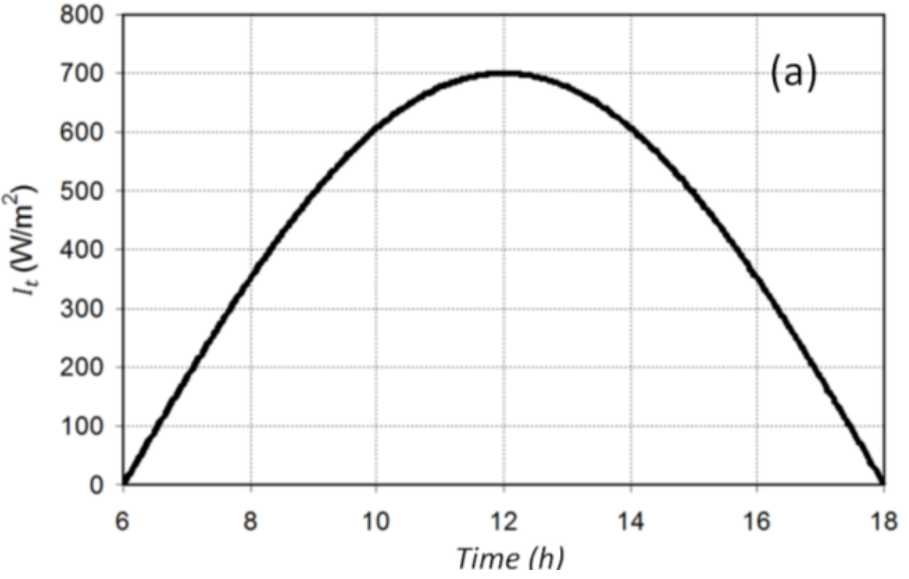

Figure 4.9. *Daily Sun radiation*

The simulation results presented in Figure 4.10 provide a detailed analysis of the temperature evolution within the solar thermal system. Specifically, the figure traces the temporal trajectory of temperatures at both the inlet and outlet of the solar collector, as well as within the thermal storage system. These results were obtained under a controlled flow rate of the heat transfer fluid (HTF), set at $\dot{m}_c = 2.57\ (\mathrm{kg/min})$.

The temperature profiles depicted in the figure offer a noteworthy understanding of the thermal behavior of the system throughout the simulation period. At the inlet of the solar collector, the temperature reflects the initial state of the HTF before it absorbs solar energy. As the fluid passes through the collector, it gains heat, leading to a noticeable increase in temperature at the outlet.

The difference between the inlet and outlet temperatures illustrates the efficiency of the solar collector in transferring solar energy to the fluid.

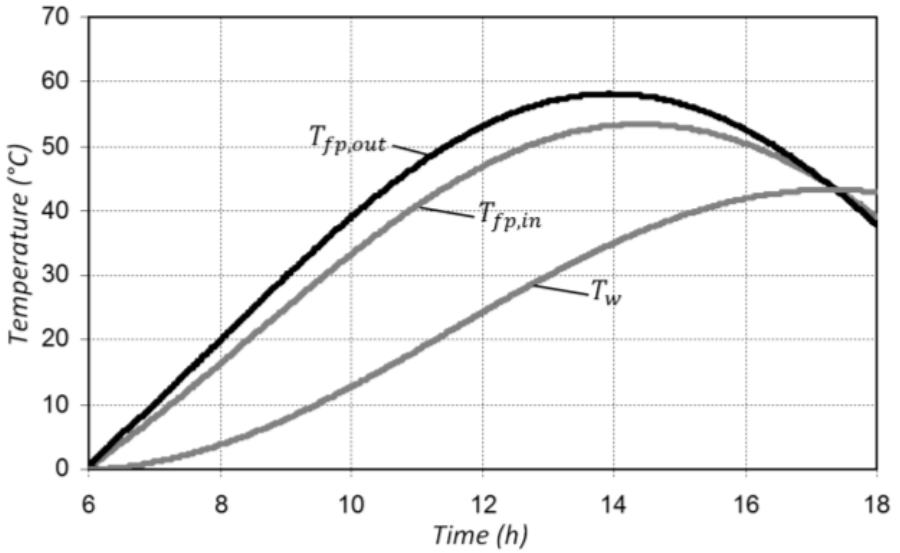

Figure 4.10. *Inlet and outlet temperatures of the flat panel and tank*

Furthermore, the simulation tracks the temperature within the thermal storage system, which plays an important role in maintaining the overall energy balance of the system. The storage temperature profile shows how effectively the system captures and retains the heat generated during the peak solar flux periods, ensuring a steady supply of thermal energy even when the solar input decreases.

Overall, the data presented in Figure 4.10 not only highlight the dynamic response of the system to the prescribed flow rate but also demonstrate the interplay between the solar collector and the storage system in optimizing thermal energy utilization. These insights are crucial for fine-tuning system parameters to increase efficiency and ensure consistent performance under varying operating conditions.

Remarkably, the temporal alignment between the peak values of solar radiation and the corresponding temperatures at the inlet and outlet of the solar collector exhibited a discernible temporal lag of approximately two hours. This temporal disparity underscores the transient nature of the thermal energy absorption and dissipation processes within the collector system, reflecting the inherent thermal inertia and response time of the constituent materials.

Furthermore, the onset of temperature variation within the storage tank manifests beyond a threshold, indicative of the requisite time for sufficient thermal energy accumulation. Additionally, an observation pertains to the temporal offset observed between the maximum temperature attained within the storage system and the inlet/outlet temperatures of the solar collector, implying a non-instantaneous interplay of heat transfer dynamics and thermal mass distribution within the overall system architecture. Indeed, each component of the solar system has a certain degree of thermal inertia. Thus, they require time to absorb, transfer or release heat. Consequently, even if the solar flux peaks at a given time, the system components react with a certain delay because of this thermal inertia.

4.3.2. *Effect of the calorific fluid flow rate*

The thermal behavior of the storage tank was systematically analyzed under varying HTF flow rates, with two distinct operational configurations established to evaluate its performance. The first configuration represented a scenario in which no domestic hot water was drawn from the system, corresponding to a zero mass flow rate of domestic water ($\dot{m}_w = 0$). This setup allowed for an assessment of the intrinsic thermal behavior, particularly heat retention, within the storage tank in the absence of external demand. In contrast, the second configuration incorporated a non-zero domestic hot water flow rate ($\dot{m}_w \neq 0$), indicating active consumption. This scenario provided insights into the system dynamic response to real-time hot water usage and the associated thermal fluctuations.

To conduct this parametric analysis, a representative solar flux profile was used as an input for the thermal simulations of the solar water heating system. This profile was measured using a pyranometer positioned in close proximity to the flat-panel collector to ensure accuracy in capturing the incident solar radiation. The recorded solar flux exhibited a peak intensity of approximately 1,100 W/m^2,

effectively depicting the temporal evolution of solar radiation over the course of a typical sunny day.

To assess the thermal performance of the storage system under various solar conditions, the originally measured solar flux profile was subjected to controlled attenuation.

This approach enables the simulation of different attenuated flux profiles, allowing for a comprehensive evaluation of the storage tank thermal response under reduced solar energy input. The resulting attenuated flux profiles, which are graphically represented in Figure 4.11, illustrate the effect of solar energy fluctuations on the overall system efficiency and thermal stability.

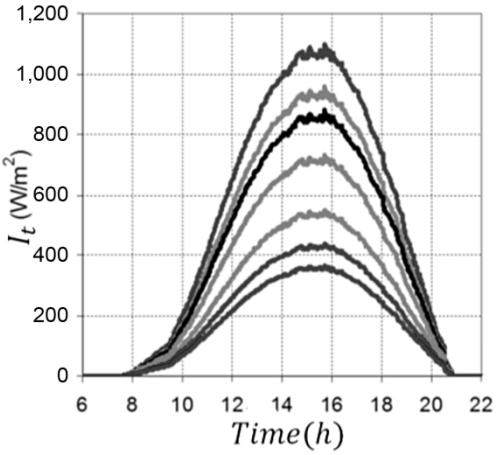

Figure 4.11. *Daily variation in solar radiation on sunny days*

By systematically inspecting the resultant temperature profiles of the storage tank under these attenuated flux scenarios, comprehensive insights were gathered regarding the system thermal response with respect to diverse solar radiation conditions.

4.3.2.1. *Without consumption of domestic hot water*

The various profiles depicted in Figure 4.11 were used to simulate the thermal dynamics of the solar system across a spectrum of HTF flow rates. Figure 4.12 serves as an illustrative example, showcasing the temporal evolution of temperature under varying HTF flow rates, all while employing a flux profile from Figure 4.11 characterized by solar radiation reaching its maximum at 1,100 W.m^{-2}.

The temperature within the storage system demonstrates a gradual rise over the observation period. As the flow rate increases, facilitating a greater influx of thermal energy, the temperature of the storage medium increases. This relationship underlines the important role of heat transfer dynamics in governing the thermal behavior of the system. Note that the recommended temperature for a hot water tank varies depending on several factors, including individual preferences, hot water needs and considerations of safety and energy efficiency. Generally, the hot water tank temperature is set between 49°C and 60°C. Indeed, water temperature below 49°C can promote the growth of pathogenic bacteria, such as Legionella, in the hot water tank. Conversely, excessively high temperatures can pose a risk of scalding.

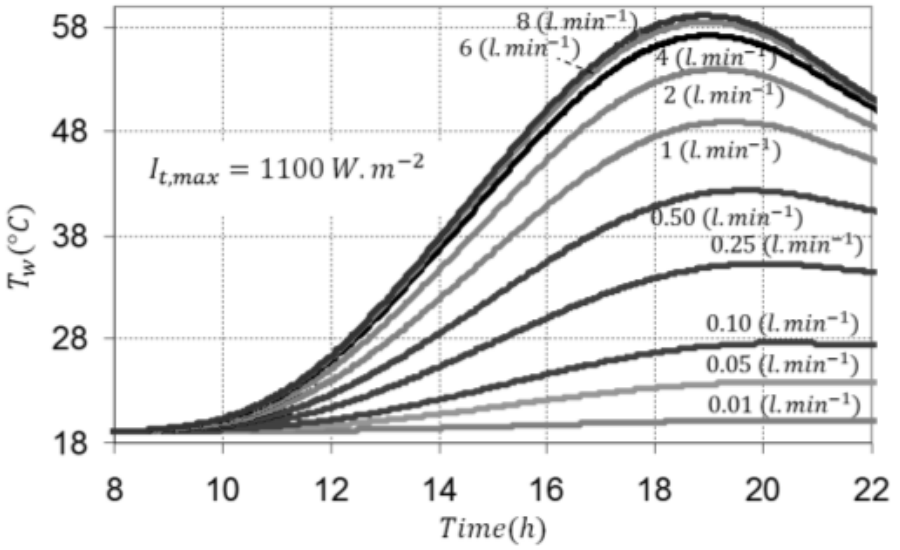

Figure 4.12. *Solar water storage tank temperature with no running tap water for different calorific fluid flow rates*

With these considerations, beyond a flow rate of $Q_c = 2\ (\mathrm{L.min^{-1}})$, the storage system attains temperatures deemed suitable for the provision of domestic hot water. This signifies the attainment of thermal conditions conducive to fulfilling the requisite demands of domestic hot water usage, thereby underscoring the practical viability of the system in meeting residential heating requirements.

By utilizing the diverse solar flux amplitudes outlined in Figure 4.11, the maximum temperature attained within the storage system is graphically represented in Figure 4.13. This graphical depiction offers insight into the dynamic evolution of the maximum temperature of the water storage system $T_{w,max}$ according to

variations in the HTF flow rate, setting distinct scenarios for different solar flux intensities. The maximum temperature observed within the storage system exhibits a direct correlation with the calorific fluid flow rate, as reflected by its increase with increasing flow rate. This trend suggests increased thermal input into the system, leading to greater thermal energy accumulation in the storage tank as the flow rate increases. For a flow rate of 2 ($\mathrm{L.min^{-1}}$), the increase in the maximum temperature closely approximates around 87% of the trend value.

This analysis signifies convergence toward the anticipated thermal behavior of the system, particularly in terms of rating the solar flat panel. This key point is essential to optimize the efficiency of the solar system and predict the thermal dynamics according to various operational parameters.

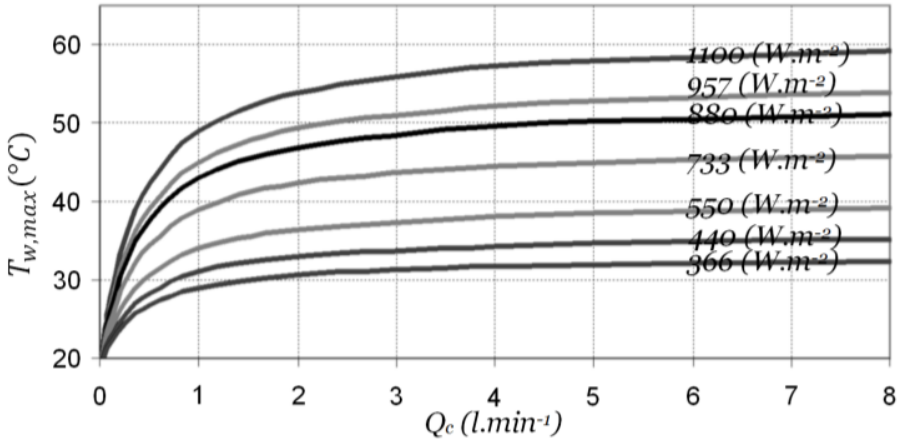

Figure 4.13. *Maximum temperature of water tank storage for different solar flux*

Importantly, as previously illustrated in Figure 4.12, the time at which the storage system reaches its maximum temperature is influenced by the flow rate of the calorific fluid. This temporal dependence is further examined and visually represented in Figure 4.14, which highlights the relationship between the time parameter t_{max} (the time at which the maximum temperature is attained) and the flow rate of the HTF.

The flux profile used for this analysis corresponds to the one depicted in Figure 4.11, characterized by a peak solar flux intensity of $I_{t,max} = 1{,}100\ \mathrm{W.m^{-2}}$. This flux profile was chosen to simulate the solar radiation conditions experienced during a typical sunny day, providing a realistic basis for assessing the system thermal dynamics.

The trend observed in Figure 4.14 clearly demonstrates a systematic reduction in the time required for the storage system to reach its maximum temperature as the flow rate of the HTF increases. This inverse relationship underscores the crucial role of fluid flow dynamics in influencing the thermal behavior of the storage system. Specifically, as the flow rate increases, the increased convective heat transfer accelerates the thermal response of the system, allowing it to reach its peak temperature more rapidly.

Moreover, the trend exhibited in the data approaches a limiting value, suggesting that the time to reach the maximum temperature tends toward a certain threshold as the flow rate continues to increase.

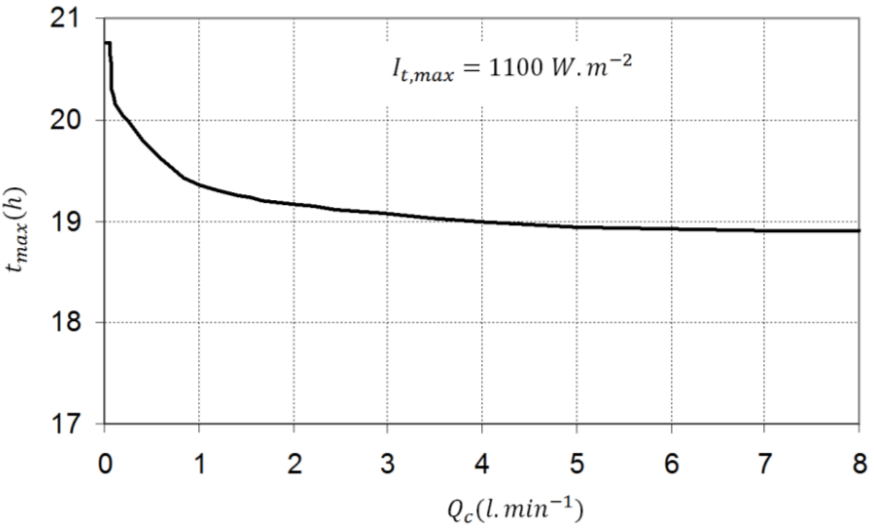

Figure 4.14. *Time to reach the maximum temperature as a function of the calorific flow rate*

This asymptotic behavior indicates the presence of a critical point beyond which further increases in the HTF flow rate result in only marginal improvements in the rate at which the system reaches its maximum temperature.

Consequently, once this limiting value is approached, further enhancements in the flow rate may yield diminishing returns, with the time to peak temperature stabilizing despite additional increases in fluid velocity. This behavior highlights the complexity of the thermal response and suggests that, beyond a certain point, further optimizing the flow rate may have little impact on system performance.

4.3.2.2. *With consumption of domestic hot water*

In this scenario, the solar system operates with consumption of domestic hot water sourced from the storage system. The solar flux profiles from Figure 4.11 are also employed for calculating the various temperatures in this configuration. Figure 4.15 depicts the evolution of the storage temperature with a withdrawal flow rate of $Q_w = 3\ \mathrm{L.min^{-1}}$.

Moreover, the higher the calorific fluid flow rate is, the greater the temperature of the storage tank. The act of drawing domestic hot water from the system induces a discernible reduction in the maximum temperature attained within the storage tank. This decrease is attributed to the extraction of thermal energy from the stored water for domestic usage, thereby diminishing the overall thermal energy content within the tank.

Moreover, the timing of the maximum temperature occurrence shifts when domestic hot water is drawn from the system. Compared with scenarios without drawing, the maximum temperature is reached at an earlier time, reflecting the accelerated depletion of thermal energy reserves due to the additional demand for domestic hot water. Furthermore, the temperature decline toward the end of the day shows a more pronounced relative variation when domestic hot water is drawn.

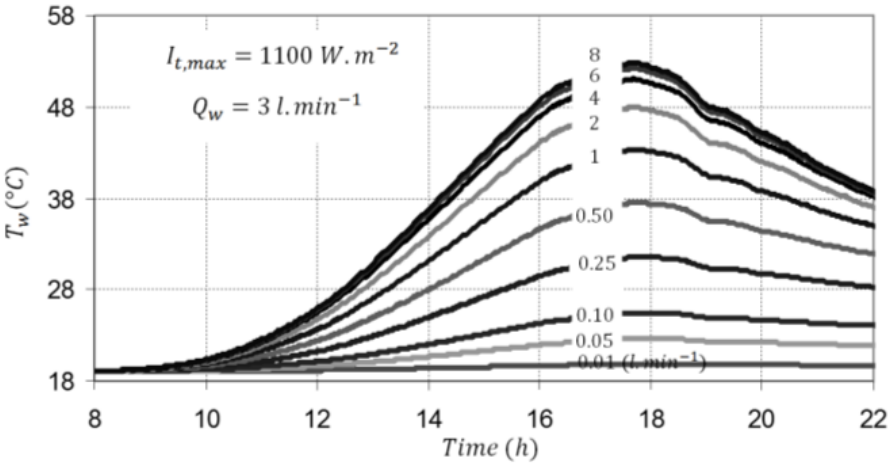

Figure 4.15. *Daily evolution of the domestic water temperature under withdrawal flow rate*

This phenomenon is attributable to the increased energy loss resulting from the extraction of hot water for domestic use, accentuating the decrease in temperature as

the day progresses. However, it is noteworthy that the time to reach the maximum temperature exhibits little variation in comparison to that in scenarios where no withdrawal occurs. This observation suggests that the temporal occurrence of the maximum temperature within the system remains relatively stable when the storage tank is subjected to withdrawal operations.

Figure 4.16 shows how the maximum temperature of the storage tank evolves with respect to changes in the calorific fluid flow rate across different amplitudes of solar flux. This depiction refers to the withdrawal configuration, where domestic hot water is drawn from the system at a constant flow rate of $Q_w = 3\ \mathrm{L.\,min^{-1}}$.

Each curve on the graph is relative to distinct amplitude of solar flux, providing insights into how variations in solar radiation levels impact the maximum temperature reached within the tank at different flow rates. The behavior of these curves highlights the dynamic relationships among the calorific fluid flow rate, the solar flux intensity, and the resulting thermal response of the storage system subjected to drawing water.

As solar radiation intensifies, the maximum temperature within the system increases accordingly. As noted in the case without drawing water, there is a clear upward trend in the maximum temperature with increasing calorific fluid flow rate, converging toward a limiting trend value. This limiting value is lower than the maximum temperature achieved in scenarios where no withdrawal occurs.

The use of domestic hot water is closely linked to the behaviors observed among occupants of residential buildings. A specific usage profile has been methodically crafted via a statistical approach, as documented in the Guide AICVF (2004).

The profile shown in Figure 4.17 is derived from comprehensive data collected across a sample set comprising 50 residential units, ensuring a robust representation of individual usage behaviors. In particular, the usage profile reveals three distinct peaks in demand. The first peak is observed during the morning hours, typically at approximately 7 a.m., followed by a secondary peak around midday. However, the most substantial surge in demand occurs in the evening, at approximately 7 p.m. This detailed profile of daily domestic hot water consumption, as depicted in Figure 4.17, serves as a valuable resource for understanding and modeling the temporal dynamics of hot water usage within residential settings.

Taking into account fluctuations in demand throughout the day enables a more precise assessment of the thermal requirements and operational challenges faced by solar heating systems in meeting the varying needs of occupants. This daily consumption pattern was incorporated into the simulation software to evaluate the diverse temperature dynamics within the thermal solar system.

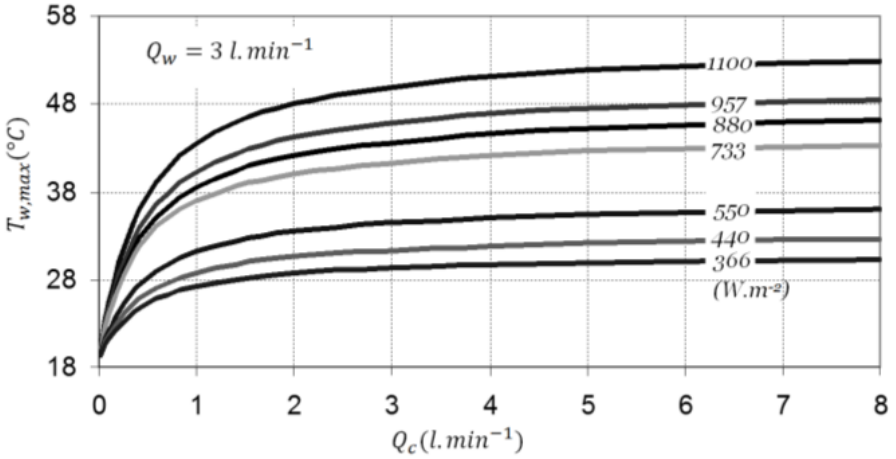

Figure 4.16. *Maximum temperature of water tank storage for different solar fluxes with drawing water*

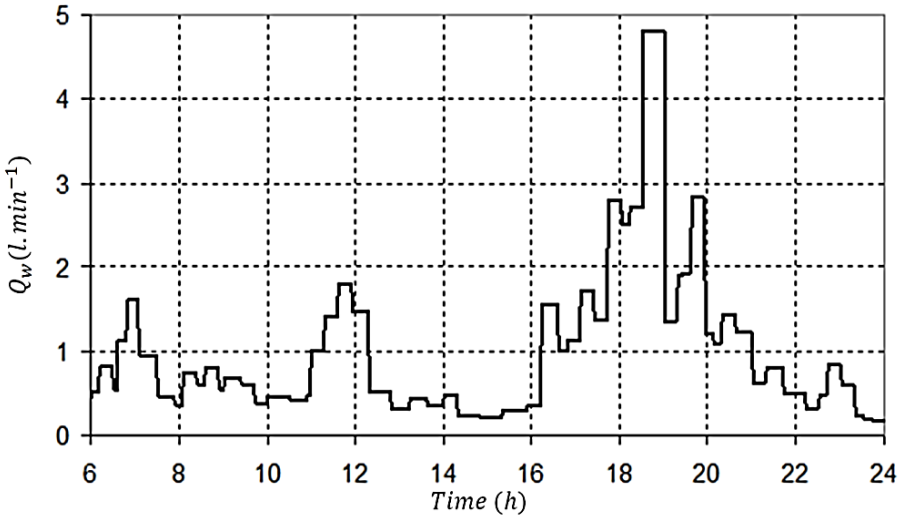

Figure 4.17. *Typical consumption of hot domestic water (AICVF 2004)*

Given the variability in withdrawal flow rates, the solar system demonstrates a nonlinear response. Indeed, the thermal convexity coefficient γ_w and the time constant τ_w indicated by expressions [4.21] and [4.25], respectively, depend on the domestic hot water flow rate. These model parameters undergo continuous

assessment throughout the day, adjusting in response to variations in the withdrawal flow rate over time.

This iterative process allows for a dynamic assessment of system performance under changing operational conditions, capturing the nuanced interactions between the withdrawal flow rate and the corresponding thermal responses within the solar heating system.

Figure 4.18 outlines the daily progression of the storage system temperature, considering both the withdrawal flow rate profile depicted in Figure 4.17 and a constant flow rate equivalent to the average withdrawal flow rate. In both scenarios, the calorific fluid flow rate remains constant at $Q_c = 3\ l.min^{-1}$. This figure illustrates that the temperatures initially increase at a similar rate during system startup. However, it becomes apparent that the temperature with a variable withdrawal flow rate surpasses that achieved under conditions of a constant average flow rate. As the flow rate increases, the rate of temperature decrease becomes more pronounced. This phenomenon can be attributed to the reduced time constant associated with the storage system when the domestic water flow rate is elevated.

Essentially, the system exhibits heightened thermal responsiveness to fluctuations in water demand, which results in a more rapid temperature decrease under conditions of increased water usage.

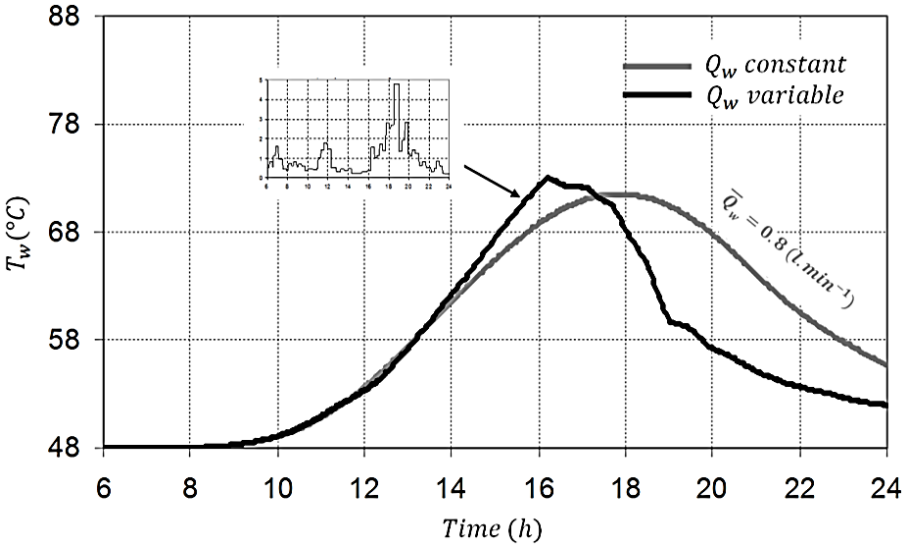

Figure 4.18. *Daily domestic storage tank temperature evolution with withdrawal flow rate*

Figure 4.19 presents the dynamic changes in the withdrawal thermal flow rates alongside the cumulative thermal energies over time.

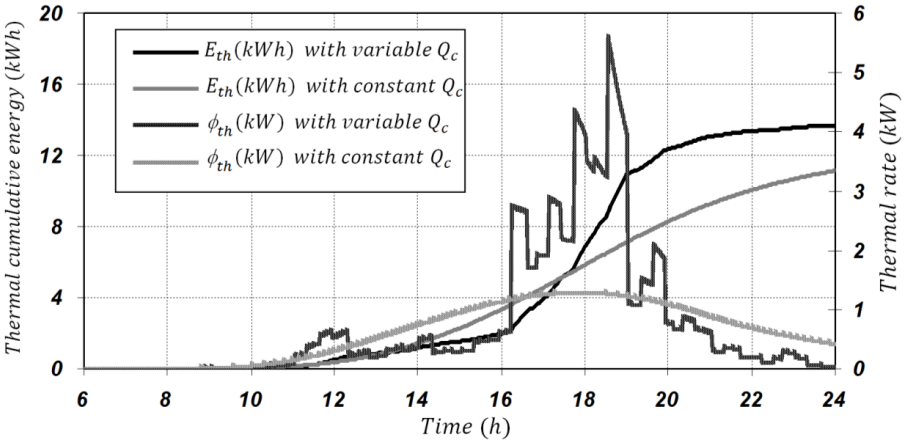

Figure 4.19. *Thermal cumulative energy and thermal rate in the storage system*

While the total cumulative withdrawal volume remains consistent across both scenarios, there is a contrast in the cumulative energy accumulation. Specifically, in the case of withdrawal with a variable flow rate reflecting human behavior patterns, the cumulative thermal energy is greater than that achieved with a constant withdrawal flow rate. This underlines the impact of varying withdrawal rates on the overall thermal energy balance of the system. The variable flow rate, synchronized with human behavior profiles, leads to more opportunistic utilization of available thermal energy, resulting in enhanced cumulative energy accumulation over time. Furthermore, the thermal flow rate dynamics are closely linked to both the temporal variations in solar flux intensity and the fluctuations in domestic hot water withdrawal rates.

These interdependencies highlight the intricate interactions among external environmental factors, user behavior patterns, and the thermal performance of the solar heating system.

4.4. Experimental results with a fixed solar collector

4.4.1. *Without consumption of domestic hot water*

Numerous experiments have been conducted to assess system performance under diverse climatic conditions. Initially, the results from a day characterized by mild

sunlight are outlined, providing insight into system behavior under such conditions. Following this, the results from days with varying degrees of solar intensity, ranging from mild to strong disturbances, are analyzed. This comprehensive examination aims to describe how the system responds to fluctuations in solar irradiance. Additionally, an illustrative example is provided, showing system performance on a day with clear morning sunshine, followed by disruptions in the afternoon. This multifaceted approach allows for a thorough understanding of system dynamics across a spectrum of climatic scenarios.

4.4.1.1. *Low-sunlight days*

Figure 4.20 provides a detailed representation of the fluctuation in solar radiation intensity throughout the day, as recorded by the pyranometer. Positioned within the same plane as the solar collectors, the pyranometer offers accurate measurements of incident solar radiation levels as well as diffuse radiation over time. This graph shows the diurnal pattern of solar radiation, capturing variations in intensity from sunrise to sunset. This measured radiation indicates a maximum intensity of approximately 450 W/m^2.

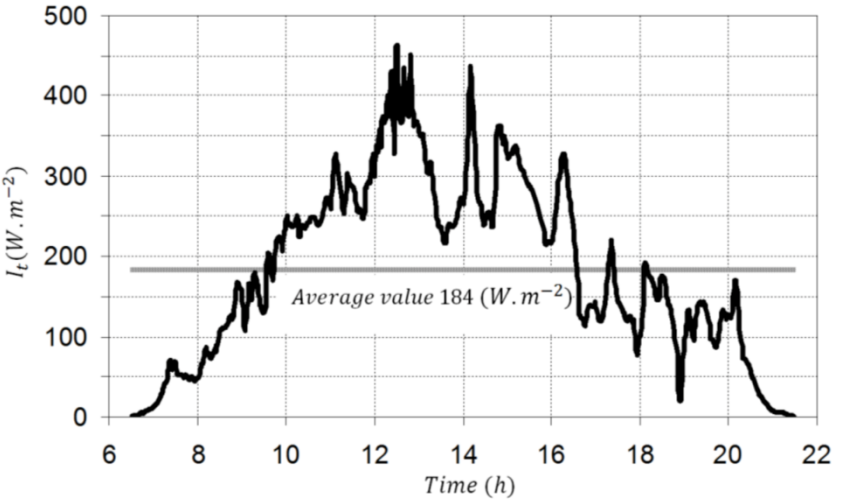

Figure 4.20. *Experimental solar radiation*

This day was characterized by low solar radiation intensity due to some climatic disturbances despite being expected to be continuously sunny. However, the daily average value of radiation intensity remains at approximately ≈ 184 (W.m^{-2}).

To obtain various simulated temperatures, the actual measured solar radiation is considered in the simulation tool to obtain the theoretical water tank temperature. This result is reported in Figure 4.21 in comparison with the experimental temperature over time.

These experimental and theoretical results are in good agreement, with an error margin of approximately 3%.

Compared with the solar flux, the experimental temperature of the water storage tank exhibited a delayed response. This temperature measurement is carried out halfway up the storage tank. Given the closed storage system, the evolution of its temperature is driven mainly by sensible heat.

Therefore, the temperature gradually increases until it reaches a stable value. Additionally, sudden fluctuations in the solar flux have a minimal impact on the storage system.

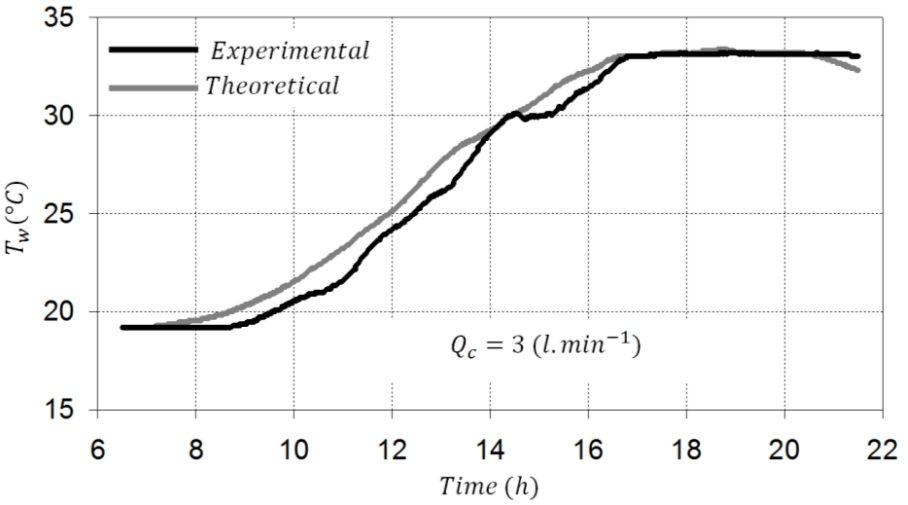

Figure 4.21. *Water storage temperature*

Figures 4.22 and 4.23 depict the evolution of the experimental and theoretical temperatures, respectively, at the inlet and outlet of the solar collector. In these two graphs, the theoretical predictions closely match the experimental data, showing an agreement within a margin of error not exceeding 10%. Both the inlet and outlet temperatures at the solar collector exhibit the same pattern, where they rise steadily until reaching their peak values, after which they gradually decline as the solar flux diminishes toward the end of the day.

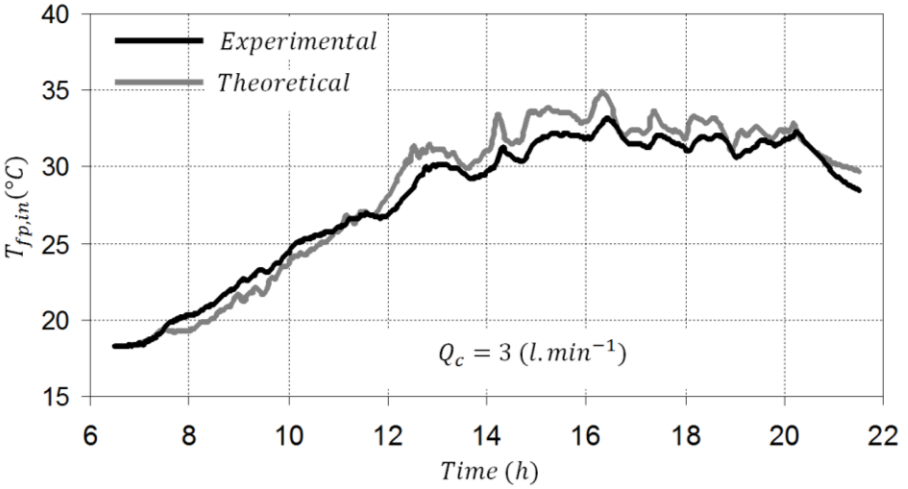

Figure 4.22. *Solar flat-panel inlet temperature during a low-sunlight day*

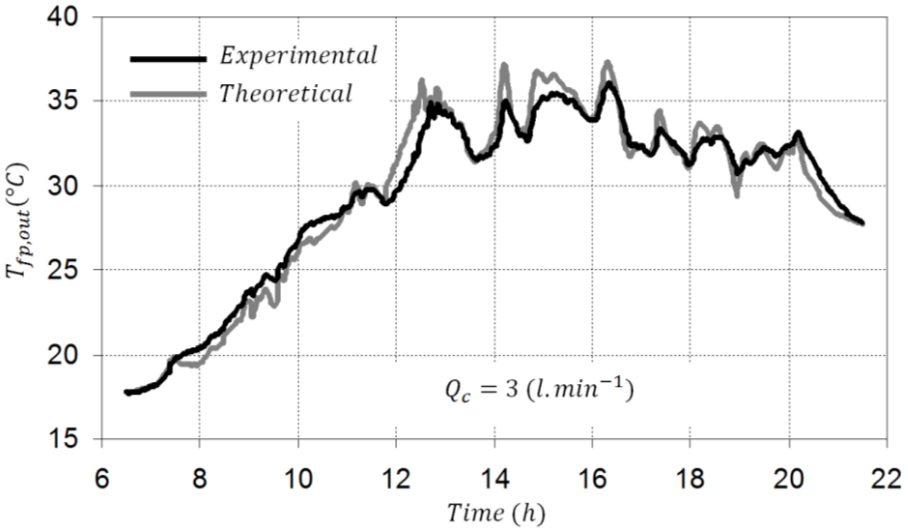

Figure 4.23. *Solar flat-panel outlet temperature during a low-sunlight day*

The temperatures of the heat fluid at the entrance and exit of the solar collector are sensitive to sudden fluctuations in the solar flux. This sensitivity underlines the dynamic interaction between the intensity of solar radiation and the thermal behavior of the calorific fluid within the solar collector.

The inlet and outlet temperatures of the solar collector serve as crucial parameters for determining the thermal power exchanged within the system. By monitoring these temperatures, it becomes possible to quantify the rate of heat transfer occurring within the collector.

This thermal power exchange is fundamental for assessing the efficiency and performance of solar heating systems. The relationship between these temperatures and the exchanged thermal power can be derived via principles of heat transfer. By applying relevant equations and considering factors such as the flow rate of the calorific fluid and its specific heat capacity, it becomes feasible to calculate the thermal rate transferred through the collector via expression [4.27].

Figure 4.24 provides a comparison between the experimental and theoretical thermal power outputs of the solar collector, specifically for a day characterized by low Sun radiation conditions. As indicated below, this comparison is derived from calculations based on equation [4.27], which expresses the thermal power exchange within the solar collector.

By plotting both the experimental and theoretical thermal power values on the same graph, this figure shows how well the theoretical predictions align with the performance of the solar collector under low sunlight conditions. Understanding this alignment is crucial for validating the accuracy of theoretical models and assessing the reliability of predictions.

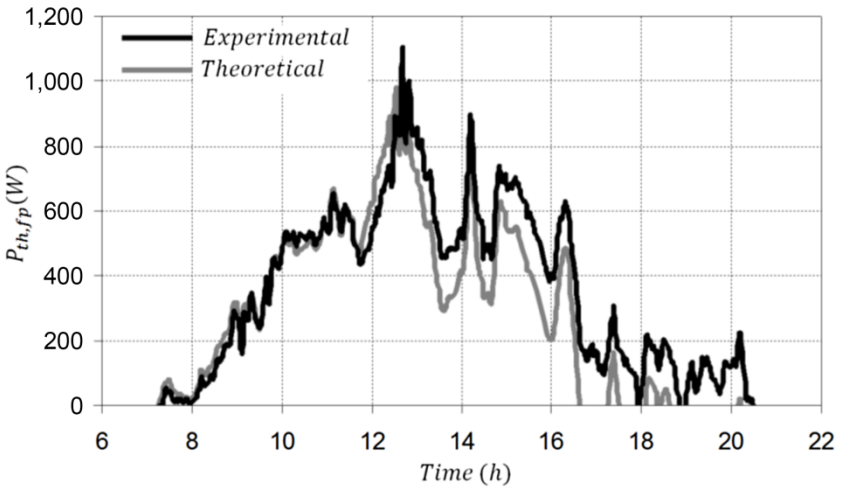

Figure 4.24. *Solar flat-plate thermal rate during a sunny disturbed day*

This thermal power, generated by the solar collector, is transferred by the pump to the heat exchanger integrated within the storage system, facilitating the exchange of heat between the calorific fluid circulating through the solar collector and the water stored in the storage tank.

4.4.1.2. *Sunny days with mild disturbances*

Another scenario, depicted in Figure 4.25, is characterized by a relatively high level of solar radiation intensity.

The graph in Figure 4.25, which shows the evolution of solar radiation intensity over time, indicates an average intensity value of approximately ≈ 516 (W.m^{-2}).

Despite the elevated solar radiation, the impact of climatic disturbances is less pronounced, resulting in a more stable environment for solar energy capture and utilization.

This comparison allows for a nuanced understanding of how varying levels of solar radiation and climatic disturbances can influence the performance and reliability of solar energy systems.

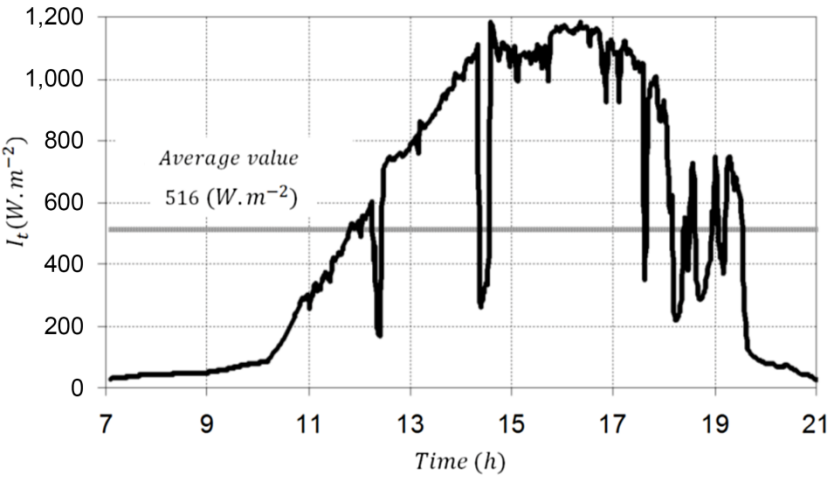

Figure 4.25. *Experimental solar radiation during a day with mild disturbances*

Similar to the previous example, the theoretical temperature of the water storage tank, reported in Figure 4.26, corroborates the experimental temperature.

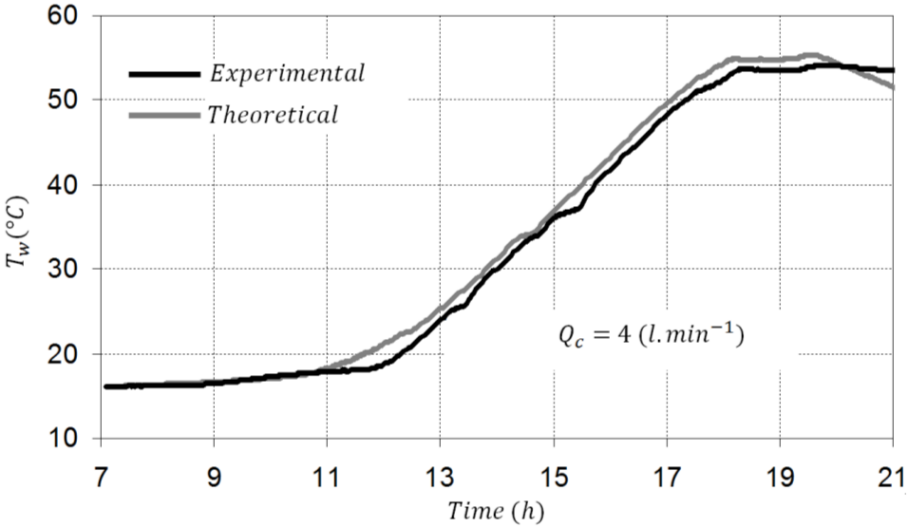

Figure 4.26. *Water storage temperature during a day with mild disturbances*

Figure 4.27 shows the inlet temperatures of the solar collector, whereas Figure 4.28 shows the outlet temperatures.

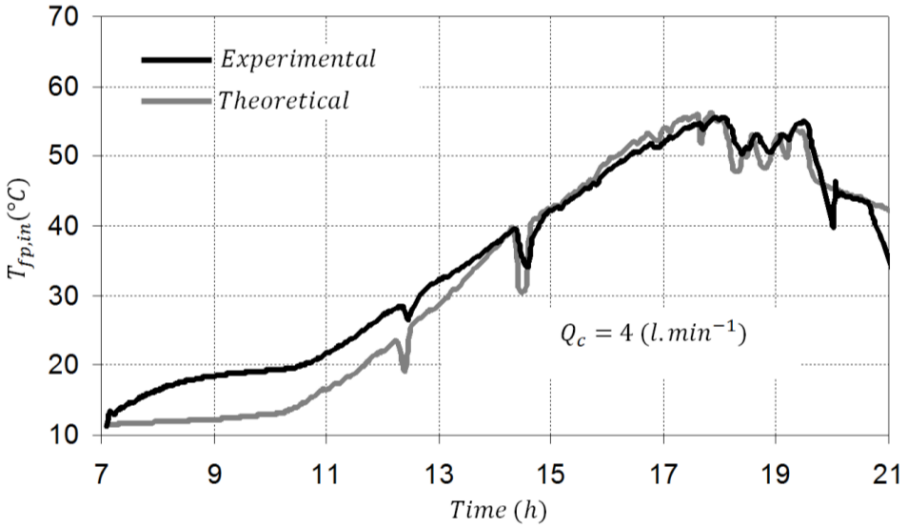

Figure 4.27. *Solar flat-panel inlet temperature during a day with mild disturbances*

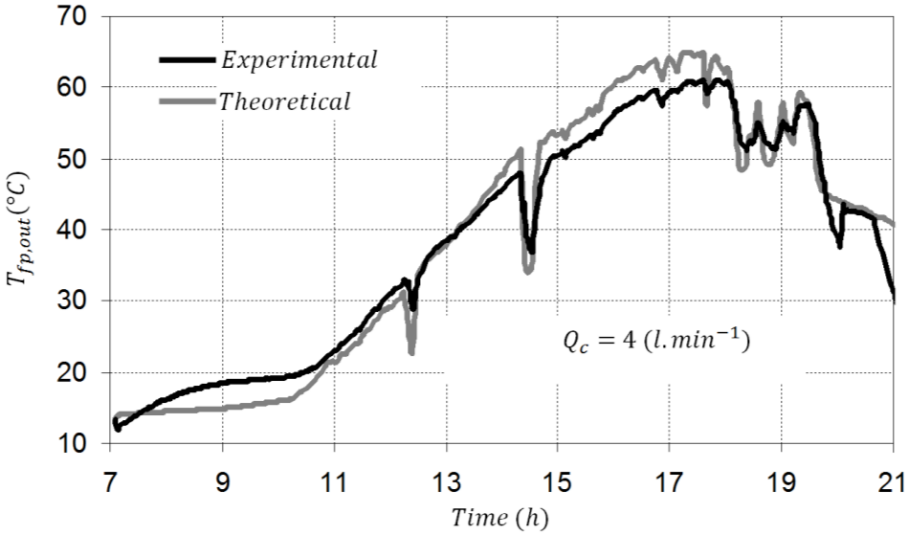

Figure 4.28. *Solar flat-panel outlet temperature during a day with mild disturbances*

These results also validate that the theoretical temperatures follow the same trend as the experimental temperatures.

Sudden fluctuations in solar radiation are evident in the temperature shifts of the calorific fluid at both the inlet and outlet of the solar collector. The theoretical temperature of the domestic hot water closely fits with the experimental measurements, exhibiting an average deviation of only 2%.

When examining the temperatures of the calorific fluid, there is a difference at the inlet of approximately 4% between the theoretical and experimental values, whereas at the outlet, this difference diminishes to approximately 1%.

4.4.2. *With consumption of domestic hot water*

During these experiments, intermittent withdrawals of hot water are systematically performed at various intervals throughout the day. These fluctuations in the hot water flow rate are incorporated into the simulation model to facilitate a comprehensive comparison with experimental observations.

This approach not only ensures model validity but also validates its performance under realistic operating conditions.

The graph in Figure 4.29 portrays the diurnal fluctuations in solar radiation intensity on a sunlit day.

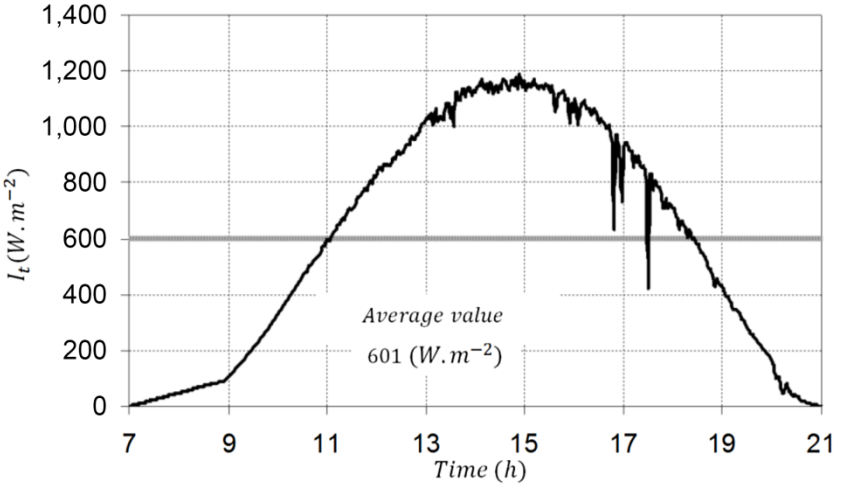

Figure 4.29. *Experimental solar radiation during a sunlit day*

The average solar flux value is estimated to be approximately 600 ($W.m^{-2}$), reflecting the typical radiation levels experienced during such conditions.

Figure 4.30 shows the water storage tank temperature evolution over time. These results are obtained with a water withdrawal profile from the tank, as shown in Figure 4.31. This profile includes three distinct withdrawal events initiated by the opening of the water tap.

The first withdrawal spanned from 10:00 a.m. to 11:00 a.m., followed by a second withdrawal occurring between 1:00 p.m. and 2:00 p.m. Lastly, the third withdrawal event occurred from 3:00 p.m. to 4:00 p.m.

The temperature of the water storage tank demonstrates a clear pattern of decline during each withdrawal event, reflecting the consumption of hot water. As water is drawn from the tank, the thermal energy stored within it is gradually depleted, causing the temperature to decrease. However, once the withdrawal ceases, the temperature of the tank begins to rise again, as the solar collector resumes its function of absorbing and transferring thermal energy into the system.

This process highlights the dynamic interaction between the energy demand and the solar heating system ability to replenish the stored thermal energy.

Both theoretical predictions and experimental observations reveal a high degree of alignment, with the average error remaining below 6%.

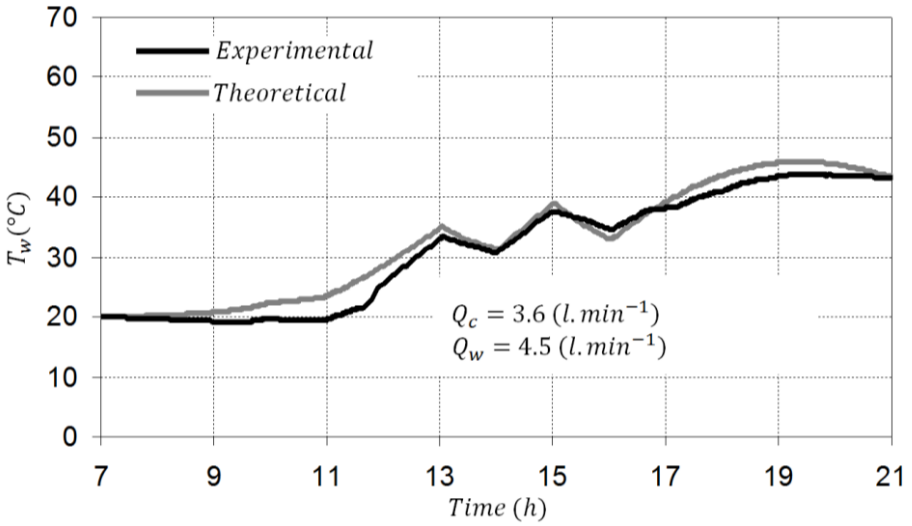

Figure 4.30. *Water storage temperature during a sunlit day with a water withdraw*

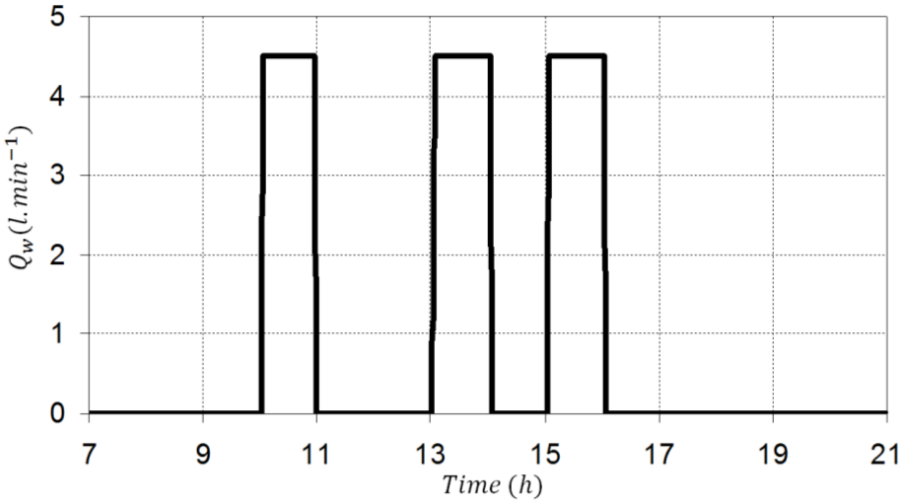

Figure 4.31. *Hot water flow rate profile*

This close agreement between theory and experiment suggests that the underlying mathematical models accurately reflect the behavior of the system, offering confidence in their predictive capability.

To provide a more comprehensive and detailed visual representation of the thermal dynamics at play, Figures 4.32 and 4.33 present the experimental and theoretical temperature profiles, respectively, measured at both the inlet and outlet of the solar collector during a typical withdrawal cycle. These figures serve as a critical comparison between the observed experimental data and the predictions made by the theoretical models.

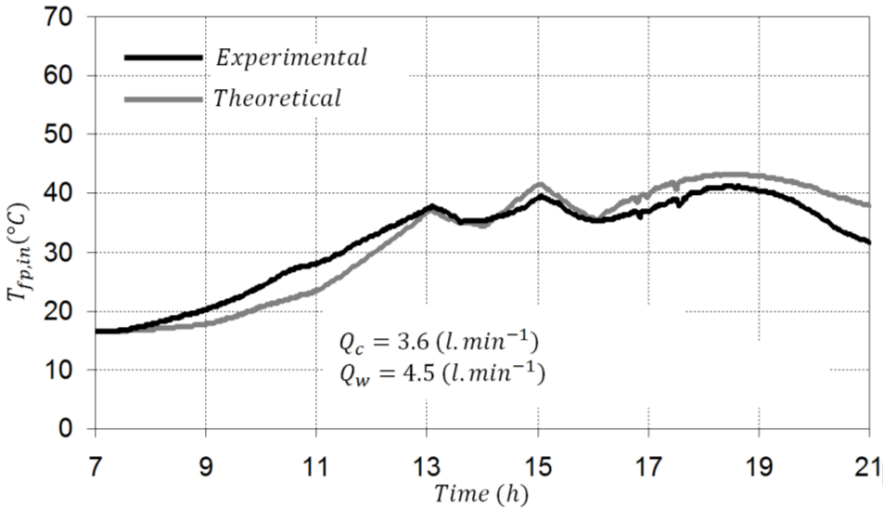

Figure 4.32. *Solar flat-panel inlet temperature during a sunlit day with a water withdraw*

Upon examination, there is a high degree of consistency between the experimental results and the theoretical predictions. The temperature variations at both the inlet and outlet correctly follow similar trends, which reinforces that the theoretical models are well aligned with the practical behavior of the system. This alignment indicates that the models effectively capture the underlying thermal processes, including heat transfer, fluid flow and energy storage, providing a reliable framework for describing system performance.

As discussed, one of the key aspects highlighted by these figures is the minimal discrepancy between the theoretical and experimental temperature profiles. The average error observed between the two datasets remains extremely low, with the deviation not exceeding 2%.

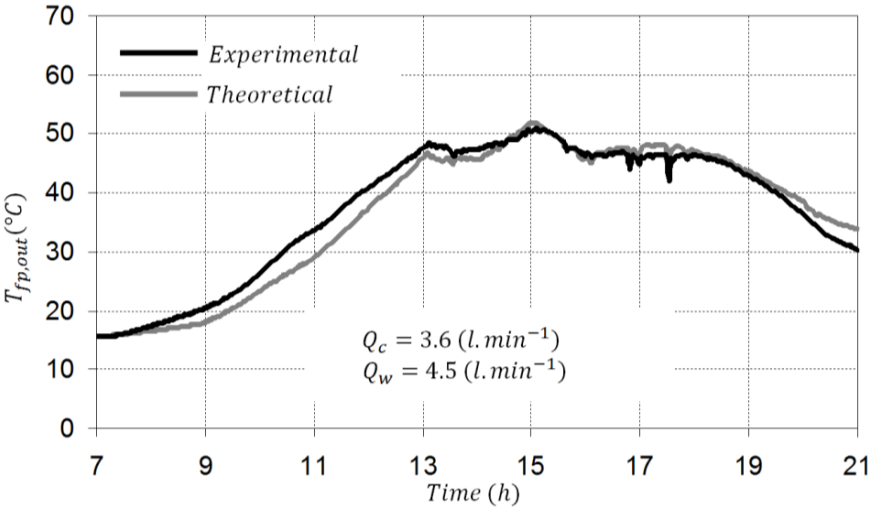

Figure 4.33. *Solar flat-panel outlet temperature during a sunlit day with a water withdraw*

This small error margin underscores the robustness and accuracy of the theoretical framework employed in this investigation. The close match between the experimental and predicted temperatures suggests that the model accurately reflects the practical thermal behavior of the solar collector under the conditions tested, further validating the assumptions and parameters used in the simulation.

4.5. Experimental results with the solar tracker

The efficiency of solar energy absorption relies significantly on the alignment of the receiving surface with the position of the Sun throughout the day. While optimal energy capture occurs when the receiver is facing the Sun directly, achieving this alignment is interesting because of the dynamic nature of solar movement. As a result, conventional solar panel installations often adopt fixed orientations, which are determined on the basis of average daily energy storage considerations. To address this limitation and enhance energy capture, solar trackers have emerged as a promising solution. These systems dynamically adjust the orientation of solar panels to track Sun movement, ensuring optimal alignment for energy absorption. Research indicates that solar trackers can significantly improve energy productivity, with studies reporting up to a 33% increase in energy capture compared with fixed installations (Huang et al. 2011). Moreover, advancements in Sun-tracking technology have led to a notable 22% increase in solar still productivity (Abdallah and Badran 2008). Solar trackers offer flexibility in their design, allowing

movement along either a single axis or a dual axis, depending on the desired level of precision and complexity (Kalogirou 1996; Khalifa and Al-Mutawalli 1998; Bakos 2006). These systems continuously optimize the panel orientation to maximize the energy yield, making them particularly beneficial in regions with varying sunlight intensities and angles throughout the day. Furthermore, studies have extensively compared different maximum power point tracking techniques for photovoltaic (PV) systems (Rezk and Eltamaly 2012), providing valuable insights into the most effective strategies for optimizing energy conversion and overall system performance.

Sun tracking systems are commonly categorized into passive and active trackers (Clifford and Eastwood 2004; Mousazadeh et al. 2009). Passive solar trackers utilize mechanisms such as aluminum/steel bimetallic strips and viscous dampers to adjust the panel orientation based on changes in temperature and sunlight intensity. The passive trackers can enhance efficiency by up to 23% compared to fixed solar panels (Clifford and Eastwood 2004). On the other hand, active trackers employ motorized mechanisms and control systems to adjust the panel orientation dynamically throughout the day. Various studies have explored the effectiveness of active trackers for solar PV cells (Abdallah and Nijmeh 2004; Canada et al. 2007). These systems utilize motors and sophisticated control algorithms to continuously optimize panel alignment for maximum energy capture. One of the advancements in active tracking technology is the development of self-powered solar trackers designed specifically for low-concentration PV systems. These trackers utilize onboard power generation mechanisms to operate autonomously, eliminating the need for external power sources and enhancing reliability. A notable example of such a system has been presented in the literature (Poulek et al. 2016). The previously mentioned literature primarily discusses solar trackers in the context of PV panels. Conversely, the emphasis of this chapter lies in investigating a solar thermal water heating system featuring a solar tracker. This system takes advantage of accurate calculations of solar location, as discussed in the section dedicated to solar positioning. The objective of the automatic solar tracker is to enable solar panels to dynamically adjust their orientation throughout the day, maintaining alignment with the Sun's position within a 2° range. To facilitate this investigation, enhancements were made to the experimental setup outlined in Khalfallaoui et al. (2011), incorporating equipment capable of continuously tracking the Sun's movement throughout the day. This solar tracker considers key factors such as the geographical position of the installation, including its altitude and latitude, along with the Sun's elevation. These parameters, presented previously and resulting from relationships proposed in the literature (Brichambaut and Vauge 1982; Bernard 2004; Duffie and Beckman 2013), are integrated into a control system. This system ensures that the solar panels remain optimally positioned to capture maximum solar energy throughout the day.

The intensity and duration of Sun radiation vary with the changing seasons, primarily influenced by the Sun's maximum height of the sky.

Figure 4.34 provides a depiction of how the Sun's elevation changes throughout the course of a day, contrasting the patterns observed in both winter and summer.

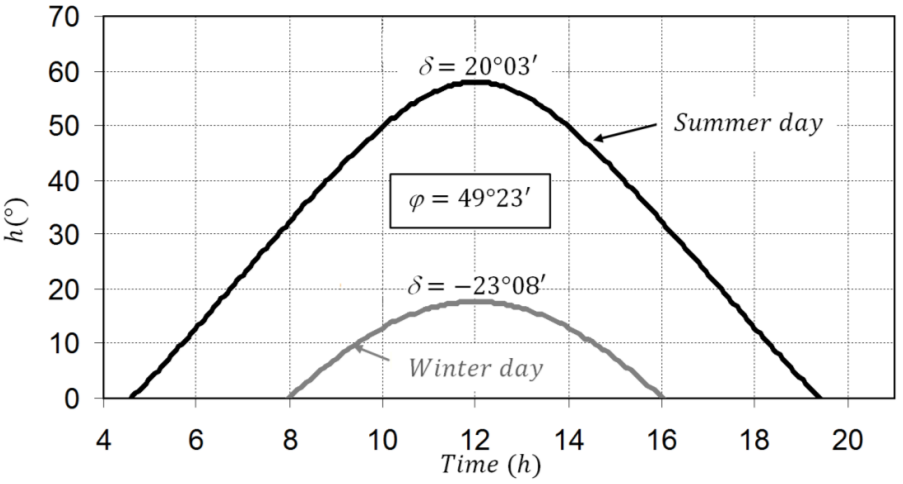

Figure 4.34. *Variation in the solar elevation angle over time on both winter and summer days*

The calculation of the solar height, which is key for considering solar exposure, is derived from equation [4.30], which factors in variables such as latitude and declination. This equation allows for the precise determination of the Sun's position in relation to the observer location on the Earth's surface.

From sunrise to sunset, the solar elevation gradually increases, reaching its zenith at solar noon before it decreases toward the horizon as evening approaches. Notably, the maximum Sun height varies significantly between seasons, with winter peak heights typically approximately 18° and summer heights increasing to approximately 60°.

Figure 4.35 offers an overview of the dynamic fluctuations in solar flux throughout a typical summer day, illustrating the effects of different solar panel inclination angles on energy capture. This figure provides a detailed analysis of how the angle of inclination influences the amount of solar energy received by the panel at various times of day.

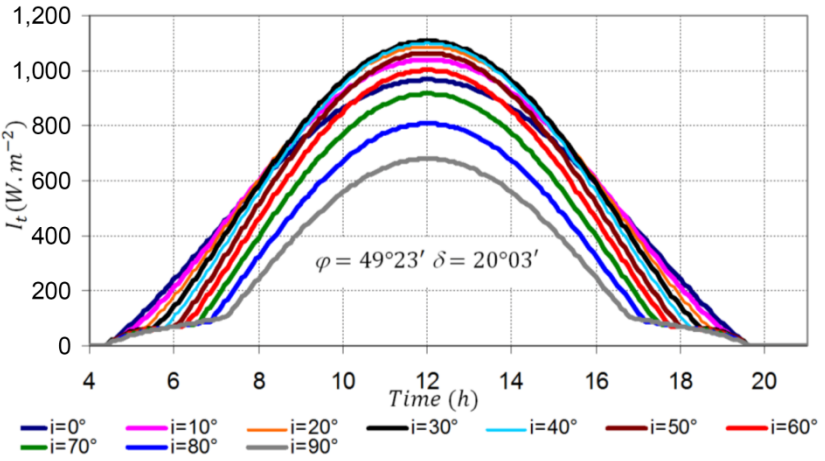

Figure 4.35. *Solar radiation at various inclinations of solar panel during a summer season day. For a color version of this figure, see www.iste.co.uk/abdelghani-idrissi/solarwaterheating.zip*

Similarly, Figure 4.36 presents an in-depth examination of solar flux variations over the course of a winter day, again emphasizing the impact of the inclination angle on energy absorption under different seasonal conditions.

Both figures are derived from the relationships outlined earlier in Table 4.1, which serve as the foundation for simulating the time-dependent behavior of solar radiation. Each profile in these figures captures the intricate relationship between solar flux and time, shedding light on the changing patterns of solar energy availability throughout the day. In the case of a summer day, the data reveal that the maximum solar flux occurs around midday, with values peaking at approximately 1,100 W/m² for inclination angles ranging from 30° to 40°. This peak illustrates the optimal conditions for solar energy capture during summer, where the angle of the panel maximizes its exposure to direct sunlight.

Furthermore, the temporal distribution of solar flux throughout the day underscores the dominance of diffuse radiation during the early and late hours. The onset of the day and the conclusion of daylight hours exhibit a notable increase in diffuse radiation, which is scattered and less direct than midday direct sunlight. This shift in radiation type throughout the day highlights the importance of not only considering the intensity of solar radiation but also accounting for its nature when designing and optimizing solar energy systems. Systems must be capable of efficiently capturing both direct and diffuse radiation to ensure optimal energy generation across various times of day.

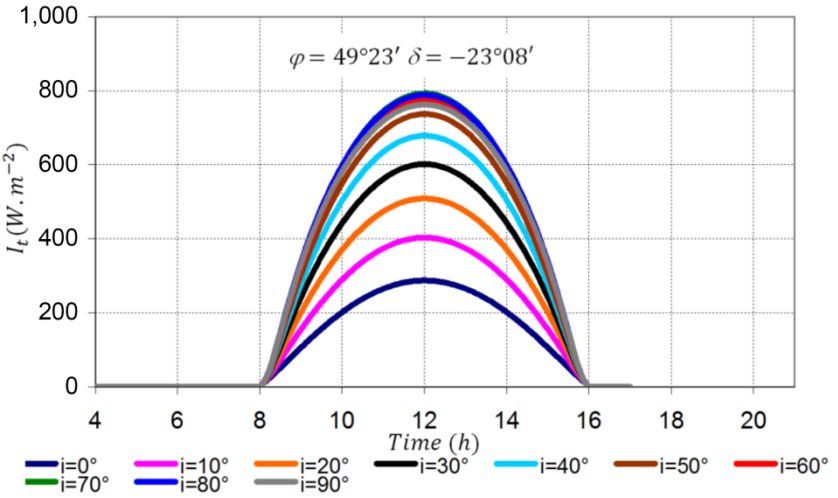

Figure 4.36. *Solar radiation at various inclinations of solar panel during a winter season day. For a color version of this figure, see www.iste.co.uk/abdelghani-idrissi/solarwaterheating.zip*

The profiles for winter exhibit distinct differences that reflect the seasonal variation in solar radiation patterns. In winter, the maximum solar flux typically occurs at inclination angles between 60° and 80°, with peak flux values reaching approximately 800 W/m². This clearly contrasts with the summer profiles, where the maximum flux is greater and the optimal inclination angles are lower.

This seasonal shift in peak flux values and the corresponding changes in the ideal angles of inclination underscore the significant variability in solar energy availability between the summer and winter months.

This highlights the need for adaptive strategies in the design and operation of solar energy systems, which can adjust for the differing conditions between seasons to maximize energy capture and utilization year-round.

By analyzing the radiation components presented in Figures 4.35 and 4.36, the simulation model based on the thermal convexity analysis, which was discussed earlier, generates the results depicted in Figure 4.37. This model accounts for the dynamic interaction of solar flux, system orientation and resulting thermal performance, providing a more complete picture of how these factors combine to influence overall system efficiency.

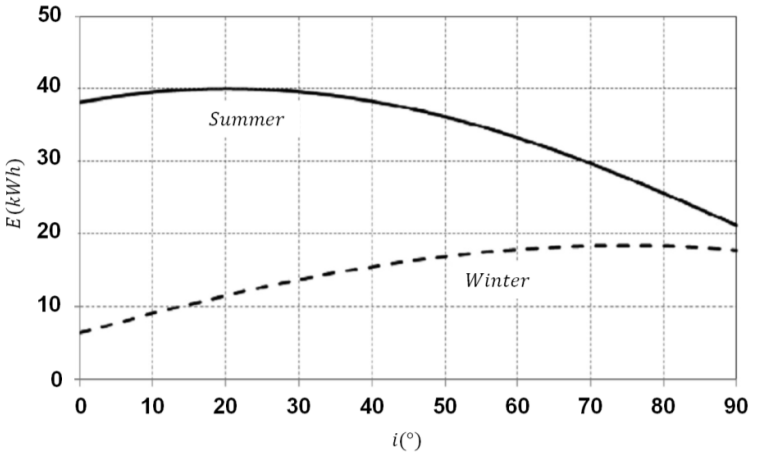

Figure 4.37. *Stored solar energy per day for different inclinations in both the winter and summer seasons*

This figure shows a comparative examination of the cumulative solar energy throughout a sunny day, encompassing both the winter (December) and summer (July) seasons. In particular, the presentation of the cumulative energy highlights visible trends depending on the orientation of the solar panels.

During the summer months, there is a discernible decrease in the daily cumulative energy as the inclination of the solar collector increases.

Conversely, in winter, there is a manifest rise in cumulative energy with increasing panel inclination. It is important to consider the influence of latitude on these observations.

The latitude plays a significant role in determining the solar elevation angle, thus impacting the amount of solar energy received at a particular location. Therefore, the trends observed in the cumulative solar energy profiles are relevant across different geographical locations worldwide.

Figures 4.38–4.40 provide a detailed comparative analysis between the experimental and theoretical variations in solar flux over time for a fixed solar panel set at different inclination angles of 35°, 45° and 65°, respectively.

These figures illustrate how the solar flux evolves throughout the course of the experiment and highlight the relationship between the theoretical predictions and measurements.

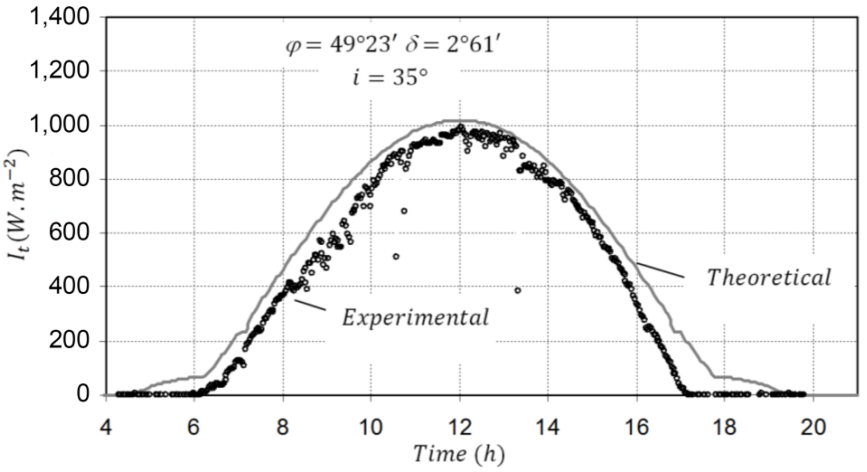

Figure 4.38. *Theoretical and experimental solar radiation for a fixed inclination angle of 35°*

The theoretical calculations of solar flux closely align with the observed trends in the experimental results, demonstrating agreement between the two sets of data.

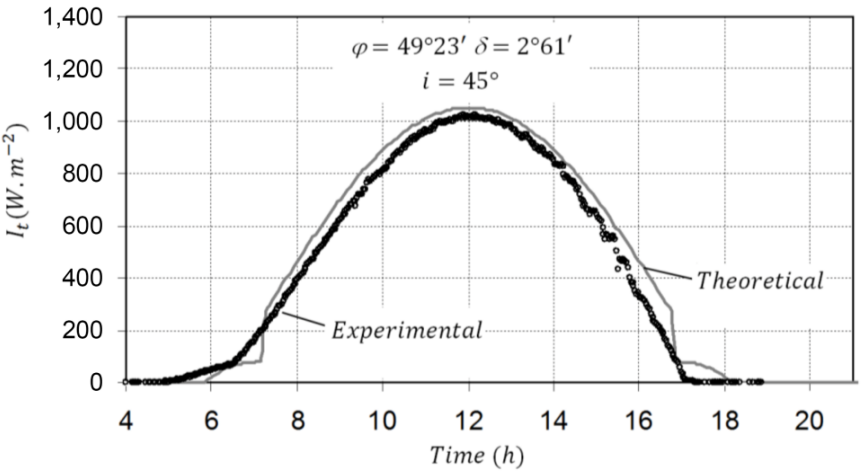

Figure 4.39. *Theoretical and experimental solar radiation for a fixed inclination angle of 45°*

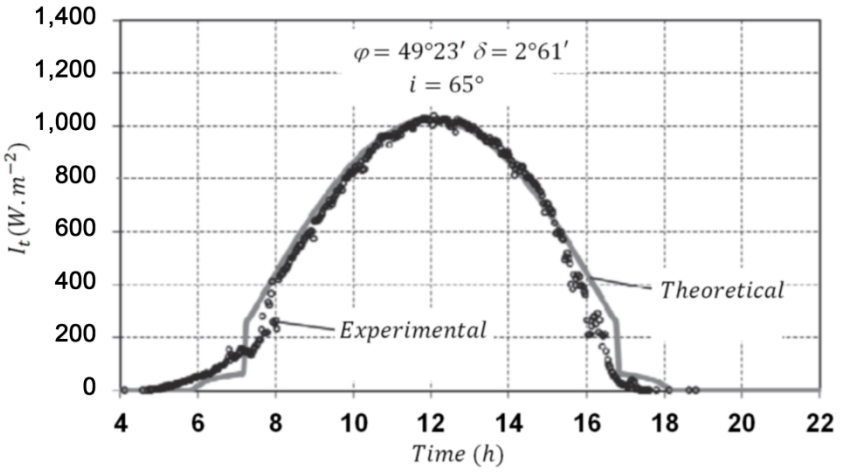

Figure 4.40. *Theoretical and experimental solar radiation for a fixed inclination angle of 65°*

The theoretical models, which are based on established principles of solar radiation, capture the overall patterns of flux variation over time, suggesting that the system performance can be accurately predicted using the given parameters.

This alignment between theory and experiment underscores the validity of the models used to predict solar flux behavior and provides valuable insight into the impact of panel inclination on the efficiency of solar energy absorption.

Figure 4.41 provides a theoretical representation of the solar flux with the aid of a solar tracker, which dynamically adjusts the orientation of the solar panel to maintain it perpendicular to the direct incident solar radiation. The solar flux composition is displayed, detailing the direct and diffuse fluxes derived from the established relationships reported in Table 4.1 and contributing to the total solar energy received by the solar panel.

Figure 4.42 presents a comparison between the theoretical flux, calculated based on the solar position and irradiance data, and the experimental flux, measured by the pyranometer positioned alongside the solar collector, providing an assessment of the tracker performance in aligning the panel optimally with the incident sunlight.

These curves demonstrate a close alignment between the theoretical predictions and experimental measurements. The focus lies on the solar tracker role in adjusting the inclination angle to optimize the alignment of the solar collector with the Sun's trajectory throughout the day.

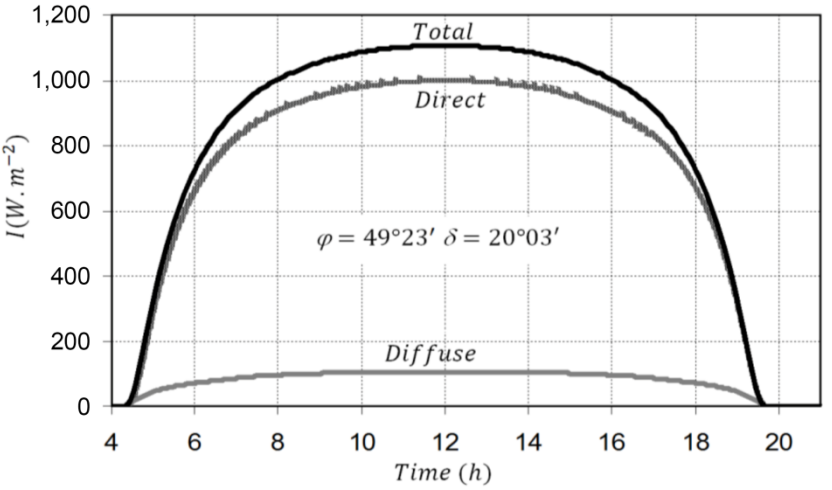

Figure 4.41. *Theoretical solar radiation with a solar tracker*

By maintaining the solar panel perpendicular to the incident Sun rays, maximum solar energy absorption is ensured. This necessitates a continual assessment of the inclination angle to accurately track Sun movement. The precise calculation of this angle is determined dynamically based on factors such as the Sun's position, the time of day and the geographical location. This iterative process, which is based on relations [4.30] and [4.31], ensures optimal solar panel positioning for efficient energy capture.

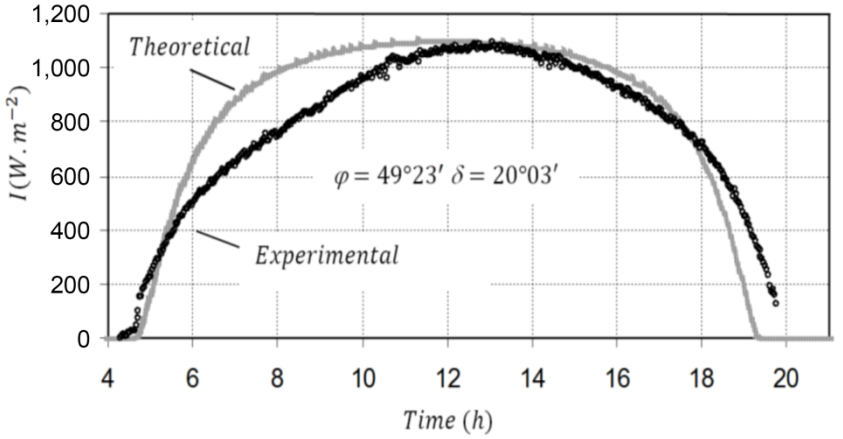

Figure 4.42. *Theoretical and experimental solar radiation with a solar tracker*

Figure 4.43 shows how both the inclination angle (i) and the solar elevation angle (h) evolve throughout the course of the day.

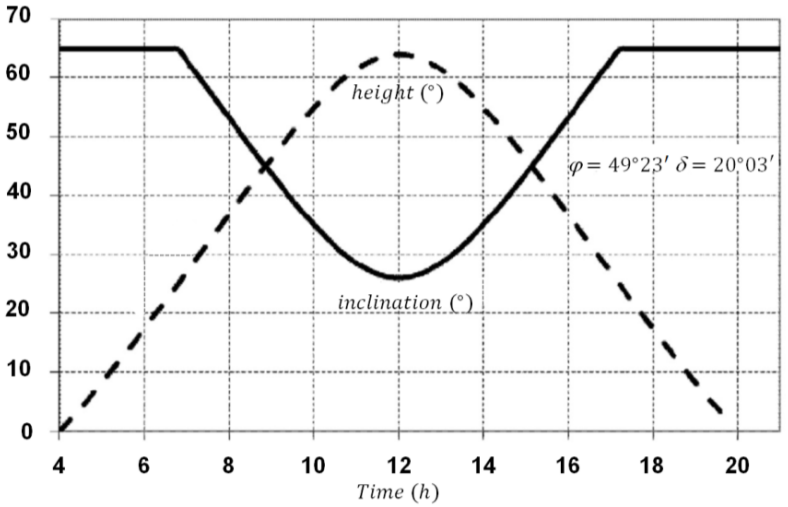

Figure 4.43. *Sun height and solar panel inclination during the day with a solar tracker*

The inclination angle has to respect the relation [4.31] in order to maintain the solar collector facing the Sun's rays in the normal position. The inclination angle is constrained between 5° and 65° because of mechanical considerations, and the inclination angle is continuously adjusted to optimize the solar panel orientation. Notably, angles greater than 65° correspond to sunrise and sunset times, which are characterized by moderate solar flux and are influenced mainly by diffuse radiation.

Figure 4.44 provides an overview of the cumulative solar energy obtained for various fixed inclinations, juxtaposed with the cumulative energy harnessed with the aid of a solar tracker. This comparison highlights the significant enhancement in solar energy utilization facilitated by the solar tracker across different fixed positions.

Furthermore, Figure 4.45 illustrates the quantitative increase in solar energy captured by the system when a solar tracker is employed, in contrast to the energy harvested by panels set at static inclinations. This figure highlights the remarkable performance of the solar tracker, which adjusts the panel position throughout the day to continuously face the Sun, maximizing energy absorption. Over the course of a full 24-hour operational cycle, the solar tracker clearly demonstrates its effectiveness in significantly enhancing the amount of solar energy that the solar panel is able to capture.

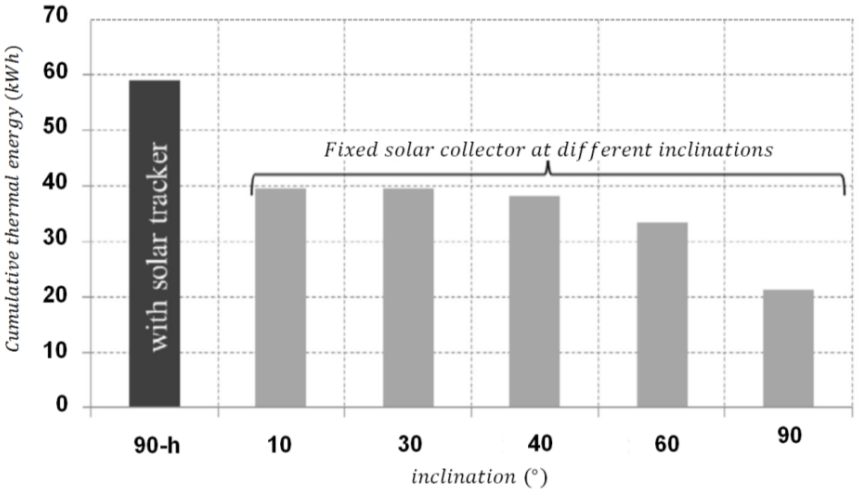

Figure 4.44. *Energy storage with a solar tracker compared with various fixed inclinations*

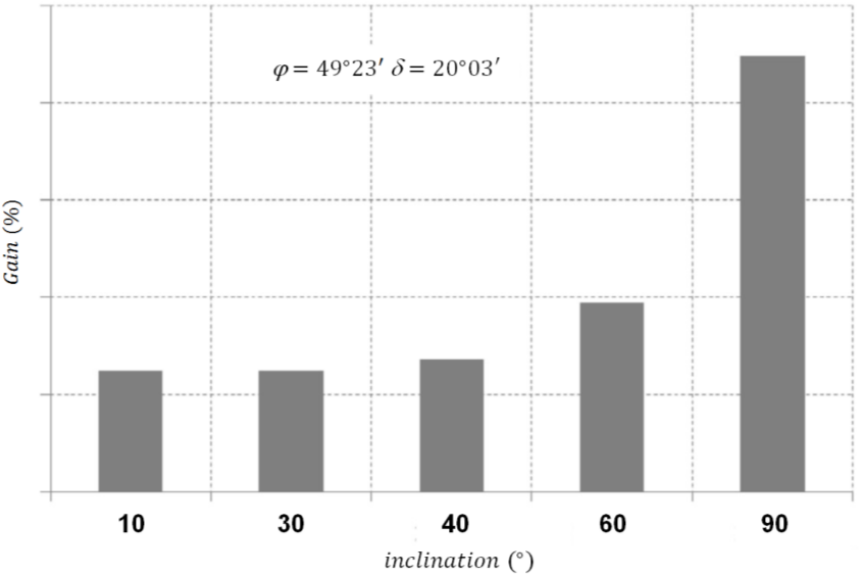

Figure 4.45. *Thermal energy gain with the solar tracker compared with different fixed inclinations*

Unlike fixed panels, which remain positioned at a predetermined angle throughout the day, the tracker ensures that the panel is optimally oriented at all times, allowing it to absorb more solar radiation. This dynamic positioning enables the system to capture substantially more energy, surpassing the energy absorption capabilities of static setups.

Most notably, when compared to the optimal fixed inclination, the angle that theoretically maximizes solar absorption at a particular geographic location, the solar tracker results in a remarkable increase in solar energy capture efficiency. Specifically, the tracker boosts energy capture by approximately 49.5%, resulting in a significant improvement in performance. This substantial gain underscores the potential of the tracker to enhance solar energy harvesting, making it a highly effective solution for maximizing the efficiency of solar energy systems.

Conclusion

This book has explored the principles and applications of solar thermal energy, focusing on the mechanisms of heat transfer and the optimization of solar water heating systems. Solar thermal energy, which harnesses the heat from the Sun through various technologies, plays a crucial role in the transition to sustainable energy solutions. Unlike solar photovoltaic (PV) systems, which convert sunlight directly into electricity, solar thermal systems use sunlight to generate heat. This heat can then be utilized for a wide range of applications, such as space heating, water heating and industrial processes, making it an essential component of renewable energy strategies.

The core principle of solar thermal energy lies in the collection and conversion of solar radiation into thermal energy through collectors. Solar collectors are designed to capture the Sun's heat and transfer it to a working fluid, typically a water or antifreeze solution, which is then circulated through the system to either store the heat or directly use it in heating applications. The efficiency of these collectors, and by extension the overall performance of solar thermal systems, is heavily influenced by factors such as the angle of incidence, the collector material properties, the flow rate of the fluid and the ambient environmental conditions.

Through an analysis of high- and low-temperature solar thermal systems, this book gives the critical differences in their design, application and performance. High-temperature solar thermal systems, often utilized in large-scale applications such as power plants, operate at temperatures significantly higher than their low-temperature counterparts, allowing them to produce heat capable of driving turbines or supplying industrial processes. These systems typically include concentrated solar power technologies such as parabolic troughs, tower plants and dish Stirling systems, which use mirrors or lenses to concentrate sunlight onto a small area, significantly increasing the intensity of solar radiation and thereby

raising the temperature of the working fluid to levels suitable for electricity generation.

Parabolic concentrators represent one of the most common forms of high-temperature solar thermal technology. These concentrators use parabolic mirrors to focus Sun radiation onto a receiver tube, which contains the working fluid. The concentrated sunlight heats the fluid, and the heat is then transferred to a power generation system or storage unit. The key advantage of parabolic concentrators lies in their ability to achieve relatively high temperatures (up to 400°C), making them suitable for generating electricity or providing high-temperature heat for industrial processes. However, their efficiency is heavily dependent on the accuracy of the tracking system used to maintain the optimal angle of sunlight incidence, and their performance can be affected by geographic location, weather patterns and seasonal changes.

Tower plants, another high-temperature solar technology, use a large field of mirrors (heliostats) to focus sunlight on a central receiver located atop a tower. These systems can reach even higher temperatures than parabolic concentrators, up to 1,000°C or more, making them particularly effective for generating superheated steam to drive turbines in electricity generation. A significant advantage of tower plants is their ability to store thermal energy for use during periods of cloud cover or at night, enhancing their overall efficiency and reliability. However, tower plants are complex, require precise alignment and maintenance of the heliostats and are most effective in areas with high direct solar radiation.

Cylindrical-parabolic collectors, a third form of high-temperature solar collector, combine the features of parabolic concentrators with a cylindrical design. These systems use curved mirrors to focus sunlight onto a receiver tube that runs along the focal line of the parabola. Cylindrical-parabolic collectors are typically used in applications requiring medium to high temperatures, such as industrial process heating and desalination. They offer a balance between the high temperatures achievable with tower plants and the simplicity and lower cost of parabolic concentrators. These collectors can be scaled up for large systems or adapted for smaller, decentralized applications, providing flexibility in both commercial and residential solar thermal systems.

In addition to high-temperature systems, this study has also examined the significance of low-temperature solar thermal systems, which are widely used for residential and commercial applications. These systems operate at lower temperatures (usually below 100°C) and are primarily employed for water heating and space heating. Low-temperature solar thermal systems are highly effective in

regions with moderate to high levels of solar radiation and have become increasingly popular for domestic water heating, pool heating and space heating in both new and existing buildings. These systems offer a practical and cost-effective solution to reduce energy consumption and reliance on fossil fuels for heating purposes.

A key component of low-temperature systems is the solar water heater, which is typically composed of flat-plate or evacuated tube collectors. Flat-plate collectors are the most commonly used technology for domestic water heating. These collectors consist of a dark absorber plate, which absorbs sunlight, and a transparent cover that minimizes heat loss while allowing sunlight to pass through. The absorbed heat is transferred to a fluid circulating through pipes attached to the absorber plate. While flat-plate collectors are generally less efficient in colder climates or in areas with low solar radiation, they are durable, cost effective and easy to install.

Evacuated tube collectors represent a more advanced form of solar water heater, offering better performance in colder climates. These collectors consist of glass tubes with a vacuum inside, which acts as an insulator, reducing heat loss. The evacuated tube design allows for better heat retention and greater efficiency in low-light or cloudy conditions. These systems are more expensive than flat-plate collectors but are well-suited for high-performance applications where greater efficiency is required.

The choice of solar collector technology plays a significant role in the efficiency and practical implementation of solar thermal systems. Factors such as climate, installation costs, available space and energy needs all influence the selection of the appropriate technology.

High-temperature systems, while more complex and expensive, offer substantial benefits in large-scale applications and power generation, whereas low-temperature systems provide an efficient and affordable solution for residential and commercial heating applications.

Moreover, optimizing solar thermal systems is not limited to the selection of the right collector technology but also involves improving system components such as heat exchangers, storage tanks and controllers. The efficiency of heat transfer between the solar collector and the fluid, the ability to store thermal energy for later use, and the control of fluid flow rates all contribute to the overall performance of the system. Advanced technologies such as solar trackers, which keep the collectors oriented toward the Sun throughout the day, can further enhance the efficiency of solar thermal systems, ensuring that the maximum amount of solar radiation is captured.

The thermal convexity principle introduces a novel approach to understanding how heat transfer operates within various fluid systems. It focuses on how temperature gradients behave and evolve, particularly in complex environments where fluids interact with each other or with isothermal surfaces. This principle offers a more detailed picture of how heat flows through a system, especially when dealing with nonlinear temperature profiles.

The thermal convexity principle brings into focus the convexity of temperature profiles, essentially how the temperature changes within the system, especially where heat exchange between fluids and surfaces occurs. This principle has been particularly transformative in understanding single-phase fluid mixing and the interactions of fluids with isothermal surfaces, which are crucial to the effective functioning of solar thermal systems, particularly return fluid mixing helps control of temperatures in thermal systems. The outlet temperature is given in a convex form $T_{out} = \gamma\, T_{in} + (1-\gamma)T_{in}$, where γ is the thermal convexity coefficient. The outlet temperature varies based on the flow rates through a nonlinear function, while its variation is linear according to the inlet temperatures. The outlet temperature is convex with respect to the inlet temperatures provided that the thermal convexity coefficient is bounded between 0 and 1.

This property is also generalized in many thermal systems. An isothermal surface is one that maintains a constant temperature, often used in the context of heat exchangers or solar collectors. These surfaces play a crucial role in the efficiency of solar water heating systems, as they are where heat is transferred between the solar-heated fluid and the domestic water supply. When a fluid flows over or interacts with an isothermal surface, the temperature distribution within the fluid also exhibits a convex behavior as well. The temperature of the fluid near the surface will rise due to heat transfer, while the bulk fluid, farther from the surface, may remain cooler.

Particularly, in solar water heating systems, the heat from the hot fluid circulating through the solar collector is transferred to the cold domestic water supplied to the system, typically through heat exchangers or directly to storage tanks. The thermal convexity principle allows for a better understanding of how this heat exchange happens, especially under conditions of varying flow rates and temperatures.

When applied to solar water heating systems, the thermal convexity principle provides a more precise and nuanced way of modeling heat transfer and understanding system performance. Solar water heating systems are made up of several interconnected components, such as solar collectors, heat exchangers and

storage tanks, where the thermal convexity principle can be applied to each component to enhance performance.

Solar collectors are designed to absorb sunlight and convert it into heat. The interaction of the solar collector with the working fluid is where the principle of thermal convexity becomes particularly relevant.

As the solar radiation heats the fluid, the temperature profile along the collector surface is often not linear according to the flow rate of heat transfer fluid (HTF). The thermal convexity principle helps model this nonlinear dependence of temperature on flow rates.

Heat exchangers are integral to solar water heating systems, as they transfer heat from the solar-heated fluid to the domestic water supply. The application of the thermal convexity principle helps in understanding the interactions between the hot fluid from the solar collector and the cold domestic water.

In a solar water heating system, hot water is typically stored in a storage tank until it is needed for domestic use. The behavior of the water within the tank is subject to the thermal convexity principle as well.

The application of the thermal convexity principle to the different components of the solar water heating systems has significantly improved the ability to model and predict the behavior of these systems. By considering a systemic representation, the nonlinear temperature profiles and convex behavior of heat transfer, efficient models of solar thermal systems were established.

The positioning of the Sun in the sky at different times of the day and year plays a crucial role in determining the amount of solar energy a system can capture. By analyzing solar position such as the solar azimuth and altitude angles, we can accurately model how the Sun's radiations interact with a solar collector. These angles change depending on geographic location, the time of day and the season. Solar radiation varies throughout the day and across seasons. It is influenced by several atmospheric conditions, such as cloud cover, humidity and air pollution.

Refining the modeling of solar energy capture involves calculating how much of this solar radiation is incident on the solar collectors, and it accounts for variables such as tilt angle, orientation and shading effects. Accurate modeling must consider all of these factors in order to predict the system's efficiency in real-world conditions. Solar energy models often integrate complex algorithms that calculate radiation patterns, intensity and the solar position at any given time, providing a more realistic representation of how a solar system will perform throughout the year.

In the process of refining solar energy systems, simulations play a vital role. By creating numerical models of solar collectors and their environmental interactions, the behavior under a range of conditions without needing to test every possible scenario was investigated. To validate the simulation results, experimental tests are carried out under controlled conditions. These tests could include tracking solar radiation levels, fluid flow rates and system efficiency under varied practical scenarios. The experimental setup may include physical prototypes of solar collectors or models that predict the full-scale systems, allowing for direct measurement of key parameters like temperature variation, collector output and energy storage.

Through these experiments, factors like solar radiation variation, fluid flow rates and domestic hot water consumption affect the efficiency of a system. The amount of energy received from the Sun varies throughout the day and with weather conditions. A more refined model can simulate how these fluctuations impact the thermal energy captured by the system.

The efficiency of heat transfer within solar thermal systems depends significantly on the flow rate of the HTF. If the flow rate is too low, heat transfer efficiency can be reduced. Conversely, too high a flow rate may also affect efficiency by increasing pump energy consumption.

Domestic hot water consumption ties into the load demand side of the system. Hot water consumption varies by hour, day and season, and these fluctuations affect the overall performance of solar systems. Accurate modeling can help ensure that the system can meet peak demand while also taking advantage of off-peak periods when solar radiation is higher.

A significant component of solar energy systems is how the solar collectors are oriented relative to the Sun. Fixed solar collectors are mounted at a fixed angle and orientation, typically optimized for the average solar radiation over the course of a year. While these systems are simple and low maintenance, they may not capture the maximum possible energy, as they cannot adjust to the changing position of the Sun throughout the day.

In contrast, solar tracking systems are designed to follow the Sun’s movement across the sky, ensuring that the collector surface is always oriented to receive maximum direct Sun radiation. These systems typically use motors and sensors to adjust the angle of the collectors, either in one axis (horizontal or vertical) or two axes. While solar tracking systems are more efficient at capturing solar radiation (sometimes up to 40% more energy), they come with higher initial costs, increased complexity and higher maintenance requirements due to the moving parts involved.

Overall, this book presents a contribution to the advancement of solar thermal technology by integrating theoretical principles with practical evaluations. Future research could explore advanced heat exchanger designs, novel materials for improved solar absorption and hybrid systems that combine solar thermal and PV technologies. As the demand for sustainable energy solutions continues to grow, further optimization of solar thermal systems will play a crucial role in the transition to renewable energy sources.

Appendix

Principles of Heat Transfer

The thermal analysis of solar systems is mainly based on heat transfer principles. In this appendix, a recall of these principles is useful for the development of investigation of solar systems.

Heat transfer is a fundamental phenomenon in thermal engineering science, involved in many natural and technological processes. This involves the transmission of thermal energy between different systems or within the same system in response to a temperature gradient. Heat is intrinsically driven by the gradient, moving naturally from areas of higher temperature to those of lower temperature in a continuous effort to reach thermal equilibrium. This process, while seemingly simple, is governed by complex interactions between thermodynamic principles and fluid dynamics, requiring a nuanced understanding of both to fully grasp its behavior.

To master the intricacies of heat transfer, we must bridge the foundational concepts of thermodynamics such as energy conservation and the laws governing entropy with the dynamics of fluid flow, which dictates how heat is carried within gases and liquids. Heat transfer itself, however, is a distinct discipline with its own specialized terminology, methodologies and governing principles, which differ from those of basic thermodynamics or fluid mechanics. It encompasses three primary modes of transfer: conduction, convection and radiation, each with unique mechanisms and mathematical descriptions.

In this section, the core concepts of heat transfer are presented by their fundamental principles along with detailed mathematical representations that describe how heat moves in different systems. The focus will also include typical applications, particularly solar thermal systems. Understanding this interplay between theory and application also helps the development of tools to analyze, predict and optimize thermal systems across a wide range of industries.

In the domain of heat transfer, only conduction and radiation are driven purely by temperature differences, making them true forms of heat transfer in the strictest sense. In contrast, convection involves the transport of heat via the movement of a fluid or gas, thus relying not only on temperature gradients but also on the physical motion of matter. Despite this distinction, the term "heat transfer by convection" has become widely accepted because of its undeniable role in conveying energy from regions of higher temperature to those of lower temperature.

The fundamental equations governing each of these three heat transfer mechanisms decrease. The primary objective is to develop a broad understanding of the field without delving too deeply into complex scenarios, thus focusing on simpler cases for clarity. Importantly, however, in most real situations, heat is rarely transferred by a single mechanism. Rather, multiple modes of heat transfer typically act in concert, often in complex and interdependent ways.

The integration of the basic equations for simultaneous heat transfer mechanisms, such as conduction, convection and radiation corresponds to the general configuration when these mechanisms work together in a given system, particularly in solar heating systems.

A.1. Heat conduction

Whenever a temperature gradient exists within a solid medium, heat will inherently flow from the region of higher temperature to the region of lower temperature, as part of the natural drive toward thermal equilibrium. This transfer of energy, known as heat conduction, occurs at a rate that is governed by fundamental physical principles.

The rate at which heat is transferred by conduction, denoted as ϕ_c, is proportional to the temperature gradient, essentially the difference in temperature between two points per unit distance, multiplied by the area A through which the heat flows. This relationship reflects the intuitive idea that a steeper temperature gradient leads to a faster rate of heat transfer and that a larger surface area facilitates greater energy flow.

Mathematically, this is expressed by the Fourier law of heat conduction:

$$\phi_c = -k\,A\,\frac{dT}{\mathrm{dx}} \qquad [A.1]$$

where:

– k is the thermal conductivity of the material;

– A is the cross-sectional area through which the heat flows;

– $\frac{dT}{\mathrm{dx}}$ is the monodirectional temperature gradient, which is the rate of change in temperature with respect to distance.

The negative sign is a consequence of the second law of thermodynamics, which requires that heat must flow in the direction from higher to lower temperatures.

This equation highlights several key factors in heat conduction: materials with high thermal conductivity, such as metals, will transfer heat more rapidly, whereas insulating materials with low conductivity will slow down the process. Similarly, the larger the surface area available for heat flow, the greater the energy transferred per unit time.

Understanding this relationship allows the design of systems that either maximize or minimize heat transfer, depending on the application, to improve the thermal efficiency of heating systems or reduce energy loss through insulation in buildings. This interplay between temperature gradients, material properties and geometry forms the foundation of thermal analysis in a wide range of thermal science engineering.

When the general distribution of temperature toward a three-dimensional body is considered, the temperature gradient can be expressed according to the three Cartesian coordinate vectors $(\vec{\imath}, \vec{\jmath}, \vec{k})$ as:

$$\vec{\nabla}\, T = \vec{\imath}\, \frac{\partial T}{\partial x} + \vec{\jmath}\, \frac{\partial T}{\partial y} + \vec{k}\, \frac{\partial T}{\partial z} \qquad [A.2]$$

The temperature gradient represents both the maximum variation in magnitude and its direction. The Fourier law expresses the surface thermal conductive transfer through an elementary area dA:

$$\overrightarrow{\varphi_c} = -k\, \vec{\nabla}\, T \qquad [A.3]$$

where the nabla operator $\vec{\nabla}$ is defined as:

$$\vec{\nabla} = \vec{\imath}\, \frac{\partial}{\partial x} + \vec{\jmath}\, \frac{\partial}{\partial y} + \vec{k}\, \frac{\partial}{\partial z} \qquad [A.4]$$

The temperature gradient at each point is perpendicular to the isotherm line passing through that point. The streamlines are also perpendicular to the isotherm lines.

The orders of magnitude of the thermal conductivity of various types of materials are presented in Table A.1.

Material	Thermal conductivity at 300 K
Copper	399
Aluminum	237
Carbon steel, 1% C	43
Glass	0.81
Plastics	0.2–0.3
Water	0.6
Ethylene glycol	0.26
Engine oil	0.15
Freon (liquid)	0.07
Hydrogen	0.18
Air	0.026

Table A.1. *Thermal conductivities of some materials*

Although, in general, the thermal conductivity varies with temperature, but in many application problems, the variation is sufficiently small to be neglected.

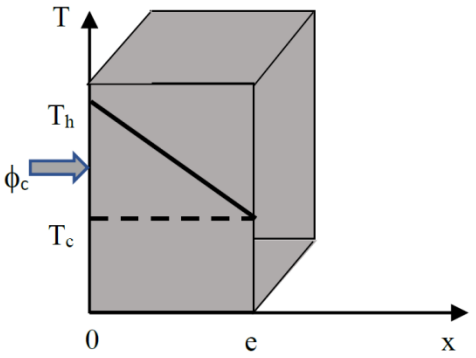

Figure A.1. *Temperature distribution for steady-state conduction through a plane wall*

For most calculations, the values of thermal conductivity rely on experimental assessment. While the kinetic theory of gases can accurately predict these values for gases at moderate temperatures, the situation is more complex for liquids and solids.

Although various theories have been proposed to estimate the thermal conductivities of these materials, they generally fall short in providing predictions with satisfactory accuracy.

Figure A.1 shows a simple plane wall, with a thickness e and a maintained hot temperature of one side T_h while the other side is maintained at cold temperature T_c.

According to the Fourier law, the temperature in the thickness of the plane wall is obtained by integration:

$$T(x) = -\phi_c \frac{1}{k\,A}\, x + T_h \qquad [A.5]$$

The difference in temperature between the wall sides is given as follows:

$$\Delta T = (T_h - T_c) = \frac{e}{k\,A}\,\phi_c \qquad [A.6]$$

In this formulation, the difference between the hot temperature T_h and the cold temperature T_c is the driving potential that causes the flow of heat.

The term $\frac{e}{k\,A}$ is equivalent to the thermal resistance R_k that the wall resists to the conductive heat flow:

$$\Delta T = R_k\ \phi_c \qquad [A.7]$$

This expression shows the link between the thermal potential and the thermal current, which illustrates the analogy between heat flow systems and electric circuits. This analogy is a convenient tool, especially for visualizing more complex situations, for analyzing solar heating systems.

The thermal conductivity varies as a function of the temperature and can be approximated for many materials as a linear function over limited temperature ranges:

$$k = k_0(1 + \beta_k\ T) \qquad [A.8]$$

where β_k, a characteristic of the medium, is an empirical constant and k_0 is the conductivity value at a reference temperature. In such a case, the thermal flux can be written as:

$$\phi_c = \frac{k_0\,A}{e}\left((T_h - T_c) + \frac{1}{2}\beta_k\left({T_h}^2 - {T_c}^2\right)\right) \qquad [A.9]$$

$$\phi_c = \frac{k_0\, A}{e}\,(T_h - T_c)\left(1 + \frac{1}{2}\beta_k(T_h + T_c)\right) \quad [A.10]$$

$$\phi_c = \frac{\bar{k}\, A}{e}\,\Delta T \quad [A.11]$$

where $\bar{k}$ corresponds to the thermal conductivity value of the average temperature $\frac{(T_h+T_c)}{2}$.

Figure A.2 shows the temperature profile according to the sign of β_k. Indeed, the thermal conductivity can increase or decrease with temperature depending on the material nature.

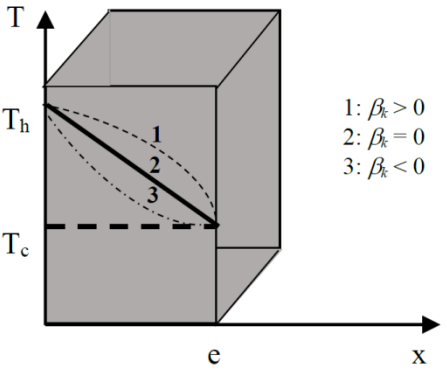

Figure A.2. *Temperature distribution in conduction through a plane wall with constant and variable thermal conductivity*

Figure A.3 shows the thermal conductivity variation according to the temperature for some gases and fluids (ASHRAE 2005).

The conductive heat transfer equation in the unsteady state can be obtained from the Fourier law. The balance of energy flux exchanged by a volume reflects the fact that the conductive flux entering through the surface has solely served to heat or cool the mass of solid contained within the volume. The internal volumetric heat source can also be considered in order to be more thorough. The mathematical integration by the surface for the conductive flux, extended to the volume according to the Ostrogradski theorem, leads to the conductive heat equation with an internal volumetric energy source:

$$\nabla^2 \mathrm{T} + \frac{1}{k}\,\dot{q}_v = \frac{1}{\alpha}\,\frac{\partial T}{\partial t} \quad [A.12]$$

where $\dot{q}_v$ is the volumetric internal heat source and where α is the thermal diffusivity, a group of material properties defined as:

$$\alpha = \frac{\rho\, C_p}{k} \qquad [A.13]$$

In this formulation, ρ is the density and C_p is the specific heat. The symbol ∇^2 represents the Laplace operator, which corresponds to the scalar product of the nabla vector $(\vec{\nabla}.\vec{\nabla})$.

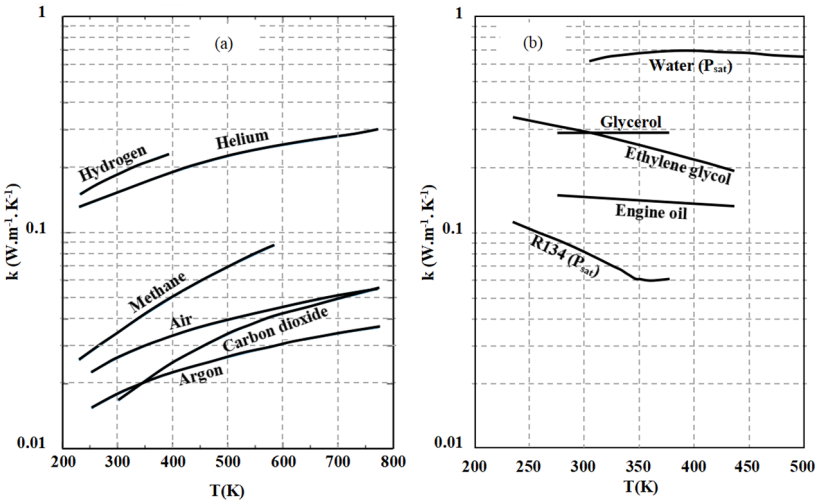

Figure A.3. *Thermal conductivity variation according to the temperature of typical fluids and gases: (a) gases and (b) liquids*

The conductive heat equation can be subjected to many boundary conditions:

– isothermal exchange through a surface;

– constant thermal flux at the frontier;

– convective exchange;

– radiative exchange;

– frontier between two different solids.

These boundary conditions can be used in the analysis of solar thermal systems.

In many scientific applications, the geometrical configuration of a system can vary significantly depending on the specific use case. Therefore, it is essential to recall the conductive heat transfer equation in different coordinate systems, as these variations in geometry can greatly influence the behavior of heat conduction and the choice of appropriate mathematical models.

A.1.1. *Cartesian coordinates*

As described in the previous section, the conductive heat transfer equation in Cartesian coordinates is given as:

$$\frac{\partial^2 T}{\partial x^2}+\frac{\partial^2 T}{\partial y^2}+\frac{\partial^2 T}{\partial z^2}+\frac{1}{k}\,\dot{q}_v=\frac{1}{\alpha}\,\frac{\partial T}{\partial t} \qquad [A.14]$$

Figure A.4 shows the differential control volume for three-dimensional conduction in rectangular coordinates.

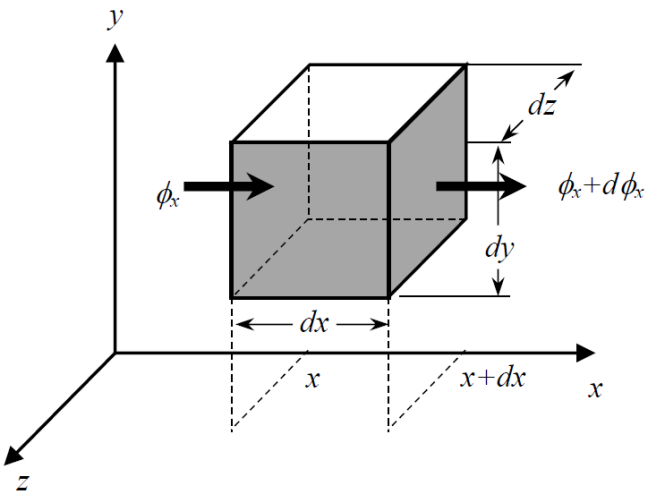

Figure A.4. *Differential control volume for three-dimensional conduction in rectangular coordinates*

The conduction heat equation solutions can be obtained by numerical methods with specified and realistic boundary conditions.

The conduction heat equation is also given with the nabla operator:

$$\nabla^2 T + \frac{1}{k}\,\dot{q}_v = \frac{1}{\alpha}\,\frac{\partial T}{\partial t} \qquad [A.15]$$

In the steady state with no internal generated heat, the conduction equation further simplifies to:

$$\nabla^2 T = 0 \qquad [A.16]$$

This equation is known as the Laplace equation.

The conduction heat equation can also be expressed with regard to the conductive heat flux in three dimensions:

$$\frac{\partial}{\partial x}\left(k\frac{\partial T}{\partial x}\right) + \frac{\partial}{\partial y}\left(k\frac{\partial T}{\partial y}\right) + \frac{\partial}{\partial z}\left(k\frac{\partial T}{\partial z}\right) + \dot{q}_v = \frac{k}{\alpha}\,\frac{\partial T}{\partial t} \qquad [A.17]$$

The components of the surface heat flow rates by conduction are defined as:

$$\begin{cases} \varphi_x = \dfrac{d\phi_x}{dA_x} = \left(-k\dfrac{\partial T}{\partial x}\right) \\ \varphi_y = \dfrac{d\phi_y}{dA_y} = \left(-k\dfrac{\partial T}{\partial y}\right) \\ \varphi_z = \dfrac{d\phi_z}{dA_z} = \left(-k\dfrac{\partial T}{\partial z}\right) \end{cases} \qquad [A.18]$$

where the elementary control surfaces are defined as:

$$\begin{cases} dA_x = dy\,dz \\ dA_y = dx\,dz \\ dA_z = dx\,dy \end{cases} \qquad [A.19]$$

A plate panel with generation of internal heat is considered, as illustrated in Figure A.5.

Here, e denotes its thickness and A corresponds to its lateral area. In this example, a mono-dimensional case is discussed in the steady state where the temperature does not vary in time. The conductive heat transfer equation becomes:

$$\frac{d}{dz}\left(k\frac{dT}{dz}\right) + \dot{q}_v = 0 \qquad [A.20]$$

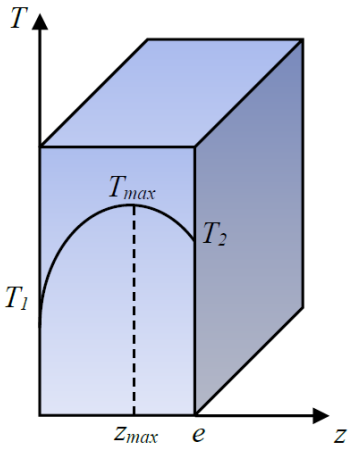

Figure A.5. *Temperature distribution of a panel subjected to uniform volumetric heat generation*

By solving the heat transfer equation, the temperature distribution along the thickness is given as:

$$T(z) = -\frac{\dot{q}_v}{2\,k} z^2 + \left[\frac{(T_2 - T_1)}{e} + \frac{\dot{q}_v}{2\,k}\, e\right] z + T_1 \qquad \text{[A.21]}$$

The temperatures T_1 and T_2 depend on the environment conditions of the external areas of the panel, which define the boundary conditions.

The temperature distribution can be expressed in dimensionless form as:

$$T^*(z^*) = \frac{T(z) - T_1}{T_2 - T_1} = -\frac{1}{2}\beta\, z^{*2} + \left(1 + \frac{1}{2}\beta\right) z^* \qquad \text{[A.22]}$$

where β represents the ratio of the internal power to the conductive thermal energy rate with no internal energy generation:

$$\beta = \frac{\dot{q}_v\, V}{\frac{k\,A}{e}\,(T_2 - T_1)} \qquad \text{[A.23]}$$

z* is the dimensionless position along the thickness of the panel:

$$z^* = \frac{z}{e} \qquad \text{[A.24]}$$

The temperature reaches its maximum when the conductive heat flux becomes zero $\left(\frac{dT}{dz} = 0\right)$. The location of the maximum temperature is given as:

$$z_{max} = \frac{k}{\dot{q}_v\, e}(T_2 - T_1) + \frac{1}{2}\, e \qquad [A.25]$$

The maximum temperature is given as:

$$T_{max} = \frac{1}{2}\frac{\dot{q}_v}{k}\left[\frac{k}{\dot{q}_v}\frac{(T_2 - T_1)}{e} + \frac{1}{2}e\right]^2 + T_1 \qquad [A.26]$$

Figure A.6 shows the dimensionless temperature distribution as a function of the panel thickness depth for different values of β. The maximum temperature increases and shifts to the left when the internal generated energy rate increases.

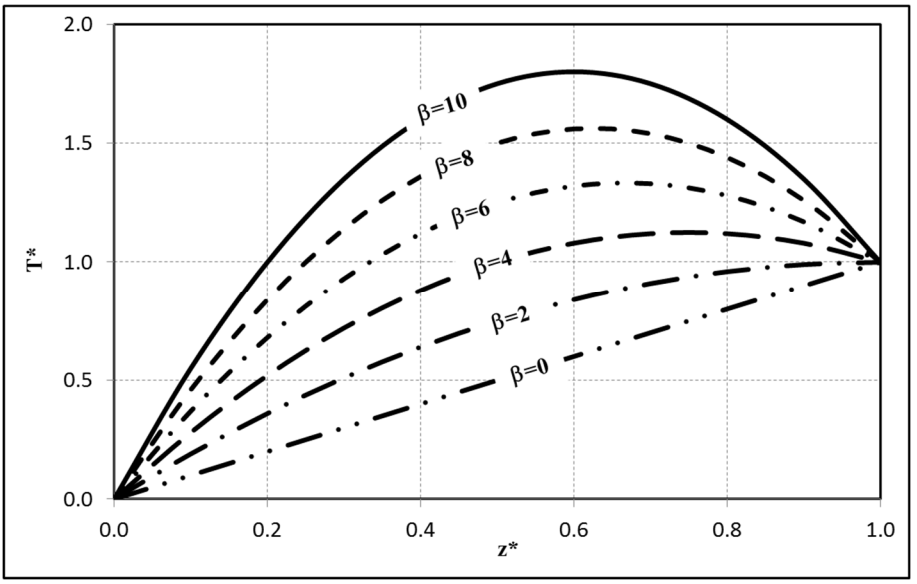

Figure A.6. *Temperature distribution of a panel for different volumetric heat generation rate*

In dimensionless form, the temperature maximum is given as:

$$T^*_{max} = \frac{(2+\beta)^2}{8\,\beta} \qquad [A.27]$$

and

$$z^*_{max} = \frac{1+\frac{1}{2}\beta}{\beta} \quad [A.28]$$

Figure A.7 shows the evolution of the maximum temperature and its location as a function of the parameter β. The maximum temperature increases with the internal generated energy rate while its location decreases.

Note that if the two sides of the panel are maintained at the same temperature, the maximum temperature is located at the middle and is given as:

$$T_{max} = \frac{\dot{q}_v\, e^2}{8\, k} + T_1 \quad [A.29]$$

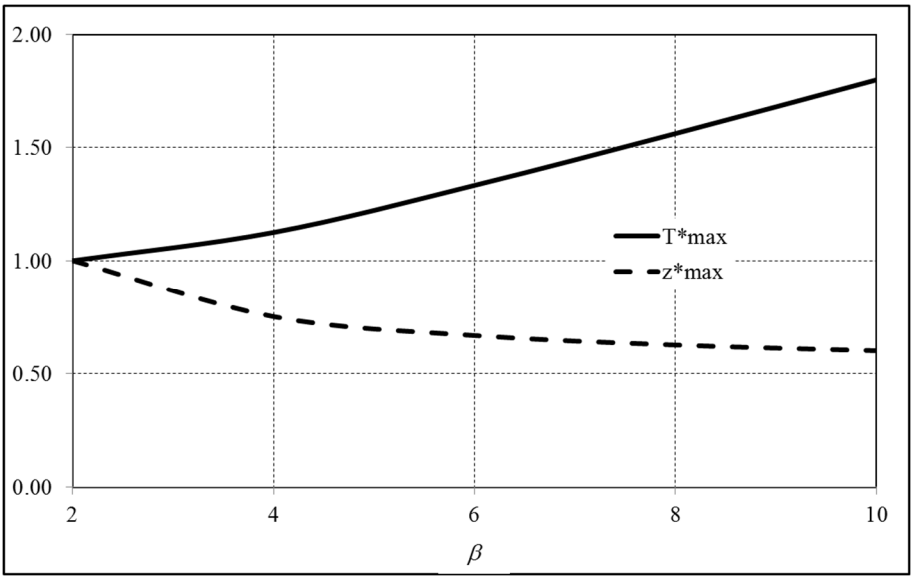

Figure A.7. *Maximal temperature and its location along the thickness according to different volumetric heat generation rate*

The conservation of energy at boundaries is important to describe the thermal behavior such as the case of solar panel analysis.

The thermal fluxes at the boundaries are given by the following relationships:

$$\begin{cases} -k\,A\left(\dfrac{dT}{dz}\right)_{z=0} = \dfrac{k\,A}{e}(T_1 - T_2) - \dfrac{1}{2}\,\dot{q}_v\,V \\ -k\,A\left(\dfrac{dT}{dz}\right)_{z=e} = \dfrac{k\,A}{e}(T_1 - T_2) + \dot{q}_v\,V \end{cases} \qquad [A.30]$$

These fluxes can be utilized in a variety of configurations, depending on the specific heat transfer processes involved. For example, they may be applied when surfaces experience conductive heat transfer through direct contact, where heat flows from one surface to another due to a temperature difference. Additionally, these fluxes can account for convective heat transfer, which occurs when heat is transferred through a fluid medium, such as air or water, in contact with the surface. In some cases, radiative transfer may also be considered, where heat is emitted and absorbed in the form of electromagnetic radiation, either alongside or independently of the convective processes.

A.1.2. *Cylindrical coordinates*

In cylindrical coordinates, the temperature is expressed as a function of polar coordinates (r, θ) and z, as shown in Figure A.8.

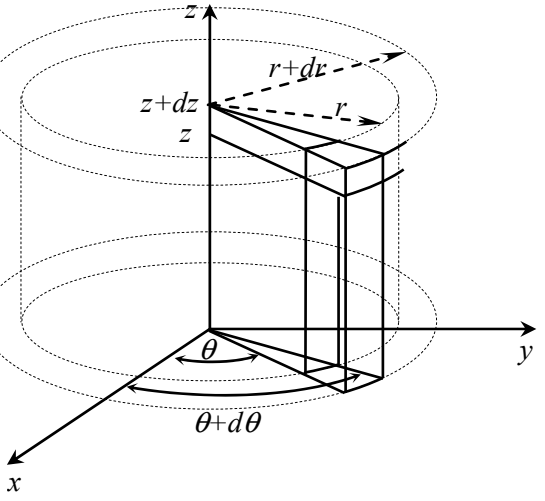

Figure A.8. *Differential control volume for three-dimensional conduction in cylindrical coordinates*

The transformation into cylindrical coordinates is based on the relations of the Cartesian coordinates to cylindrical coordinates:

$$\begin{cases} x = r\cos(\theta) \\ y = r\sin(\theta) \end{cases} \quad [A.31]$$

The components of the temperature gradient can be written as:

$$\begin{cases} G_x = \dfrac{\partial T}{\partial x} = \left(\dfrac{\partial T}{\partial r}\right)\left(\dfrac{\partial r}{\partial x}\right) + \left(\dfrac{\partial T}{\partial \theta}\right)\left(\dfrac{\partial \theta}{\partial x}\right) \\ G_y = \dfrac{\partial T}{\partial y} = \left(\dfrac{\partial T}{\partial r}\right)\left(\dfrac{\partial r}{\partial y}\right) + \left(\dfrac{\partial T}{\partial \theta}\right)\left(\dfrac{\partial \theta}{\partial y}\right) \\ G_z = \dfrac{\partial T}{\partial z} \end{cases} \quad [A.32]$$

The derivatives of r with respect to the variables x and y are given by the following relations:

$$\begin{cases} \dfrac{\partial r}{\partial x} = \cos(\theta) \\ \dfrac{\partial r}{\partial y} = \sin(\theta) \end{cases} \quad [A.33]$$

The derivatives of θ are given as:

$$\begin{cases} \dfrac{\partial \theta}{\partial x} = -\dfrac{1}{r}\sin(\theta) \\ \dfrac{\partial \theta}{\partial y} = \dfrac{1}{r}\cos(\theta) \end{cases} \quad [A.34]$$

By reporting the expressions of $\left(\frac{\partial r}{\partial x}\right)$, $\left(\frac{\partial \theta}{\partial x}\right)$, $\left(\frac{\partial r}{\partial y}\right)$ and $\left(\frac{\partial \theta}{\partial y}\right)$, the temperature gradient components are obtained by the following expressions:

$$\begin{cases} G_x = \dfrac{\partial T}{\partial x} = \left(\dfrac{\partial T}{\partial r}\right)\cos(\theta) - \dfrac{1}{r}\left(\dfrac{\partial T}{\partial \theta}\right)\sin(\theta) \\ G_y = \dfrac{\partial T}{\partial y} = \left(\dfrac{\partial T}{\partial r}\right)\sin(\theta) + \dfrac{1}{r}\left(\dfrac{\partial T}{\partial \theta}\right)\cos(\theta) \\ G_z = \dfrac{\partial T}{\partial z} \end{cases} \quad [A.35]$$

The conductive heat transfer equation is then given as:

$$\frac{\partial G_x}{\partial x}+\frac{\partial G_y}{\partial y}+\frac{\partial G_z}{\partial z}+\frac{1}{k}\,\dot{q}_v=\frac{1}{\alpha}\,\frac{\partial T}{\partial t} \qquad [A.36]$$

In a similar manner, the second derivative of the temperature gradient components is calculated by differentiating the temperature gradient once again, resulting in the following expression:

$$\begin{cases}\dfrac{\partial G_x}{\partial x}=\left(\dfrac{\partial G_x}{\partial r}\right)\left(\dfrac{\partial r}{\partial x}\right)+\left(\dfrac{\partial G_x}{\partial \theta}\right)\left(\dfrac{\partial \theta}{\partial x}\right)\\ \dfrac{\partial G_y}{\partial y}=\left(\dfrac{\partial G_y}{\partial r}\right)\left(\dfrac{\partial r}{\partial y}\right)+\left(\dfrac{\partial G_y}{\partial \theta}\right)\left(\dfrac{\partial \theta}{\partial y}\right)\\ \dfrac{\partial G_z}{\partial y}=\dfrac{\partial^2 T}{\partial z^2}\end{cases} \qquad [A.37]$$

The derivative of the first component is given as:

$$\frac{\partial G_x}{\partial x}=\frac{\partial^2 T}{\partial r^2}cos^2(\theta)+\frac{1}{r^2}\frac{\partial^2 T}{\partial \theta^2}sin^2(\theta)+\frac{1}{r}\frac{\partial T}{\partial r}sin^2(\theta)+\frac{2}{r}\left(\frac{1}{r}\frac{\partial T}{\partial \theta}-\frac{\partial^2 T}{\partial r\partial \theta}\right)\cos(\theta)\sin(\theta) \qquad [A.38]$$

The derivative of the second component is expressed as:

$$\frac{\partial G_y}{\partial y}=\frac{\partial^2 T}{\partial r^2}sin^2(\theta)+\frac{1}{r^2}\frac{\partial^2 T}{\partial \theta^2}cos^2(\theta)+\frac{1}{r}\frac{\partial T}{\partial r}cos^2(\theta)-\frac{2}{r}\left(\frac{1}{r}\frac{\partial T}{\partial \theta}-\frac{\partial^2 T}{\partial r\partial \theta}\right)\cos(\theta)\sin(\theta) \qquad [A.39]$$

The conductive heat transfer equation is then given in cylindrical coordinates as:

$$\frac{1}{r}\frac{\partial}{\partial r}\left(r\frac{\partial T}{\partial r}\right)+\frac{1}{r^2}\frac{\partial^2 T}{\partial \theta^2}+\frac{\partial^2 T}{\partial z^2}+\frac{1}{k}\,\dot{q}_v=\frac{1}{\alpha}\,\frac{\partial T}{\partial t} \qquad [A.40]$$

As an example, a tube with a thickness e is considered, as illustrated in Figure A.9. The inner radius is denoted r_i, and the outer radius is defined by r_o. This example demonstrates solutions to common problems frequently encountered in practice. One such case involves a solar system with tube concentrators. The challenge is to determine the temperature distribution and heat transfer rate in a

long, hollow cylinder of length L, given that the temperatures of the inner and outer surfaces are T_i and T_o, respectively. Considering a uniform volumetric energy rate generation, the temperature in the thickness depends on the radius and is free from the angle. In the steady state, the conduction heat equation is given as:

$$\frac{1}{r}\frac{\partial}{\partial r}\left(r\frac{\partial T}{\partial r}\right)+\frac{1}{k}\,\dot{q}_v=0 \qquad [A.41]$$

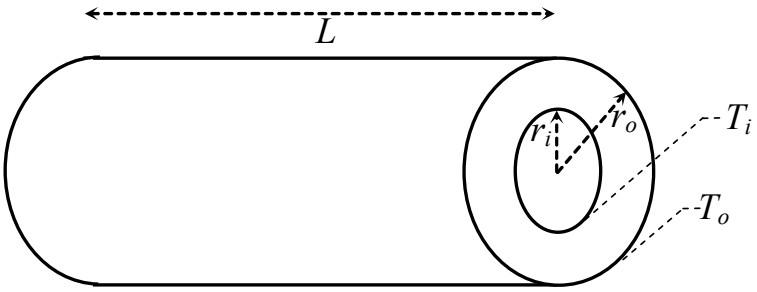

Figure A.9. *Radial heat conduction through the thickness of a cylindrical tube*

The integration of the heat equation leads to the expression of the radial temperature:

$$T(r)-T_i=-\frac{\dot{q}_v}{4\,k}\,(r^2-r_i^2) + \left(\frac{(T_o-T_i)+\frac{\dot{q}_v}{4\,k}(r_o^2-r_i^2)}{ln\left(\frac{r_o}{r_i}\right)}\right)ln\left(\frac{r}{r_i}\right) \qquad [A.42]$$

Similar to the case of Cartesian coordinates, the radial temperature can also be written in dimensionless form as a function of the radius:

$$T^*(r)=\frac{T(r)-T_i}{T_0-T_i} \qquad [A.43]$$

It can be expressed as a function of the outer and inner radius ratios ($R = r_o/r_i$), and r^* is defined as:

$$r^*=\frac{r-r_i}{r_o-r_i} \qquad [A.44]$$

In this case, the temperature is given as:

$$T^*(r) = \frac{1}{ln(R)}\left(-\frac{\beta\left(r^{*2}(R-1)-2r^*\right)}{2\,(R+1)} + \left(1+\frac{\beta}{2ln(R)}\right)\right) ln(r^*(R-1)+1) \qquad [A.45]$$

The parameter β represents the ratio of the internal generated energy rate to the conductive heat rate with no internal heat generation.

$$\beta = \frac{\dot{q}_v\, V}{\frac{k\, A_i}{r_i\, ln\left(\frac{r_o}{r_i}\right)}(T_o - T_i)} = \frac{\dot{q}_v\, V}{\frac{k\, A_o}{r_o\, ln\left(\frac{r_o}{r_i}\right)}(T_o - T_i)} \qquad [A.46]$$

where V denotes the annular volume of the tube.

Figure A.10 shows the dimensionless radial temperature as a function of r^* for different values of the parameter β.

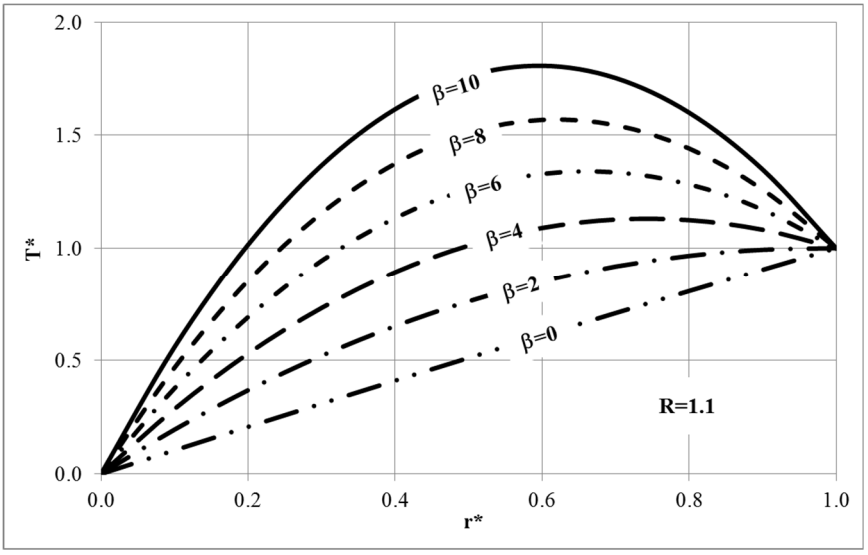

Figure A.10. *Temperature distribution with respect to the thickness of a tube for different volumetric heat generation rates*

In this figure, the outer and inner radius ratios are chosen to be equal to 1.1.

Figure A.11 illustrates the effect of the radius ratios on the distribution of the temperature.

As discussed previously, the fluxes at the boundary in the case of cylindrical coordinates can also be helpful for defining the behavior of complex thermal systems. In the case of a tubular medium, the linear flux at boundary r_i is given as:

$$\dot{\phi}(r_i) = \frac{\partial \phi}{\partial z}\Big)_{r=r_i} = -2\pi r_i \, k \frac{\partial T}{\partial r}\Big)_{r=r_i} \quad [A.47]$$

This formulation provides the possibility of describing the thermal behavior in two dimensions according to the radius and the longitudinal axis, particularly when the tube is streamed by fluids.

$$\dot{\phi}(r_i) = \frac{2\pi \ k}{ln\left(\frac{r_o}{r_i}\right)}(T_i - T_o) + \dot{q}_v \, \delta_i \quad [A.48]$$

where

$$\delta_i = S_i - \frac{1}{2}\frac{(S_o - S_i)}{ln\left(\frac{r_o}{r_i}\right)} \quad [A.49]$$

S_i and S_o denote the cross-sections of the tube:

$$\begin{cases} S_i = \pi \, r_i^2 \\ S_o = \pi \, r_o^2 \end{cases} \quad [A.50]$$

Similarly, the linear thermal flux at the boundary r_o is given as:

$$\dot{\phi}(r_o) = \frac{2\pi \ k}{\ln\left(\frac{r_o}{r_i}\right)}(T_i - T_o) + \dot{q}_v \, \delta_o \quad [A.51]$$

where

$$\delta_o = S_o - \frac{1}{2}\frac{(S_o - S_i)}{\ln\left(\frac{r_o}{r_i}\right)} \quad [A.52]$$

The cross-sections S_i and S_o were defined above.

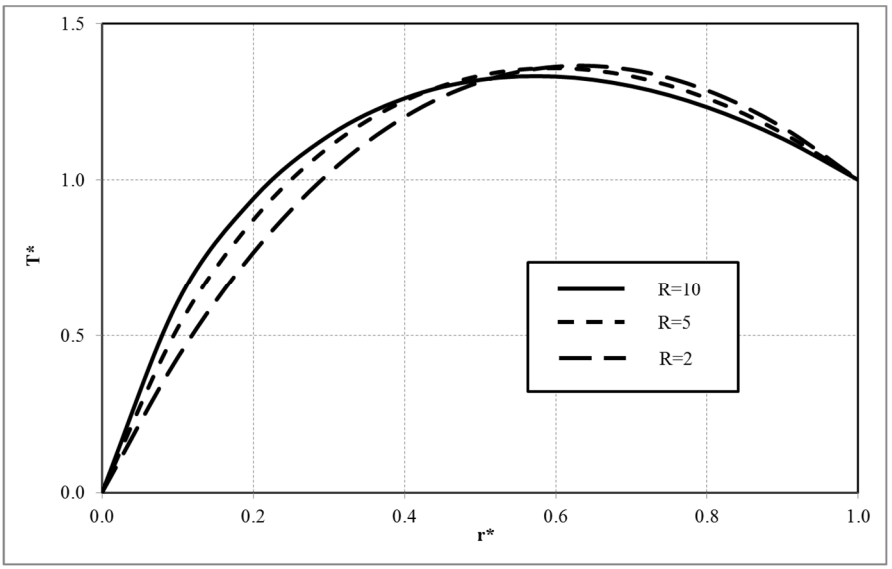

Figure A.11. *Temperature distribution with respect to the thickness of a tube for different radius ratios (β = 6)*

A.1.3. *Spherical coordinates*

As illustrated in Figure A.12, the spherical coordinate system defines a point in three-dimensional space through the radial distance (r), the polar angle (θ) and the azimuthal angle (φ).

The radial distance corresponds to the distance from the point to the origin along the radial line. The polar angle is relative to the angle between the radial line and a designated polar axis and represents the rotation of the radial line around the polar axis.

The transformation to spherical coordinates is derived from the relationships between Cartesian and spherical coordinates, as illustrated in Figure A.12:

$$\begin{cases} x = r\sin(\theta)\cos(\varphi) \\ y = r\sin(\theta)\sin(\varphi) \\ z = r\cos(\theta) \end{cases} \quad [A.53]$$

Similar to the cylindrical coordinates, the components of the temperature gradient can be written by adding the z coordinate transformation as:

$$\begin{cases} G_x = \dfrac{\partial T}{\partial x} = \left(\dfrac{\partial T}{\partial r}\right)\left(\dfrac{\partial r}{\partial x}\right) + \left(\dfrac{\partial T}{\partial \theta}\right)\left(\dfrac{\partial \theta}{\partial x}\right) + \left(\dfrac{\partial T}{\partial \varphi}\right)\left(\dfrac{\partial \varphi}{\partial x}\right) \\ G_y = \dfrac{\partial T}{\partial y} = \left(\dfrac{\partial T}{\partial r}\right)\left(\dfrac{\partial r}{\partial y}\right) + \left(\dfrac{\partial T}{\partial \theta}\right)\left(\dfrac{\partial \theta}{\partial y}\right) + \left(\dfrac{\partial T}{\partial \varphi}\right)\left(\dfrac{\partial \varphi}{\partial y}\right) \\ G_z = \dfrac{\partial T}{\partial z} = \left(\dfrac{\partial T}{\partial r}\right)\left(\dfrac{\partial r}{\partial z}\right) + \left(\dfrac{\partial T}{\partial \theta}\right)\left(\dfrac{\partial \theta}{\partial z}\right) + \left(\dfrac{\partial T}{\partial \varphi}\right)\left(\dfrac{\partial \varphi}{\partial z}\right) \end{cases} \quad [A.54]$$

The spherical coordinates are given as a function of the Cartesian coordinates as:

$$\begin{cases} r = \sqrt{x^2 + y^2 + z^2} \\ \theta = Arctan\left(\dfrac{\sqrt{x^2 + y^2}}{z}\right) \\ \varphi = Arctan\left(\dfrac{y}{x}\right) \end{cases} \quad [A.55]$$

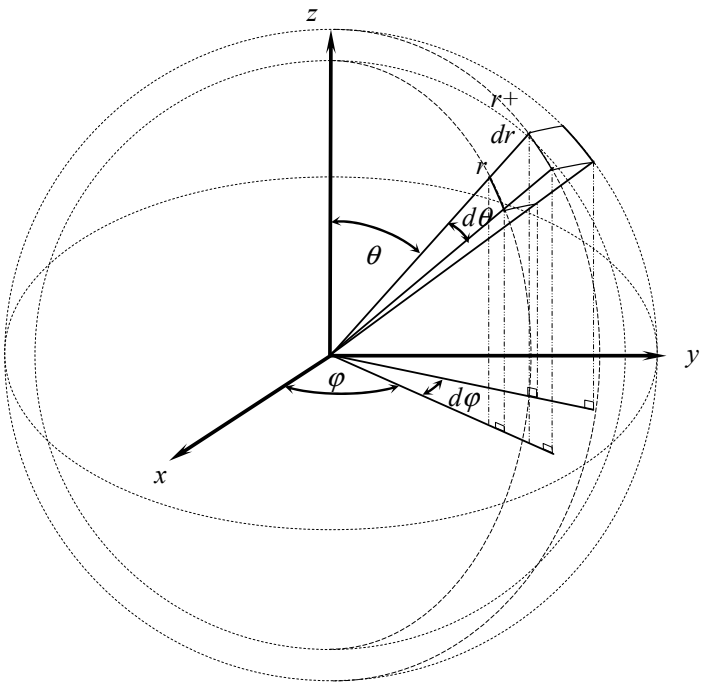

Figure A.12. *Differential control volume for three-dimensional conduction in spherical coordinates*

The derivatives of r with respect to the variables x, y and z are given by the following relations:

$$\begin{cases} \dfrac{\partial r}{\partial x} = \sin(\theta)\cos(\varphi) \\ \dfrac{\partial r}{\partial y} = \sin(\theta)\sin(\varphi) \\ \dfrac{\partial r}{\partial z} = \cos(\theta) \end{cases} \quad [A.56]$$

The derivatives of θ are given as:

$$\begin{cases} \dfrac{\partial \theta}{\partial x} = \dfrac{1}{r}\cos(\theta)\cos(\varphi) \\ \dfrac{\partial \theta}{\partial y} = \dfrac{1}{r}\cos(\theta)\sin(\varphi) \\ \dfrac{\partial \theta}{\partial z} = -\dfrac{1}{r}\sin(\theta) \end{cases} \quad [A.57]$$

The derivatives of φ with respect to the cataract variables are as follows:

$$\begin{cases} \dfrac{\partial \varphi}{\partial x} = -\dfrac{1}{r}\dfrac{\sin(\varphi)}{\sin(\theta)} \\ \dfrac{\partial \varphi}{\partial y} = \dfrac{1}{r}\dfrac{\cos(\varphi)}{\sin(\theta)} \\ \dfrac{\partial \varphi}{\partial z} = 0 \end{cases} \quad [A.58]$$

By reporting the derivatives of the spherical coordinates in the scalar Laplacian of the temperature, the conduction heat transfer equation becomes:

$$\left(\frac{\partial^2 T}{\partial r^2} + \frac{2}{r}\frac{\partial T}{\partial r}\right) + \left(\frac{1}{r^2}\frac{\partial^2 T}{\partial \theta^2} + \frac{\cos(\theta)}{r^2\sin(\theta)}\frac{\partial T}{\partial \theta}\right) + \left(\frac{1}{r^2\sin^2(\theta)}\frac{\partial^2 T}{\partial \varphi^2}\right) + \frac{1}{k}\,\dot{q}_v = \frac{1}{\alpha}\,\frac{\partial T}{\partial t} \quad [A.59]$$

After rearrangement, the conduction heat equation is given in its general formulation as:

$$\frac{1}{r^2}\frac{\partial}{\partial r}\left(r^2\frac{\partial T}{\partial r}\right) + \frac{1}{r^2\sin(\theta)}\frac{\partial}{\partial \theta}\left(\sin(\theta)\frac{\partial T}{\partial \theta}\right) + \frac{1}{r^2\sin^2(\theta)}\frac{\partial^2 T}{\partial \varphi^2} + \frac{1}{k}\,\dot{q}_v = \frac{1}{\alpha}\,\frac{\partial T}{\partial t} \quad [A.60]$$

As an example, a hollow sphere with a thickness e is considered, as illustrated in Figure A.13.

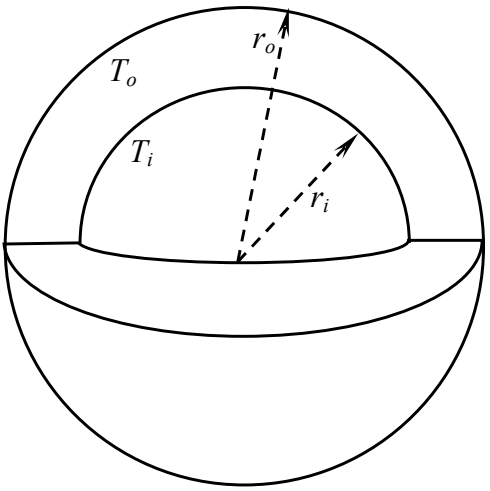

Figure A.13. *Radial heat conduction through the thickness of a hollow sphere*

The inner radius is denoted r_i, and the outer radius is defined by r_o. In this case, the temperature distribution and heat transfer rate through a hollow sphere are considered, given that the temperatures of the inner and outer surfaces are T_i and T_o, respectively. Considering a uniform volumetric energy rate generation, the temperature in the thickness depends on the radius and is supposed to be free from the angles. In the steady state, the conduction heat equation is then given as:

$$\frac{1}{r^2}\frac{\partial}{\partial r}\left(r^2\frac{\partial T}{\partial r}\right)+\frac{1}{k}\,\dot{q}_v=0 \qquad \text{[A.61]}$$

The integration of the heat equation leads to the expression of the radial temperature:

$$T(r)-T_i=-\frac{\dot{q}_v}{6\,k}\,(r^2-r_i^2) + \left(\frac{(T_o-T_i)+\frac{\dot{q}_v}{6\,k}(r_o^2-r_i^2)}{\left(\frac{1}{r_o}-\frac{1}{r_i}\right)}\right)\left(\frac{1}{r}-\frac{1}{r_i}\right) \qquad \text{[A.62]}$$

The radial temperature can also be written in dimensionless form as a function of the radius:

$$T^*(r) = \frac{T(r) - T_i}{T_0 - T_i} \quad [A.63]$$

The dimensionless radius thickness is defined as:

$$r^* = \frac{r - r_i}{r_o - r_i} \quad [A.64]$$

The dimensionless temperature can be expressed as a function of the outer and inner radius ratios ($R = r_o/r_i$), and r^* is defined as:

$$T^*(r) = \left(\frac{R}{1-R}\right)\left\{\frac{1}{2}\frac{\beta\,(1-R)}{(1-R^3)}\left(r^{*2}(R-1) + 2r^*\right) + \left(1 + \frac{1}{2}\frac{\beta(1+R)R}{(1-R^3)}\right)\right\}\left(\frac{1}{r^*(R-1)+1}\right) \quad [A.65]$$

The parameter β represents the ratio of the internal generated energy rate to the conductive heat rate with no internal heat generation.

$$\beta = \frac{\dot{q}_v\, V}{\dfrac{k\, A_i (T_o - T_i)}{r_i^2\left(\dfrac{1}{r_o} - \dfrac{1}{r_i}\right)}} = \frac{\dot{q}_v\, V}{\dfrac{k\, A_o (T_o - T_i)}{r_o^2\left(\dfrac{1}{r_o} - \dfrac{1}{r_i}\right)}} \quad [A.66]$$

where V denotes the volume between the two radiuses of the sphere:

$$V = \frac{4}{3}\pi(r_o^3 - r_i^3) \quad [A.67]$$

The fluxes at the boundary in the case of spherical coordinates can also be helpful for defining the behavior of complex thermal systems. In the case of a spherical medium, the flux at the boundary r_i is given as:

$$\phi(r_i) = -k\, A_i \frac{\partial T}{\partial r}\Big)_{r=r_i} = -4\pi r_i^2\, k \frac{\partial T}{\partial r}\Big)_{r=r_i} \quad [A.68]$$

This formulation provides the possibility to describe the thermal behavior at the medium boundary.

$$\phi(r_i) = \frac{4\pi\ \ k(T_o - T_i)}{\left(\dfrac{1}{r_o} - \dfrac{1}{r_i}\right)} + \dot{q}_v\, \delta_i \quad [A.69]$$

where

$$\delta_i = V_i - \frac{1}{2}\frac{(V_o - R\,V_i)}{(R-1)} \qquad [A.70]$$

V_i and V_o denote the volumes at r_i and r_o, respectively, of the sphere:

$$\begin{cases} V_i = \frac{4}{3}\pi\, r_i^3 \\ V_o = \frac{4}{3}\pi\, r_o^3 \end{cases} \qquad [A.71]$$

Similarly, the thermal flux at the boundary r_o is given as:

$$\phi(r_o) = \frac{4\pi\ k(T_o - T_i)}{\left(\frac{1}{r_o} - \frac{1}{r_i}\right)} + \dot{q}_v\,\delta_o \qquad [A.72]$$

where

$$\delta_o = V_o - \frac{1}{2}\frac{(V_o - R\,V_i)}{(R-1)} \qquad [A.73]$$

A.2. Convective heat transfer

Convective heat transfer is governed by two distinct yet interrelated mechanisms, conduction and fluid motion, both of which contribute to the overall thermal exchange between a surface and a fluid.

The first mechanism, conduction, refers to the transfer of thermal energy via molecular interactions within a medium. In this process, thermal energy is transmitted from one molecule to another through direct contact. This is typically observed in solids or immobile fluids where heat transfer occurs at the microscopic level. Molecules collide and exchange energy, resulting in the redistribution of thermal energy from regions of higher temperature to those of lower temperature.

In contrast, the second mechanism, fluid motion, involves the bulk movement of fluid parcels, which are groups of molecules that move collectively under the influence of external forces. This bulk movement can occur in two primary forms: natural convection and forced convection. In natural convection, fluid motion arises due to variations in fluid density caused by temperature gradients. Warmer regions of the fluid become less dense and rise, whereas cooler, denser regions sink, creating

a circulating flow. On the other hand, forced convection is driven by external pressure differences, typically generated by pumps or fans, which propel the fluid in a controlled, directional flow.

In many practical systems, both conduction and convection occur simultaneously. Conduction takes place at the molecular level within the fluid, especially within the boundary layer where the fluid is in direct contact with the heat transfer surface. Moreover, bulk fluid motion is influenced by either natural or forced convection, leading to complex interactions between the two mechanisms.

Figure A.14 presents a schematic of a plate with a surface temperature denoted as T_{f0}, in contact with a fluid flowing parallel to it at a temperature $T_{f\infty}$. As the fluid moves along the surface of the plate, its velocity varies due to the influence of viscous forces. Near the surface, the fluid velocity is zero, adhering to the no-slip boundary condition, meaning that the fluid at the surface is essentially stationary. As one of them moves away from the surface, the velocity gradually increases, eventually approaching the free-stream velocity V_∞, as shown in Figure A.14.

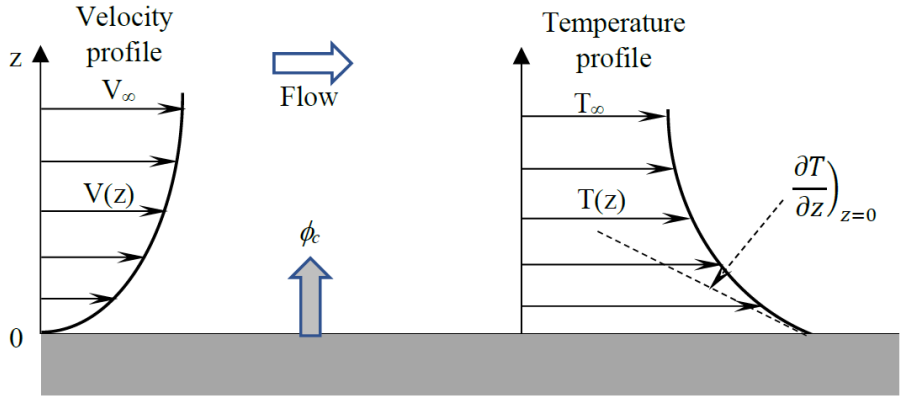

Figure A.14. *Velocity and temperature distribution in the case of convection heat transfer through a heated panel*

At the interface between the fluid and the plate, stagnation occurs, which results in a temperature gradient within the fluid layer adjacent to the surface. Heat transfer at this interface primarily occurs through conduction within the boundary layer, as the fluid molecules near the wall have insufficient velocity to transport thermal energy via convection.

When the temperature gradient and the fluid thermal conductivity at the wall are known, the rate of heat transfer can be determined. This rate is a key factor in

assessing the thermal performance of the system and can be quantified using Fourier's law of heat conduction. The equation for this heat transfer rate accounts for the temperature difference between the surface and the fluid, as well as the material's thermal properties, thus enabling the precise calculation of the conductive heat transfer at the surface.

The mechanisms of heat transfer in natural convection mirror those in forced convection with a critical distinction. In forced convection, the fluid velocity, at distances far from the surface, asymptotically approaches the free-stream velocity imposed by an external force. In contrast, under natural convection, the fluid velocity initially increases with distance from the heat transfer surface, reaches a maximum and then gradually decreases, as described in Figure A.15.

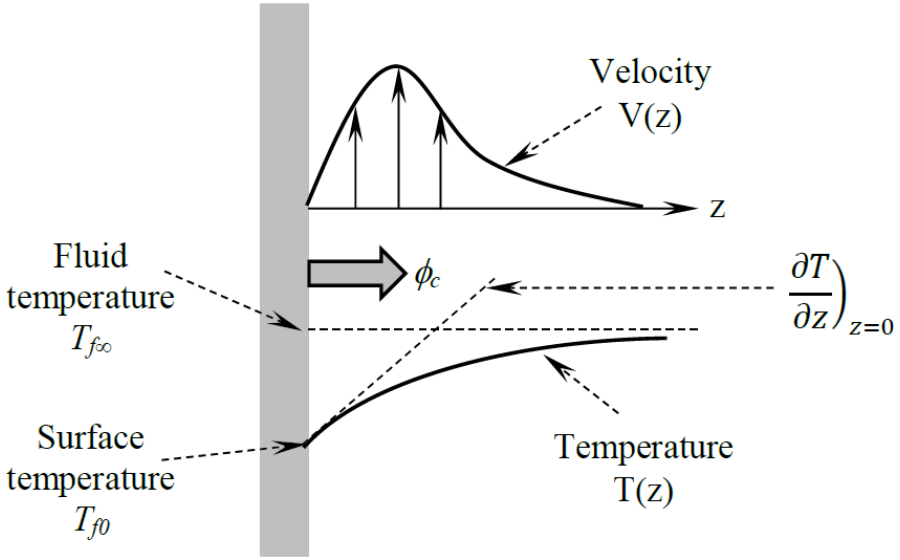

Figure A.15. *Velocity and temperature distribution in the case of natural convection heat transfer through a heated panel*

This behavior is primarily due to the interplay between the viscous forces and buoyancy forces. Near the surface, the effect of viscosity dominates, leading to an increase in fluid velocity as one of them moves away from the surface. However, the influence of viscosity decreases more rapidly with increasing distance, whereas the buoyancy force, driven by the temperature-dependent density differences, decreases more gradually. As the fluid density approaches that of the surrounding, unheated fluid, the buoyancy force weakens, causing the velocity to peak and then decline toward zero as the distance from the surface increases.

Despite these differences in the fluid velocity profiles, the temperature distributions under both natural and forced convection tend to follow similar trends. In both cases, the heat transfer at the fluid–solid interface is governed primarily by conduction, as thermal energy is transferred directly through molecular interactions within the boundary layer near the wall.

A.2.1. *Newton's law*

The stationary fluid layer adjacent to the wall dictates the heat transfer process, which can be modeled as conductive heat flux. The thermal flux through area A can be expressed as:

$$\phi = -k_f \, A \, \frac{\partial T}{\partial z}\Big)_{z=0} \qquad [A.74]$$

where k_f is the thermal conductivity of the fluid. Alternatively, the heat flux can also be represented as:

$$\phi = h \, A \, \left(T_{f\infty} - T_{f_0}\right) \qquad [A.75]$$

This equation follows Newton's law of cooling, where h is the convective heat transfer coefficient. The evaluation of h can be challenging due to the complex nature of convection phenomena, as it depends on factors such as the surface geometry, fluid velocity and physical properties of the fluid. Importantly, h varies with the geometry of the system, the velocity of the fluid and the temperature difference.

Consequently, the convective heat transfer coefficient is not necessarily constant across the surface, and it may vary spatially, leading to a distinction between the local and average convection heat transfer coefficients.

The local coefficient h is defined as:

$$d\phi = h \, dA \, \left(T_{f\infty} - T_{f_0}\right) \qquad [A.76]$$

Moreover, the average coefficient can be derived by integrating the local coefficient over the surface area A:

$$\bar{h} = \frac{1}{A} \iint_A h \, dA \qquad [A.77]$$

The average values of the convection heat transfer coefficient are commonly used in practical applications. Figure A.16 shows typical orders of magnitude for these average values encountered in various systems.

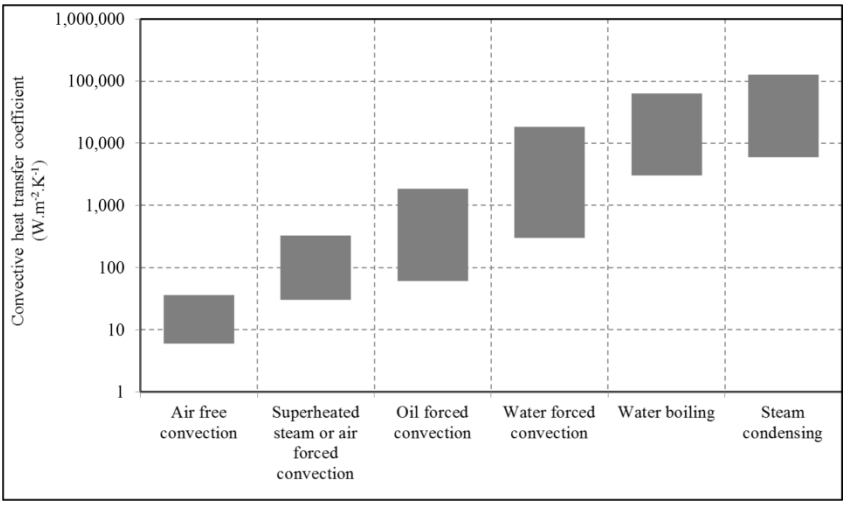

Figure A.16. *Order of magnitude of the convective heat transfer coefficients*

Finally, the convective thermal resistance is defined as the ratio of the temperature difference to the thermal current:

$$\left(T_{f_\infty} - T_{f_0}\right) = R_{th}\,\phi \qquad [A.78]$$

where

$$R_{th_h} = \frac{1}{h\,A} \qquad [A.79]$$

As indicated by the preceding discussion, the convection heat transfer coefficient depends on several factors, including the fluid density, viscosity, velocity and thermal properties. In forced convection, the velocity is generally imposed by an external device such as a pump or fan.

In natural convection, the fluid velocity is driven by buoyancy effects, which are determined by the temperature difference between the surface and the surrounding fluid, the fluid coefficient of thermal expansion, which dictates density changes per unit temperature difference, and the gravitational force acting on the fluid.

A.2.2. *Convective heat transfer coefficient assessment*

As discussed previously, convective heat transfer is a combination of conductive heat transfer nearby interface between fluids and solids and the motion of the fluid carrying energy. This phenomenon can be expressed by the following ratio:

$$\frac{k_f\ A}{h\ A} = \frac{-\frac{\partial T}{\partial z}\Big)_{z=0}}{\left(T_{f_\infty} - T_{f_0}\right)} \qquad [A.80]$$

If the area is considered to have a characteristic length L, the following relation is obtained to assess the ratio of the conductive part to the convective share of the fluid:

$$\frac{k_f\ L}{h\ L} = \frac{-\frac{\partial T}{\partial z}\Big)_{z=0}}{\left(T_{f_\infty} - T_{f_0}\right)} \qquad [A.81]$$

The dimensionless number Nusselt is introduced to evaluate this ratio as:

$$Nu = \frac{k_f\ L}{h} = \frac{-\frac{\partial T}{\partial z}\Big)_{z=0}}{\frac{\left(T_{f_\infty} - T_{f_0}\right)}{L}} \qquad [A.82]$$

The Nusselt number can be interpreted physically as the ratio of the thermal gradient at the interface between the fluid and the solid surface to the reference thermal gradient, typically representing the heat transfer that would occur through pure conduction. In essence, it quantifies the enhancement of heat transfer due to convection relative to conduction alone. The Nusselt number reflects the relative importance of convective heat transfer compared with conductive heat transfer in a fluid near a solid surface. A higher Nusselt number indicates more effective convective heat transfer, as the fluid near the surface is able to transport heat more efficiently.

In practical applications, the Nusselt number serves as a convenient, dimensionless measure of the convective heat transfer coefficient. Once the Nusselt number is known for a given system, the convective heat transfer coefficient can be determined using the following relationship:

$$h = \frac{k_f\ L}{Nu} \qquad [A.83]$$

The characteristic length can be the hydraulic diameter for flow over a surface or the length of a plate such as a solar panel.

The Nusselt number is one of dimensionless numbers to analyze convection. The inherent complexity of convection phenomena necessitates the use of generalized techniques that reduce the number of governing parameters in a given problem. Dimensional analysis requires only knowledge of the relevant physical quantities and their respective dimensions, making it a broadly applicable method.

To determine the number of independent dimensionless groups necessary to formulate a relationship describing a physical phenomenon, we can apply Buckingham's π theorem. This fundamental principle states that the number of independent dimensionless groups that can be derived from the physical variables governing a problem is given by the difference between the total number of these physical quantities, p (such as density, viscosity and heat transfer coefficient), and the number of fundamental dimensions, q, required to express their dimensional formulas. The number of independent dimensionless groups corresponds to (p – q).

The equation that relates the different dimensionless groups ($\pi_1,\pi_2 \ldots \pi_{p-q}$) is given by:

$$F(\pi_1, \pi_2, \ldots, \pi_{p-q}) = 0 \qquad [A.84]$$

A.2.2.1. *Forced convection*

A straightforward approach to identifying dimensionless groups will now be demonstrated for a fluid flowing across a heated tube or different scenarios involving fluid flow through a tube or over a flat plate.

Physical quantities	Symbol	Dimension
Tube diameter	D	[L]
Fluid velocity	V	[Lt^{-1}]
Fluid density	ρ	[ML^{-3}]
Dynamic viscosity	μ	[$ML^{-1}t^{-1}$]
Thermal conductivity of fluid	k	[$MLt^{-3}T^{-1}$]
Specific heat at constant pressure	C_p	[$L^2t^{-2}T^{-1}$]
Heat transfer coefficient	h	[$Mt^{-3}T^{-1}$]
Temperature difference	ΔT	[T]

Table A.2. *Pertinent physical quantities in convection heat transfer*

On the basis of the description of the heat transfer process by convection, it is reasonable to assume that the physical quantities listed in Table A.2 are appropriate for the problem.

The physical parameters equation can be derived as:

$$f\left(D, V, \rho, \mu, k, C_p, h, \Delta T\right) = 0 \qquad [A.85]$$

In this formulation, the number of physical quantities is eight, and the number of fundamental dimensions is four.

This leads to the following equation with four dimensionless groups:

$$F(\pi_1, \pi_2, \pi_3, \pi_4) = 0 \qquad [A.86]$$

Each dimensionless group is defined as:

$$\pi_i = D^{a_i}.V^{b_i}.\rho^{c_i}.\mu^{d_i}.k^{e_i}.C_p^{f_i}.h^{g_i}.\Delta T^{h_i} \qquad [A.87]$$

The groups π_i are given in terms of dimensions as:

$$[\pi_i] = [M]^{b_i+d_i+e_i+g_i}.[L]^{a_i+b_i+c_i-3d_i-e_i+2f_i} \\ [t]^{-3b_i-c_i-e_i-2f_i-3g_i}\,[T]^{-b_i-f_i-g_i-h_i} \qquad [A.88]$$

The combination of the parameters a_i, b_i...h_i must guarantee the dimensionlessness of the π_i groups:

$$\begin{cases} b_i + d_i + e_i + g_i = 0 \\ a_i + b_i + c_i - 3d_i - e_i + 2f_i = 0 \\ -3b_i - c_i - e_i - 2f_i - 3g_i = 0 \\ -b_i - f_i - g_i - h_i = 0 \end{cases} \qquad [A.89]$$

Four equations with eight unknowns allow the selection of four arbitrary parameters. With respect to the convective heat transfer coefficient, the parameter g_1 takes a value of 1, and the choice of $c_1 = d_1 = h_1 = 0$ leads to $a_1 = 1$, $b_1 = -1$ and $e_1 = f_1 = 0$.

This leads to the following Nusselt number:

$$\pi_1 = Nu = \frac{h\,D}{k} \qquad [A.90]$$

When $g_2 = 0$, $a_2 = 1$ and $f_2 = h_2 = 0$, the second dimensionless group corresponds to the dimensionless Reynolds number:

$$\pi_2 = Re = \frac{\rho\, V\, D}{\mu} \quad [A.91]$$

The Reynolds number indicates the fluid flow regime.

The choice of $c_3 = g_3 = e_3 = h_3 = 0$ leads to the dimensionless Prandtl number:

$$\pi_3 = Pr = \frac{\mu\, C_p}{k} \quad [A.92]$$

The choice of $a_4 = b_4 = d_4 = e_4 = 0$ leads to the dimensionless Eckert number:

$$\pi_4 = Ec = \frac{V^2}{C_p\, \Delta T} \quad [A.93]$$

The dimensionless equation can be written in the following form:

$$Nu = f(Re, Pr, Ec) \quad [A.94]$$

Note that the Eckert number is frequently considered in supersonic and hypersonic flows, where the kinetic energy of the fluid is significant with important viscous dissipation.

A.2.2.2. *Natural convection*

Natural convection occurs when fluid motion is caused by buoyancy forces that result from density thermal variations in the fluid. The density change according to the temperature is given by the Boussinesq approximation:

$$\rho = \rho_0(1 + \beta \Delta T) \quad [A.95]$$

where β denotes the thermal expansion of the fluid. Driven by density variations, the movement of the fluid in natural convection arises.

Near a heated surface, a fluid element with density ρ and volume dv will be subjected to the resulting vertical force per unit mass between its height and buoyancy force:

$$f = \frac{\Delta\rho}{\rho_0} g = \beta\, g\, \Delta T \quad [A.96]$$

where g represents gravity.

With these considerations, there is a coupling between the velocity and temperature fields through the term $\beta g\ \Delta T$.

In this case, the relevant physical quantities indicated in Table A.3 are considered to determine the dimensionless groups for free convection. Seven physical quantities are combined with four dimensions. In this case, three dimensionless groups can be derived.

Physical quantities	Symbol	Dimension
Length (m)	l	[L]
Kinematic viscosity ($m^2.s^{-1}$)	ϑ	[$L^2\ t^{-1}$]
Gravitational thermal expansion ($m.K^{-1}\ s^{-2}$)	$g\beta$	[$L\ T^{-1}\ t^{-2}$]
Temperature difference (K)	ΔT	[T]
Thermal diffusivity ($m^2.s^{-1}$)	α	[$L^2\ t^{-1}$]
Thermal conductivity ($W.m^{-1}.K^{-1}$)	k	[$M\ L\ t^{-3}T^{-1}$]
Surface heat flux ($W.m^{-2}$)	φ	[$M\ t^{-1}$]

Table A.3. *Pertinent physical quantities in convection heat transfer*

$$F(\pi_1, \pi_2, \pi_3) = 0 \qquad [A.97]$$

where

$$\pi_i = l^{a_i}.\vartheta^{b_i}.(g\beta)^{c_i}.\Delta T^{d_i}.\alpha^{e_i}.k^{f_i}.\varphi^{g_i} \qquad [A.98]$$

The groups π_i are given in terms of dimensions as:

$$[\pi_i] = [L]^{a_i+2b_i+c_i+2e_i+f_i}.[t]^{-b_i-2c_i-e_i-3f_i-3g_i}.[T]^{-c_i+d_i-f_i}\ [M]^{f_i+g_i} \qquad [A.99]$$

To maintain the dimensionlessness of π_i, the following conditions must be met for the parameters:

$$\begin{cases} a_i + 2b_i + c_i + 2e_i + f_i = 0 \\ -b_i - 2c_i - e_i - 3f_i - 3g_i = 0 \\ -c_i + d_i - f_i = 0 \\ f_i + g_i = 0 \end{cases} \qquad [A.100]$$

These conditions lead to the first dimensionless group:

$$\pi_1 = Nu = \frac{l\,\varphi}{k\,\Delta T} = \frac{h\,l}{k} \qquad [A.101]$$

The second is obtained as:

$$\pi_2 = Pr = \frac{\vartheta}{\alpha} = \frac{\mu}{\rho_0}\frac{\rho_0 C_p}{k} = \frac{\mu\, C_p}{k} \qquad [A.102]$$

The third dimensionless group corresponds to the Grashof number:

$$\pi_3 = Gr = \frac{\beta\, g\, \Delta T\, l^3}{\vartheta^2} \qquad [A.103]$$

The Grashof number represents the ratio of buoyant forces to viscous forces. The larger the Grashof number is, the greater the influence of buoyancy, which in turn has a significant effect on initiating fluid motion.

With these three dimensionless groups, the Nusselt number can be obtained as a function of the Prandtl and Grashof numbers according to correlations derived from experimental data.

$$Nu = \frac{h\, l}{k} = f(Gr, Pr) \qquad [A.104]$$

In free convection, the Reynolds number does not play a role in determining the heat transfer coefficient, as the flow is not driven by external forces such as pumps or fans.

A.3. Radiative heat transfer

Thermal radiation refers to the transfer of heat from one body to another due to their respective temperatures, occurring without the need for any intermediate medium. Unlike conduction and convection, which rely on the presence of a material substance (such as a solid or fluid) to facilitate heat transfer, radiation can take place in a vacuum, where no physical substance is required to carry the energy. This process is governed by the emission of electromagnetic waves, primarily in the infrared spectrum, which carry energy away from the emitting body and are absorbed by the receiving body, thereby transferring heat.

The emission of thermal radiation is fundamentally dictated by the temperature of the radiating body. As an object temperature increases, it emits electromagnetic waves over a broad spectrum of wavelengths. Thermal radiation spans a range approximately from 0.1 to 100 μm, encompassing various segments of the electromagnetic spectrum. This range is conventionally classified into three main regions: ultraviolet, visible and infrared radiation. The ultraviolet portion corresponds to the shortest wavelengths, typically emitted by extremely hot bodies.

The visible range, which is perceptible to the human eye, represents only a small fraction of the total radiation emitted. The infrared region, which accounts for the majority of thermal radiation at common temperatures, is primarily responsible for heat transfer.

A black body is an object that, at any given temperature, emits and absorbs the maximum possible amount of radiation at any specified wavelength. This theoretical concept establishes an upper limit for radiation emission, in accordance with the second law of thermodynamics. This serves as a standard against which the radiative properties of other materials are measured.

The rate at which a black body emits radiant energy per unit of time and per unit of surface area at a specific wavelength within a given range is referred to as E_b. This value is known as the monochromatic emissive power of the black body. It is distributed across various wavelengths λ according to Planck's law:

$$E_{b\lambda} = \frac{C_1}{\lambda^5 \left(e^{\frac{C_2}{\lambda T}} - 1\right)} \qquad [A.105]$$

where

$C_1 = 3.7415 \times 10^{-16}$ W m^2 and $C_2 = 1.4388 \times 10^{-2}$ m K

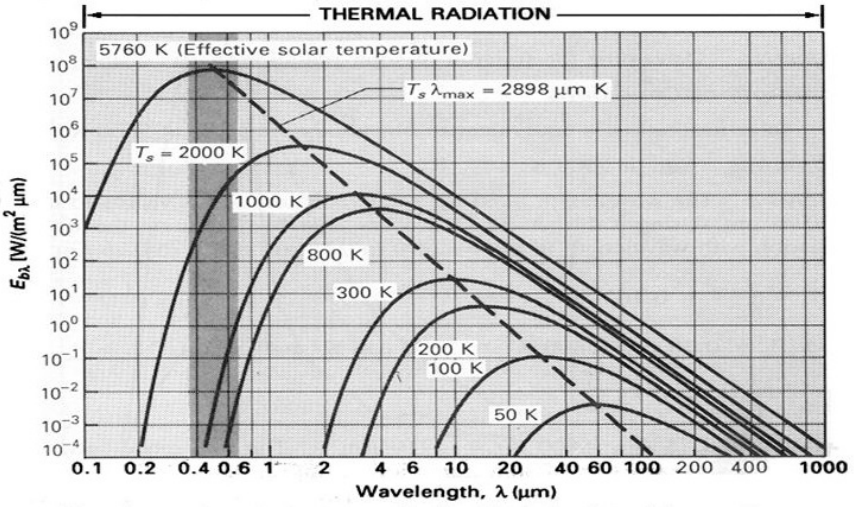

Figure A.17. *Monochromatic emissive power of a black body at different temperatures*

Figure A.17 shows the monochromatic emissive power of a black body at different temperatures. Note that the temperature presents a maximum, which increases according to the black body temperature. The wavelength corresponding to this maximum decreases with increasing temperature.

Wien's law gives the link between the maximum temperature and the corresponding wavelength:

$$(\lambda\, T)_{max} = 2{,}898\ \mu\text{m K} \qquad [A.106]$$

This relationship is obtained when:

$$\frac{dE_{b\lambda}}{d\lambda}(T_{max}) = 0 \qquad [A.107]$$

According to the Stefan–Boltzmann law, the total emissive power of a black body is proportional to the fourth power of its absolute temperature:

$$E_b = \int_0^{\infty} \frac{C_1}{\lambda^5 \left(e^{\frac{C_2}{\lambda T}} - 1\right)} d\lambda = \sigma\, T^4 \qquad [A.108]$$

where $\sigma = 5.670 \times 10^{-8}$ W.M^{-2} K^{-4}.

When radiation is incident upon a surface, a portion of the total irradiation is absorbed by the material, a portion is reflected by the surface and the remainder is transmitted through the body.

Absorptivity, reflectivity and transmissivity describe the distributions of the total irradiation.

The radiative energy conservation leads to:

$$Ab + R + \tau = 1 \qquad [A.109]$$

When a body is opaque, there is no transmission of incident radiation:

$$Ab + R = 1 \qquad [A.110]$$

These three parameters also consider multiple reflections into the bodies receiving incident radiation.

The emissivity, which is also an important parameter of a real body, is defined as the total radiation emitted divided by the total radiation that would be emitted by a blackbody at the same temperature:

$$\varepsilon = \frac{E(T)}{\sigma\, T^4} \qquad [A.111]$$

The emissivity depends on the wavelength. However, in several applications, the emissivity average is typically considered. Note that the monochromatic emissivity of graybodies is independent of wavelength. However, real bodies do not meet this specification. Therefore, it is often possible to choose suitable average values.

In general, the intensity of the thermal radiation passing between surfaces is not affected by the presence of transparent intermediate media. Most surfaces can be treated as diffuse emitters and reflectors of radiation. The analysis of radiative heat transfer between surfaces involves determining the fraction of total diffuse radiation leaving one surface and being intercepted by another and vice versa. Figure A.18 shows radiative heat exchange between two black elementary areas.

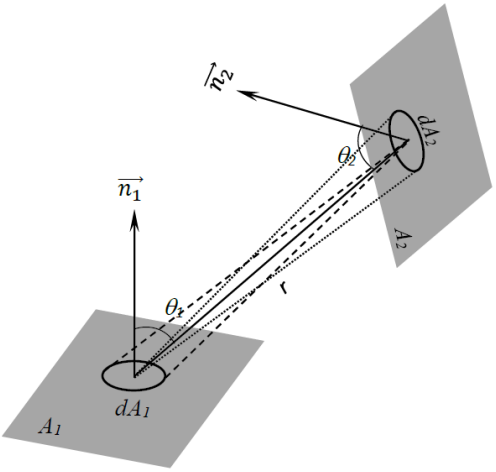

Figure A.18. *Shape factor for radiative heat exchange*

The radiation leaving dA_1 and arriving at dA_2 is given according to the projected elementary area and the solid angle from dA_1 to dA_2:

$$d\phi_{1\to 2} = I_1 cos(\theta_1)\, dA_1 d\omega_{1-2} \qquad [A.112]$$

where the solid angle subtended by the receiving surface dA_2 with respect to the central point of dA_1 is given by:

$$d\omega_{1-2} = cos(\theta_2)\frac{dA_2}{r^2} \quad [A.113]$$

I_1 is the radiation intensity from dA_1. The radiation rate can be written as:

$$d\phi_{1\to 2} = E_{b1}\, dA_1\, \frac{cos(\theta_1)\, cos(\theta_2) dA_2}{\pi\, r^2} \quad [A.114]$$

Similarly, the fraction of the radiation emitted from dA_2 that reaches $dA1$ is given as:

$$d\phi_{2\to 1} = E_{b2}\, dA_2 \frac{cos(\theta_1)\, cos(\theta_2) dA_1}{\pi\, r^2} \quad [A.115]$$

The net rate of radiation between the entire areas A_1 and A_2 is obtained by integrating the fraction over both surfaces:

$$\phi_{2\rightleftharpoons 1} = (E_{b1} - E_{b2}) \int_{A_1}\int_{A_2} \frac{cos(\theta_1)\, cos(\theta_2) dA_1 dA_2}{\pi\, r^2} \quad [A.116]$$

The net rate is given as a function of the shape-form defined as:

$$\begin{cases} F_{1-2} = \dfrac{1}{A_1} \displaystyle\int_{A_1}\int_{A_2} \frac{cos(\theta_1)\, cos(\theta_2) dA_1 dA_2}{\pi\, r^2} \\ F_{2-1} = \dfrac{1}{A_2} \displaystyle\int_{A_1}\int_{A_2} \frac{cos(\theta_1)\, cos(\theta_2) dA_1 dA_2}{\pi\, r^2} \end{cases} \quad [A.117]$$

The net rate of radiation is then given as:

$$\phi_{2\rightleftharpoons 1} = (E_{b1} - E_{b2})\, A_1\, F_{1-2} = (E_{b1} - E_{b2})\, A_2\, F_{2-1} \quad [A.118]$$

In this formulation, the two surfaces were considered black:

$$\phi_{2\rightleftharpoons 1} = \sigma\, A_1\, F_{1-2}(T_1^4 - T_2^4) = \sigma\, A_2\, F_{2-1}(T_1^4 - T_2^4) \quad [A.119]$$

For graybodies, the emissivity must be considered according to the geometrical scenarios.

$$\begin{aligned}\phi_{2\rightleftharpoons1} &= \sigma\, A_1\, F_{1-2}(\varepsilon_1 T_1^4 - \varepsilon_2 T_2^4) \\ &= \sigma\, A_2\, F_{2-1}(\varepsilon_1 T_1^4 - \varepsilon_2 T_2^4)\end{aligned} \quad [A.120]$$

An effective emissivity can be introduced to express the net rate radiation by considering the emissivity and reflectivity of each area. For this, the radiosity J is considered to take into account both the emitted and reflected radiations:

$$\begin{cases} J_1 = \varepsilon_1 \sigma\, T_1^4 + (1-\varepsilon_1)\, G_1 \\ J_2 = \varepsilon_2 \sigma\, T_2^4 + (1-\varepsilon_2)\, G_2 \end{cases} \quad [A.121]$$

where G_1 and G_2 represent the incident rates of radiation for areas A_1 and A_2, respectively.

The net flux emitted or received by each surface is given by:

$$\begin{cases} \phi_1 = A_1(J_1 - G_1) \\ \phi_2 = A_2(J_2 - G_2) \end{cases} \quad [A.122]$$

If the surfaces are enclosed, the energy leaving one surface is entirely absorbed by the other. In this case:

$$A_1 G_1 = A_2 G_2 \quad [A.123]$$

Note that the intensity of the incident radiation received by a surface comes from the radiosity of the other surface:

$$\begin{cases} G_1 = J_2 \\ G_2 = J_1 \end{cases} \quad [A.124]$$

With these considerations, the net rate of radiation is expressed by:

$$\begin{aligned}\phi_{2\rightleftharpoons1} &= \sigma\, A_1\, F_{1-2}\, \varepsilon_{eff}(T_1^4 - T_2^4) \\ &= \sigma\, A_2\, F_{2-1}\, \varepsilon_{eff}(T_1^4 - T_2^4)\end{aligned} \quad [A.125]$$

where the general formulation of the effective emissivity considering each area with its own emissivity is given as:

$$\frac{1}{\varepsilon_{eff}} = \frac{1}{\varepsilon_1} + \frac{A_1}{A_2}\left(\frac{1}{\varepsilon_2} - 1\right) \quad [A.126]$$

When the surfaces are very large, the effective emissivity is given by the following relation:

$$\frac{1}{\varepsilon_{eff}} = \frac{1}{\varepsilon_1} + \frac{1}{\varepsilon_2} - 1 \qquad [A.127]$$

References

Abdallah, S. and Badran, O.O. (2008). Sun tracking system for productivity enhancement of solar still. *Desalination*, 220(1–3), 669–676.

Abdallah, S. and Nijmeh, S. (2004). Two axes sun tracking system with PLC control. *Energy Convers. Manag.*, 45(11–12), 1931–1939.

Abdelghani-Idrissi, M.A., Bagui, F., Estel, L. (2001). Analytical and experimental response time to flow rate step along a counter flow double pipe heat exchanger. *Int. J. Heat Mass Transfer*, 44(19), 3721–3730.

Abdelghani-Idrissi, M.A., Seguin, D., Vernières, L., Mouhab, M. (2015). Thermal convexity of tubular heat exchangers in steady state. *Journal of Advanced Thermal Science Research*, 2(2), 54–63.

Abu-Khader, M.M., Badran, O.O., Abdallah, S. (2008). Evaluating multi-axes suntracking system at different modes of operation in Jordan. *Renew. Sustain. Energy Rev.*, 12(3), 864–873.

Ahmad, A., Prakash, O., Kausher, R., Kumar, G., Pandey, S., Hasnain, S.M. (2024). Parabolic trough solar collectors: A sustainable and efficient energy source. *Mat. Sci. Energy Technol.*, 7, 99–106.

Al-Mamun Md., R., Roy, H., Islam, M.S., Ali, M.R., Hossain, M.I., Saad Aly, M.A., Khan, M.Z.H, Marwani, H.M, Islam, A., Haque, E. et al. (2023). State-of-the-art in solar water heating (SWH) systems for sustainable solar energy utilization: A comprehensive review. *Solar Energy*, 264, 111998.

Al-Mohamad, A. (2004). Efficiency improvements of photovoltaic panels using a suntracking system. *Appl. Energy*, 79(3), 345–354.

Ansari, M.R. and Mortazavi, V. (2006). Simulation of dynamical response of a countercurrent heat exchanger to inlet temperature or mass flow rate change. *Applied Thermal Eng.*, 26(17–18), 2401–2408.

ASHRAE (2005). *ASHRAE Handbook: Fundamentals*. ASHRAE Research, Atlanta.

Ataer, Ö. (2004). An approximate method for transient behavior of finned-tube cross-flow heat exchangers. *Int. J. Ref.*, 27(5), 529–539.

Ayompe, L.M., Duffy, A., McCormack, S.J., Conlon, M. (2011). Validated TRNSYS model for forced circulation solar water heating systems with flat plate and heat pipe evacuated tube collectors. *Appl. Therm. Eng.*, 31(8–9), 1536–1542.

Bailey, W.J. (1909). Solar heater. Patent US966070A, 480,954.

Bakos, G.C. (2006). Design and construction of a two-axis sun tracking system for parabolic trough collector (PTC) efficiency improvement. *Renew. Energy*, 31(15), 2411–2421.

Baum, H.P. and Gordon, J.M. (1984). Geometric characteristics of ideal nonimaging (CPC) solar collectors with cylindrical absorber. *Sol. Energy*, 33(5), 455–458.

Bellos, E. and Tzivanidis, C. (2017). Energetic and financial sustainability of solar assisted heat pump heating systems in Europe. *Sustain. Cities Soc.*, 33, 70–84.

Bellos, E. and Tzivanidis, C. (2018). Analytical expression of parabolic trough solar collector performance. *Designs*, 2(1), 9.

Bernard, J. (2004). *Energie solaire calculs et optimisation*. Ellipses, Paris.

Brichambaut, C.P. and Vauge, C. (1982). *Le gisement solaire. Evaluation de la ressource énergétique*. Tec-Doc Lavoisier, Paris.

Burch, J., Christensen, C., Salasovich, J., Thornton, J. (2004). Simulation of an unglazed collector system for domestic hot water and space heating and cooling. *Solar Energy*, 77(4), 399–406.

Butti, K. and Perlin, J. (eds) (1979). Early solar water heaters. In *A Golden Thread*. Van Nostrand Reinhold Company, New York.

Butti, K. and Perlin, J. (1981). *A Golden Thread*. Van Nostrand Reinhold Company, New York.

Buzás, J. and Kicsiny, R. (2014). Transfer functions of solar collectors for dynamical analysis and control design. *Renewable Energy*, 68, 146–155.

Canada, J., Utrillas, M.P., Martinez-Lozano, J.A., Pedros, Gomez-Amo, J.L., Maj, A. (2007). Design of a sun tracker for the automatic measurement of spectral irradiance and construction of an irradiance database in the 330–1100 nm range. *Renew. Energy*, 32(12), 2053–2068.

Churchill, S.W. and Chu, H.S. (1975). Correlating equations for laminar and turbulent free convection from a vertical plate. *International Journal of Heat and Mass Transfer*, 18(11), 1323–1329.

Claesson, J. (2005). Correction of logarithmic mean temperature difference in a compact brazed plate evaporator assuming heat flux governed flow boiling heat transfer coefficient. *International Journal of Refrigeration*, 28(4), 573–578.

Clifford, M.J. and Eastwood, D. (2004). Design of a novel passive solar tracker. *Sol. Energy*, 77(3), 269–280.

Cui, X., Chua, K.J., Islam, M.R., Yang, W.M. (2014). Fundamental formulation of a modified LMTD method to study indirect evaporative heat exchangers. *Energy Conversion and Management*, 88, 372–381.

Duffie, J.A. and Beckman, W.A. (2013). *Solar Engineering of Thermal Processes*, 4th edition. John Wiley & Sons, New York.

Esen, M. (2004). Thermal performance of a solar cooker integrated vacuum-tube collector with heat pipes containing different refrigerants. *Solar Energy*, 76(6), 751–757.

Fakheri, A. (2007). Heat exchanger efficiency. *ASME J. Heat Transfer*, 129(9), 1268–1276.

Fakheri, A. (2014). Efficiency analysis of heat exchangers and heat exchanger network. *Int. J. Heat Mass Transfer*, 76, 99–104.

Göğüs, Y.A. and Ataer, O.E. (1996). Transient behavior of heat exchangers, In *International Symposium on Transient Convective Heat Transfer*, Padet, F. and Arnc, F. (eds). Begell House Digital Library, Danbury.

Góngora-Gallardo, G., Castro-Gil, M., Colmenar-Santos, A., Tawfik, M. (2013). Efficiency factors of solar collectors of parallel plates for water. *Solar Energy*, 94, 335–343.

Gueguen, R., Sahuquet, G., Tessoneaud, M., Sans, J.-L., Guillot, E., Le Gal, A., Garcia, R., Mer, S., Toutant, A., Bataille, F., Flamant, G. (2023). Heat transfer in a fluidized bed tubular solar receiver. On-sun experimental investigation. *Solar Energy*, 265, 112118.

Guide AICVF (2004). *Eau chaude sanitaire, concevoir les systèmes : recommandation AICVF 2-2004*. AICVF, Paris.

Hischier, I., Hess, D., Lipinski, W., Modest, M., Steinfeld, A. (2009). Heat transfer analysis of a novel pressurized air receiver for concentrated solar power via combined cycles. *Journal of Thermal Science and Engineering Applications*, 1(4), 041002.

Hossain, M.S., Saidur, R., Fayaz, H., Rahim, N.A., Islam, M.R., Ahamed, J.U., Rahman, M.M. (2011). Review on solar water heater collector and thermal energy performance of circulating pipe. *Renew. Sustain. Energy Rev.*, 15(8), 3801–3812.

Hottel, H.C. and Woertz, B.B. (1942). The performance of flat plate solar heat collectors. *Trans. Am. Soc. Mech. Eng.*, 64(2), 91–104.

Hsieh, C.K. (1981). Thermal analysis of CPC collectors. *Sol. Energy*, 27(1), 19–29.

Huang, B.J., Ding, W.L., Huang, Y.C. (2011). Long-term field test of solar PV power generation using one-axis 3-position sun tracker. *Sol. Energy*, 85(9), 1935–1944.

Ibrahim, O., Fardoun, F., Younes, R., Louahlia-Gualous, H. (2014). Review of water-heating systems: General selection approach based on energy and environmental aspects. *Build. Environ.*, 72, 259–286.

IEA (2021). *World Energy Balances*. IEA, Paris [Online]. Available at: https://www.iea.org/data-and-statistics/data-product/world-energy-balances.

Incropera, F.P. and DeWitt, D.P. (1996). *Fundamentals of Heat and Mass Transfer*, 4th edition. John Wiley & Sons, New York.

Jadhav, A.S., Gudekar, A.S., Patil, R.G., Kale, D.M., Panse, S.V., Joshi, J.B. (2013). Performance analysis of a novel and cost effective CPC system. *Energ. Conver. Manage.*, 66, 56–65.

Jamar, A., Majid, Z.A.A., Azmi, W.H., Norhafana, M., Razak, A.A. (2016). A review of water heating system for solar energy applications. *Int. Commun. Heat Mass Transfer*, 76, 178–187.

Jurges, I.W. (1924). *Der Wärmeübergang an einer ebenen Wand*. Druck und Verlag von R. Oldenbourg, Munich.

Kakaç, S. and Liu, H. (2002). *Heat Exchanger: Selection, Rating, and Thermal Design*. CRC Press, Boca Raton.

Kalogirou, S.A. (1996). Design and construction of a one-axis sun tracking. *Sol. Energy*, 7(6), 465–469.

Kalogirou, S.A. (2004). Solar thermal collectors and applications. *Prog Energy Combust. Sci.*, 30(3), 231–295.

Kalogirou, S.A. (2013). *Solar Energy Engineering: Processes and Systems*. Academic Press, New York.

Kays, W.M. and London, A.L. (1998). *Compact Heat Exchangers*, 3rd edition. McGraw Hill, New York.

Kemp, C.M. (1891). Climax solar water heater. US Patent No. 451384.

Khalfallaoui, S., Seguin, D., Abdelghani-Idrissi, M.A., Mouhab, N., Miller, A., Ip, K. (2011). Theoretical and experimental unsteady-state thermal behaviour of domestic solar water heating. *Int. J. Sustainable Energy*, 3(30), 129–148.

Khalifa, A.-J.N. and Al-Mutawalli, S.S. (1998). Effect of two-axis sun tracking on the performance of compound parabolic concentrators. *Energy Convers. Manag.*, 39(10), 1073–1079.

Klein, S. (1975). Calculation of flat plate collector loss coefficients. *Sol. Energy*, 17, 79–80.

Klemens, P.G. (1969). Theory of the thermal conductivity of solids. In *Thermal Conductivity*, volume 1, Tye, R.P. (ed.). Academic Press, London.

Lachi, M., El Wakil, N., Padet, J. (1995). Comportement transitoire des échangeurs bitubes fonctionnant avec débits variables. In *Colloque Interuniversitaire Franco-Québecois. Thermique des Systèmes à Température Modérée*, Sherbrooke.

Lu, J., Ding, J., Yang, J., Yang, X. (2013). Nonuniform heat transfer model and performance of parabolic trough solar receiver. *Energy*, 59, 666–675.

Luna, G., Franco, G., Carrasco, D., Domínguez, R., García, J. (2018). Integration of the experimental results of a parabolic trough collector (PTC) solar plant to an absorption air-conditioning system. *Applied Sci.*, 8(11), 2163.

Malinowski, L. and Bielski, S. (2004). An analytical method for calculation of transient temperature field in the counter-flow heat exchangers. *Int. Comm. Heat Mass Transfer*, 31(5), 683–691.

McAdams, W.H. (1954). *Heat Transmission*, 3rd edition. McGraw-Hill, Tokyo.

McLaughlin, E. (1969). Theory of the thermal conductivity of fluids. In *Thermal Conductivity*, volume 2, Tye, R.P. (ed.). Academic Press, London.

Mousazadeh, H., Keyhani, A., Javadi, A., Mobli, H., Abrinia, K., Sharifi, A. (2009). A review of principle and sun-tracking methods for maximizing solar systems output. *Renew. Sustain. Energy Rev.*, 13(8), 1800–1818.

Noie, S.H. (2006). Investigation of thermal performance of an air-to-air thermosyphon heat exchanger using ε-NTU method. *Appl. Thermal Eng.*, 26(5–6), 559–567.

Olalde, G. and Pierrot, A. (1988). High temperature honeycomb solar receiver for gas heating. In *Advances In Solar Energy Technology. Proceedings of the Biennial Congress of the International Solar Energy Society*, Bloss, W.H. and Pfisterer, F. (eds). Pergamon Press, Oxford.

Pierson, P. and Padet, J. (1985). Evaluation des transferts thermoconvectifs en régime instationnaire. Approche théorique et expérimentale. *Int. J. Therm. Sc.*, 287(287), 781–788.

Pierson, P. and Padet, J. (1988). Étude théorique et expérimentale des échangeurs en régime thermique instationnaire : simulation d'une phase de relaxation. *Int. J. Heat Mass Transfer*, 31(8) , 1577–1586.

Pomianowski, M.Z., Johra, H., Marszal-Pomianowska, A., Zhang, C. (2020). Sustainable and energy-efficient domestic hot water systems: A review. *Renew. Sustain. Energy Rev.*, 128, 109900.

Poulek, V., Khudysh, A., Libra, M. (2016). Self-powered solar tracker for Low Concentration PV (LCPV) systems. *Sol. Energy*, 127, 109–112.

Pranesh, V., Velraj, R., Christopher, S., Kumaresan, V. (2019). A 50 year review of basic and applied research in compound parabolic concentrating solar thermal collector for domestic and industrial applications. *Sol. Energy*, 187, 293–340.

Pucar, M. and Despic, A. (2005). The effect of diffuse/indirect light on the energy gain of solar thermal collectors. *Renew. Energy*, 30(11), 1749–1758.

Ranong, C.N. and Roetzel, W. (2002). Steady-state and transient behaviour of two heat exchangers coupled by a circulating flowstream. *International J. of Thermal Sci.*, 41(11), 1029–1043.

Ratzel, A., Hickox, C., Gartling, D. (1979). Techniques for reducing thermal conduction and natural convection heat losses in annular receiver geometries. *J. Heat Transfer*, 101(1), 108–113.

Rezk, H. and Eltamaly, A.M. (2012). A comprehensive comparison of different MPPT techniques for photovoltaic systems. *Sol. Energy*, 112, 1–11.

Ritchie, H., Roser, M., Rosado, P. (2020). Renewable energy. *Our World in Data* [Online]. Available at: https://ourworldindata.org/renewable-energy.

Rohsenow, W.M., Hartnett, J.P., Ganic, E.N. (1985). *Handbook of Heat Transfer Applications*. McGraw Hill, New York.

Rübel, A. (1976). Solar concentrators with maximal concentration for cylindrical absorbers. *Appl. Opt.*, 15(7), 1871–1873.

Saini, M., Sharma, A., Singh, V.P., Dwivedi, G., Jain, S. (2022). Solar thermal receivers – A review. In *Advancement in Materials, Manufacturing and Energy Engineering*, volume II, Verma, P., Samuel, O.D., Verma, T.N., Dwivedi, G. (eds). Springer, Singapore.

Salunkhe, P.B. and Krishna, D.J. (2017). Investigations on latent heat storage materials for solar water and space heating applications. *J. Storage Mater.*, 12, 243–260.

dos Santos Bernardes, M.A. and Aurélio, M. (2010). Solar chimney power plants – Developments and advancements. In *Solar Energy*, Rugescu, R.D. (ed.). InTech, Rijeka.

Serth, R.W. (2014). Heat exchangers. In *Process Heat Transfer*, 2nd edition, Serth, R.W. and Lestina, T. (eds). Academic Press, San Diego.

Shah, R. (2006). Advances in science and technology of compact heat exchangers. *Heat Transfer Eng.*, 27(5), 3–22.

Sharples, S. and Charlesworth, P.S. (1998). Full-scale measurements of wind-induced convective heat transfer from a roof-mounted flat plate solar collector. *Solar Energy*, 62(2), 69–77.

Tagliafico, L.A., Scarpa, F., De Rosa, M. (2014). Dynamic thermal models and CFD analysis for flat-plate thermal solar collectors – A review. *Renewable and Sustainable Energy Reviews*, 30, 526–537.

Tripathy, A.K., Ray, S., Sahoo, S.S., Chakrabarty, S. (2018). Structural analysis of absorber tube used in parabolic trough solar collector and effect of materials on its bending: A computational study. *Sol. Energy*, 163, 471–485.

Vengadesan, E. and Senthil, R. (2020). A review on recent development of thermal performance enhancement methods of flat plate solar water heater. *Sol. Energy*, 206, 935–961.

Wattmuff, J.H., Charters, W.W.S., Proctor, D. (1977). Solar and wind induced external coefficients for solar collectors. *Revue internationale d'heliotechnique*, 2, 56.

Winston, R. and Hinterberger, H. (1975). Principles of cylindrical concentrators for solar energy. *Sol. Energy*, 17(4), 255–258.

de Winter, F. (1994). Twenty-year progress report on the copper development association do-it-yourself solar swimming pool heating manual and on the associated prototype heater. *Solar Energy*, 53(1), 33–36.

de Winter, F. (2014). An owner-built solar swimming pool heater and the associated do-it-yourself manual after 40 years of operation and experience. *Energy Procedia*, 57, 2914–2919.

Zhou, X and Xu, Y. (2016). Solar updraft tower power generation. *Sol. Energy*, 128, 95–125.

Index

C, D

collectors
  cylindrical-parabolic, 36
  model(s), 139
domestic hot water, 73, 77, 83, 161–163, 166–168, 170, 177

E, F

energy
  efficiency, 1, 9, 13, 36, 66, 67, 77, 92, 148, 159, 163
  sustainable, 1, 2, 5, 14, 15, 17, 23, 36, 72, 73
fluid heat exchange, 120

H, N

heat
  exchanger(s), 9, 37, 41, 56, 62, 71, 73–75, 81, 82, 115, 116, 124–138, 143–146, 175
  transfer, 14, 15, 23, 34, 37, 39–44, 46, 47, 49–64, 68, 71, 73, 75, 78, 81–89, 93, 94, 99, 101–103, 115, 116, 120, 123, 124, 126–128, 134, 135, 138, 140, 141, 143, 146, 160, 161, 163, 165, 174, 180
net zero emissions (NZEs), 3, 4

S, T

solar
  collector(s), 11–13, 22–24, 26–28, 73–75, 78, 82–89, 92, 93, 104, 140–143, 158, 160, 161, 170–178, 180, 181, 186, 188, 190
  energy development, 5, 7
  sustainable development goals (SDGs), 3
  thermal system(s), 11–13, 57, 60, 63–65, 69, 70, 72, 73, 77, 81, 82, 158–160
temperature modeling, 138
thermal model, 139
tower plants, 13, 31, 33
transient behavior, 116

Other titles from

in

Mechanical Engineering and Solid Mechanics

2025

LEROY Maurice
Rheology, Physical and Mechanical Behavior of Materials 4: Rigidity and Resistance of Composite Materials, Sizings of Laminate
Rheology, Physical and Mechanical Behavior of Materials 5: Fractures and Fatigue of Metal and Composites

EL HAMI Abdelkhalak
Methods and Applications of Artificial Intelligence: Dynamic Response, Learning, Random Forest, Linear Regression, Interoperability, Additive Manufacturing and Mechatronics
(Artificial Intelligence in Mechanics Set – Volume 2)

EL HAMI Abdelkhalak, RADI Bouchaïb
Multi-physics Optimization: Mechanics, Fluid Interaction Structure, Shaping, Stochastic Finite Elements, Random Vibrations, Fatigue
(Reliability of Multiphysical Systems Set – Volume 20)

2024

LE VAN Anh
Contact in Structural Mechanics: A Weighted Residual Approach

LEROY Maurice
Rheology, Physical and Mechanical Behavior of Materials 2: Working at High Strain Rates, Forming, Sintering, Joining and Welding
Rheology, Physical and Mechanical Behavior of Materials 3: Rigidity and Resistance of Materials, Sizings, Pieces and Structures

SAOUAB Abdelghani, CHAMPMARTIN Stéphane, KHALID NACIRI Jaafar
Some Complex Phenomena in Fluid and Solid Mechanics
(Mathematical and Mechanical Engineering Set – Volume 13)

2023

EL HAMI Abdelkhalak
Uncertainty and Artificial Intelligence: Additive Manufacturing, Vibratory Control, Agro-composite, Mechatronics
(Artificial Intelligence in Mechanics Set – Volume 1)

EL HAMI Abdelkhalak, EID Mohamed
Reliability-based Modeling of System Performance
(Reliability of Multiphysical Systems Set – Volume 19)

EL HAMI Abdelkhalak, DELAUX David, GRZESKOWIAK Henri
Applied Reliability for Industry 1: Predictive Reliability for the Automobile, Aeronautics, Defense, Medical, Marine and Space Industries
(Reliability of Multiphysical Systems Set – Volume 16)
Applied Reliability for Industry 2: Experimental Reliability for the Automobile, Aeronautics, Defense, Medical, Marine and Space Industries
(Reliability of Multiphysical Systems Set – Volume 17)
Applied Reliability for Industry 3: Operational Reliability for the Automobile, Aeronautics, Defense, Medical, Marine and Space Industries
(Reliability of Multiphysical Systems Set – Volume 18)

LEROY Maurice
Rheology, Physical and Mechanical Behavior of Materials 1: Physical Mechanisms of Deformation and Dynamic Behavior

2022

BAYLE Franck
Product Maturity 1: Theoretical Principles and Industrial Applications (Reliability of Multiphysical Systems Set – Volume 12)
Product Maturity 2: Principles and Illustrations (Reliability of Multiphysical Systems Set – Volume 13)

EL HAMI Abdelkhalak, DELAUX David, GRZESKOWIAK Henri
Reliability and Physics-of-Healthy in Mechatronics (Reliability of Multiphysical Systems Set – Volume 15)

LANNOY André
Reliability of Nuclear Power Plants: Methods, Data and Applications (Reliability of Multiphysical Systems Set – Volume 14)

LEDOUX Michel, EL HAMI Abdelkhalak
Heat Transfer 3: Convection, Fundamentals and Monophasic Flows (Mathematical and Mechanical Engineering Set – Volume 11)
Heat Transfer 4: Convection, Two-Phase Flows and Special Problems (Mathematical and Mechanical Engineering Set – Volume 12)

PLANCHETTE Guy
Cindynics, The Science of Danger: A Wake-up Call (Reliability of Multiphysical Systems Set – Volume 11)

2021

CHALLAMEL Noël, KAPLUNOV Julius, TAKEWAKI Izuru
Modern Trends in Structural and Solid Mechanics 1: Static and Stability
Modern Trends in Structural and Solid Mechanics 2: Vibrations
Modern Trends in Structural and Solid Mechanics 3: Non-deterministic Mechanics

DAHOO Pierre Richard, POUGNET Philippe, EL HAMI Abdelkhalak
Applications and Metrology at Nanometer Scale 1: Smart Materials, Electromagnetic Waves and Uncertainties
(Reliability of Multiphysical Systems Set – Volume 9)
Applications and Metrology at Nanometer Scale 2: Measurement Systems, Quantum Engineering and RBDO Method
(Reliability of Multiphysical Systems Set – Volume 10)

LEDOUX Michel, EL HAMI Abdelkhalak
Heat Transfer 1: Conduction
(Mathematical and Mechanical Engineering Set – Volume 9)
Heat Transfer 2: Radiative Transfer
(Mathematical and Mechanical Engineering Set – Volume 10)

2020

SALENÇON Jean
Elastoplastic Modeling

2019

BAYLE Franck
Reliability of Maintained Systems Subjected to Wear Failure Mechanisms: Theory and Applications
(Reliability of Multiphysical Systems Set – Volume 8)

BEN KAHLA Rabeb, BARKAOUI Abdelwahed, MERZOUKI Tarek
Finite Element Method and Medical Imaging Techniques in Bone Biomechanics
(Mathematical and Mechanical Engineering Set – Volume 8)

IONESCU Ioan R., QUEYREAU Sylvain, PICU Catalin R., SALMAN Oguz Umut
Mechanics and Physics of Solids at Micro- and Nano-Scales

LE VAN Anh, BOUZIDI Rabah
Lagrangian Mechanics: An Advanced Analytical Approach

MICHELITSCH Thomas, PÉREZ RIASCOS Alejandro, COLLET Bernard, NOWAKOWSKI Andrzej, NICOLLEAU Franck
Fractional Dynamics on Networks and Lattices

SALENÇON Jean
Viscoelastic Modeling for Structural Analysis

VÉNIZÉLOS Georges, EL HAMI Abdelkhalak
Movement Equations 5: Dynamics of a Set of Solids
(Non-deformable Solid Mechanics Set – Volume 5)

2018

BOREL Michel, VÉNIZÉLOS Georges
Movement Equations 4: Equilibriums and Small Movements
(Non-deformable Solid Mechanics Set – Volume 4)

FROSSARD Etienne
Granular Geomaterials Dissipative Mechanics: Theory and Applications in Civil Engineering

RADI Bouchaib, EL HAMI Abdelkhalak
Advanced Numerical Methods with Matlab® 1: Function Approximation and System Resolution
(Mathematical and Mechanical Engineering Set – Volume 6)
Advanced Numerical Methods with Matlab® 2: Resolution of Nonlinear, Differential and Partial Differential Equations
(Mathematical and Mechanical Engineering Set – Volume 7)

SALENÇON Jean
Virtual Work Approach to Mechanical Modeling

2017

BOREL Michel, VÉNIZÉLOS Georges
Movement Equations 2: Mathematical and Methodological Supplements
(Non-deformable Solid Mechanics Set – Volume 2)
Movement Equations 3: Dynamics and Fundamental Principle
(Non-deformable Solid Mechanics Set – Volume 3)

BOUVET Christophe
Mechanics of Aeronautical Solids, Materials and Structures
Mechanics of Aeronautical Composite Materials

BRANCHERIE Delphine, FEISSEL Pierre, BOUVIER Salima, IBRAHIMBEGOVIC Adnan
From Microstructure Investigations to Multiscale Modeling: Bridging the Gap

CHEBEL-MORELLO Brigitte, NICOD Jean-Marc, VARNIER Christophe
From Prognostics and Health Systems Management to Predictive Maintenance 2: Knowledge, Traceability and Decision (Reliability of Multiphysical Systems Set – Volume 7)

EL HAMI Abdelkhalak, RADI Bouchaib
Dynamics of Large Structures and Inverse Problems (*Mathematical and Mechanical Engineering Set – Volume 5*)
Fluid-Structure Interactions and Uncertainties: Ansys and Fluent Tools (Reliability of Multiphysical Systems Set – Volume 6)

KHARMANDA Ghias, EL HAMI Abdelkhalak
Biomechanics: Optimization, Uncertainties and Reliability (Reliability of Multiphysical Systems Set – Volume 5)

LEDOUX Michel, EL HAMI Abdelkhalak
Compressible Flow Propulsion and Digital Approaches in Fluid Mechanics (Mathematical and Mechanical Engineering Set – Volume 4)
Fluid Mechanics: Analytical Methods (Mathematical and Mechanical Engineering Set – Volume 3)

MORI Yvon
Mechanical Vibrations: Applications to Equipment

2016

BOREL Michel, VÉNIZÉLOS Georges
Movement Equations 1: Location, Kinematics and Kinetics (Non-deformable Solid Mechanics Set – Volume 1)

BOYARD Nicolas
Heat Transfer in Polymer Composite Materials

CARDON Alain, ITMI Mhamed
New Autonomous Systems
(Reliability of Multiphysical Systems Set – Volume 1)

DAHOO Pierre Richard, POUGNET Philippe, EL HAMI Abdelkhalak
Nanometer-scale Defect Detection Using Polarized Light
(Reliability of Multiphysical Systems Set – Volume 2)

DORMIEUX Luc, KONDO Djimédo
Micromechanics of Fracture and Damage
(Micromechanics Set – Volume 1)

EL HAMI Abdelkhalak, RADI Bouchaib
Stochastic Dynamics of Structures
(Mathematical and Mechanical Engineering Set – Volume 2)

GOURIVEAU Rafael, MEDJAHER Kamal, ZERHOUNI Noureddine
From Prognostics and Health Systems Management to Predictive Maintenance 1: Monitoring and Prognostics
(Reliability of Multiphysical Systems Set – Volume 4)

KHARMANDA Ghias, EL HAMI Abdelkhalak
Reliability in Biomechanics
(Reliability of Multiphysical Systems Set –Volume 3)

MOLIMARD Jérôme
Experimental Mechanics of Solids and Structures

RADI Bouchaib, EL HAMI Abdelkhalak
Material Forming Processes: Simulation, Drawing, Hydroforming and Additive Manufacturing
(Mathematical and Mechanical Engineering Set – Volume 1)

DE SAXCÉ Géry, VALLÉE Claude
Galilean Mechanics and Thermodynamics of Continua

2015

JEBAHI Mohamed, ANDRE Damien, TERREROS Inigo, IORDANOFF Ivan
Discrete Element Method to Model 3D Continuous Materials
Discrete Element Model and Simulation of Continuous Materials Behavior Set – Volume 1

JEBAHI Mohamed, DAU Frédéric, CHARLES Jean-Luc, IORDANOFF Ivan
Discrete-continuum Coupling Method to Simulate Highly Dynamic Multi-scale Problems: Simulation of Laser-induced Damage in Silica Glass
Discrete Element Model and Simulation of Continuous Materials Behavior Set – Volume 2

KARLIČIĆ Danilo, MURMU Tony, ADHIKARI Sondipon, MCCARTHY Michael
Non-local Structural Mechanics

SAB Karam, LEBÉE Arthur
Homogenization of Heterogeneous Thin and Thick Plates

2014

ATANACKOVIC M. Teodor, PILIPOVIC Stevan, STANKOVIC Bogoljub, ZORICA Dusan
Fractional Calculus with Applications in Mechanics: Vibrations and Diffusion Processes
Fractional Calculus with Applications in Mechanics: Wave Propagation, Impact and Variational Principles

CIBLAC Thierry, MOREL Jean-Claude
Sustainable Masonry: Stability and Behavior of Structures

ILANKO Sinniah, MONTERRUBIO Luis E., MOCHIDA Yusuke
The Rayleigh−Ritz Method for Structural Analysis

LALANNE Christian
Mechanical Vibration and Shock Analysis – 5-volume series – 3rd edition
Sinusoidal Vibration – Volume 1
Mechanical Shock – Volume 2
Random Vibration – Volume 3
Fatigue Damage – Volume 4
Specification Development – Volume 5

LEMAIRE Maurice
Mechanics and Uncertainty

2013

ADHIKARI Sondipon
Structural Dynamic Analysis with Generalized Damping Models: Analysis
Structural Dynamic Analysis with Generalized Damping Models: Identification

BAILLY Patrice
Materials and Structures under Shock and Impact

BASTIEN Jérôme, BERNARDIN Frédéric, LAMARQUE Claude-Henri
Non-smooth Deterministic or Stochastic Discrete Dynamical Systems: Applications to Models with Friction or Impact

EL HAMI Abdelkhalak, RADI Bouchaib
Uncertainty and Optimization in Structural Mechanics

KIRILLOV Oleg N., PELINOVSKY Dmitry E.
Nonlinear Physical Systems: Spectral Analysis, Stability and Bifurcations

LUONGO Angelo, ZULLI Daniele
Mathematical Models of Beams and Cables

SALENÇON Jean
Yield Design

2012

DAVIM J. Paulo
Mechanical Engineering Education

DUPEUX Michel, BRACCINI Muriel
Mechanics of Solid Interfaces

ELISHAKOFF Isaac *et al.*
Carbon Nanotubes and Nanosensors: Vibration, Buckling and Ballistic Impact

GRÉDIAC Michel, HILD François
Full-Field Measurements and Identification in Solid Mechanics

GROUS Ammar
Fracture Mechanics – 3-volume series
Analysis of Reliability and Quality Control – Volume 1
Applied Reliability – Volume 2
Applied Quality Control – Volume 3

RECHO Naman
Fracture Mechanics and Crack Growth

2011

KRYSINSKI Tomasz, MALBURET François
Mechanical Instability

LAMBERT Stéphane, NICOT François
Rockfall Engineering

SOUSTELLE Michel
An Introduction to Chemical Kinetics

2010

BREITKOPF Piotr, FILOMENO COELHO Rajan
Multidisciplinary Design Optimization in Computational Mechanics

DAVIM J. Paulo
Biotribology

PAULTRE Patrick
Dynamics of Structures

SOUSTELLE Michel
Handbook of Heterogenous Kinetics

2009

BERLIOZ Alain, TROMPETTE Philippe
Solid Mechanics using the Finite Element Method

LEMAIRE Maurice
Structural Reliability

2007

GIRARD Alain, ROY Nicolas
Structural Dynamics in Industry

GUINEBRETIÈRE René
X-ray Diffraction by Polycrystalline Materials

KRYSINSKI Tomasz, MALBURET François
Mechanical Vibrations

KUNDU Tribikram
Advanced Ultrasonic Methods for Material and Structure Inspection

SIH George C., NAÏT-ABDELAZIZ Moussa, VU-KHANH Toan
Particle and Continuum Aspects of Mesomechanics

WILEY END USER LICENSE AGREEMENT

Go to www.wiley.com/go/eula to access Wiley’s ebook EULA.